The effect of Fe and Al on the elasticity of akimotoite

DISSERTATION

zur Erlangung des akademischen Grades einer Doktorin

der Naturwissenschaften (Dr. rer. nat.)

in der Bayreuther Graduiertenschule für Mathematik und Naturwissenschaften (BayNAT)

der Universität Bayreuth

vorgelegt von

Nicki Caroline Siersch

aus *Göppingen*

Bayreuth, 2019

This doctoral thesis was prepared at the Bayerisches Geoinstitut at the University of Bayreuth from November 2015 until November 2019 and was supervised by Prof. Dr. Daniel Frost and Dr. Tiziana Boffa Ballaran.

This is a full reprint of the thesis submitted to obtain the academic degree of Doctor of Natural Sciences (Dr. rer. nat.) and approved by the Bayreuth Graduate School of Mathematical and Natural Sciences (BayNAT) of the University of Bayreuth.

Date of submission: 15.11.2019

Date of defence: 05.12.2019

Acting director: Prof. Dr. Markus Lippitz

Doctoral committee:

Prof. Dr. Daniel Frost	(reviewer)
PD Dr. Gerd Steinle-Neumann	(reviewer)
Prof. Dr. David Rubie	(chairman)
Prof. Dr. Hauke Marquardt	

Table of contents

Summary

The Earth's transition zone between 410 and 660 km depth is a region of raised seismic wave velocity gradients separating the upper and lower mantle and is also marked by a number of seismic discontinuities. Mineralogical models for peridotitic and mid-ocean ridge basalt (MORB) lithologies fail to reproduce the high seismic velocities indicated by reference models for the base of the transition zone (~550-660 km), due to the prevalence of majoritic garnet in these lithologies, which propagates seismic waves relatively slowly. A lower average mantle temperature at the base of the transition zone due to an accumulation of subducted lithosphere would be one way to explain the higher velocities. However, a further possibility is that the mantle at this depth contains melt depleted harzburgite material where majoritic garnet is replaced by the mineral akimotoite.

Akimotoite is an $MgSiO_3$ polymorph stable between 20 and 25 GPa and 900 to 2200 K and if present it might be responsible for raising the seismic wave velocities. Additional seismic discontinuities identified near the base of the transition zone might also be attributed to phase transitions involving akimotoite, as could some seismic anisotropy observations. The objectives of this study were to determine the elastic properties, anisotropic behavior and structural evolution of $MgSiO_3$ akimotoite up to transition zone pressures. Furthermore, the effects of Al and Fe on the elasticity of akimotoite were investigated at high pressures and high temperatures. This enabled seismic wave velocities of relevant mantle lithologies to be accurately determined at these conditions and, through a comparison with seismic reference models, constraints were placed on the composition of the lower transition zone.

In the first part of the study, large single-crystals of $MgSiO_3$ akimotoite were synthesized and used to investigate the full elastic tensor by means of single-crystal Brillouin spectroscopy up to transition zone pressures. In combination with single-crystal X-ray diffraction, the bulk and axial compressibility of the same crystals were studied. Results show that the wave velocities of $MgSiO_3$ akimotoite are faster than those of majoritic garnet. Furthermore, akimotoite remains a highly anisotropic mineral at the base of the transition zone even though the anisotropy decreases with pressure. Akimotoite axial compressibility is highly anisotropic because oxygens of the face-sharing octahedra lie along the *a*-axis and form a very stiff unit along that direction.

In the second part of this study, the crystal chemistry of the $MgSiO_3$ akimotoite $– Al_2O_3$ corundum solid solution was investigated through X-ray structure determinations on eight single-crystals of different composition. The unit-cell volume change across the akimotoite-corundum solid solution is near linear but the lattice parameters deviate strongly from ideality. Furthermore, the influence of Al on the elasticity of akimotoite was studied on two polycrystalline Al-bearing akimotoite samples up to 25 GPa and 1100 K using ultrasonic interferometry combined with synchrotron X-ray diffraction and radiography in a large volume press. A decrease in wave velocities was observed with increasing Al content. This is an unexpected result since wave velocities in corundum are much faster than in akimotoite. This strongly non-ideal behavior means that corundum properties cannot be employed as those of the akimotoite Al_2O_3 end-member, as previously assumed. By the same argument it is unlikely that akimotoite is an effective $MgSiO_3$ end-member of corundum.

The effect of Fe^{2+} substitution on the elastic properties of a polycrystalline akimotoite sample were investigated in the third part of this study using ultrasonic interferometry and synchrotron X-ray diffraction up to 26 GPa and 800 K. The incorporation of Fe was also found to reduce the compressional and shear wave velocities. This effect is further increased when substituting both Fe and Al into the akimotoite structure, which was investigated up to 23 GPa. The coupled substitution of Fe^{3+} and Al into $MgSiO_3$ akimotoite is shown to have a major effect on the structure, most likely as a result of Al and Fe^{3+} being randomly distributed across both cation sites.

Lastly, the obtained elastic properties of $MgSiO_3$ akimotoite and those of Fe- and Al-bearing solid solutions were used to calculate the elastic properties of fictive $FeSiO_3$ and Al_2O_3 akimotoite end-members. These data were used both in a thermodynamic model to determine the phase relations of akimotoite in a harzburgite assemblage between 20.5 and 23 GPa and to calculate the seismic velocity for this assemblage along a mantle adiabat. Above 22 GPa, the wave velocities for harzburgite, in contrast to peridotite and MORB lithologies, are found to be in excellent agreement with seismic reference models. The observation of multiple discontinuities in the proximity of the 660 km discontinuity is consistent with the sharp transformation of garnet to akimotoite determined to occur between 600 and 625 km. These observations provide strong evidence for the accumulation of harzburgitic material at the base of the transition zone.

Zusammenfassung

Die Übergangszone zwischen dem oberen und unteren Erdmantel in 410 bis 660 km Tiefe, ist eine Region mit erhöhten seismischen Wellengeschwindigkeitsgradienten, die mehrere seismische Diskontinuitäten aufweist. Mineralogische Modelle für peridotitische oder basaltische Zusammensetzungen, die zu großen Teilen aus Majorit-reichem Granat mit relativ niedrigen Wellenausbreitungsgeschwindigkeiten bestehen, können die hohen seismischen Geschwindigkeiten der Referenzmodelle im unteren Teil der Übergangszone (~550-660 km) nicht erklären. Eine durch die Anhäufung subduzierter Lithosphäre verringerte Durchschnittstemperatur in der unteren Übergangszone kann höhere Geschwindigkeiten verursachen. Eine weitere Möglichkeit zur Erhöhung der seismischen Geschwindigkeiten ist zudem die Umwandlung von Majorit-Granat zu Akimotoit in einer harzburgitischen Zusammensetzung.

Akimotoit ist ein $MgSiO_3$-Polymorph, welches zwischen 20 und 25 GPa und 900 bis 2200 K stabil ist und sich durch hohe seismische Geschwindigkeiten auszeichnet. Sowohl seismische Diskontinuitäten an der Basis der Übergangszone als auch Beobachtungen von seismischen Anisotropien könnten durch die Präsenz von Akimotoit erklärbar sein. Ziel dieser Arbeit war es daher, die elastischen Eigenschaften, sowie die Anisotropie und das strukturelle Verhalten von $MgSiO_3$-Akimotoit bis zu Drücken der Übergangszone zu untersuchen. Zudem wurde der Einfluss des Al- und Fe-Gehalts auf die Elastizität von Akimotoit unter hohem Druck und hoher Temperatur bestimmt. Mit Hilfe der Ergebnisse dieser Arbeit konnten die seismischen Geschwindigkeiten relevanter Zusammensetzungen neu berechnet und – durch Vergleich mit seismischen Referenzmodellen – die Zusammensetzung der unteren Übergangszone besser eingegrenzt werden.

Im ersten Teil dieser Arbeit wurden große $MgSiO_3$-Akimotoit-Einkristalle synthetisiert, um mit Hilfe der Brillouin-Spektroskopie den elastischen Tensor dieses Minerals bis hin zu Drücken der Übergangszone zu bestimmen. Diese Messungen wurden mit Röntgenbeugung an Einkristallen kombiniert, um die Volumen- und Axialkompressibilität zu untersuchen. Die Ergebnisse zeigen eine deutliche Zunahme der Wellengeschwindigkeiten durch Akimotoit im Vergleich zu Majorit-reichem Granat. Zusätzlich konnte gezeigt werden, dass Akimotoit im Vergleich zu anderen Mineralen der unteren Übergangszone eine deutlich höhere seismische Anisotropie aufweist,

wobei diese mit zunehmendem Druck abnimmt. Auch die axiale Kompressibilität in Akimotoit ist stark anisotrop, da die Sauerstoffatome entlang der *a*-Achse eine relativ starre Einheit bilden.

Im zweiten Teil der Arbeit wurden Strukturbestimmungen an acht Einkristallen der $MgSiO_3$-Akimotoit - Al_2O_3-Korund Mischkristallreihe mit Hilfe von Röntgenbeugung durchgeführt. Die Änderung des Einheitsvolumens in dieser Mischkristallreihe ist annähernd linear, die Gitterparameter hingegen weichen stark von denen einer idealen Mischung ab. Der Einfluss von Al auf die elastischen Eigenschaften von Akimotoit wurde mit Hilfe von Ultraschallinterferometrie kombiniert mit energiedispersiver Röntgenbeugung und Radiographie *in-situ* an zwei polykristallinen, Al-reichen Akimotoit Proben bis 25 GPa und 1100 K untersucht. Die seismischen Wellengeschwindigkeiten nehmen mit steigendem Al-Gehalt in der Probe ab. Dieses Ergebnis widerspricht den Erwartungen, dass sie zwischen den höheren Wellengeschwindigkeiten der Endglieder Akimotoit und Korund liegen und Korund das effektive Englied für Akimotoit bildet. Durch diese Erkenntnis ist zudem zu erwarten, dass Akimotoit kein effektives Endglied für Korund darstellt.

Der Einfluss von Fe^{2+}-Substitution auf die elastischen Eigenschaften von Akimotoit wurde mit Hilfe von Ultraschallinterferometrie und Synchrotron-Röntgenbeugung bis 26 GPa und 800 K untersucht. Dadurch wurde gezeigt, dass die Inkorporation von Fe^{2+} in die Akimotoit-Struktur ebenfalls eine Abnahme der Wellengeschwindigkeiten zur Folge hat. Dieser Effekt wird verstärkt, wenn zusätzlich Al eingebaut wird, was bis 23 GPa untersucht wurde. Die gekoppelte Substitution von Fe^{3+} und Al hat einen signifikanten Einfluss auf die Akimotoit Struktur, was höchstwahrscheinlich durch die ungeordnete Verteilung von Fe^{3+} und Al auf den beiden Kation-Positionen verursacht wird.

Mit Hilfe der elastischen Eigenschaften aller untersuchten Al- und Fe-reichen Mischkristallreihen konnten die elastischen Parameter der fiktiven $FeSiO_3$- und Al_2O_3-Akimotoit-Endglieder berechnet werden. Anhand dieser Daten konnten sowohl die Phasenanteile in einer harzburgitischen Zusammensetzung zwischen 20.5 und 23 GPa entlang einer Manteladiabate bestimmt, als auch die seismischen Geschwindigkeiten für diese Zusammensetzung berechnet werden. Im Gegensatz zu peridotitischen und basaltischen Zusammensetzungen stimmen die neu berechneten Wellengeschwindigkeiten für Harzburgit mit denen der seismischen Referenzmodelle überein. Zudem passt die Beobachtung mehrerer Diskontinuitäten in der Nähe der 660 km-Diskontinuität zum scharfen Übergang von Granat zu Akimotoit in 600 bis 625 km

Tiefe. Diese Übereinstimmung unterstützt die Annahme einer Ansammlung von harzburgitischen Material in der unteren Übergangszone.

1. Introduction

1.1 The Earth's mantle

1.1.1 Insights into the Earth

The internal division of the Earth into three main layers, namely the crust, mantle and core with further subdivision into the upper mantle, transition zone, lower mantle, outer and inner core can be directly obtained from the analysis of seismic observations of body waves and normal modes. Compressional seismic waves (P-waves) are waves which give rise to a displacement of the medium parallel to the propagation direction. Shear waves (S-waves) on the other hand are waves which give rise to a displacement of the medium perpendicular to the propagation direction and travel slower than compressional waves. Both P- and S-waves are triggered by earthquakes all around the globe. After travelling through the Earth, they are detected by seismometer stations distributed across the Earth's surface and the travel times of direct and reflected waves provide the most direct and precise information on the structure of the deep interior of the Earth. Although in most cases the picture of seismic properties that emerges is globally or at best regionally averaged, the interpretation of such seismic travel time information still provides one of the only mechanisms through which to determine the composition and temperature of the deep interior. This is important since the Earth's bulk composition is still uncertain but is a crucial factor in determining how and from what the Earth was formed. Similarly, the chemistry and temperature distribution in the interior provides information on how mantle convection influences the chemical evolution of the Earth. The interpretation of seismic wave velocities in the Earth's transition zone, between approximately 410 and 660 km depth, has, in particular, been employed to support models for the long term evolution and dynamics of the Earth's mantle (Anderson and Bass 1986; Ringwood 1994). The raised velocity gradients (Agee 1998), the proximity of numerous seismic discontinuities (Shearer 2000) and observations of the stagnation of subducting slabs (Fukao et al. 2009, 2013) not only make this region of particular interest but also provide numerous independent constraints that could be interpreted with suitable mineral physical information.

1.1.2 Seismic reference models

The two seismic reference models mainly referred to are the preliminary Earth reference model (PREM, Dziewonski and Anderson 1981) and AK135 (Kennet et al. 1995) and are plotted in Figure 1-1. They are both radially symmetric velocity-depth profiles based on the global inversion of normal modes, surface wave and body wave data (Dziewonski and Anderson 1981, Kennet et al. 1995). Both models assume that discontinuities inside the Earth are located at a certain depth and therefore refine a set of functions for each layer individually to obtain the velocities and density through the Earth's interior. Discontinuities between layers are characterized by rapid changes in wave velocities and density (Figure 1-1) and are linked to chemical or structural changes of the mineral assemblages stable at respective pressures and temperatures.
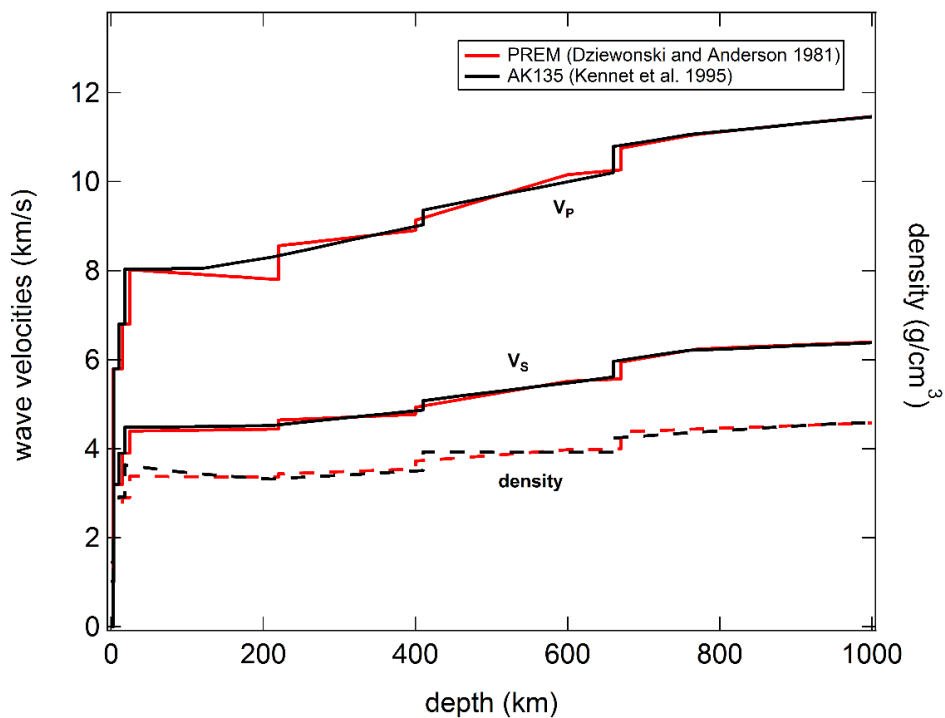
Figure 1-1: *Seismic reference models PREM (red, Dziewonski and Anderson 1981) and AK135 (black, Kennet et al. 1995) versus depth down to the mid lower mantle. Compressional and shear wave velocities are shown as well as the density determined from both models that use slightly different seismic data and constraints.*

A different approach was performed by Cammarano et al. (2005) who fit global seismic data against a simple mineralogical model assuming a pyrolitic bulk composition with phase transitions and an adiabatic temperature gradient through the Earth with a whole mantle convection. They found that a pyrolitic upper mantle and transition zone is compatible with the global seismic data under the set constraints and that coupled variations in velocity gradients and discontinuity amplitudes in the transition zone can still fit the same seismic data set.

1.1.3 Mineralogical models

Xenolith rock samples from the Earth's mantle are derived only from the top ~250 km of the lithosphere, which in most cases has been altered by the processes of partial melting and metasomatism compared to the underlying asthenosphere or what might be considered the pristine mantle. Diamonds containing mineral inclusions from the transition zone and possibly the lower mantle (e.g. Stachel et al. 2005, Thomson et al. 2014) have been identified but their rarity implies that it is impossible to judge how typical these minerals are for these regions and many seem to be derived from non-peridotite source rocks. In order to constrain the mineralogy of the Earth's deeper interior, the mineralogy of the Earth has been investigated experimentally by making assumptions on the bulk chemical composition. One of the most generally employed compositions for this purpose is pyrolite, a proposed primitive mantle composition obtained by mixing the known products of mantle melting with the residue i.e. a mixture comprised of a 1:4 ratio of MORB (mid oceanic ridge basalt) and harzburgite components, respectively (Ringwood 1962, see Table 1-1). Using this composition, the Earth's upper mantle between ~6 to 410 km depth has been found to predominantly contain the minerals olivine, garnet and pyroxenes (e.g. Frost 2008). At the 410 km discontinuity, olivine changes its structure to the denser β-phase, called wadsleyite and to the spinel-structured γ-phase called ringwoodite at 520 km depth. The transition zone (410 to 660 km) consists mainly of wadsleyite or ringwoodite, garnets and some amount of Ca-perovskite at greater depths (e.g. Frost 2008). The 660 km discontinuity marks the transition between the upper mantle and lower mantle believed to be mainly caused by the transition from ringwoodite to bridgmanite and magnesiowüstite. In the lower mantle ranging from 660 to 2900 km depth mainly bridgmanite is stable coexisting with magnesiowüstite and Ca-perovskite (e.g. Frost 2008).

In order to link seismic wave velocities observed from seismic measurements to specific minerals stable in the deep Earth, the elastic properties bulk modulus K and shear modulus G of minerals need to be investigated experimentally. The bulk modulus describes the incompressibility of a material and the shear modulus describes the rigidity of a material in response to shear stress. With those two parameters it is possible to calculate the compressional (v_P) and shear wave velocities (v_S) through the studied material of known density following the Adams-Williamson equations:

$$v_P = \sqrt{\frac{K + \frac{4}{3}G}{\rho}} \text{ and } v_S = \sqrt{\frac{G}{\rho}}.$$

1.2 The 660 km-discontinuity: boundary between the upper and lower mantle

Studies on whether the upper and lower mantle are composed of the same material led to conflicting results in the past. While Ringwood (1962) suggested a mantle solely made of a peridotitic composition, there are geochemical and geophysical evidences that the Earth's lower mantle may have a different composition than the upper mantle with an enrichment in Si (Liu 1982, Hart and Zinder 1986, O'Neill and Palme 1998, Weidner and Wang 2000, Murakami et al. 2012). Many of these studies have implied a chondritic composition for the lower mantle with a Mg/Si ratio of 1.0, similar to the ratio in chondritic meteorites, instead of a peridotitic composition with a Mg/Si ratio of 1.3 (Murakami et al. 2012). The most compelling evidence to support this is that the seismic wave velocities of the lower mantle do not fit experimentally determined wave velocities of lithologies with upper mantle composition (e.g. Murakami et al. 2012, Kurnosov et al. 2017). Further evidence supporting a compositional stratification of the Earth's mantle is the stagnation of subducting slabs at the base of the transition zone shown in Figure 1-2 (Fukao et al. 2001, 2009, Fukao and Obayashi 2013) indicating a separated mantle convection in both parts of the mantle.

However, in some cases slabs can also penetrate the 660-discontinuity and sink down to the core-mantle boundary (e.g. Central American arc) (Fukao et al. 2001, 2009, Fukao and Obayashi 2013) which then trigger upwelling plumes from the D'' layer and get erupted as ocean-island-basalts (OIB) (Campbell and O'Neill 2012). Such a mechanism could lead to a mixing of the

whole mantle but still there is the possibility that only the base of the lower mantle is influenced and the bulk of the lower mantle still remains isolated (Ballmer et al. 2017).
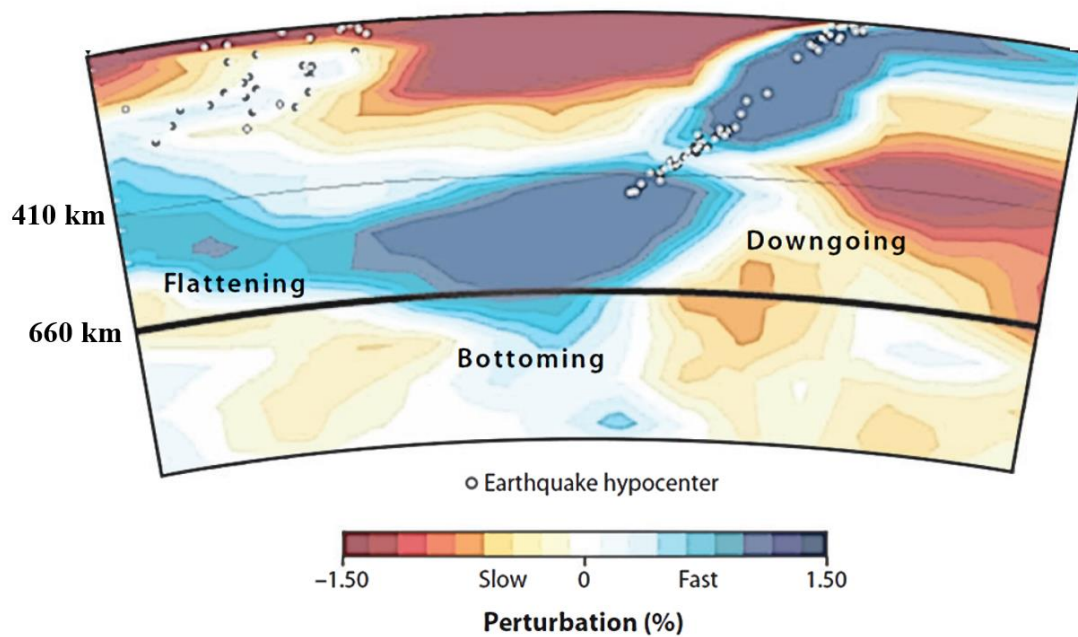
Figure 1-2: *Tomographic image of a subducting slab flattening out horizontally above the 660 km-discontinuity (indicated by the thick black line) in the Izu-Bonin subduction arc (modified from Fukao et al. 2009). The blue shaded areas represent fast cold areas (e.g. the cold slab) through which waves travel faster. The areas in red represent the hot surrounding mantle with slower wave propagation.*

Understanding whether the 660 km-discontinuity is caused by a simple phase transformation or also represents a boundary between two distinct chemical reservoirs is therefore crucial for constraining the composition of the lower mantle.

1.2.1 Phase relations at the 660 km-discontinuity

The two main minerals stable in the lower part of the transition zone between 520 and 660 km depth in a pyrolitic mineral assemblage are ringwoodite and majoritic garnet (e.g. Frost 2008, see

Table 1-1). When using the elastic parameters of these two minerals to calculate the mineralogical models of a pyrolitic bulk mantle composition, the resulting velocities fail to reproduce the seismic velocity profile of the transition zone (Dziewonski and Anderson 1981, Kennet et al. 1995), especially at its base close to the 660 km-discontinuity. The mineralogical models systematically underestimate the wave velocities for both compressional (~0.15 km/s) and shear wave velocities (~0.25 km/s). This discrepancy can be mainly attributed to the relatively slow wave velocities of majoritic garnet (e.g. Irifune et al. 2008, Pamato 2014, Pamato et al. 2016). One possible explanation is the stagnation and accumulation of slab material at the 660 km-discontinuity that was observed in several tomographic studies (e.g. Van der Hilst et al. 1991, Fukao et al. 2001, 2009 Fukao and Obayashi 2013), which could raise velocities through creating globally significant chemical or thermal anomalies. Subducting slabs have a distinct stratification consisting of three layers: a top layer of mid-ocean-ridge basalt (MORB), a harzburgite middle layer and a pyrolitic bottom layer (see Ringwood and Irifune 1988, Figure 1-3). Proposed average compositions of these three lithologies are reported in Table 1-1.

Table 1-1: Compositions of the three dry lithologies stable in a slab environment: pyrolite (Sun 1982), harzburgite (Michael and Bonatti 1985) and mid-ocean ridge basalt (MORB) (Green et al. 1979).

	pyrolite	harzburgite	MORB
SiO_2	44.5	43.6	50.4
TiO_2	0.2		0.6
Al_2O_3	4.3	0.7	16.1
Cr_2O_3	0.4	0.5	
FeO	8.6	7.8	7.7
MgO	38.0	46.4	10.5
CaO	3.5	0.5	13.1
Na_2O	0.4		1.9
K_2O	0.1		0.1

Depth (km)

Basalt/gabbro crust	
	6.5
Residual harzburgite 82 % Ol 18 % Opx	
	30
Residual lherzolite Ol + Opx + Cpx	
	40
Depleted pyrolite 62 % Ol 38 % Opx, Cpx, Gnt	
	80
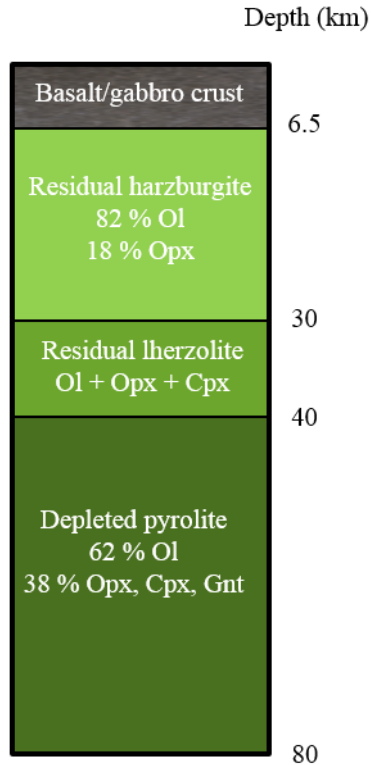
Figure 1-3: Schematic cross section through a subducting slab, modified after Ringwood and Irifune (1988). The three main layers in this approximately 80 km thick slab are a basaltic crust layer on top (MORB), a middle harzburgite layer and a depleted pyrolite layer at the bottom.

The MORB layer is denser than the harzburgite and pyrolite layers all the way down to 650 km depth due to a higher Al_2O_3 content stabilizing the dense garnet component (Ringwood and Irifune 1988). This stabilization of garnet due to a larger Al_2O_3 content, however, leads to a sharp reversal in the MORB density relative to pyrolite between 650 and 730 km depth because the garnet component in MORB transforms to the even denser bridgmanite over a wider depth range than in pyrolite, which contains less Al_2O_3 (Ringwood and Irifune 1988). The harzburgite layer on the other hand is less dense than the pyrolite layer due to a depletion in Al_2O_3 and FeO resulting in the formation of less garnet (Ringwood and Irifune 1988). Between 570 and 640 km depth, both lithologies form mostly ringwoodite and garnet making their densities very similar. Harzburgite, however, becomes denser than pyrolite between 650 to 690 km depth due to less amounts of garnet and therefore the formation of bridgmanite whereas the garnet in pyrolite remains stable to larger depths (Ringwood and Irifune 1988). Due to the density contrasts in these three layers between 650 to 700 km depth, it was suggested that harzburgite is gravitationally

13

stable in this region and may form globally stratified layers of ancient subducted lithosphere around the 660 km-discontinuity, which were referred to as "megaliths" by Ringwood and Irifune (1988). Following the suggestion of stable harzburgite and MORB layers at the base of the transition zone, seismic wave velocities were modelled based on the mineral assemblages of these two lithologies (e.g. Irifune and Ringwood 1987). It was found, however, that also these modelled wave velocities underrepresented the compressional and shear wave velocities of the two seismic reference models PREM and AK135 (Pamato 2014, Pamato et al. 2016).

Another important observation is that subducted slabs do not equilibrate rapidly with the environment of the hot mantle (Ringwood and Irifune 1988). This means that in areas where cold subducting slab material is accumulated around the 660 km-discontinuity, the temperature could be significantly lower (~400 K, suggested by Ringwood and Irifune 1988) than the average mantle geotherm. In this colder environment, majoritic garnet becomes (partially) unstable with respect to akimotoite (Sawamoto 1987, Gasparik 1990, Hirose 2002, Ishii et al. 2011, Ishii et al. 2019). The amount of akimotoite stable in different lithologies such as pyrolite and harzburgite has been investigated and it was found that at temperatures around 1673-1873 K, akimotoite can make up to 15 vol.% of the harzburgitic mineral assemblage (Irifune and Ringwood 1987, Ishii et al. 2019). For a pyrolitic composition, previous studies reported contradictory results. Hirose (2002) found 15 vol.% of akimotoite forming at 1873 K, however, Ishii et al. (2011, 2018) showed that no akimotoite formed from a pyrolitic composition at these temperatures. The presence of around 10 vol.% akimotoite in a pyrolitic composition was only observed at 1673 K (Ishii et al. 2011). Although akimotoite is not the major phase in those lithologies, its contribution to the seismic properties may still be significant although current data makes this hard to judge.

1.2.2 Observation of anisotropic features and multiple discontinuities around 660 km depth

Another feature that has been observed at the base of the transition zone and uppermost lower mantle is that the 660 km-discontinuity in reality is not one sharp transition but consists of multiple discontinuities (Niu and Kawakatsu 1996, Simmons and Gurrola 2000, Castillo et al. 2001, Ai et al. 2003, see Figure 1-4). Vacher et al. (1998) computed seismic profiles with the mineral physics data available at that time and came to the conclusion that the transition from ringwoodite to Mg-perovskite and Mg-wüstite in combination with the formation of akimotoite at the expense of garnet would form a strong 660 km-discontinuity and smaller seismic gradients at

the top of the lower mantle. Based on a systematic phase relation study, Akaogi et al. (2002) suggested the origin of the multiple discontinuities along the cold mantle geotherm to be the transformation first of garnet to akimotoite between 610 and 690 km depth followed by a sharp velocity increase at 690 km depth when the post-spinel transformation occurs, and another steep velocity gradient between 700 and 740 km depth that corresponds to the akimotoite-bridgmanite transition. They also proposed a high-velocity layer forming when slab material is sitting on the 660 km-discontinuity which has also been discussed before by Weidner and Wang (2000). Wang et al. (2004), however, suggested that this high-velocity layer is a pure akimotoite layer formed in colder slab material surroundings and is not a pile up of subducted slab material.
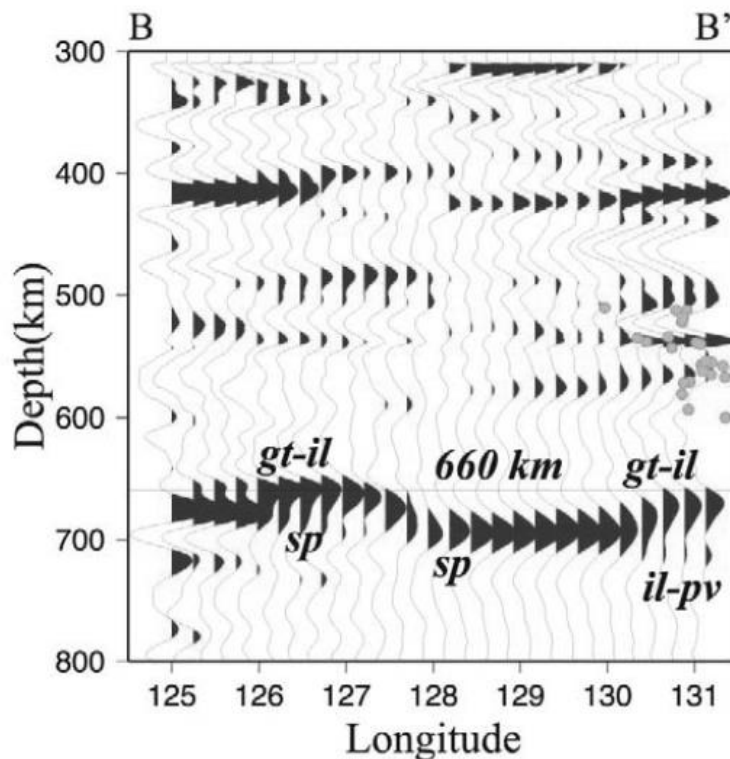
Figure 1-4: Observation of multiple discontinuities around the 660 km-discontinuity (modified from Ai et al. (2003). While the main discontinuity is attributed to the transformation of ringwoodite to bridgmanite and magnesiowüstite, there are two weaker discontinuities detected above and below. The shallower one possibly represents the transformation from garnet (gt) to akimotoite (il) and the deeper one refers to the akimotoite (il) to bridgmanite (pv) transformation.

Such a layer of akimotoite would also likely explain another feature observed from seismic studies which is a large wave velocity anisotropy in the lower part of the transition zone (Wookey et al. 2002, Nowacki et al. 2015) which up until this point had been believed to be mainly

isotropic. Akimotoite was found to be a highly anisotropic mineral (Weidner and Ito 1985, Da Silva et al. 1999, Zhang et al. 2005, Shiraishi et al. 2008) and would be stable in cold slab environments in preference to garnet, hence the anisotropic behavior of akimotoite at the pressures of the lower transition zone is of high interest. Several studies investigated its anisotropic properties using ab initio simulations and molecular dynamics (Da Silva et al. 1999, Zhang et al. 2005) or experiments on polycrystalline samples (Shiraishi et al. 2008). Da Silva et al. (1999) was the first study to report that the anisotropy of akimotoite at transition zone pressures is much larger than the anisotropy of other transition zone phases. Zhang et al. (2005) incorporated his anisotropy results of akimotoite into a modelled phase assemblage with akimotoite, ringwoodite and Ca-perovskite and found that the overall wave velocity anisotropy of this assemblage was significantly lower but had the same anisotropic features as akimotoite. Shiraishi et al. (2008) investigated the crystallographic preferred orientation of akimotoite crystals at high pressure and at different temperatures and was able to explain the different anisotropic features observed in the Northern and Southern segments of the Tonga slab based on the obtained textures of akimotoite.

Akimotoite being stable at the base of the transition zone close to the 660 km-discontinuity at colder temperatures relative to the hot mantle surrounding introduced by subducted slab material could therefore be the missing link to 1) account for the large deviation of the seismic reference models for relevant mantle lithologies, 2) explain the anisotropic features and 3) observations of multiple discontinuities around 660 km depth.

1.3 MgSiO₃ akimotoite

MgSiO$_3$ akimotoite was first synthesized and described by Kawai et al. (1974) and is referred to as MgSiO$_3$ ilmenite (Il) (Horiuchi et al. 1982) because of its FeTiO$_3$ ilmenite-type structure. It was given its name after the high-pressure researcher Syun-iti Akimoto once it was identified in the Tenham chondritic L6 meteorite (Sharp et al. 1997, Tomioka and Fujino 1997). MgSiO$_3$ akimotoite crystallizes in the $R\bar{3}$ space group (No. 147) with a distorted hexagonal closed packed setting. The MgO$_6$ and SiO$_6$ octahedra form alternating face-sharing layers as shown by Horiuchi et al. (1982) (Figure 1-5). The MgO$_6$ octahedra are more distorted than the SiO$_6$ octahedra (Horiuchi et al. 1982) due to a larger shift of the Mg^{2+} cation from their center.
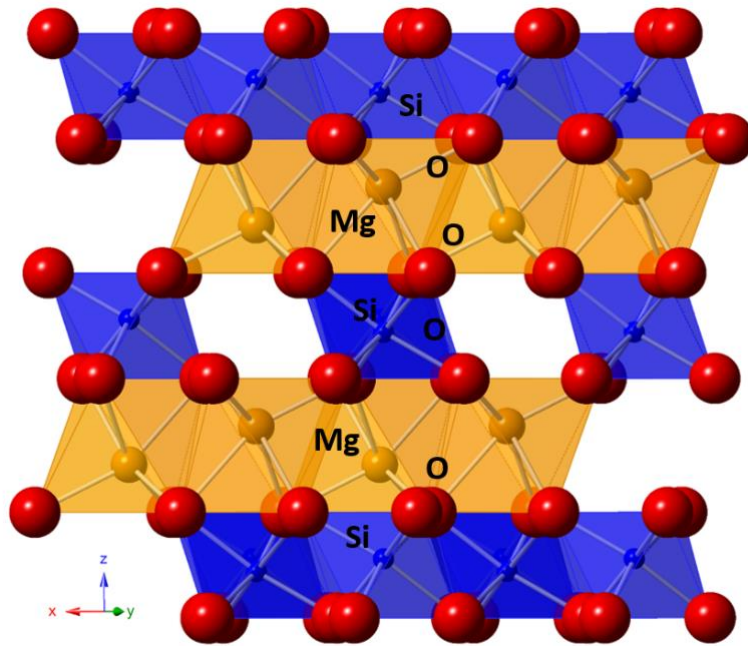
Figure 1-5*: Crystal structure of MgSiO₃ akimotoite in the trigonal space group R$\overline{3}$. The structure consists of alternating layers of MgO₆ and SiO₆ octahedra perpendicular to the c-axis.*

Experiments investigating the phase relation in the $MgSiO_3$ system showed that akimotoite is a stable mineral phase at transition zone and uppermost lower mantle conditions between 18 and 25 GPa and 900 to 2200 K (Ito and Yamada 1982, Sawamoto 1987, Gasparik 1990). The akimotoite-garnet transformation has a positive Clapeyron slope, whereas the akimotoite-bridgmanite transition has a negative Clapeyron slope. The negative slope implies a downward deflection of the akimotoite-bridgmanite phase transition to greater depths relative to the garnet to bridgmanite phase transition having a positive Clapeyron slope (e.g. Weidner and Wang 2000). Sawamoto (1987) interpreted this negative Clapeyron slope between akimotoite and bridgmanite as grounds that mantle convection between the upper and lower mantle would be hindered. Weidner and Wang (2000) argued, on the other hand, that as the volume change from garnet to akimotoite and akimotoite to bridgmanite is similar, the net effect on the buoyancy is the same for the garnet → akimotoite → bridgmanite transition as for the garnet to bridgmanite transition.

Naturally occurring akimotoite was found in the Tenham chondritic L6 meteorite, which mainly consists of olivine and hypersthene and a network of <1 mm thin shock-induced veins (Sharp et al. 1997, Tomioka and Fujino 1997, Miyajima et al. 2007). In these veins, akimotoite crystallized

next to bridgmanite, majorite and ringwoodite (Sharp et al. 1997, Tomioka and Fujino 1997, Miyajima et al. 2007) having a maximum grain size of ~0.3 to 3 µm in length (see Figure 1-6). Analyses of the composition of the crystallized akimotoite grains performed found that akimotoite can incorporate between 3.72-13.54 wt.% FeO, 0.07-10.46 wt.% Al_2O_3, 0.16-0.69 wt.% Cr_2O_3 and 0.00-0.38 wt.% CaO in its structure (Sharp et al. 1997, Tomioka and Fujino 1997, Miyajima et al. 2007). The formation of akimotoite crystals in the shocked veins of a meteorite was discussed by Tschauner et al. (2018) who suggested that akimotoite formed by a prograde solid-solid transformation from orthopyroxene and has not crystallized from a melt which would require a depletion in Fe.
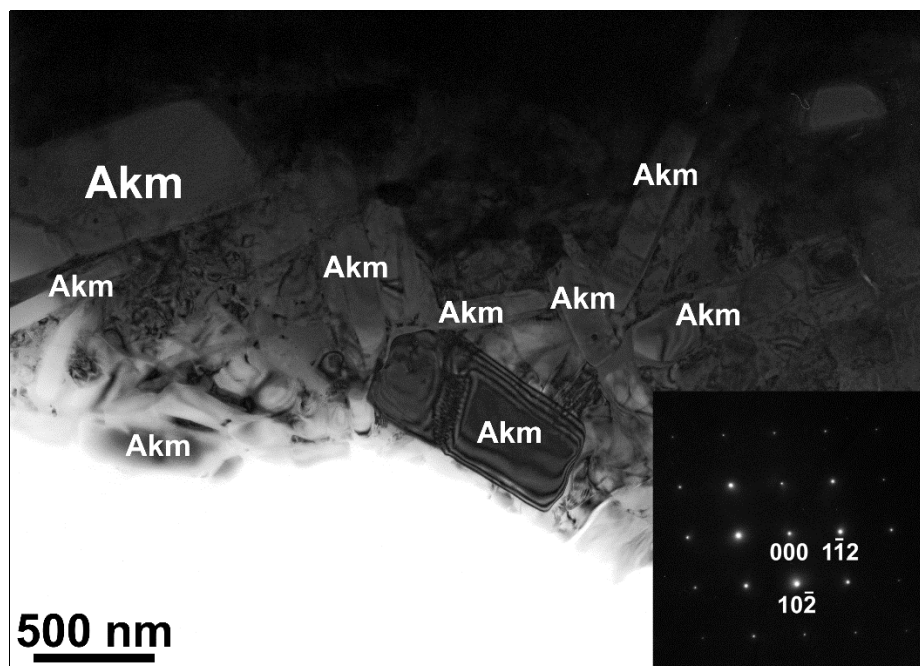
Figure 1-6: Natural occurring akimotoite crystals in shocked veins of the L6 Tenham chondritic meteorite (Photograph courtesy of Nobuyoshi Miyajima). Akimotoite crystallized next to bridgmanite, majorite and ringwoodite forming grains up to 3 µm in size. Natural occurring akimotoite contains varying amounts of FeO and Al_2O_3 and other minor elements (Sharp et al. 1997, Tomioka and Fujino 1997, Miyajima et al. 2007).

Recently, an Fe-analogue of akimotoite was also discovered in the same L6 chondritic meteorite and was named hemleyite (Bindi et al. 2017). The composition of the naturally crystallized Mg-rich hemleyite in the shocked vein of the L6 chondrite was determined to be $(Fe^{2+}_{0.48}Mg_{0.37}Ca_{0.04}Na_{0.04}Mn^{2+}_{0.03}Al_{0.03}Cr^{3+}_{0.01})SiO_3$ and was additionally characterized using X-

ray diffraction, concluding that hemleyite has the same crystal structure as $MgSiO_3$ akimotoite (Bindi et al. 2017).

1.3.1 The influence of Fe and Al on the stability of akimotoite

Since both pyrolitic and harzburgitic compositions contain FeO (8.61 and 7.83 wt.%, respectively, Irifune and Ringwood 1987) and Al_2O_3 (4.31 and 0.65 wt.%, respectively, Irifune and Ringwood 1987) and since it has been found that natural akimotoite crystals in meteorites can incorporate significant amounts of these oxides, it is very likely that the composition of akimotoite in the Earth's mantle is not that of the pure end-member.

The solubility of $FeSiO_3$ into the akimotoite structure was experimentally investigated (see Figure 1-7) using the multi-anvil apparatus and claimed to be limited to 10 mol.% (Ito and Yamada 1982) although the only single-phase akimotoite sample synthesized in their study contained 5 mol.% $FeSiO_3$. Also, in the mentioned study, the phase boundaries among different high-pressure phases are not well constrained (Figure 1-7). With increasing pressure above ~25.5 GPa, Ito and Yamada (1982) proposed a four-phase field of coexisting akimotoite, perovskite, ringwoodite and stishovite or akimotoite, perovskite, magnesiowüstite and stishovite with very narrow stability fields which makes it challenging to investigate the Fe partitioning between akimotoite and these other phases (Ito and Yamada 1982, Kato 1986, Ohtani et al. 1991). Preliminary studies, however, showed that Fe favors the coexisting ringwoodite and majorite garnet over akimotoite (Irifune and Ringwood 1987).

The incorporation of Al into akimotoite follows a coupled substitution: $Mg^{2+} + Si^{4+} = 2\ Al^{3+}$ and was studied extensively (Irifune and Ringwood 1987, Kubo and Akaogi 2000, Akaogi et al. 2002). Al incorporation into the Il-structure (Figure 1-8) was found to be possible up to the pyrope composition $Mg_3Al_2Si_3O_{12}$ (25 mol.% Al_2O_3) between 25 to 27 GPa and 1173 K (Kubo and Akaogi 2000) or around 26 GPa at 1273 K (Akaogi et al. 2002). With increasing temperature to 1873 K, the stability field of akimotoite is limited to an Al_2O_3 content of 2.5 mol.% at pressures between 21 and 23 GPa (Kubo and Akaogi 2000, Akaogi et al. 2002).
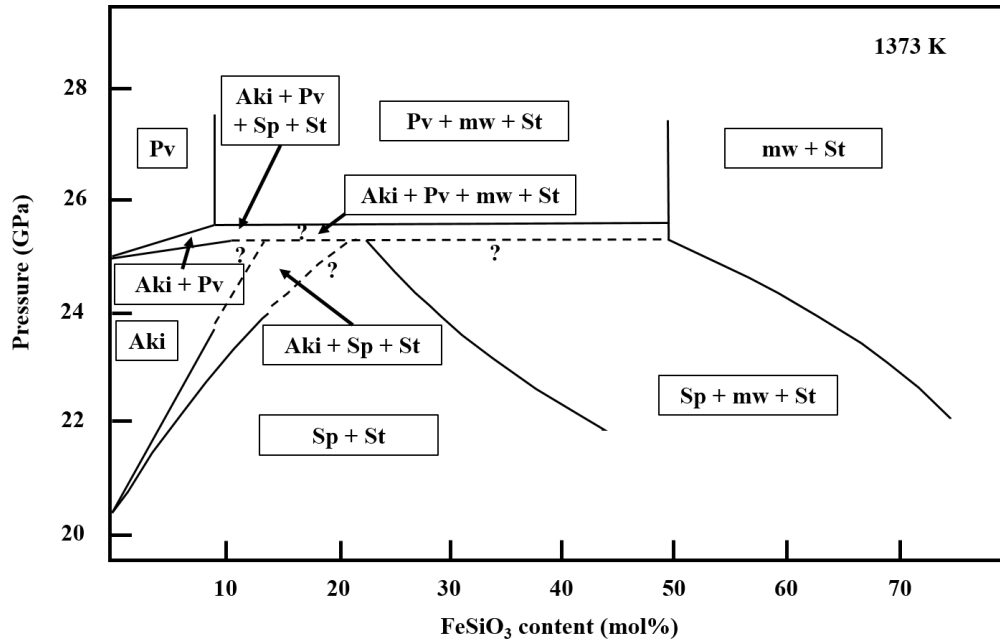
Figure 1-7: *Stability field of akimotoite in the MgSiO₃-FeSiO₃-joint at pressures of the transition zone and uppermost lower mantle at 1373 K (modified after Ito and Yamada 1982). The stability field of akimotoite is not well defined at the FeSiO₃-rich end. Aki: akimotoite, Pv: bridgmanite, Sp: ringwoodite, St: stishovite, mw: magnesiowüstite.*
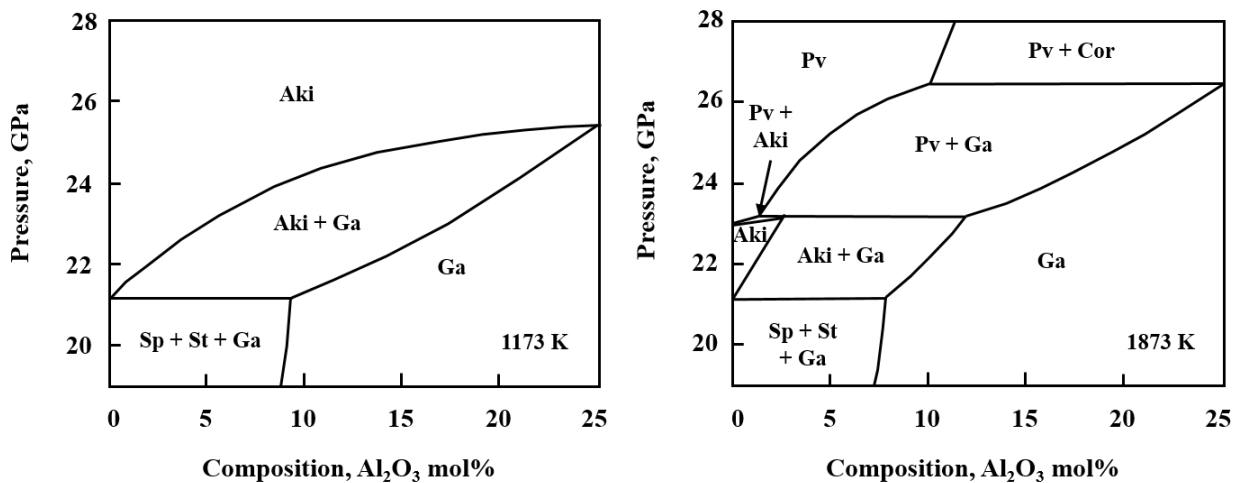
Figure 1-8: *Stability of akimotoite in the MgSiO₃-Mg₃Al₂Si₃O₁₂ joint at 1173 K (left) and 1873 K (right) modified after Kubo and Akaogi (2000) and Akaogi et al. (2002). At lower temperatures pure akimotoite is stable also with the pyrope composition. With increasing temperature, the stability field of akimotoite becomes narrower and at 1873 K akimotoite can have a maximum Al₂O₃ component of ~2.5 mol.%. Aki: akimotoite, Ga: garnet, Sp: ringwoodite, St: stishovite, Pv: bridgmanite, Cor: corundum.*

20

1.3.2 Elastic properties of the MgSiO₃ akimotoite end-member

The elasticity of the MgSiO$_3$ akimotoite end-member has been investigated by several experimental and computational studies (e.g. Weidner and Ito 1985, Reynard et al. 1996, Wang et al. 2004, Zhou et al. 2014, Da Silva et al. 1999, Zhang et al. 2005). The first study to determine the full elastic tensor at room pressure and temperature was performed by Weidner and Ito (1985) who investigated a single-crystal of MgSiO$_3$ akimotoite using Brillouin spectroscopy. These are the only measurements performed on a single-crystal of akimotoite that experimentally determine the elastic coefficients. Reynard et al. (1996) performed a high-pressure equation of state study on MgSiO$_3$ akimotoite on a powdered sample in the diamond anvil cell (DAC) up to 28 GPa using H$_2$O as pressure transmitting medium. They fixed the bulk modulus to K_{S0} = 212 GPa that was previously determined by Weidner and Ito (1985) and fitted a K_0' = 5.6(10) using the ice VII equation of state (Hemley et al. 1987) for pressure determination. The first thermal equation of state was determined by Wang et al. (2004) who conducted synchrotron X-ray diffraction experiments on polycrystalline akimotoite in the large volume press up to 19 GPa and 1373 K. Also in this study, the bulk modulus was fixed to K_{S0} = 212 GPa (K_{T0} = 210 GPa) which resulted in K_{T0}' = 5.6(8), in excellent agreement with Reynard et al. (1996). The latest study that successfully determined both bulk and shear moduli of the MgSiO$_3$ end-member experimentally was conducted by Zhou et al. (2014) using ultrasonic measurements on a polycrystalline akimotoite sample performed up to the actual stability field of akimotoite, 25.7 GPa and 1500 K. The adiabatic bulk modulus was determined to be K_{S0}=219.4(7) GPa which is larger than the bulk modulus obtained by Weidner and Ito (1985) with a K_0' = 4.62(3). The shear modulus G_0 = 132.1(7) GPa (G_0' = 1.63(4)) is instead in excellent agreement with the shear modulus of 132 GPa reported by Weidner and Ito (1985). Since the elastic parameters of akimotoite are larger and the wave velocities faster than those reported for majoritic garnet (K_{S0} = 167(2) GPa and G_0 = 91.8(7) GPa for Py$_{76}$Mj$_{24}$, Pamato et al. (2016), the incorporation of MgSiO$_3$ akimotite into the phase assemblages of pyrolitic and harzburgitic lithologies for wave velocity calculations appears to give a better fit of the seismic velocity profiles (Zhou et al. 2014).

Up to now, however, the elastic properties of akimotoite at high pressure have been only investigated on polycrystalline samples. Therefore, no information on the anisotropic behavior or structural evolution of akimotoite has been obtained, which requires the investigation of a single-

crystal of akimotoite. Additionally, the influence of Fe and Al end-members on the elasticity of akimotoite is unknown but of importance since akimotoite inside the Earth will contain these components. Furthermore, determining the effects of these components on the equation of state of akimotoite is essential for thermodynamic calculations of its stability field. Due to experimental uncertainties and difficulties under the conditions of akimotoite stability such calculations are essential for combining and interpreting the results of various experiments to arrive at firm conclusions concerting its stability field.

1.4 The objectives of this thesis

In order to investigate the elasticity of $MgSiO_3$ akimotoite as well as the effect of Fe and Al on the elastic properties of akimotoite at high pressure and temperature, the objectives of this thesis are the following:

(1) Synthesis of large high-quality single-crystals of $MgSiO_3$ akimotoite containing no impurities and inclusions to allow single-crystal X-ray diffraction and Brillouin spectroscopy measurements to determine the equation of state and elastic tensor of this material as a function of pressure.

(2) To determine the full elastic tensor of akimotoite at pressure and use this to derive aggregate compressional and shear wave velocities at the pressure conditions of $MgSiO_3$ akimotoite stability at the base of the transition zone. Also to constrain the anisotropic behavior of $MgSiO_3$ akimotoite in order to allow the interpretation of regions of seismic anisotropy observed near the 660 km-discontinuity.

(3) To determine the structural evolution of akimotoite at high pressure by making full intensity measurements on a single-crystal as a function of pressure.

(4) To determine the mixing behavior in the $MgSiO_3$ akimotoite - Al_2O_3-corundum solid solution and the structural evolution between the isostructural akimotoite and corundum end-members by performing single-crystal X-ray diffraction measurements at ambient conditions.

(5) To determine the influence of Al and Fe on the wave velocities and elasticity of $MgSiO_3$ akimotoite at high-pressures and temperatures.

(6) To examine the implications for the state of the mantle at the base of the transition zone through the interpretation of seismic velocity profiles taking specific account of akimotoite stability.

2. Methods

2.1 Synthesis of the starting materials

2.1.1 Single-crystals

In order to perform single-crystal elasticity measurements at both ambient and high pressure conditions and to characterize the crystal chemistry of the $(Mg,Al)(Al,Si)O_3$ system, it is crucial to synthesize high-quality single-crystals of several tens of µm in size. Eight single-crystals in the solid solution $MgSiO_3$ akimotoite - Al_2O_3 corundum were synthesized (Table 2-1). The starting material for synthesizing pure $MgSiO_3$ akimotoite single-crystals was produced by mixing the two synthetic oxides MgO and SiO_2 in a 1:1 ratio and grinding it under ethanol for 1h to obtain a homogeneous mixture. This mixture was then placed into a Pt crucible and heated in a high-temperature furnace up to 1873 K where it was kept for 3h. The starting material was then rapidly quenched in an icy water bath to obtain a glass. The glass was ground again for 1h under ethanol and held at 1473 K for 2h to crystallize enstatite. The crystallized starting material was mixed with 15% excess MgO to avoid the growth of stishovite crystals as reported by Shatskiy et al. (2007). The starting mixture was filled into a 3.5 mm long Pt capsule and a drop of H_2O was added as flux material to enhance crystal growth.

For all other single-crystal syntheses, starting materials were prepared from synthetic MgO, SiO_2, Al_2O_3 and $Al(OH)_3$ oxides ground in an agate mortar under ethanol for one hour to produce fine-grained homogenous mixtures. Water in the form of $Al(OH)_3$ was added to facilitate the growth of large single-crystals. The starting materials were heated at 1873 K for 3h and then quenched in an icy water bath into glasses. In two experiments $MgCl_2$ was added as flux material to test whether it would enhance the crystal growth even further (see Table 2-1). Also these starting mixtures were filled into Pt capsules.

All capsules were welded carefully with a Lampert PUK U3 welding device in micro mode (power: 7 %, time: 3-5 ms). The capsules had to be perfectly sealed to prevent the leakage of the solvent or melt produced during the synthesis experiments.

Table 2-1. *Multi-anvil synthesis conditions, resulting run products and sample compositions.*

experiment		starting material	pressure (GPa)	temperature (K)	heating (h)	run products	Composition	crystal size (μm)
S6925	Ak100	$Mg_{1.15}SiO_{3.15}$ + ~15% H_2O	22	1873*	4	akimotoite + melt	$Mg_{0.993(1)}Si_{1.003(1)}O_3$	<500
S7179	Ak99	Ak90Cor10 + ~10% H_2O	22	1773	23	Al_2O_3-rich akimotoite + garnet (+ stishovite)	$Mg_{0.975(8)}Al_{0.016(3)}Si_{1.001(4)}O_3$	<30
I796	Cor75	Ak40Cor60 + $MgCl_2$	27	2300*	3.3	$MgSiO_3$-rich corundum + MgO + melt	$Al_{1.501(9)}Mg_{0.239(5)}Si_{0.260(6)}O_3$	<100
I789	Cor80	Ak40Cor60 + $MgCl_2$	27	2100*	2	$MgSiO_3$-rich corundum + MgO + melt	$Al_{1.599(11)}Mg_{0.192(8)}Si_{0.209(4)}O_3$	<100
S7237a	Cor81	Ak40Cor60 + $MgCl_2$	24	1673*	2	$MgSiO_3$-rich corundum + MgO + melt	$Al_{1.628(12)}Mg_{0.162(4)}Si_{0.186(5)}O_3$	<250
S7156b	Cor92	Ak20Cor80 + ~10% $Al(OH)_3$	24	1873	22	$MgSiO_3$-rich corundum + hydrous Al-phases + melt	$Al_{1.847(4)}Mg_{0.073(3)}Si_{0.080(2)}O_3$	<250
S7156a	Cor97	Ak10Cor90 + ~10% $Al(OH)_3$	24	1873	22	$MgSiO_3$-rich corundum + hydrous Al-phases + melt	$Al_{1.947(3)}Mg_{0.025(2)}Si_{0.028(2)}O_3$	<200
S7203	Cor100	Al_2O_3:$Al(OH)_3$ (6:4)	24	1873	25.5	corundum + hydrous Al phases + melt	$Al_{1.962(2)}O_3$	<250
S6741	Ak97.5	Ak2.5Cor97.5 glass	27	1173	1	akimotoite	$Mg_{0.977(11)}Al_{0.043(12)}Si_{0.980(8)}O_3$	<3
I444	Ak80	Ak20Cor80 glass	26	1123	1	akimotoite	$Mg_{0.820(7)}Al_{0.405(7)}Si_{0.775(11)}O_3$	<5
I436	Fe10	$Mg_{0.9}Fe_{0.1}SiO_3$ glass	25	1123	1	akimotoite	$Mg_{0.918(8)}Fe_{0.080(10)}Si_{1.000(7)}O_3$	<10
I594	Fe10Al10	$Mg_{0.9}Fe_{0.1}Si_{0.9}Al_{0.1}O_3$ glass	27	1073	10	akimotoite	$Mg_{0.899(6)}Fe^{3+}_{0.089(2)}Si_{0.911(7)}Al_{0.101(2)}O_3$	<5
I788	Fe10Al10	$Mg_{0.9}Fe_{0.1}Si_{0.9}Al_{0.1}O_3$ glass	27	1173	24	akimotoite	$Mg_{0.911(6)}Fe^{3+}_{0.090(3)}Si_{0.895(7)}Al_{0.104(2)}O_3$	<5

* temperature estimated from power-temperature relationships

Ak: akimotoite, Cor: corundum

All synthesis experiments were performed in the Sumitomo 1200t Kawai-type large volume press or the Iris-15 Voggenreiter LPH 1500-840/200 at the Bayerisches Geoinstitut. Pressures between 22-24 GPa were reached using F08 WC anvils with 4 mm truncation edge length (TEL) employing the maximum oil pressure load of 480 to 500 bar in the Sumitomo press. Pressures of up to 27 GPa were reached in synthesis runs in the Iris press using 3 mm truncated TF05 WC anvils. Assemblies consisting of a 10 mm edge-length MgO octahedron doped with Cr_2O_3 that acts as pressure medium and 4 mm truncated WC anvils (10/4) (Figure 2-1 left) were employed. Each Pt capsule was placed into a MgO sleeve to separate the sample from the $LaCrO_3$ furnace. In addition, a ZrO_2 sleeve was placed between the $LaCrO_3$ heater and the octahedron acting as a thermal insulator. Connection between the heater and the WC anvils is provided by a Mo ring and disk placed on the top and bottom of the assembly, respectively. No thermocouples were used in runs S6925 and S7237a due to the length of the Pt capsules (Table 2-1), however, reliable power-temperature relationships were used from previously conducted experiments performed at exactly the same *P-T* conditions. For all other single-crystal synthesis runs, the temperature was monitored using a D-type thermocouple ($W_{97}Re_3$-$W_{75}Re_{25}$) of 0.005'' of diameter. Synthesis details are reported in Table 2-1.
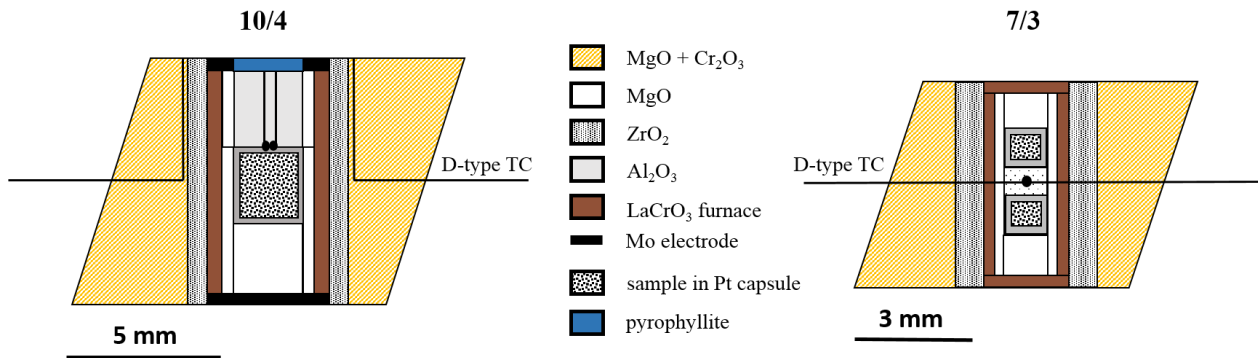
Figure 2-1: *Schematic setup of the 10/4 and 7/3 assembly types used for single-crystal and polycrystalline sample syntheses. For single-crystal syntheses and one polycrystalline sample synthesis, the 10/4 assembly (left) has been used. The 7/3 assembly (right) was used for two single-crystal syntheses at pressures of 27 GPa. D-type thermocouples were inserted into both assemblies, but failed at reading the temperature at high-pressure.*

Two further experiments, I796 and I789, were performed in the Iris-15 Voggenreiter press using a 7/3 assembly consisting of a 7 mm edge-length MgO octahedron doped with C_2O_3 (Figure 2-1 right). Two Pt capsules were placed on top and bottom of the D-type thermocouple inserted into the center part of the assembly where any void space was filled with MgO powder. The capsules

were again surrounded by a MgO sleeve, a $LaCrO_3$ heater and a ZrO_2 spacer acting as thermal insulator. On top and bottom, $LaCrO_3$ disks were placed to provide connection between heater and WC anvils. During both experiments, the thermocouples failed to read the temperature at high pressure, hence, reliable power-temperature relationships were used to estimate the temperatures inside the assembly. After recovering the Pt capsules from the multi-anvil experiments, they were polished sideways from one side to approximately $1/4^{th}$ of the capsule diameter to get an overview of the crystallized phases without removing the majority of the run product.

2.1.2 Polycrystalline samples

The synthesis of polycrystalline samples was needed to conduct high pressure and temperature elasticity studies using the ultrasonic interferometry method. The samples have to be single-phased without any contamination of other minor phases. In addition, they have to be well-sintered and large enough to be double-sided polished to have parallel faces in order to perform ultrasonic experiments. Polycrystalline akimotoite samples having different Fe- and Al contents were synthesized from mixtures of synthetic MgO, SiO_2, Fe_2O_3 and Al_2O_3 oxides finely ground in ethanol in an agate mortar for one hour. These mixtures were then heated up to 1873 K in a high-temperature furnace, kept there for 4 hours and then quenched in an icy water bath to produce glasses. The glasses were subsequently ground in order to obtain fine-grained homogeneous starting materials. Powder X-ray diffraction was performed on all glass samples to ensure that no crystallization occurred during quenching.

The synthesis experiments were performed using the Iris-15 Voggenreiter LPH 1500-840/200 multi-anvil press and the Sumitomo 1200t Kawai-type large volume press at BGI. To reach pressures of up to 28 GPa in the Iris-15 Voggenreiter press, a modified 7/3 assembly has been used (Figure 2-2) which consists of a 7 mm edge length of the Cr_2O_3-doped MgO octahedron and of a 3 mm TEL of the TF05 WC anvils. The starting materials were encapsulated by Mo-foil capsules that also acted as furnaces and were then inserted into a ZrO_2 sleeve and a Cr_2O_3-doped MgO octahedron that served as pressure medium. Connection between the furnace and the anvils was ensured by 0.5 mm thick Mo electrodes that were put inside two ZrO_2 spacers placed at the top and bottom of the Mo capsule (Figure 2-2). The temperature was monitored using a D-type

thermocouple ($W_{97}Re_3$-$W_{75}Re_{25}$) that was inserted through pre-drilled holes at the center of the octahedron. One experiment was performed in the Sumitomo 1200t Kawai-type large volume press using a 10/4 BGI standard assembly as described above (Figure 2-1 left). All synthesis experiments to produce polycrystalline samples were performed between 24 and 28 GPa and temperatures between 1073 to 1243 K for heating durations between one hour and 24 h (see Table 2-1) before being rapidly quenched by switching off the power. After the multi-anvil experiments, the Mo capsules were carefully opened to avoid breaking the run product. The extracted cylinders were glued with super glue on a glass slide or fixed in epoxy and one-sided polished for further characterization.
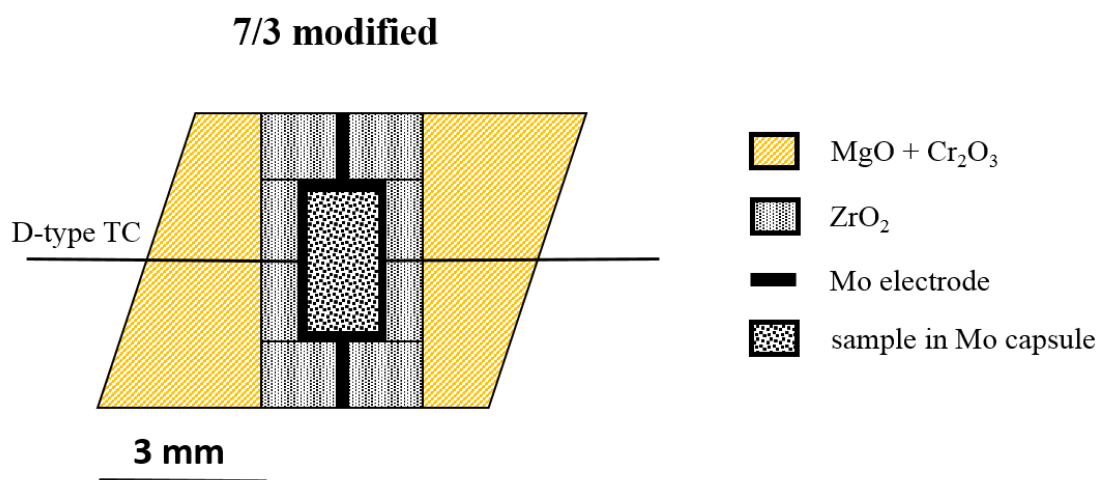
7/3 modified

Figure 2-2: Schematic setup of the modified 7/3 assembly type used for the polycrystalline sample syntheses above 24 GPa. To make the sample size as large as possible, the assembly has been modified from the original BGI standard 7/3 (see Figure 2-1 right) by removing the LaCrO₃ heater and MgO sleeves and by using the Mo capsule as furnace connected by two Mo electrodes to the anvils. In this way, the capsule diameter could be increased from 1 mm to 1.7 mm.

2.2 X-ray diffraction

X-ray diffraction is a powerful tool to determine the unit-cell lattice parameters and atomic structures of crystalline materials and it is based on the Bragg equation:

$$n\lambda = 2dsin\theta \qquad\qquad (eq. 1)$$

which describes the relationship between the wavelength λ of the incident radiation, the lattice spacing d of crystalline materials and the scattering angle θ. When an incoming beam is diffracted from two successive *hkl* planes, the path difference between the beams scattered from the two *hkl* planes is $AB + BC = 2d\sin\theta$ (Figure 2-3). In addition, Bragg found that the path difference for diffraction from two *hkl* planes are an integral number n of the wavelength. In polycrystalline samples the Bragg equation is satisfied for all different d spacing at once since the different crystallites are randomly distributed. For single-crystals, different Bragg angles can be satisfied only by rotating the sample (e.g. Putnis 1992). In this study, one powder diffractometer and two four-circle diffractometers have been used to characterize the synthetized samples as described in the following.
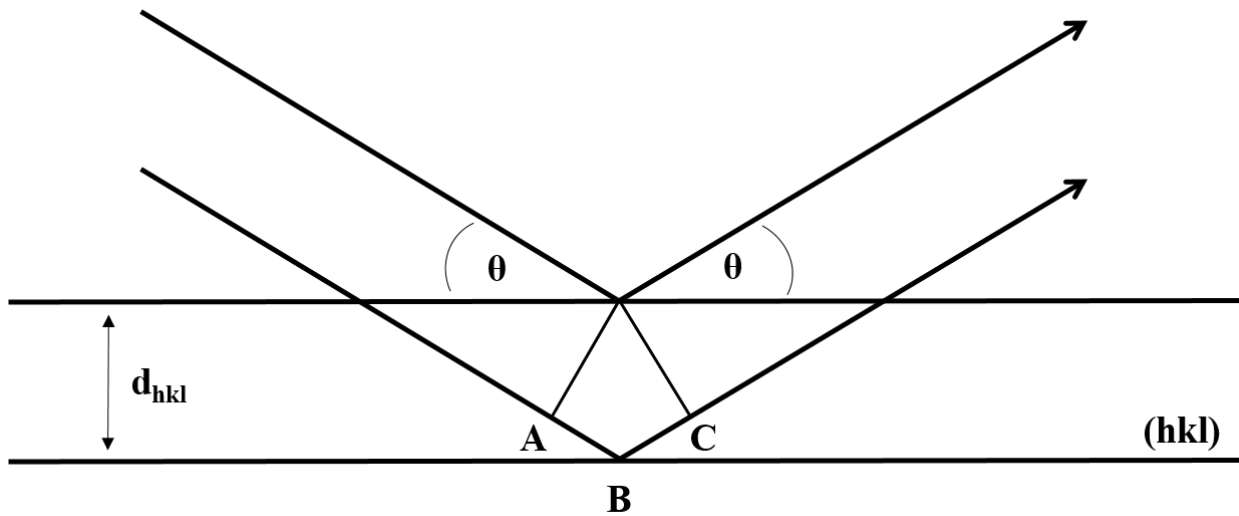
Figure 2-3: *The condition for a Bragg reflection from plane (hkl) with a d spacing d_{hkl} at a scattering angle of θ. The path difference between the two beams diffracting from two adjacent planes is AB+BC which is an integral number of λ. This image has been modified from Putnis (1992).*

2.2.1 Powder X-ray diffraction

Experimental run products that contain polycrystalline samples were polished from one side after being recovered from the multi-anvil experiment either embedded in epoxy or glued with super glue on a glass slide. They were characterized by X-ray diffraction using a Bruker Discover X-ray micro-diffractometer equipped with a two-dimensional solid-state detector (VÅNTEC500) and a micro-focus source (IµS) of Co-Kα radiation operated at 40 kV and 500 µA. The X-ray

beam was focused to 50 μm using a IFG polycapillary X-ray mini-lens. Data collections were performed in a 2θ range between 18° and 102° for a total measurement time ranging between 600 s and 12,000 s per frame in order to exclude the presence of minor phases using the software DIFFRACMC-V3.3.43. Several points on different parts of the run-products were measured to investigate the homogeneity of the sample throughout the capsules. The collected X-ray patterns were integrated using the DIFFRACEVA-V3.1 package and compared to the "Crystallography Open Data" data base (www.crystallography.net/cod/). The unit-cell parameters of the Al-bearing (Table 4-1) were determined using full profile LeBail refinements with the GSAS software package in the EXPGUI interface (Toby 2001, Larson and Von Dreele 2004).

2.2.2 Single-crystal diffractometers with area detector

An Oxford Xcalibur diffractometer equipped with a graphite monochromator and a Sapphire 2 CCD area detector (90-92 mm diagonal, 1024x1024 pixels) (Figure 2-4) was used in order to determine the orientation matrices of the selected single-crystals and to perform full intensity data collections for structural refinements both at room conditions and at high pressures in the diamond anvil cell (DAC). The diffractometer operates with a MoKα radiation (λ=0.70784 Å), monochromated using a graphite crystal at 50 kV and 40 mA. The single-crystals measured at room pressure were glued to the tip of a glass capillary. Complete and redundant intensity data (redundancy of 5) were collected using ω scans with a width of 1° and a default time of 5 to 10 s in a 2θ range between 2 and 75°. For measurements performed on crystals in the DAC, ω scans with a width of 1° and a default time of 60 s in a 2θ range between 2 and 70° were employed. In addition, the cell was not tilted or reversed during the data collection.
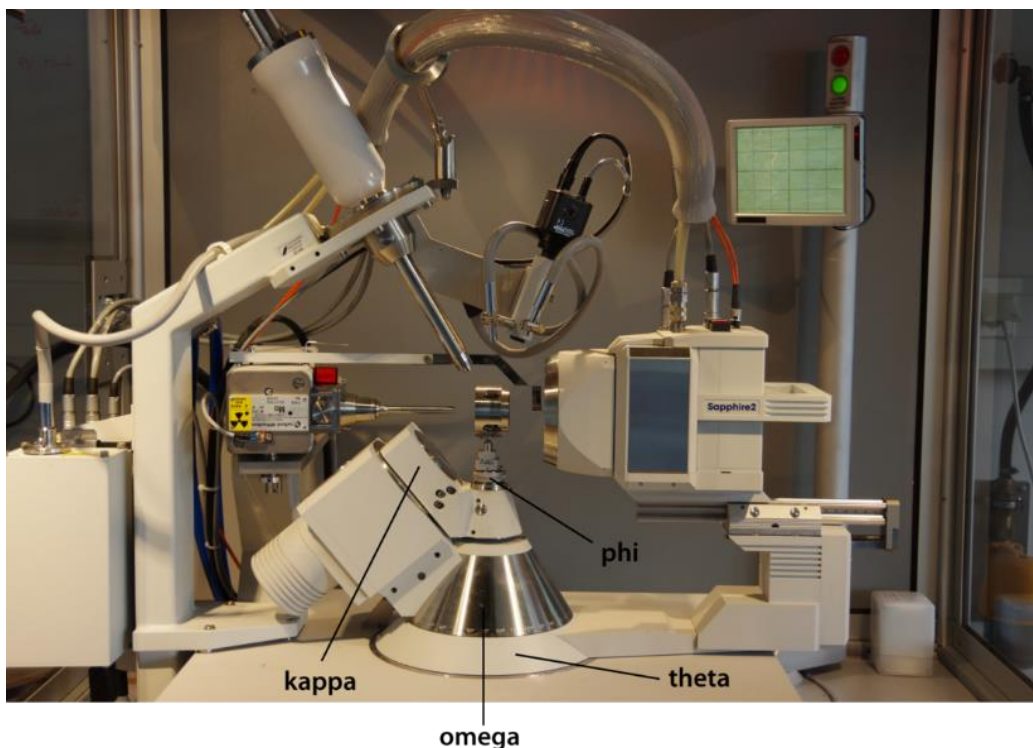
Figure 2-4: Single-crystal Oxford Diffraction Xcalibur diffractometer with a four-circle goniometer having a kappa geometry. It is equipped with a Mo ceramic X-ray tube, a graphite monochromator and a Sapphire 2 CCD area detector (90-92 mm diagonal, 1024x1024 pixels).

One intensity data collection on a very small crystal of sample S7179 having each size less than 30 µm was performed on a Bruker IµS Inside diffractometer using AgKα radiation (λ=0.55941 Å) provided through a microfocusing X-ray tube operated at 50 kV and 880 µA and having a beam size of 50 µm. The crystal was measured in a 2θ range between 4 and 29° using an exposure time of 40 s.

2.2.3 Single-crystal diffractometers with point detectors

Accurate unit-cell lattice parameters of single-crystals belonging to the akimotoite-corundum system were measured on a Huber four-circle diffractometer with a Eulerian cradle geometry (Figure 2-5). It is equipped with a point detector, that can maximize the signal to noise ratio in intensity measurements by collimating the diffracted beam, and a MoKα glass X-ray tube

operated at 50 kV and 40 mA. The diffractometer is driven by the SINGLE software described in Angel and Finger (2011).

theta   **omega**   **phi**   **chi**
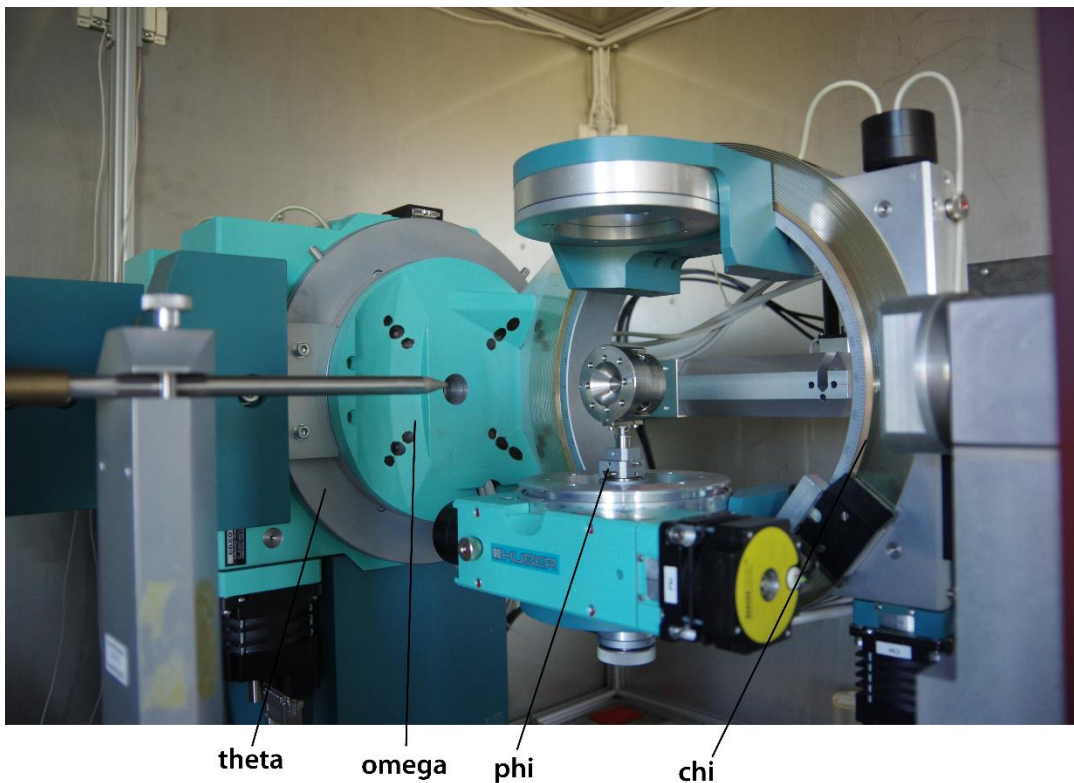
Figure 2-5: Huber four-circle Eulerian cradle diffractometer equipped with a point detector. This diffractometer has been used to perform eight positions centering of several reflections on akimotoite-corundum single-crystals to determine accurate lattice parameters as well as to orient three single-crystals on opportune planes for Brillouin spectroscopy.

The eight position centering method described in King and Finger (1979) and Angel et al. (2000) has been used where each reflection is centered at eight equivalent positions. In this way it is possible to account for experimental aberrations such as crystal offsets or incorrect zero positions of the 2θ, ω, χ and φ circles of the diffractometer. X-ray diffraction measurements at room pressure were performed on eight samples (S6925, S7179, I796, I789, S7237a, S7156 a and b, S7203, see Table 2-1) using up to 28 reflections for each single-crystal. Accurate unit-cell lattice parameters were then obtained by means of the vector least squares method (Ralph and Finger 1982) and were constrained to the trigonal system (Table 4-1). Constrained and unconstrained unit cell parameters were identical within the uncertainties. Single-crystals having the sharpest

reflections with a full-width at half maximum between 0.05 and 0.09 were used for further investigations such a Brillouin spectroscopy measurements or structural refinement studies.

This diffractometer has also been used to orient three $MgSiO_3$ akimotoite single-crystals of the $MgSiO_3$ akimotoite end-member sample (S6925) according to the planes (0 0 1), (0.43 -3.28 8.91) and (-3.08 4.60 -2.36), respectively. The oriented crystals were then fixed inside a drop of UV glue which was dried using a UV light lamp for about 30 min. After the glued hardened it was possible to double-side polish the single-crystals down to a 15 μm thickness.

In-situ single-crystal X-ray diffraction measurements at high-pressure using a diamond anvil cell (DAC) were performed using a Huber four-circle Eulerian cradle diffractometer equipped with a high-brilliance rotating anode X-ray source FR-E + SuperBright using MoKα radiation (λ=0.70784 Å) operated at 55 kV and 45 mA (Figure 2-6). A multilayer optics VaryMax^{TM} is used to focus the X-ray beam at 800 mm distance. The detector consists of a YAP:Ce scintillator coupled to a photomultiplier, amplifier and two discriminators. This diffractometer is preferred over the conventional Huber diffractometer described above because the rotating anode setup can increase the reflection intensity by up to 80 times (Trots et al. 2011, Pamato 2014).
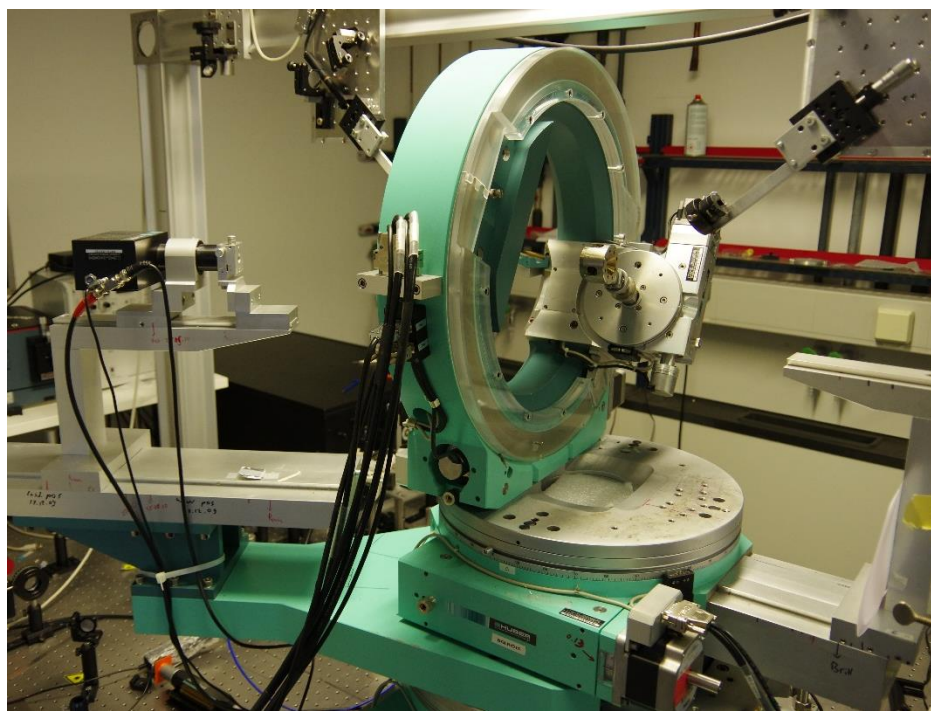
Figure 2-6: *Eulerian cradle four-circle diffractometer in combination with the Brillouin spectroscopy setup at BGI. The diffractometer has a high-brilliance rotating anode and a point detector allowing the measurements also of small single-crystals.*

This makes it possible to measure also several small single-crystals in the DAC as done for DAC1 and DAC2 where two crystals of different orientations were loaded into the DAC together. Figure 2-7 shows the unit-cells of the two single-crystals in DAC2 having the orientation (0.43 - 3.28 8.91) and (-3.08 4.60 -2.36), respectively. The eight positions centering method as described in the previous section has also been used to center up to 14 individual reflections for each sample. Due to the complex $K\alpha_1/K\alpha_2$ ratio due to the focusing mirrors, after the centering procedure, each reflection was individually fitted using the software WinIntegrStp 372 (Angel 2003) that allows the integration of single-crystal intensity data using pseudo-Voigt functions. The integrated intensity, the full width at half maximum (FWHM) of each individual reflection as well as the position of the reflections, their $K\alpha_1/K\alpha_2$ ratio and the background were refined for MgSiO$_3$ akimotoite loaded into DAC1, 2 and 3 (Table 3-1).
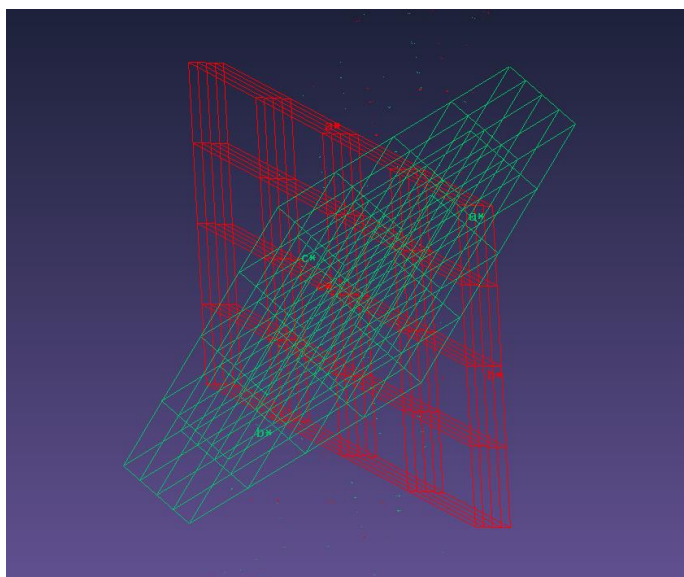
Figure 2-7: Unit-cells of two single-crystals having the orientations (0.43 -3.28 8.91) (red) and (- 3.08 4.60 -2.36) (green) loaded together in a DAC. This measurement has been performed in the Xcalibur diffractometer having an area detector in order to determine the orientation matrices of the two single-crystals.

2.3 Focused ion beam device

Previously oriented and polished MgSiO$_3$ akimotoite single-crystals were cut using the focused ion beam device (FIB) to ensure an efficient loading into the diamond anvil cell. The single-

crystals were firstly glued with a small drop of super glue onto a polished WC holder pin paying attention not to cover the surfaces with the glue. Moreover, care has been taken to ensure that the single-crystals were in contact to the sample holder in order to ensure electrical conductivity during the cutting procedure. The Focused Ion Beam machine FEI Scios DualBeam has then been used to cut two to three half-circles out of each single-crystal using a Ga^+ ion beam at 20 kV and 0.80 nA. The resulting half-circles have a diameter between 88 to 100 µm (Figure 2-8).
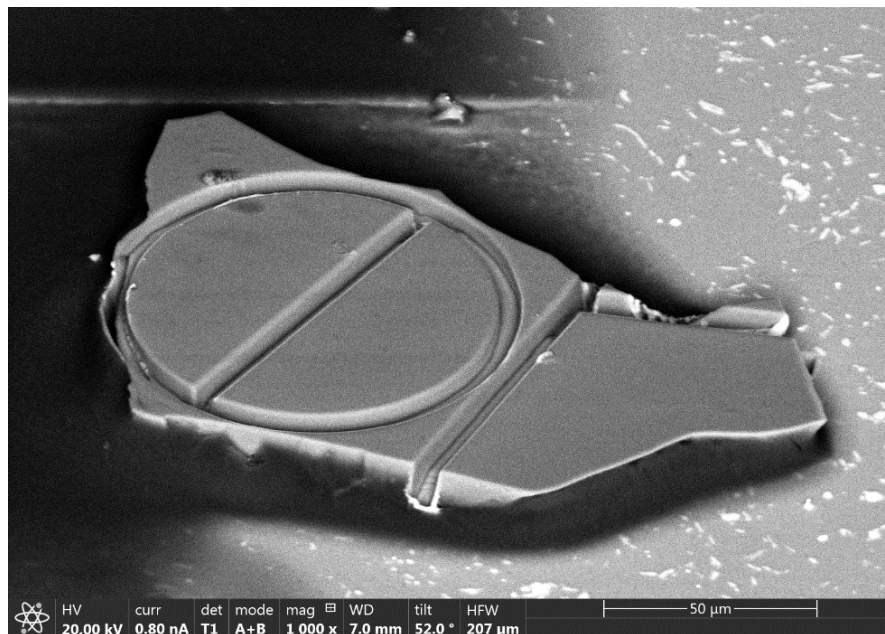
Figure 2-8: Half circles were cut from previously polished and oriented single-crystals using the focused ion beam device. It operates with a Ga^+ ion beam at 20 kV and 0.80 nA producing half circles with diameters of 88 to 100 µm.

2.4 Full intensity data handling

2.4.1 Data integration

The intensity data collected in the Xcalibur Oxford diffractometer and the Bruker IµS Inside diffractometer were integrated using the CrysAlis 171.36.28 software. First, a peak hunting was performed searching for all possible reflections in all measured frames. Then, the best possible lattice parameters for the individual samples were searched with an automatic indexing procedure. Once the orientation matrix and the correct unit-cell lattice parameters have been obtained, an automatic integration which also takes into account the background is run over all collected frames, so that the intensity of each reflection is calculated. During this integration,

Lorentz and polarization corrections as well as an empirical absorption correction are included. For data collections performed on crystals in a diamond anvil cell, all diamond peaks were rejected manually. Furthermore, an additional analytical absorption correction was taken into account due to the partial absorption of the incident and diffracted X-ray beams by the diamond anvils, the Re gasket, the pressure transmitting medium neon and the crystal itself. A numerical absorption correction called Absorb6.0 by Angel (2004) is implemented into the Crysalis absorption correction software. It performs path length calculations over a Gaussian grid of unequally spaced points to determine differences between the incident and scattered X-ray beams (Angel 2004). The absorption coefficient for the diamond anvils of 2.03 cm^{-1} (Creagh and Hubbell 1992) is integrated into the Absorb6.0 package, the pressures transmitting medium neon on the other hand can be neglected due to its low absorption coefficient. The Re gasket plays a crucial role for the absorption correction procedure since its shape changes with increasing pressure and comes closer to the single-crystal. At high pressures, the X-ray beams can therefore be absorbed also by the Re gasket at low inclination angles (Angel 2004). To determine the shape of the sample, faces are manually drawn around the sample to estimate its shape. After inserting the sample thickness and specifying whether it is positioned on the incident or the diffracted side of the diamond anvil cell, the absorption correction runs during the integration procedure described above. The resulting *hkl*-files provide a list of all reflections with their Miller indices, their observed intensities and standard deviations. These are further used in the structural refinements as described in the following section. A good indication of a good, high-quality crystal is the discrepancy factor R_{int} value calculated according to the following equation which should lie close to 0:

$$R_{int} = \frac{\sum |F_0^2 - F_0^2(mean)|}{\sum F_0^2}$$

(eq. 2)

where F_o^2 represents the observed intensity.

2.4.2 Structural refinements

The intensity data were used for structural refinements in the ShelX software (Sheldrick 2008) integrated in the WinGX program system (Farrugia 1999). For the structural refinements in the akimotoite-corundum solid solution, neutral scattering factors for Mg, Al, Si and O were used. The occupancies of Mg, Al and Si on the octahedral sites were constrained using the chemical composition obtained from microprobe analyses and were not refined due to the similar scattering factors of Mg, Al and Si. In the akimotoite structure (space group R$\bar{3}$) Mg and Si were perfectly ordered in the two distinct octahedral sites, whereas Al was distributed among the two sites according to a coupled substitution. In the corundum structure (space group R$\bar{3}$c), Mg and Si were incorporated into the Al-octahedra maintaining a random distribution. In addition, all cations and oxygen sites were refined anisotropically. Between 136 and 378 unique reflections were used to refine 10 parameters for corundum-rich samples (I796, I789, S7237a, S7156b, S7156a and S7203) to 16 parameters for akimotoite-rich samples (S6925 and S7179). Structural refinements converged to discrepancy values, *R1*, in the range between 0.0185 and 0.0275 (Table 2-2a) with:

$$R1 = \frac{\sum ||F_0| - |F_c||}{\sum |F_0|} \qquad \text{(eq. 3)}$$

where F_o represents the observed and F_c the calculated structural factors larger than *4σ(F)*. The weighted discrepancy indexes (which are the quantities minimized during the structural refinements) are usually much larger than the conventional R1, given that they are based on $F_o{}^2$ according to:

$$wR2 = \sqrt{\frac{\sum w \, (F_0^2 - F_c^2)^2}{\sum w \, (F_0^2)^2}} \qquad \text{(eq. 4)}$$

where *w* stands for weight. *wR2* values obtained from the structural refinements lie between 0.0462 to 0.0731. The goodness-of-fit parameter (*GooF*) is an indicator for the distribution of the

difference between the calculated and the measured intensities to the distribution expected from the weight of the refinement and should lie close to 1.

$$GooF = \sqrt{\frac{\sum w \, (|F_0| - |F_c|)^2}{n - m}} \qquad \text{(eq. 5)}$$

n describes the number of data points and m the number of refined parameters. The structural refinements converged to GooF values from 1.126 to 1.273. The weighting scheme in ShelX is simplified to

$$w = \frac{1}{\sigma^2(F_o^2) + (aP)^2 + bP} \qquad \text{(eq. 6)}$$

with $P = \frac{2F_c^2 + Max(F_0^2, 0)}{3}$ and where a and b are parameters chosen by the program.

Details of the structural refinements conducted on single-crystals in the $MgSiO_3$ akimotoite - Al_2O_3 corundum solid solution are reported in Table 2-2a. The atomic coordinates and displacement parameters are shown in Table A-2 and the resulting bond distances and octahedral volumes in Table 4-2.

For the structural refinements of $MgSiO_3$ akimotoite up to 10.8 GPa, performed in the $R\bar{3}$ space group, neutral scattering factors for Mg, Si and O were used. The occupancies of Mg and Si at the octahedral sites were fixed and not refined based on the perfect ordering of Mg and Si into the two distinct octahedra. The cations were refined anisotropically whereas the oxygen was refined isotropically in order to decrease the number of refined parameters, since the number of observable reflections is reduced due to the DAC obstruction. Between 147 to 151 reflections were used to refine 11 parameters at each pressure point. The structural refinements converged to discrepancy values, $R1$, in the range between 0.0324 and 0.0403. All refinement details are reported in Table 2-2b, the atomic coordinates and displacement parameters are shown in Table A-1 and the resulting bond distances and octahedral volumes in Table 3-6.

Table 2-2a. *Details of the single-crystals structural refinements of samples belonging to the MgSiO₃ akimotoite - Al₂O₃ corundum solid solution.*

experiment	No. refined parameters	No. unique reflections	R_{int}	R_1	No. $F_0>4sigma(F_0)$	wR2	GooF
S6925	16	378	0.0544	0.0275	367	0.0731	1.160
S7179	16	285	0.0192	0.0185	272	0.0462	1.126
I796	10	161	0.0328	0.0249	156	0.0660	1.143
I789	10	162	0.0459	0.0251	155	0.0675	1.273
S7237a	10	162	0.0371	0.0271	161	0.0689	1.205
S7156b	10	136	0.0432	0.0219	135	0.0605	1.266
S7156a	10	157	0.0270	0.0259	155	0.0678	1.133
S7203	10	163	0.0446	0.0247	160	0.0639	1.190

Table 2-2b: *Structural refinement details of four data collections performed on MgSiO₃ akimotoite up to 10.8(1) GPa.*

P_{ruby} (GPa)	No. refinement parameters	No. unique reflections	R_{int}	R_1	No. $F_0>4sigma(F_0)$	wR2	GooF
0.0001(1)	11	151	0.0387	0.0391	138	0.1064	1.145
2.12(11)	11	154	0.0414	0.0324	143	0.0826	1.155
8.04(1)	11	150	0.0399	0.0403	141	0.0952	1.254
10.83(3)	11	147	0.0456	0.0378	136	0.0942	1.171

2.5 Electron microscopy

For the mineralogical and chemical characterization, all synthetized samples were fixed with epoxy in a plastic holder, were one-sided polished and subsequently coated with a 10 nm thick graphite layer to perform scanning electron microscopy (SEM) and electron microprobe (EMP) analyses.

Scanning electron microscopy (SEM) was firstly used on all recovered samples to image the polished samples and to identify the crystallized phases by semi-quantitatively determining the mineral compositions. To conduct these analyses, a focused electron beam is produced by a gun and scanned over the sample. Interactions between the electron beam and the sample produce backscattered electrons (BSE) originating from elastic interactions between the beam and sample. Since BSE are strongly dependent on the average atomic number they can provide an image that varies in brightness depending on the molar mass of the crystallized phases. Moreover, inner shell electrons are ejected when the electron beam collides with the sample. When electrons from the outer shell fill up the produced vacancies, characteristic X-ray radiation is emitted. These characteristic energies depend on each element present in the sample and can be recorded in energy dispersive mode providing a qualitative chemical composition of the individual phases.

Preliminary energy-dispersive X-ray spectroscopy (EDS) analyses on the composition were performed using a GEMINI LEO 1530 scanning electron microprobe operated at 20 kV, a working distance of 14 mm and a Si(Li) detector by Oxford INCA. In this way, an overview of the crystallized phases inside the run product, their crystallite size and compositions was achieved.

The electron microprobe is a common tool to measure accurately the composition of major elements in a sample. The JEOL JXA-8200 electron microprobe (EMP) at the BGI was used to determine the composition of the different single-crystals as well as the polycrystalline samples. Similar to the SEM, interactions between the focused electron beam which is produced by a tungsten filament and the sample, characteristic X-ray radiation is emitted depending on the average atomic mass of the crystallized phases. The wavelength-dispersive mode uses different crystal spectrometers such as synthetic LiF, TAP and PET crystals with a known d spacing that allows the intensity and position of the spectral lines to be compared by those emitted by standard materials. In this way, a quantitative analysis of the composition of each phase in possible.

The electron microprobe was calibrated using enstatite as standard for Mg and Si, spinel, Fe-metal and Pt-metal as standards for Al, Fe and Pt, respectively. Pt was measured to check for any contamination of the capsule material inside the crystallized phases. A minimum of 20 points was measured on each phase per sample. During the measurements the voltage and current were set to 15 kV and 15 nA, respectively, and a focused beam with a beam size between 1-2 μm was used on regular samples. If sample damage was observed during the measurement, the beam was defocused to up to 10 μm in diameter. The measured compositions averaged among all points are reported in Table 2-1.

2.5.1 Single-crystals of Al_2O_3-bearing akimotoite and $MgSiO_3$ bearing corundum

In total, eight experiments were successful in synthesizing high-quality single-crystals belonging to the $MgSiO_3$ akimotoite - Al_2O_3 corundum solid solution. One Al-bearing akimotoite single-crystal (Ak99) has been synthesized coexisting with garnet (Figure 2-9 left). As expected, almost all Al was incorporated into the garnet structure ($Mg_{3.25(8)}Al_{1.50(17)}Si_{3.24(9)}O_{12}$), whereas the composition of akimotoite was $Mg_{0.975(8)}Al_{0.016(3)}Si_{1.001(4)}O_3$ (see Table 2-1) The crystals were relatively small even at a synthesis temperature of 1773 K having a maximum size of 30 μm. Another test experiment at lower temperature was performed to obtain an akimotoite with a higher Al composition, however, the decrease in temperature to 1673 K led to a non-equilibrated mixture of akimotoite and garnet with no clearly identifiable gain boundaries in spite of the experiment being held at temperature for 26 hours in the presence of a flux material (Figure 2-9 right). Unfortunately, it was not possible to synthetize single-crystals of akimotoite with larger amount of Al, because the stability field of akimotoite is relatively narrow at high temperatures especially when Al is included into the system.

Synthesis of $MgSiO_3$-bearing corundum on the other hand has been more successful. One corundum end-member (Cor100) and five $MgSiO_3$-bearing corundum single-crystals (Cor81-Cor97, see Table 2-1) were synthesized. SEM analyses showed that the $MgSiO_3$-bearing corundum single crystals were coexisting with hydrous Al-rich phases (totals of EMPA were ~ 80 %) due to the presence of $Al(OH)_3$ in the starting material and with Mg-rich melt (Figure 2-10). By using $Al(OH)_3$ as a flux, it was possible to grow single-crystals between 200 and 250 μm in size (Table 2-1).

The capsules containing the run products Cor75 and Cor80 have been opened immediately to extract the single-crystals that were directly tested with the single-crystal X-ray diffractometers and have not been investigated with the SEM. Single-crystals that were not chosen for X-ray diffraction were fixed in epoxy and polished from one side to perform EMP analyses (Table 2-1).
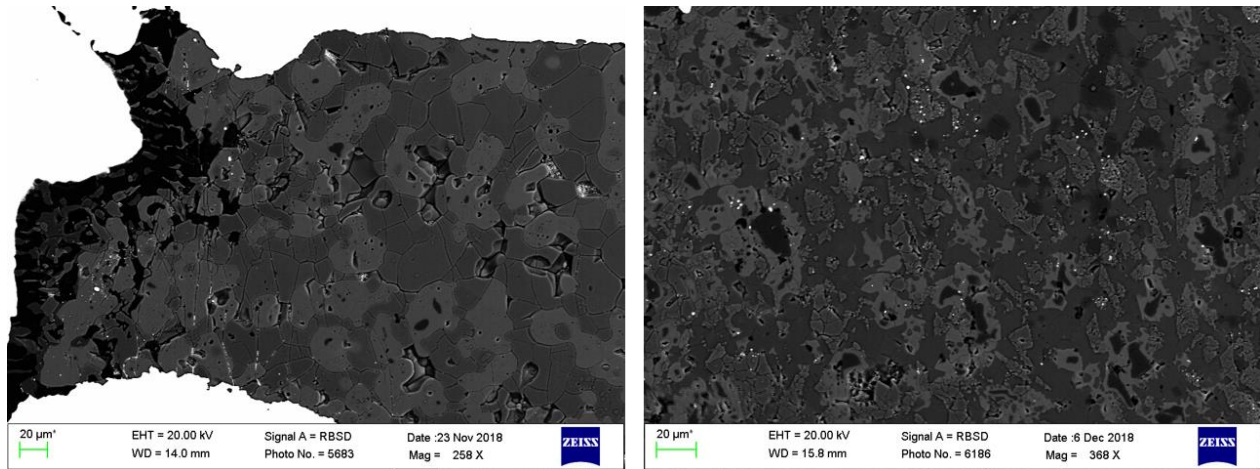
Figure 2-9: Backscattered electron images of coexisting Al-bearing akimotoite (Ak99, dark grey) and Al-bearing garnet (bright grey) in addition to melt pockets that were lost during sample preparation (black). The experiment on the left has been performed at 1773 K for 23 h, crystallizing Al-bearing akimotoite up to 30 μm in size in equilibrium with garnet. The experiment on the right has been performed 100 K lower for 26 h in order to try to introduce a larger amount of Al into the akimotoite structure, however, no equilibrium was obtained since no clear grain boundaries are visible.
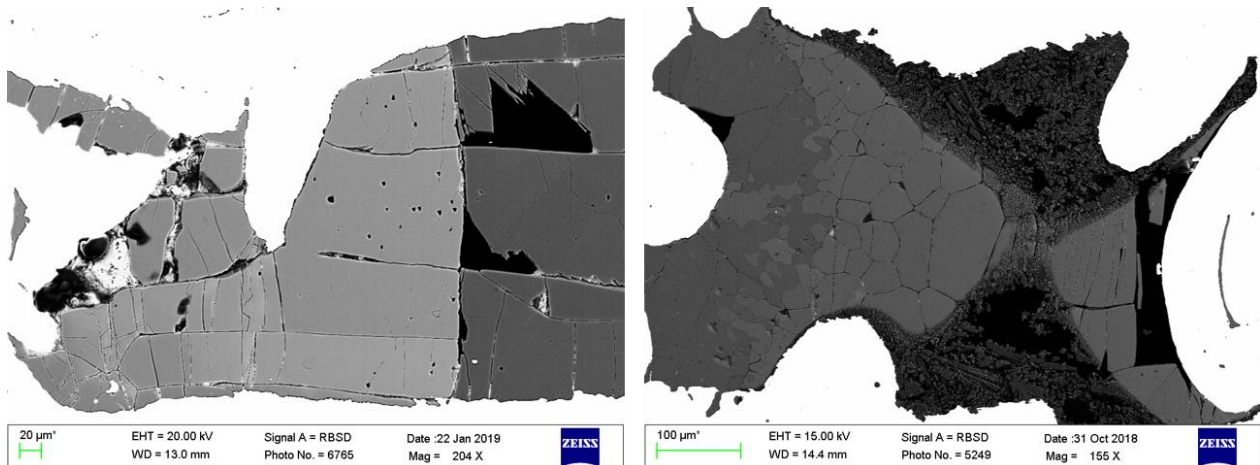
Figure 2-10: Successful syntheses of large single-crystals of the end-member Al₂O₃ corundum Cor100 (bright grey) (left) and MgSiO₃-bearing corundum Cor92 (bright grey) (right). These backscattered electron images show that the MgSiO₃-bearing corundum crystals were coexisting with hydrous Al-rich phases (dark grey) and large amounts of Mg-rich melt (black) visible especially in sample S7156b (right). The crystals had dimensions up to 250 μm.

2.5.2 Polycrystalline samples

Well-sintered polycrystalline samples having the compositions $Mg_{0.977(11)}Al_{0.043(12)}Si_{0.980(8)}O_3$ (Ak97.5), $Mg_{0.820(7)}Al_{0.405(7)}Si_{0.775(11)}O_3$ (Ak80), $Mg_{0.918(8)}Fe_{0.080(10)}Si_{1.000(7)}O_3$ (Fe10) and $Mg_{0.899(6)}Fe^{3+}_{0.089(2)}Si_{0.911(7)}Al_{0.101(2)}O_3$ and $Mg_{0.911(6)}Fe^{3+}_{0.090(3)}Si_{0.895(7)}Al_{0.104(2)}O_3$ (both Fe10Al10 and being identical within the uncertainties) were successfully synthesized as described in section 2.1.2. The grain size in all samples was smaller than 10 µm which is the perfect grain size to conduct ultrasonic measurements (Figure 2-11). Grain sizes above 10 µm are problematic due to possible reflections of the ultrasonic waves at the grain boundaries. XRD analyses confirmed the presence of just one single-phase of akimotoite in all run products as it also can be seen from the backscattered electron images taken with the SEM. The cylindrical samples were double-sided polished ensuring that both faces were perfectly parallel to each other. One or two disks were obtained from the different run products depending on the length of the recovered cylinders.
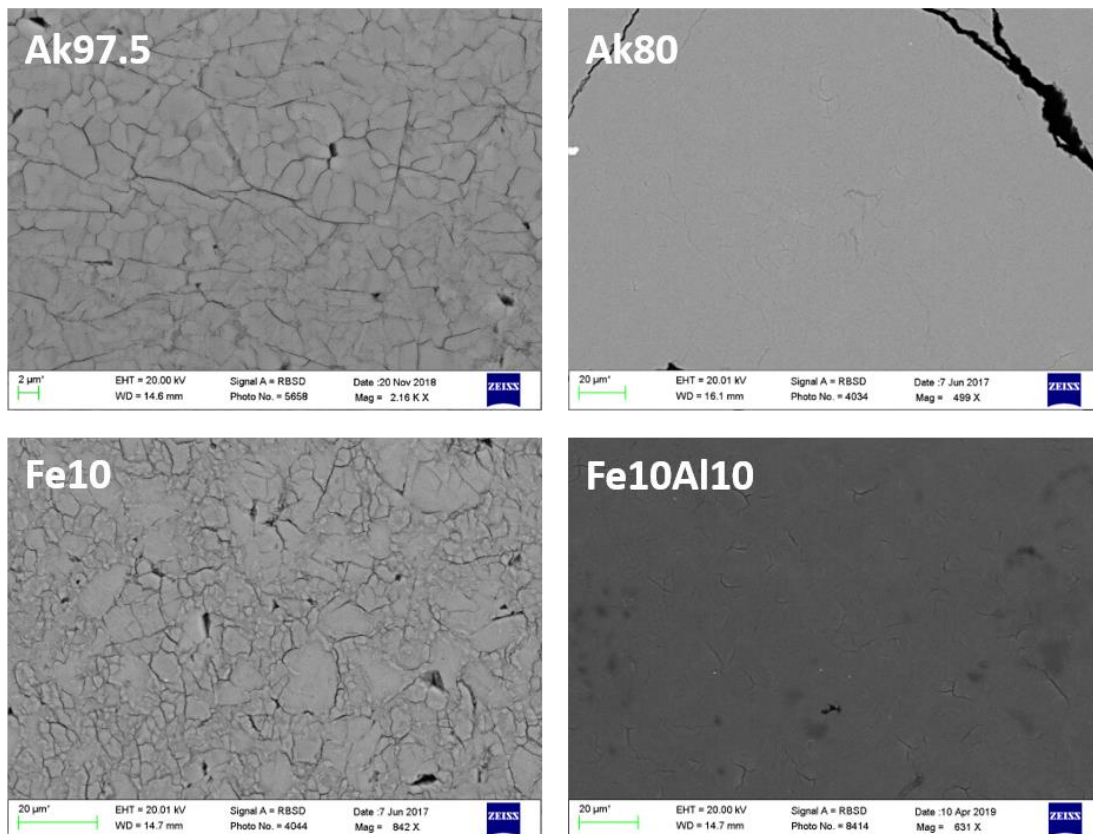
Figure 2-11: *Backscattered electron images of four polycrystalline akimotoite samples containing different amounts of Al and/or Fe. No other phases are visible next to akimotoite. Cracks through the samples (as visible for Ak80) were only located close to the top and bottom of the recovered cylinders and were removed with further polishing.*

2.6 Mössbauer spectroscopy

Mössbauer spectroscopy is commonly used in geoscience in order to examine the oxidation state of Fe in a solid specimen. The conventional Mössbauer source located at the BGI uses the decay of ^{57}Co to ^{57}Fe having a half-life of 270 days. ^{57}Fe is used to perform Mössbauer measurements although the ^{57}Fe isotope makes up only 2.2 % of natural Fe atoms (Dyar et al. 2006). After decaying from ^{57}Co to the 136.3 keV-level of ^{57}Fe, 9 % of the time, deexcitation directly to the ground level occurs emitting a 136.3 keV gamma photon whereas 91 % of the time, decay is to the 14.4 keV state and then to the ground state (Figure 2-12). ~89 % of the 14.4 keV transitions transfer the energy to an atomic electron, however, the ~11 % of the 14.4 keV state left result in the emission of characteristic gamma rays having an energy of 14.4 keV (e.g. Dyar et al. 2006, Figure 2-12). Mössbauer spectroscopy uses the Mössbauer effect which is the recoil-free absorption and emission of gamma rays from the nucleus of a specific atom incorporated into the sample of interest. The nuclear energy levels of the atom of interest are modified by its nuclear electronic environment known as hyperfine interactions. An isomer shift (IS) is created due to different local environments in the source and absorber atoms leading to a shift in Mössbauer transition energies (e.g. Dyar et al. 2006). Moreover, a quadrupole splitting (QS) occurs due to the interaction of the nuclear quadrupole moment of the atom with the electric field gradients around the nucleus, resulting in a splitting of the exited state into two different excited levels (e.g. Dyar et al. 2006). Hyperfine interactions yield characteristic information about the oxidation state and coordination of Fe in the investigated sample.

The Fe-bearing akimotoite sample (Fe10, T2082) has been polished to a thickness of 400 μm which was calculated to be the thickness giving an ideal Mössbauer signal (Long et al. 1983). The source was moved with a maximum velocity of 5 mm/s for a total measurement time of five days. The spectrum was then fitted using Lorentzian profiles in the software MossA 1.01f (Prescher et al. 2012).
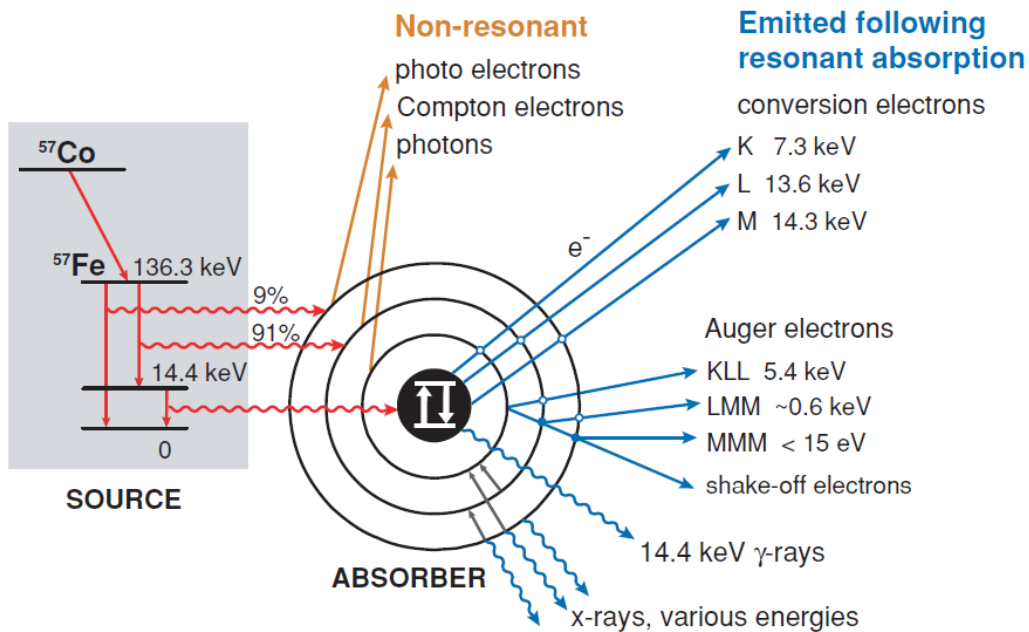
Figure 2-12: *Nuclear decay path for the ^{57}Co to ^{57}Fe transition from Dyar et al. (2006) modified after De Grave et al. (2005). Of the 14.4 keV transitions, ~11 % result in the emission of characteristic gamma rays.*

2.7 Elasticity measurements on single-crystals at high-pressure

2.7.1 Diamond anvil cell technique

The diamond anvil cell (DAC) technique is a powerful tool to study materials at pressures of hundreds of GPa using both spectroscopic or X-ray diffraction techniques. It is based on the simple relation $pressure = \frac{force}{area}$, hence high pressures of the deep Earth can be reached experimentally by decreasing the pressurized area and as a consequence the sample size (Figure 2-13). BX90 style DACs (Kantor et al. 2012) were prepared to perform high-pressure experiments up to 25 GPa, corresponding to the lower transition zone and the uppermost lower mantle where akimotoite is stable. Diamonds with a culet diameter of 400 μm were glued into Boehler-Almax seats having an opening angle of 90° using super glue. To obtain exactly parallel diamond culets, the first diamond is fixed with super glue and the second diamond is aligned relative to the first directly in the DAC before being glued onto the seat. Re gaskets with an

original thickness of 200 μm were pre-indented to a thickness of 58 μm to 61 μm. Into the center of each indentation, a hole with a diameter of 230 μm was laser-cut to produce the sample chamber.
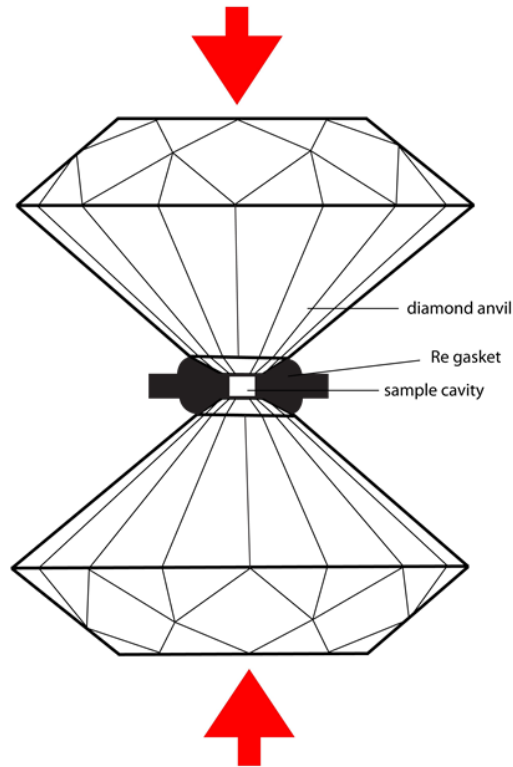
Figure 2-13: Schematic setup of the diamond anvil cell where two diamond anvils with polished tips are pressurizing a small area in between the culets by applying force (red arrows). The sample cavity is produced by laser-cutting a hole through a Re gasket.

Two different DACs were prepared to perform Brillouin spectroscopy and single-crystal X-ray diffraction measurements up to transition zone pressures. Two akimotoite single-crystals (sample S6925) with the different orientations obtained as described in section 2.2.3 and cut into half-circles as described in chapter 2.3 (Figure 2-14) were placed next to each other into the center of the sample chamber. Additionally, a small ruby sphere of 10 μm diameter was placed next to the two crystals to be able to determine the pressure inside the DACs using the ruby fluorescence bands during the experiment (see next section). Another DAC was loaded with only one polished single-crystal having dimensions of 100x100x15 μm and random orientation to collect intensity data for structural refinements. Also in this case, a small ruby sphere was placed next to the crystal to measure the pressure in-situ. The DACs were gas loaded with neon gas as pressure-

transmitting medium using the gas-loading system installed at the BGI (Kurnosov et al. 2008) using 1.5 kbar gas pressure. Neon as pressure transmitting medium can produce quasi-hydrostatic conditions in the pressure range planned for all experiments. After each pressure increase the DACs were left to stabilize for at least one day to avoid any pressure changes during XRD or Brillouin measurements.
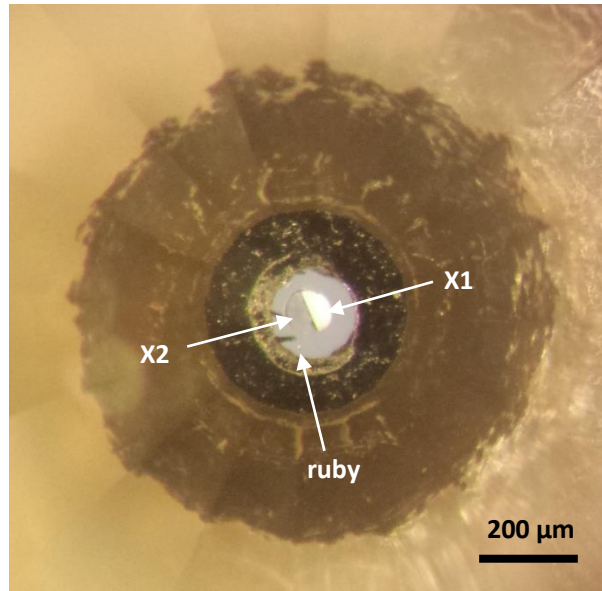
Figure 2-14: *Optical image of a loaded diamond anvil cell sample chamber at a pressure of 4.1(1) GPa. The two half-circles X1 and X2 have different orientations as shown by the different extinction colors. The small ruby sphere used for in-situ pressure determinations is visible close to the gasket.*

2.7.2 In-situ pressure determination

The pressure has been measured in-situ before and after each single-crystal X-ray diffraction measurement or Brillouin data collection using the fluorescence lines of the ruby crystal inserted into the DAC sample chamber. A Raman micro-spectrometer equipped with a red He-Ne-laser (λ = 632.8 nm) with 20 mW laser power was centered at 695 nm to measure the ruby fluorescence lines. For reference, a ruby at ambient conditions was always measured for each high-pressure data collection (Figure 2-15). The fluorescence spectra were then fitted using the program Igor Pro 6A with two Lorentzian profiles for the fluorescence lines R1 and R2, respectively. Pressures were then calculated using the ruby fluorescence calibration by Dewaele et al. (2004) following the relation:

$$P = \frac{A}{B} * \left[\left(1 + \frac{\Delta\lambda}{\lambda_0}\right)^B - 1 \right]$$

<div align="right">(eq. 7)</div>

where $\Delta\lambda$ is the difference between the wavelengths of the R1 peaks of the fluorescence band at pressure and the R1 peak of the ruby at room condition (Figure 2-15), and $A = 1904$ GPa and $B = 9.5$ as determined by Dewaele et al. (2004) by calibrating the R1 ruby fluorescence bands against the equations of state of tantalum, gold and platinum up to 94 GPa and against aluminum, copper and tungsten up to a maximum pressure of 153 GPa.
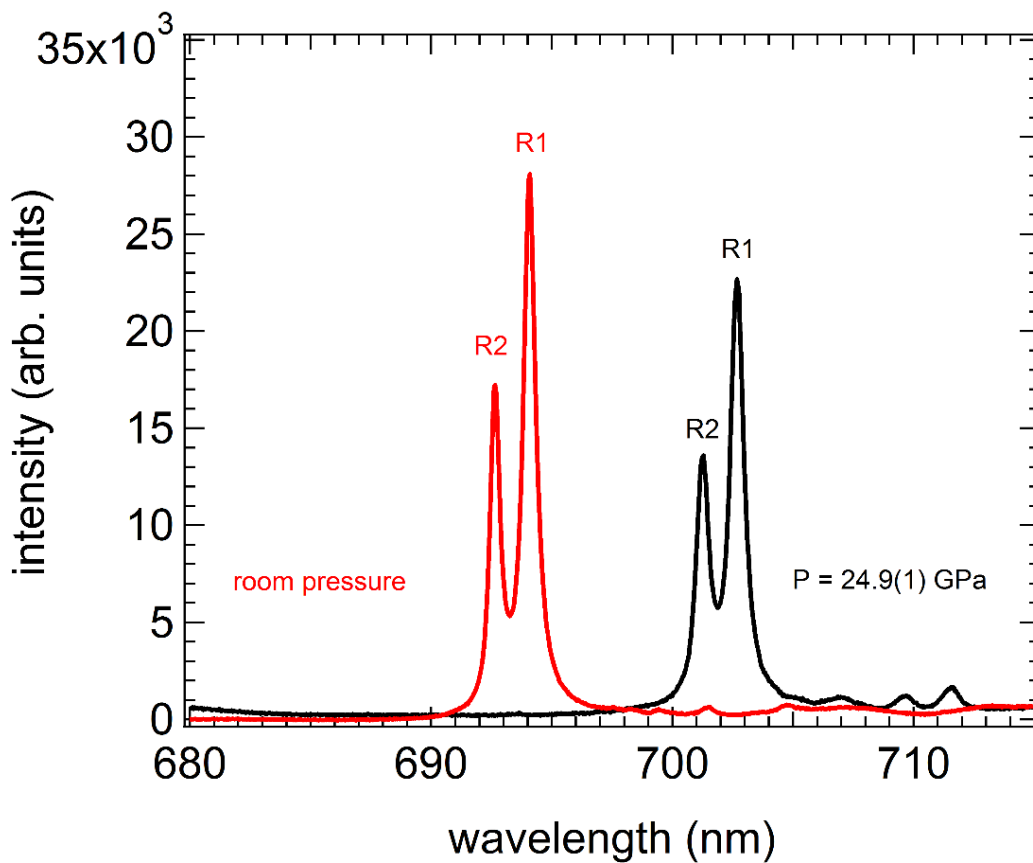
Figure 2-15: *Ruby fluorescence bands at room pressure (red) and at 24.9(1) GPa (black). The shift of the R1 fluorescence bands to higher wavelengths with increasing pressure at room temperature was calibrated by Dewaele et al. (2004) and can be used to determine the pressure inside the DAC.*

2.7.3. Elastic behavior of single-crystals

Hooke's law describes the relationship between the amount of strain and the magnitude of applied stress acting on a solid body. If the stress applied remains sufficiently small and stays below the elastic limit, the strain is proportional to the stress (e.g. Nye 1985):

$$\sigma_{ij} = c_{ijkl}\varepsilon_{kl} \qquad \text{(eq. 8)}$$

σ_{ij} represent the general homogenous stress tensor, c_{ijkl} are the stiffness coefficients and ε_{kl} is the strain tensor. In total, there are 81 possible c_{ijkl} that can be described by a 4th-rank tensor (Nye 1985). Since both stress and strain tensors are symmetric it follows that:

$$c_{ijkl} = c_{ijlk} \qquad \text{(eq. 9)},$$

$$c_{ijkl} = c_{jikl} \qquad \text{(eq. 10)}$$

and
$$c_{ijkl} = c_{jilk} \qquad \text{(eq. 11)}$$

It is therefore possible to reduce the amount of independent stiffness coefficients from 81 to 36 (Nye 1985). In addition, the change in energy results from a set of strains ε_{ij} and is given by the sum $\frac{1}{2}\sum_{ijkl} c_{ijkl}\,\varepsilon_{ij}\varepsilon_{kl}$ over all strain and tensor components (Angel et al. 2009). The energy is independent of in which order the strains appear in the summation: $c_{ijkl}\varepsilon_{ij}\varepsilon_{kl}$ and $c_{klij}\varepsilon_{kl}\varepsilon_{ij}$ are therefore equal (Angel et al. 2009). Since six of the 36 independent components meet the criterion $c_{klij} = c_{ijkl}$ (e.g. c_{1111}), the number of independent stiffness coefficients further reduces to 21 (Nye 1985). Once the symmetry of a single-crystal is applied, the amount of independent elastic coefficients decreases further. In the case of akimotoite which is trigonal (space group $R\bar{3}$) the final number of independent elastic coefficients is 7: c_{1111}, c_{3333}, c_{2332}, c_{1122}, c_{1133}, c_{1123}, c_{2213}. The tensor notation with four indices can be replaced by a matrix notation with two indices following Voigt (1928): $11 = 1$; $22 = 2$; $33 = 3$; $23,32 = 4$; $31,13 = 5$; $12,21 = 6$. The seven independent elastic coefficients of akimotoite can therefore be written as: c_{11}, c_{33}, c_{44}, c_{12}, c_{13}, c_{14}, c_{25}. The full elastic tensor for the trigonal $R\bar{3}$ space group written in Voigt notations is (Nye 1985):

$$\begin{pmatrix} c_{11} & c_{12} & c_{13} & c_{14} & -c_{25} & 0 \\ c_{12} & c_{11} & c_{13} & -c_{14} & c_{25} & 0 \\ c_{13} & c_{13} & c_{33} & 0 & 0 & 0 \\ c_{14} & -c_{14} & 0 & c_{44} & 0 & c_{25} \\ -c_{25} & c_{25} & 0 & 0 & c_{55} & c_{14} \\ 0 & 0 & 0 & c_{25} & c_{14} & c_{66} \end{pmatrix}$$

where c_{66} is related to c_{11} and c_{12} according to:

$$c_{66} = \frac{1}{2}(c_{11} - c_{12}) \qquad \text{(eq. 12)}$$

Polycrystalline aggregates consist of randomly oriented individual grains. Hooke's law does not apply to aggregates because stress and strain are not infinitesimal anymore. In order to calculate the average bulk and shear moduli of a single-phase aggregate two limits were defined. The upper limit is called Voigt bound which assumes that in a phase aggregate, the strain is equal throughout the material. Grain boundaries, however, are locked, leading to unequal stresses on the individual grains that can be calculated from the stiffness coefficients c_{ij} (e.g. Poirier 2000). For the trigonal $R\overline{3}$ space group the bulk and shear moduli K_{Voigt} and G_{Voigt} can be calculated following the equations:

$$K_{Voigt} = \frac{c_{11} + c_{11} + c_{33} + 2 * (c_{12} + c_{13} + c_{13})}{9} \qquad \text{(eq. 13)}$$

$$G_{Voigt} = \frac{(c_{11} + c_{11} + c_{33}) - (c_{12} + c_{13} + c_{13}) + 3 * (c_{44} + c_{44} + c_{66})}{15} \qquad \text{(eq. 14)}$$

The lower limit is the Reuss bound assuming all stress to be uniform on the one-phase aggregate. Since the grains are free and can slide along the grain boundaries, the strain is different for each individual grain and can be calculated from the compliance coefficients s_{ij} (e.g. Poirier 2000). For the trigonal $R\overline{3}$ space group the bulk and shear moduli of the Reuss bound K_{Reuss} and G_{Reuss} can be calculated following the equations:

$$K_{Reuss} = \frac{1}{(s_{11} + s_{11} + s_{33} + 2*(s_{12} + s_{13} + s_{13}))} \qquad \text{(eq. 15)}$$

$$G_{Reuss} = \frac{15}{4*(s_{11} + s_{11} + s_{33}) - 4*(s_{12} + s_{13} + s_{13}) + 3*(s_{44} + s_{44} + s_{66})} \qquad \text{(eq. 16)}$$

Note that the compliance coefficients are obtained by inverting the elastic stiffness matrix ($s_{ij} = c_{ij}^{-1}$) (Nye 1985).

In an elastically isotropic aggregate, every individual grain will have the same strain and is under the same stress which results in no difference between the Reuss and Voigt bounds. In the case of akimotoite, there is a large discrepancy between the Voigt and Reuss bounds due to the highly anisotropic elastic behavior of this mineral. For anisotropic materials, usually, the Reuss-Voigt-Hill (RVH) average, an arithmetic average between the Voigt and Reuss limits is calculated. Once the RVH average bulk and shear moduli are determined, it is then possible to calculate the aggregate velocities of the sample following the Adams-Williamson equations:

$$v_P = \sqrt{\frac{K + 4/3G}{\rho}} \qquad \text{(eq. 17)}$$

$$v_S = \sqrt{\frac{G}{\rho}} \qquad \text{(eq. 18)}$$

with ρ being the density of the investigated sample.

2.7.4 Equation of state

Equations of state (EoS) describe the change in volume of a given material as a function of pressure and temperature. They are used to derive elastic parameters like the incompressibility or

bulk modulus $K = -V \left(\frac{\delta P}{\delta V} \right)_T$ and its derivatives $K' = \left(\frac{\delta K}{\delta P} \right)_T$ and $K'' = \left(\frac{\delta^2 K}{\delta P^2} \right)_T$. When studying Earth materials, Hook's law cannot be applied directly since the strain is not infinitesimal. In geosciences, the Birch-Murnaghan (BM) EoS is commonly used which is valid for compressions larger than 10 % (Angel 2000) in comparison to the earlier Murnaghan EoS (Murnaghan 1937). To obtain the Birch-Murnaghan EoS, Birch (1947) suggested a finite strain EoS which is derived from the assumption that the strain energy of a solid under compression can be described as a Taylor series in finite Eulerian strain ε. In order to deal with positive values during compression, the negative of the Eulerian strain, f_E, is used:

$$ f_E = \frac{1}{2} \left[\left(\frac{V_0}{V_P} \right)^{\frac{2}{3}} - 1 \right] = -\varepsilon \qquad \text{(eq. 19)} $$

The resulting relationship between pressure and volume at a reference temperature which in this study was chosen to be 298 K is the following 4th-oder Birch-Murnaghan EoS:

$$ P(V) = 3K_{0T} f_E (1 + 2f_E)^{\frac{5}{2}} \left[1 + \frac{3}{2} (K'_{0T} - 4) f_E \right. $$
$$ \left. + \frac{3}{2} \left(K_{0T} K''_{0T} + (K'_{0T} - 4)(K'_{0T} - 3) + \frac{35}{9} \right) f_E^2 \right] \qquad \text{(eq. 20)} $$

This expression is usually truncated to the 2nd or 3rd order depending on the data quality, i.e. on whether they are precise enough to determine accurately the K'. A good way to visualize what order of truncation to use, is represented by the plot of the normalized pressure F_E versus the negative Eulerian strain f_E. The normalized pressure can be calculated by the following equation (Angel 2000):

$$ F_E = \frac{P}{3f_E (1 + 2f_E)^{\frac{5}{2}}} \qquad \text{(eq. 21)} $$

If the data points of the *F-f* plot follow a straight line, the slope of such line can give information about the value of *K'* according to the relationship: $slope = \frac{3K_0(K'-4)}{2}$. It follows that a horizontal line is consistent with a *K'* = 4 and therefore the *P-V* data can be fitted using a 2nd-order truncation of the strain energy, whereas a slope different from zero requires a 3rd-order Birch-Murnaghan (BM) EoS. In this case *K''* depends on the K_0 and *K'* values and can be calculated by using the equation:

$$K'' = \frac{-1}{K_0}\left((3 - K')(4 - K') + \frac{35}{9}\right)$$
(eq. 22)

If the data points are described by a parabolic curve, then the *P-V* data need to be fitted with a fourth-order equation of state, letting all four parameters V_0, K_0, *K'* and *K''* vary.

The program EoSfitGUI (Angel et al. 2014) has been used to fit the pressure – unit-cell lattice parameters using Birch-Murnaghan equations of state following a least-squares method which is a reliable tool for data sets which are normally distributed. The goal of the least-squares fitting is to minimize the sum of squares of the differences between the observed and calculated pressures at a given volume which is described by

$$\chi_\omega^2 = \frac{1}{n - m}\sum \omega_i \left(P_{obs} - EoS(V_{obs,i}, T_{obs,i})\right)^2$$
(eq. 23)

The *w* parameter represents the weight which is assigned to each data point, *n*, whereas *m* is the number of refined parameters.

A third-order BM EoS has been used in this study to fit the *P-V* data of akimotoite. The three parameters V_0, *K* and *K'*, that are correlated, were refined during the fitting procedure. Additionally, the unit-cell parameters and bond distances were fitted with linearized BM EoS to refine the linear moduli *M* and its first pressure derivative *M'*.

2.7.5 Brillouin spectroscopy

Brillouin spectroscopy is a powerful tool to determine the acoustic wave velocities and full elastic tensor of transparent single-crystals by measuring the scattering of an incident laser light due to interaction with the acoustic phonons of the material under study. The incident light is inelastically scattered by thermally excited acoustic waves inside the sample leading to a frequency shift relative to the frequency of the incident light. The frequency shift is described by the Doppler shift, in this case also called Brillouin shift. When the incident light transfers energy to the sample, a decrease in the overall frequency can be detected, describing a Stokes event (Figure 2-16 left). On the other hand, when the sample transfers energy to the incident light, an increase in frequency occurs corresponding to an Anti-Stokes event (Figure 2-16 right).

Since the frequency shifts are very small in the case of Brillouin scattering, a scanning Fabry-Pérot interferometer has to be used to separate the spectral lines that are very close to the unshifted incident light frequency.
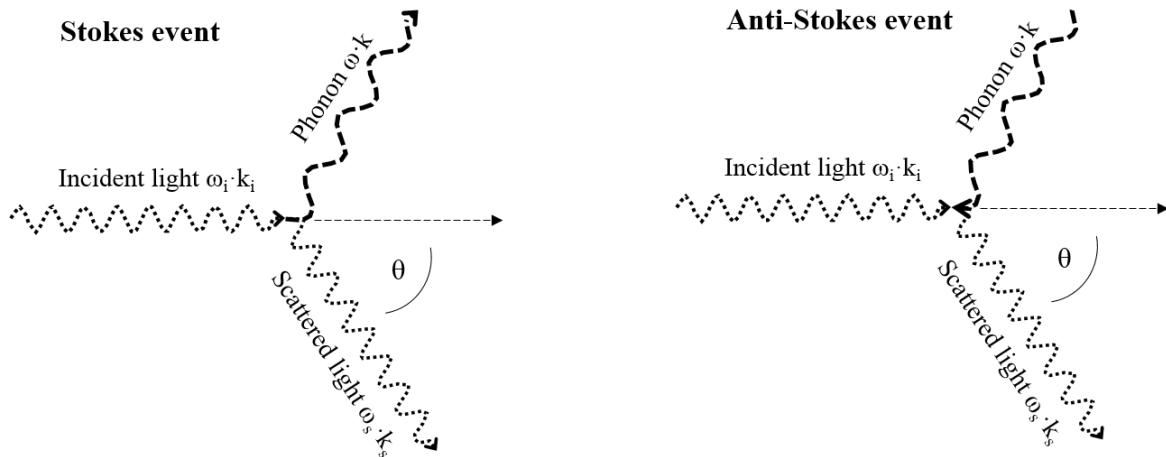
Figure 2-16: A schematic explanation for the occurrence of Stokes and Anti-Stokes events. Stokes events (left) take place when upon interaction of the incident light with the sample, a phonon with a specific energy is emitted and therefore the scattered light frequency is smaller than the incident light frequency. During an Anti-Stokes event, phonon energy is added to the incident light frequency making the overall scattered light frequency larger. This image was modified after Angel et al. (2009).

The Brillouin scattering frequency shift strongly depends on the scattering geometry, describing the angle between the incident and scattered wave normal. The velocities of the acoustic waves can therefore be calculated by the following equation:

$$v_i = \frac{\Delta\omega_i \lambda}{2n \sin\left(\frac{\theta}{2}\right)}$$

(eq. 24)

where v_i describes the material acoustic waves either the longitudinal wave v_P, or one of the two polarizations of the shear wave v_{S1} and v_{S2}. $\Delta\omega_i$ describes the Brillouin shift, λ is the wavelength of the incident light, n is the refractive index and θ is the scattering angle between the incident light and the scattering vector which depend on the material orientation. During Brillouin spectroscopy measurements at high pressure, it is therefore important to consider not only the influence of the crystallographic orientation of the crystal but also the refractive indexes of the sample, the diamonds and the pressure transmitting medium since the incident light get scattered at each interface (Figure 2-17).
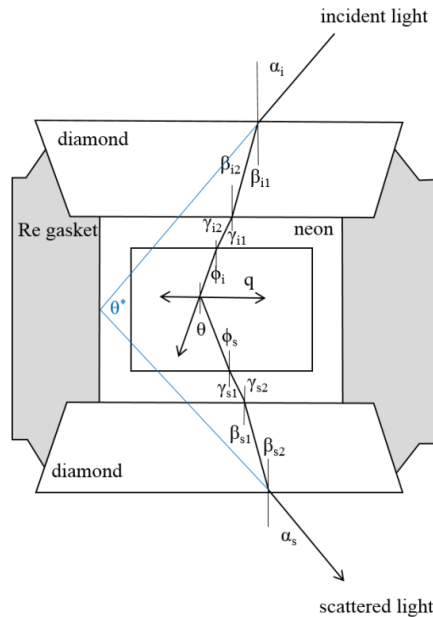
Figure 2-17: Schematic representation of the path that the incident light takes through the DAC during a Brillouin spectroscopy experiment. The incident light scatters at each interface between the diamond, the pressure transmitting medium neon and the sample. Refractive indexes must therefore be taken into account for all materials. This image was modified after Sinogeikin and Bass (2000).

To avoid this problem, a high pressure approach called forward-platelet symmetric scattering geometry as described by Whitfield et al. (1976) has been employed. The velocities of the acoustic waves are independent of the refractive indexes of sample, diamonds and pressure transmitting medium when the incident and scattered beam paths are symmetrical and the sample surfaces are exactly parallel to the polished surfaces of the diamond anvils. To avoid uncertainties as described in Sinogeikin and Bass (2000) it is therefore important to perfectly double-side polish the samples and align them perfectly with the surfaces of the diamonds. The acoustic wave velocities are then independent of the refractive indexes and can be described by the equation:

$$v_i = \frac{\Delta\omega_i\lambda}{2sin\left(\frac{\theta^*}{2}\right)}$$ (eq. 25)

where θ^* describes the external scattering angle (Figure 2-17).

The Brillouin system installed at the Bayerisches Geoinstitut (Figure 2-18) has been used to perform acoustic wave velocity measurements at eleven pressure points up to 24.9(1) GPa. The system uses a 532 nm solid-state laser light and multi-pass tandem Fabry-Pérot interferometer. For signal detection the Hamamatsu single photon counting module H11202-050 was used.

Elastic anisotropy measurements were performed on 20 individual points per sample every 10-20° to cover the whole 360° angular range with a laser power of 150 mW. In a perfect experimental setup, the velocities measured 180° apart from each other should be identical, however, inclination of the sample, not perfectly parallel polished samples or an inclination of the diamonds may affect the signal. Therefore, it is important to collect data over the whole angular range. Each Brillouin signal was individually fitted using a Voigt peak function.
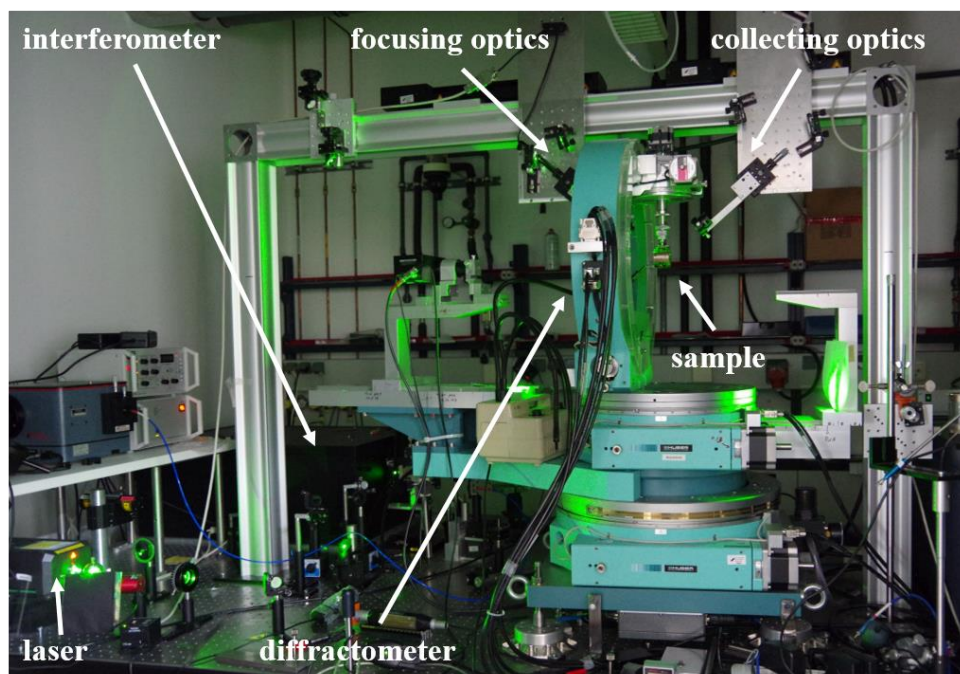
Figure 2-18: *Setup of the Brillouin spectroscopy lab at BGI. The laser path through the mirror system which focus the laser on the sample is shown in green. In the center, the Eulerian cradle four-circle Huber diffractometer is used both for rotating the sample in χ and for the density measurements after each Brillouin data collection.*

The collected Brillouin spectra all show the Rayleigh peak at the center, its ghosts at the edges, the signals from the secondary velocities of the diamonds, one longitudinal and one or two shear wave signals for the sample and in addition one or two signals from the pressure transmitting medium neon (Figure 2-19). With increasing pressure, all signals shift to higher velocities but at a different rate. The longitudinal peaks of the sample approached the diamond peaks in certain orientations, hence, a filter was added to decrease the overlapping between the two peaks. Each spectrum was collected for a minimum of 30 min up to 12 hours, depending on the orientation of the sample and the signal to noise ratio.
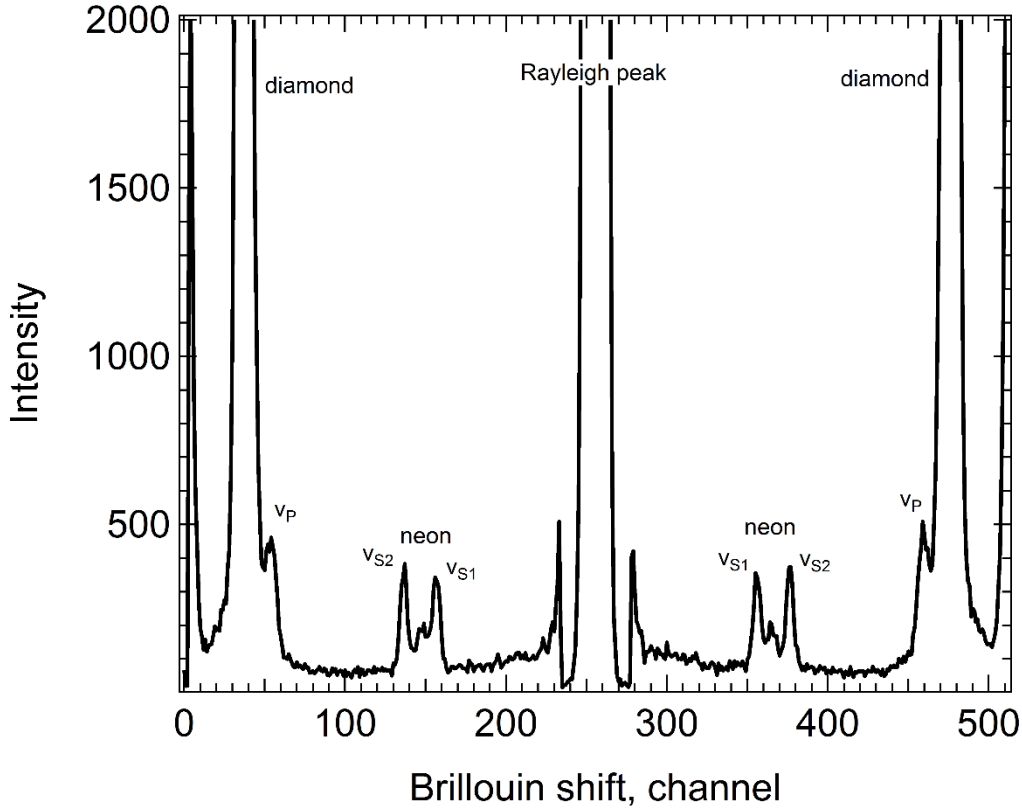
Figure 2-19: *Representative Brillouin spectrum collected on a single-crystal at 4 GPa. The Rayleigh peak corresponding to the elastic scattering can be seen in the center. Three signals from sample X2, v_P, v_{S1} and v_{S2} are visible. In between the v_{S1} and v_{S2} signals a signal of the pressure transmitting medium can be seen. All peaks shift to higher velocities with increasing pressure.*

The program Brillouin Win1024 version 2.6.3 has been used to analyze the Brillouin spectra. To convert the channel numbers into a frequency shift, an internal calibration has been performed using the inner ghosts which represent the interference of the laser light between the first pairs of mirrors. The center of the spectrum at $\Delta\omega = 0$ was determined by taking the mean position of three well-resolved ghost peaks. The frequency shift $\Delta\omega$ per channel can be calculated according to:

$$\Delta\omega = \frac{c\Delta C}{2Ld} \qquad \text{(eq. 26)}$$

with c being the speed of light, L represents the mirror spacing of 4 mm, ΔC the cannel difference between the central peak and the Brillouin peak of interest and d is the mean value between the

ghosts averaged from three well-resolved ghost pairs. The measured frequency shifts could then be directly converted into acoustic wave velocities following eq. 25. This conversion was regularly checked using a glass standard.

In order to constrain all seven independent elastic coefficients, two orientations having the most diverse dispersion curves at ambient conditions, (0 0 1) (solid lines) and (0.43 -3.28 8.91) (dashed lines) in Figure 2-20, were chosen to be oriented and cut into half circles (see chapter 2.3). For high pressure experiments the two different orientations (0.43 -3.28 8.91) and (- 3.08 4.60 -2.36) were used. Akimotoite is a highly anisotropic mineral having large differences in velocities at different rotation angles χ (Figure 2-20).
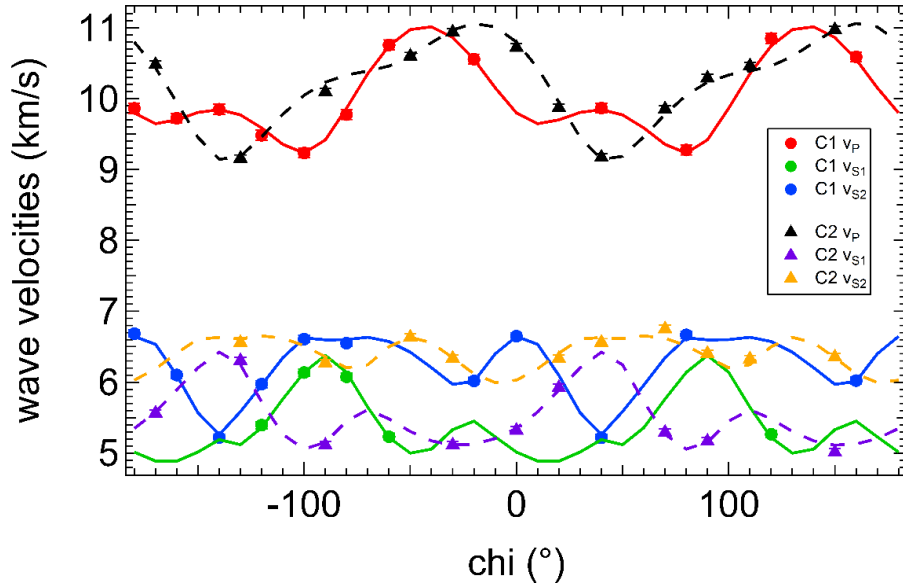
Figure 2-20: *Dispersion curves collected at room pressure as a function of the rotation angle χ for v_P, v_{S1} and v_{S2} for two single-crystals. Solid and dashed lines are the fits obtained using the Christoffel equation (eq. 27). The dispersion curves with the solid lines correspond to the crystal with (0 0 1) orientation and the dispersion curves with the dashed lines are from the (0.43 -3.28 8.91) crystal orientation.*

In order to determine the seven independent elastic coefficients of the trigonal system with space group R$\overline{3}$, c_{11}, c_{33}, c_{44}, c_{12}, c_{13}, c_{14}, c_{25}, the wave velocities of the two crystals were fitted using the Christoffel equation:

$$\left|c_{ijkl}q_jq_l - \rho v^2\delta_{ik}\right| = 0 \qquad\qquad \text{(eq. 27)}$$

where c_{ijkl} are the elastic coefficients, $q_{j,l}$ describe the crystallographic orientation of the single-crystals, ρ is the density of the sample and δ_{ik} is the Kronecker delta. The three solutions to the Christoffel equation for v_P, v_{S1} and v_{S2} were implemented into an Origin 2018 program (Buchen 2018). In order to obtain the propagation direction, the trigonal system has to be transformed to an orthogonal system where $a*$ was defined to be along X and a along Y, respectively. Density needed to conduct this fitting procedure was calculated from the X-ray diffraction measurements that were performed at the same conditions before and/or after each Brillouin measurement on both samples. After obtaining the elastic tensor, the Voigt, Reuss and Reuss-Voigt-Hill bulk and shear moduli could be calculated according to equations 13-16. The aggregate longitudinal and shear wave velocities were then calculated following the Adams-Williamson relations (eq. 17 and 18).

Because both wave velocities and density were measured simultaneously, it was possible to calculate the absolute pressure during the experiment without relying on secondary pressure gauges like, for example, the ruby pressure scale. Absolute pressure can be calculated using the equation:

$$P_{abs} = -\int_{V_0}^{V} \frac{K_T(V)}{V} dV = 3K_{T0}f(1+2f)^{\frac{5}{2}}(1 + \frac{3}{2}(K'_{T0} - 4)f) \qquad \text{(eq. 28)}$$

where the adiabatic bulk modulus K_{S0} obtained from Brillouin spectroscopy has been converted to the isothermal K_{T0} value following $K_{S0} = K_{T0} * (1 + \alpha\gamma T)$ using the parameters: $\alpha = 2.44 \times 10^{-5}$ 1/K (Ashida et al. 1988), $\gamma = 1.18$ (Stixrude and Lithgow-Bertelloni 2005) and T = 298 K and the volume is obtained by X-ray diffraction.

2.7.6 Anisotropy determination

All single-crystals are elastically anisotropic meaning that the wave velocities are dependent on the direction the waves are propagating through the crystal. In order to describe the anisotropic behavior of akimotoite for the compressional and shear wave velocities, the anisotropy A has been calculated according to (Mainprice 2015):

$$A(\%) = 200 \left(\frac{v_{max} - v_{min}}{v_{max} + v_{min}} \right) \qquad \text{(eq. 29)}$$

The maximum and minimum velocities for v_P, v_{SH} and v_{SV} are taken from the complete hemisphere of possible propagation directions (Mainprice 2007). Moreover, the anisotropy A_{SP} of the shear wave splitting which describes the anisotropy of the two shear waves v_{SH} and v_{SV} travelling in the same direction through an anisotropic material according to:

$$A_{SP}(\%) = \left(\frac{v_{S1} - v_{S2}}{v_{S1} + v_{S2}} \right) \qquad \text{(eq. 30)}$$

The software package Anis2k (Mainprice 1990) uses the elastic tensor of the investigated mineral, its density and the volume fraction of the mineral in a bulk assemblage to calculate the anisotropies of P and S-waves at any pressure or temperature throughout the complete hemisphere. The anisotropic behavior of akimotoite could therefore be determined up to transition zone pressures by using the elastic tensor at different pressures obtained from Brillouin spectroscopy.

2.8 Elasticity measurements on polycrystalline samples at high pressure and temperature

2.8.1. Ultrasonic experiments

A combination of ultrasonic interferometry in the megahertz (MHz) frequency range, X-ray diffraction and X-ray radiography has been used to determine the wave velocities and density of Fe-bearing, Fe10, Al-bearing, Ak97.5, Ak80 and Fe- and Al-bearing akimotoite, Fe10Al10. A short, high-amplitude pulse is generated with a piezoelectric transducer crystal resulting in an ultrasonic wave travelling through the specimen. From the resulting reflections at each interface throughout the experimental setup, it is possible to determine the travel time t through the sample. X-ray radiography provides a measure of the sample length l at each pressure and temperature allowing it to calculate the wave velocities of the investigated sample at the stability conditions in

the Earth's mantle according to $v = 2l/t$. The density of the measured samples at each pressure and temperature can be measured by synchrotron X-ray diffraction.

2.8.2. Large volume press setup at the Argonne Photon Source

Six ultrasonic measurements, T2082 with the Fe10 sample, T2083 and T2269 with the Ak97.5 sample, T2270 with the Ak80 sample and finally T2267 and T2452 with the Fe10Al10 samples combined with in-situ X-ray radiography and diffraction at high pressures and temperatures were performed in the Rockland Research Corp. 1000 tons large volume press at the 13-ID-D beamline of GSECARS at APS, IL (Figure 2-21).

Figure 2-21: Large volume setup at the 13-ID-D beamline of GSECARS at APS. The large volume press is modified in a way that the white X-ray beam goes right through the sample once the multi-anvil assemblage is properly aligned.

A 10/4 multi-anvil assembly was modified to fit a cylindrical rhenium (Re) furnace prepared from a 25 μm thick Re foil (Figure 2-22). Two windows were laser cut into the furnace to create a path of low absorption for the X-ray beam. The octahedral assembly made from MgO doped with Cr_2O_3 was filled from top to bottom with an Al_2O_3 buffer rod, a perfectly parallel double-sided polished sample, a mixture of MgO and Au that served as pressure marker and a MgO spacer (Figure 2-22). At the interfaces between buffer rod and sample and between sample and pressure marker, 2 μm thick Au foils were placed to increase both the bonding and the contrast

between the sample and its environment. The temperature was monitored using a D-type thermocouple inserted at the center of the assembly (as shown in Figure 2-22 left) or it was placed inside a 4-hole alumina piece (as for example shown in Figure 2-1 left) which was then cemented to the bottom part of the assembly.
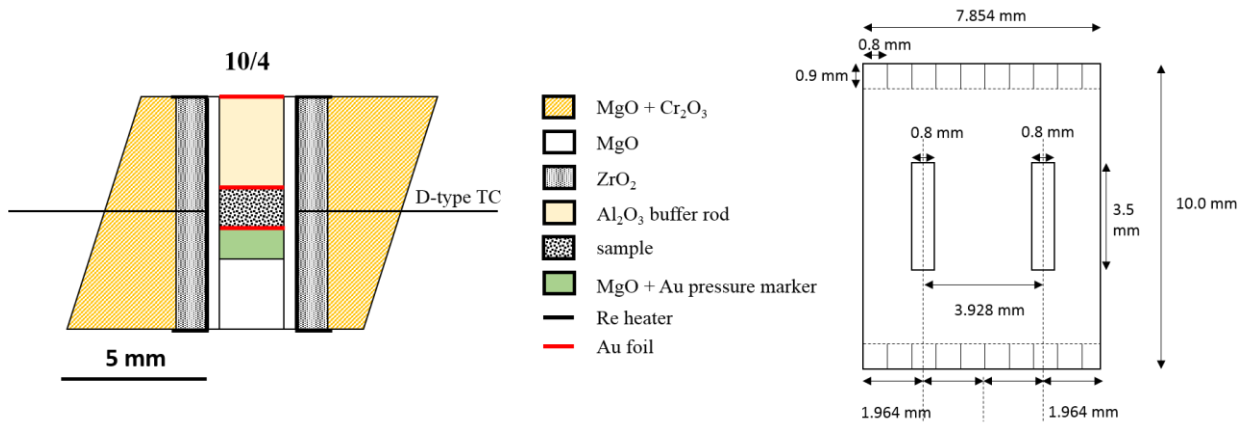
Figure 2-22: Multi-anvil assembly setup used for ultrasonic measurements at APS. A standard 10/4 assembly (left) was modified by replacing the LaCrO₃ furnace by a Re foil furnace (right) with two laser cut windows for the X-ray beam to pass through the sample to avoid absorption from Re.

 Due to problems with some of the thermocouples, heating cycles up to 1100 K were only possible for four experiments (T2083, T2269, T2082 and T2267). The heating paths are shown in Figure 2-23. For the first run with Ak97.5 (T2083), the experiment was first heated once the target pressure of 25 GPa was reached. Then three heating cycles up to 1100 K were performed with ultrasonic measurements collected upon cooling (Figure 2-23 left). For the second run (T2269), the Ak97.5 sample was heated twice to 573 K during compression to the target pressure to release stresses inside the experiment and then two heating cycles up to 800 K were performed (Figure 2-23 left). The Fe10 sample (T2082) was pressurized to target pressure and then heated up to 1100 K during four heating cycles (Figure 2-23 right). During the run with the Fe10Al10 sample (T2267) it was only possible to heat twice to 573 K (Figure 2-23 right). The high-pressure and high-temperature stability field of the MgSiO₃ majorite, ringwoodite and akimotoite polymorphs also are reported in Figure 2-23 in order to show that the actual stability field of akimotoite was reached during these experiments. For the other ultrasonic measurements (T2270 and 2452), the wave velocities could be determined up to the pressure stability field of akimotoite of 21 to 25 GPa without any heating.

Each experiment was compressed in ~ 2 GPa step size and it took between 30 min to 1.5 hours between each pressure point. Before each measurement at high temperature, the experiment was equilibrated for 10 minutes.
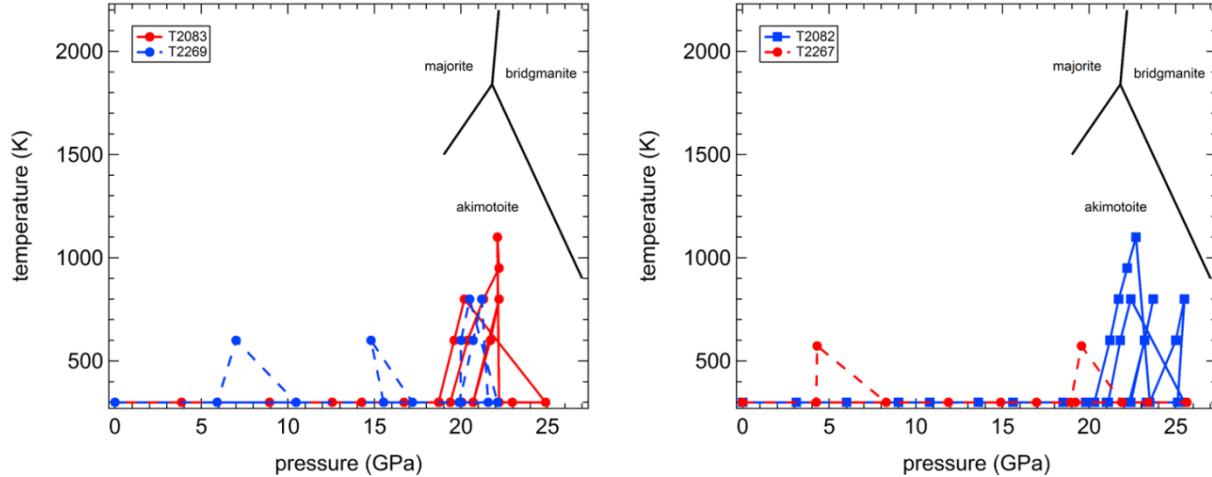
Figure 2-23: *Heating cycles for two experiments, T2083 and T2269, with the Ak97.5 sample (left) and for experiment T2082 with the Fe10 sample and experiment T2267 with the Fe10Al10 sample (right). The P-T phase stability field of MgSiO₃ akimotoite was inserted inside this diagram to show that the actual stability conditions were reached during three experiments.*

2.8.3 Piezoelectric transducers for acoustic wave production

Au-coated transducers made of $LiNbO_3$ were glued with a tiny amount of epoxy on the TEL of the WC anvils that have been polished to mirror quality (Figure 2-24). The piezoelectric properties of the 10° Y-cut $LiNbO_3$ crystal is used to produce primary P- and secondary S-waves simultaneously by applying an AC field. P- and S-wave signals can best be obtained at frequencies between 50 to 60 MHz and 30 to 40 MHz, respectively. The ultrasonic measurements were performed using the Tektronix TDS 5104 Digital Phosphor Oscilloscope or Tektronix MS054 Mixed Signal Oscilloscope and the Sony AWG2021 waveform generator or the Tektronix AFG3252C Dual Channel Arbitrary Function Generator at frequencies between 30 to 40 MHz for the v_S signal and between 50 and 60 MHz for the v_P signal.
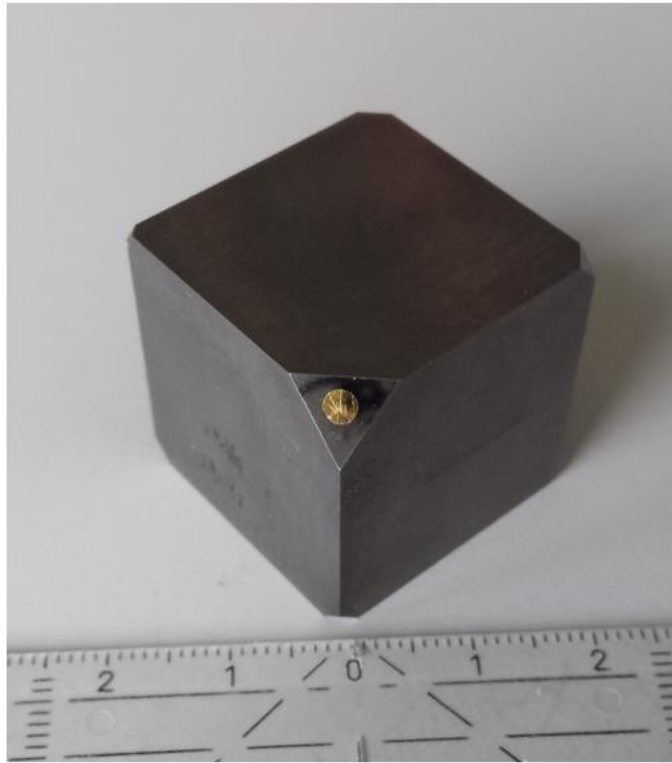
Figure 2-24: *Au-coated LiNbO₃ transducer on 8 mm truncation polished to mirror quality. The transducer is glued with a tiny amount of epoxy on a perfectly clean surface to ensure the transducer is completely bonded to the WC anvil.*

2.8.4 Digital pulse echo overlap method

The pulse echo overlap technique as described in Leisure (2017) is commonly used to determine the travel time. Previously, the pulse echo overlap technique had to be performed during the ultrasonic experiment at the oscilloscope. To improve accuracy, the digital pulse echo overlap method was developed which allows the determination of the travel time after the measurement has been performed through digital files of the recorded signals at different frequencies. The digital files contain the waveforms of each reflection at the interfaces inside the assembly (Figure 2-25). The first and largest reflection comes from the WC anvil-buffer rod interface (Figure 2-26), followed by the reflection from the buffer rod-sample (Figure 2-26). Lastly, the third reflection arises from the sample-pressure marker interface (Figure 2-26).
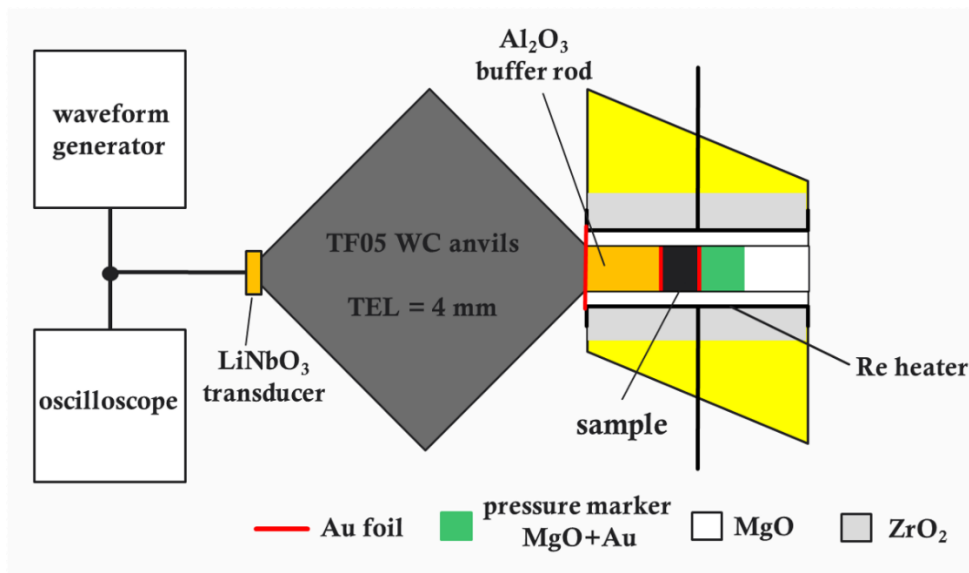
Figure 2-25: *Schematic image of the ultrasonic interferometry setup at APS. The ultrasonic waves produced by the LiNbO₃ transducer get reflected at each interface between the WC anvil, the buffer rod and the sample. Dimensions are not to scale.*
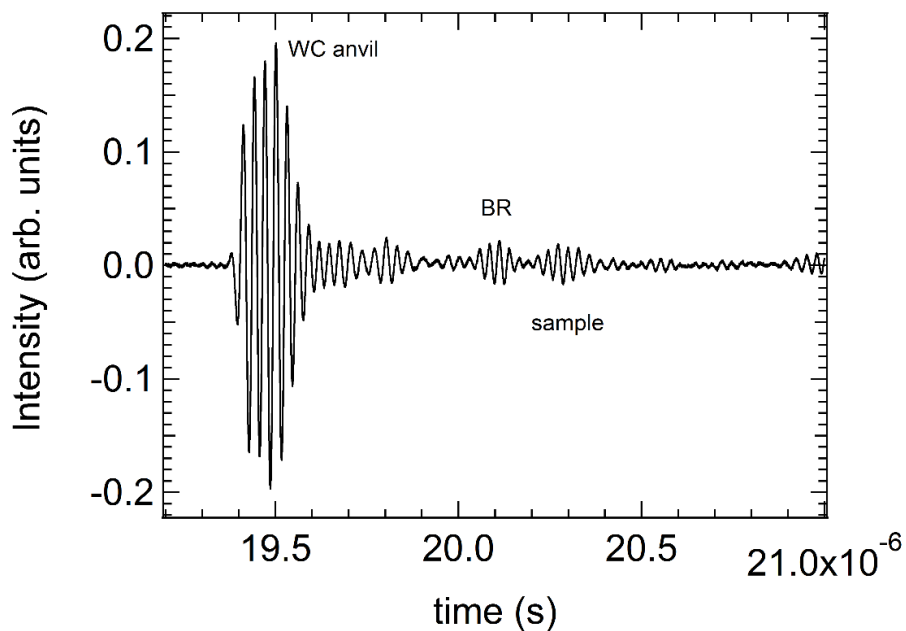
Figure 2-26: *Characteristic waveform obtained during the ultrasonic measurement T2083 at 20.8 GPa and 300 K where the intensity signal is plotted versus the time. The three reflections from the interfaces between the WC anvil, the buffer rod (BR) and the sample can be clearly distinguished.*

Ultrasonic measurements were done at each pressure and temperature in the frequency region between 30 and 60 MHz The travel time determination was performed in Igor Pro 6A. By using a cross correlation function

$$corr(g,h) = \int_{-\infty}^{\infty} g(\tau + t)d\tau\, h(\tau)d\tau \qquad \text{(eq. 31)}$$

where *g(τ)* is the buffer rod and sample signal and *h(τ)* is the buffer rod signal. The resulting correlation function show two clearly identifiable maxima (Figure 2-27). The two-way travel time through the sample is then determined by taking the delay time between the two maxima indicated with the two crosses in Figure 2-27.
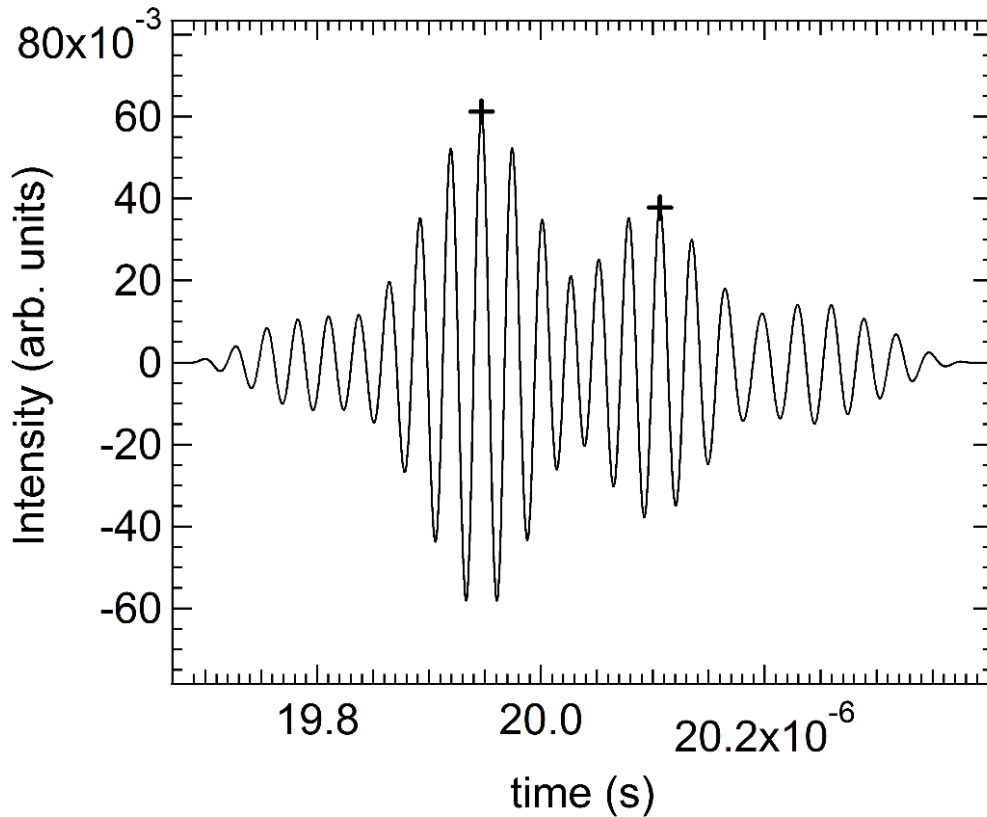
Figure 2-27: Buffer rod and sample signal after cross correlation. The two-way travel time through the sample can be determined by the difference in time between the two maxima of the buffer rod and sample signal, respectively, which are highlighted by the two crosses.

When using an experimental setup where a transducer is employed, the travel time can be influenced by several factors (see Leisure 2017) as described by the following relationship:

$$t = p\frac{2l}{v} + p\mathit{\Delta}t(\phi) + \frac{n}{f}$$ (eq. 32)

where p represents an integer that describes the number of round trips the 2nd echo has made relative to the 1st echo, l is the sample length and v is the plane-wave velocity. The term $p\mathit{\Delta}t(\phi)$ describes the time interval that occurs due to a bonding effect at the buffer rod-sample interface (Jackson et al. 1981, Niesler and Jackson 1989). It has been shown, however, that if the bond is very thin, the time shift can be neglected, especially since the majority of uncertainty arises from the error on sample length rather than the travel time determination. In this study the bond between buffer rod and sample was made of a 2 μm thin gold foil and it was therefore negligible. The term $\frac{n}{f}$, where n ideally is 0, is only relevant when choosing a wrong maxima after the cross correlation procedure. If a wrong maximum is chosen in the digital pulse echo overlap method, one period of the sound wave will be added or subtracted, however, this can be easily identified by a large deviation in travel time in comparison to the correct travel times determined at other frequencies.

2.8.5. Energy-dispersive X-ray diffraction

X-ray powder diffraction patterns were collected for 300 to 500 seconds at each pressure and temperature for both the sample and the pressure marker using an energy-dispersive system operating between 42 and 112 keV at a fixed 2θ angle of 6.04° (Figure 2-28). The unit-cell parameters of Au, MgO and akimotoite (Tables 4-3, 5-1 and 5-3) were determined using full profile LeBail refinements with the GSAS software package in the EXPGUI interface (Toby 2001, Larson and Von Dreele 2004).

The unit-cell volume of Au and MgO were then used to determine the pressure at a given temperature according to the *P-V-T* equations of state reported by Tsuchiya (2003) and Dewaele et al. (2000), respectively, implemented in the software PDIndexer 4.328 (written by Y. Seto, http://pmsl.planet.sci.kobe-u.ac.jp/~seto/?page_id=20&lang=en).
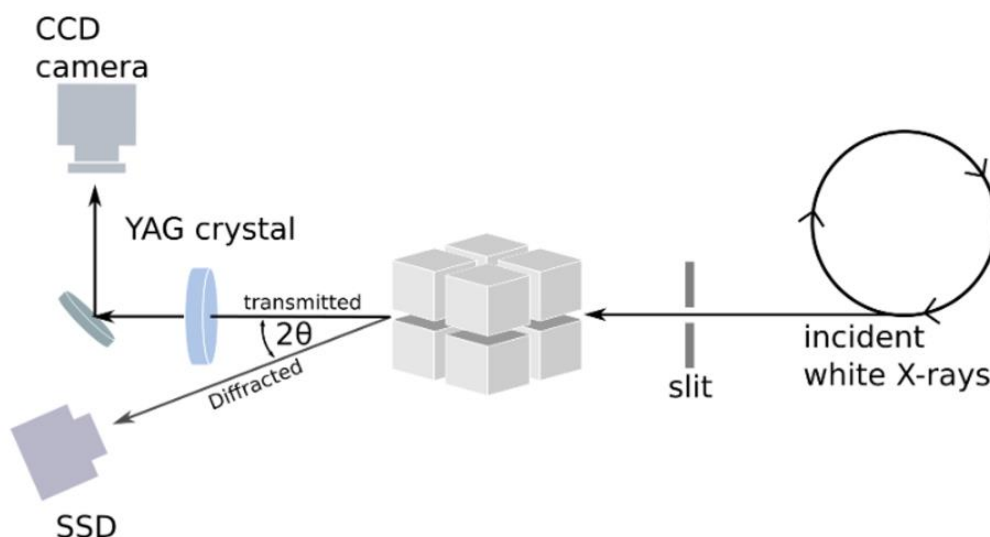
Figure 2-28: *X-ray diffraction and CCD camera setup at the beamline 13-ID-D at GSECARS at APS. The incident white X-ray beam gets focused to the sample through a slit. The transmitted X-rays then get directed through a YAG crystal and collected by a CCD camera, whereas the diffracted X-ray beam is measured by a SSD detector. This figure is modified from Armstrong (2018).*

2.8.6 X-ray radiography

X-ray radiography was employed in order to determine the sample length at any pressure and temperature inside the assembly in-situ. The two gold foils that were placed on the top and bottom of each sample absorb more X-rays due to their higher atomic number relative to the sample, making it easy to discriminate between gold foils and sample in the recorded images (Figure 2-29). Sample images were recorded by an imaging Prosilica GC1380H and a Pointgrey GS3-U3-23S6M-C coupled-charge devices (CCD) with high resolutions of 1 pixel = 2.4 μm and 1.8 μm, respectively (see camera setup in Figure 2-28). The sample length was analyzed in Igor Pro 6 where the position of the gold foils could be detected through maxima in contrast. A line was then fitted through the top and bottom gold foil resulting in the pixel distance between both maxima (Au foils).
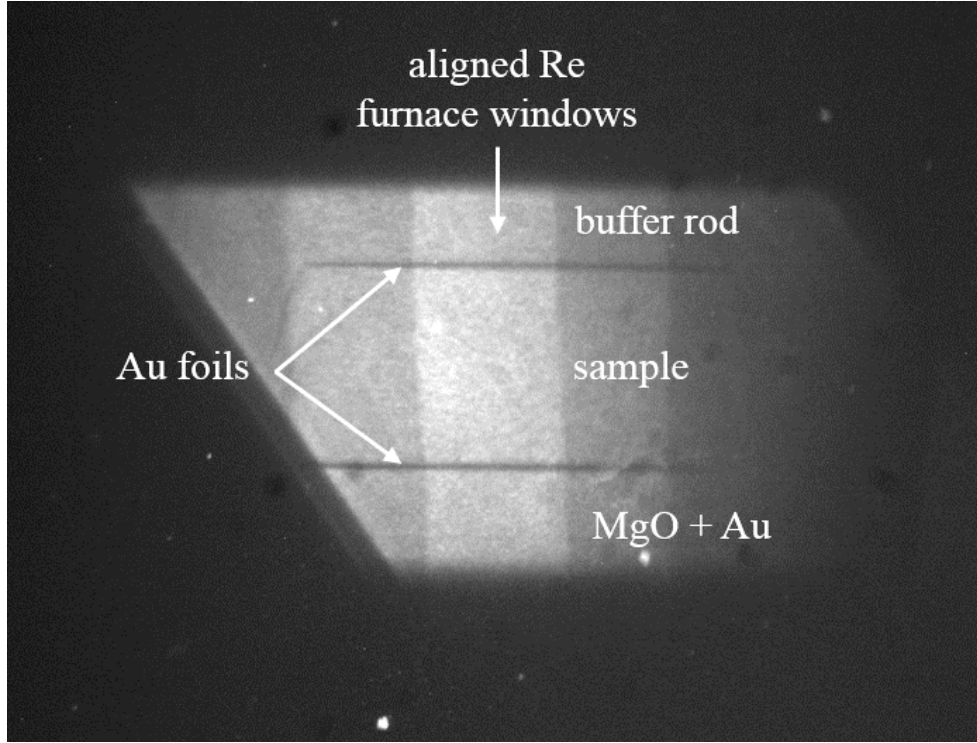
Figure 2-29: *Example of an X-ray radiography image taken for T2083 at 2 GPa and 300 K in-situ during an ultrasonic measurement. The two 2 μm thin gold foils can clearly be distinguished at the top and the bottom of the sample due to their larger absorption of the incoming X-rays. The alignment of the Re windows (brightest central part) also plays a crucial role to be able to collect energy-dispersive X-ray diffraction patterns on the sample and the pressure marker.*

2.8.7 Fitting of elastic parameters at room temperature

The zero-pressure values of the elastic properties of the akimotoite samples at high-pressure and room temperature were fitted using the fitting procedure described by Davies and Dziewonski (1975). Assuming adiabatic compression, the fourth-order equations reported by Davies and Dziewonski (1975) were truncated to third-order finite-strain equations (see Chantel et al. 2016) which can be written out as follows:

$$\rho v_P^2 = (1 - 2\varepsilon)^{5/2}(L_1 + L_2\varepsilon + L^*\varepsilon^2) \qquad \text{(eq. 33)}$$

$$\rho v_S^2 = (1 - 2\varepsilon)^{5/2}(M_1 + M_2\varepsilon + M^*\varepsilon^2) \qquad \text{(eq. 34)}$$

with the strain $\varepsilon = \frac{1}{2}\left[1 - \left(\frac{\rho}{\rho_0}\right)^{2/3}\right]$.

The zero-pressure values of the bulk K_0 and shear modulus G_0 and their first pressure derivatives (K_0' and G_0') can be iteratively fitted through the relations:

$$G_0 = M_1 \qquad\qquad \text{(eq. 35)}$$

$$K_0 = L_1 - \frac{4}{3}G_0 \qquad\qquad \text{(eq. 36)}$$

$$G_0' = \frac{1}{3}(5M_1 - M_2)/K_0 \qquad\qquad \text{(eq. 37)}$$

$$K_0' = \frac{1}{3}(5L_1 - L_2)/K_0 - \frac{4}{3}G_0' \qquad\qquad \text{(eq. 38)}$$

with implied values for M^* and L^* as following:

$$M^* = -24K_0 + \frac{9}{2}K_0K_0' - 4M_1 - 2M_2 \qquad\qquad \text{(eq. 39)}$$

$$L^* = -72K_0 + 18K_0G_0' + \frac{37}{2}L_1 - \frac{13}{2}L_2 \qquad\qquad \text{(eq. 40)}$$

In addition to the elastic parameters at ambient conditions, the absolute pressure can be calculated with the equation:

$$P = -(1 - 2\varepsilon)^{5/2}\left(C_1 + \frac{1}{2}C_2\varepsilon^2\right) \qquad\qquad \text{(eq. 41)}$$

where $C_1 = 3L_1 - 4M_1$ and $C_2 = 3L_2 - 4M_2 + 7C_1$.

Equation (41) was used to determine the absolute pressure which was then compared to the pressure obtained from the Au and MgO unit-cell parameters. The room temperature elastic parameters were then used as initial values to proceed with the fitting of the high temperature elastic parameters.

2.8.8. Fitting of elastic parameters at high temperature

The room- and high-temperature elastic parameters were fitted using the self-consistent thermodynamic model by Stixrude and Lithgow-Bertelloni (2005). By using a Mie-Grüneisen equation of state with a Debye approximation it is possible to describe thermal properties in a thermodynamically consistent way. The isothermal bulk modulus can be expressed as:

$$
\begin{aligned}
K_T = (1 - 2f_E)^{5/2} &\left[K_0 + (3K_{T0}K'_{T0} - 5K_0)f_E + \frac{27}{2}(K_0K'_0 - 4K_0)f_E^{\,2} \right] \\
&+ (\gamma + 1 - q)\gamma \frac{\Delta E_{TH}(V,T)}{V} - \frac{\gamma^2}{V}[TC_V(V,T) - T_0C_V(V,T_0)]
\end{aligned}
\tag{eq. 42}
$$

where f_E is the negative Eulerian strain (eq. 19), $q = \left(\frac{\delta ln\gamma}{\delta lnV}\right)$ where γ is the Grüneisen parameter, E_{TH} is the difference in the quasi-harmonic thermal energy between T and T_0 and C_V is the heat capacity at constant volume. The Debye temperature necessary for the fitting procedure can be expressed using the following equation:

$$
\theta_0 = \frac{h}{k}(3\frac{n}{4\pi V_0})^{\frac{1}{3}}\left[3^{\frac{1}{3}}(\frac{1}{V_{P0}^3} + \frac{2}{V_{S0}^3})^{-\frac{1}{3}} \right]
\tag{eq. 43}
$$

where h is the Planck's constant, k is the Boltzmann's constant and n is the number of atoms in the akimotoite unit cell. Finally, the shear modulus for isotropic materials can be described as:

73

$$G = (1 - 2f)^{\frac{5}{2}} \left[G_0 + (3K_0 G'_0 - 5G_0)f + (6K_0 G'_0 - 24K_0 \right.$$
$$\left. - 14G_0 + \frac{9}{2} K_0 K'_0)f^2 \right] - \eta_S \frac{\Delta E_{TH}(V,T)}{V} \qquad \text{(eq. 44)}$$

where η_S is the shear strain derivative of the Grüneisen parameter.

3. High-pressure elasticity and structural evolution of MgSiO₃ akimotoite

3.1 Large single-crystals of MgSiO₃ akimotoite

Single-crystals of $MgSiO_3$ akimotoite up to 500 μm in size (Figure 3-1) were successfully synthesized in the multi-anvil run S6925. Careful analyses using single-crystal X-ray diffraction confirmed that the run product consisted indeed of high-quality single-crystals of akimotoite having unit-cell lattice parameters $a = 4.7288(1)$ Å, $c = 13.5609(4)$ Å and $V = 262.62(1)$ Å^3 in good agreement with the parameters determined by Horiuchi et al. (1982). Analyses with the electron microprobe revealed a composition of $Mg_{0.993(1)}Si_{1.003(1)}O_3$ (see Table 2-1). The practically negligible vacancy on the MgO_6 site suggests a possible substitution of H^+ as described by Bolfan-Casanova et al. (2000, 2002) which is feasible due to the hydrous surrounding present during the synthesis. This substitution is, however, too small to cause a significant change in the elastic properties of akimotoite and it has been, therefore, neglected.
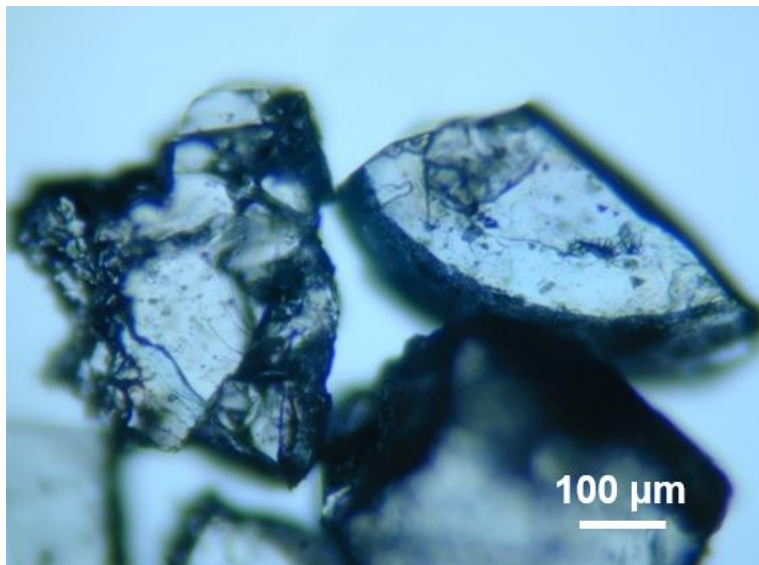
Figure 3-1: Large, high-quality single crystals obtained in the synthesis run S6925. The single crystals were inclusion free and were as large as 500 μm. Photograph courtesy of Giacomo Criniti.

Single-crystals with the highest quality were oriented as described in section 2.2 and double-sided polished to 15 μm. Three diamond anvil cell experiments were performed with sample S6925. The first two DAC experiments (DAC1 and DAC2) were loaded with two crystals (X1

and X2) cut into half-circles as shown in Figure 2-14 to perform Brillouin spectroscopy and single-crystal X-ray diffraction at high pressure. Unit-cell lattice parameters were obtained during the DAC1 experiment at 13 pressure points up to 12.1(1) GPa in steps of 1-2 GPa (Table 3-1). Due to broadening of the reflections likely caused by bridging of the crystal X2, the DAC was opened and reloaded with the same crystals X1 and X2. During the DAC2 experiment, the unit-cell lattice parameters were measured at 14 pressure points up to 24.9(1) GPa. In particular, three points at ambient pressure, after gas loading (P = 0.23(3) GPa) and at 7.37(3) GPa were measured in order to check consistency with the DAC1 experiments (Table 3-1). Broadening of the reflections during the DAC2 experiment was observed for both crystals above 14 GPa, especially X2. To release the stress that build up during compression to 19.2(1) GPa, the DAC was placed on a heating plate at 200 °C for 30 minutes. The pressure inside the DAC dropped by 8.1 GPa to 11.1(1) GPa, however, the reflections became sharper again. For example, the FWHM for reflection (-2 0 4) was 0.287 before heating at 19.2(1) GPa and became sharper having a FWHM of 0.081 after relaxation at 11.1(1) GPa. After increasing the pressure again to 17.61(1) GPa, the FWHM of reflections (2 -2 4), an equivalent to (-2 0 4) in the trigonal system, for X1 remained sharp with a FWHM of 0.111, however, the FWHM of (-2 0 4) for crystal X2 increased again to 0.164.

The third DAC experiment (DAC3) was loaded with a single-crystal of the dimensions 100x100x15 μm^3 to perform full intensity data collections at high pressure. Unit-cell lattice parameters were determined at nine pressure points up to 10.6(2) GPa (Table 3-1), whereas full intensity data collection were performed at 4 pressure points (Table 2-2b). At 9.15(1) GPa, a broadening of the reflections was observed. Therefore, the DAC was heated on a heating plate at 200 °C for 2 hours to release stress. As for DAC2, the reflections became sharper after the stress release and the pressure dropped to 8.1(2) GPa. The experiment was continued from this pressure point up to 10.6(2) GPa.

3.2 High-pressure compressibility of MgSiO₃ akimotoite

The variation with pressure of the unit-cell lattice parameters *a* and *c* is shown in Figure 3-2 for all crystals (Table 3-1). At 14-17 GPa the unit-cell axis values obtained for X1 and X2 are clearly different, likely due to some non-hydrostatic stresses developing in the DAC chamber as suggested by the reflection broadening. This is particularly visible in the *c/a* ratio (Figure 3-3),

which shows a larger scatter for the pressure points between 14 to 17 GPa. After having heated the DAC as described in section 3.1 in order to relax the stresses, the *c/a* ratio values become very similar again up to 24.9(1) GPa. To fit the axial compressibility, the data points between 14 to 17 GPa of DAC2 were, therefore excluded.
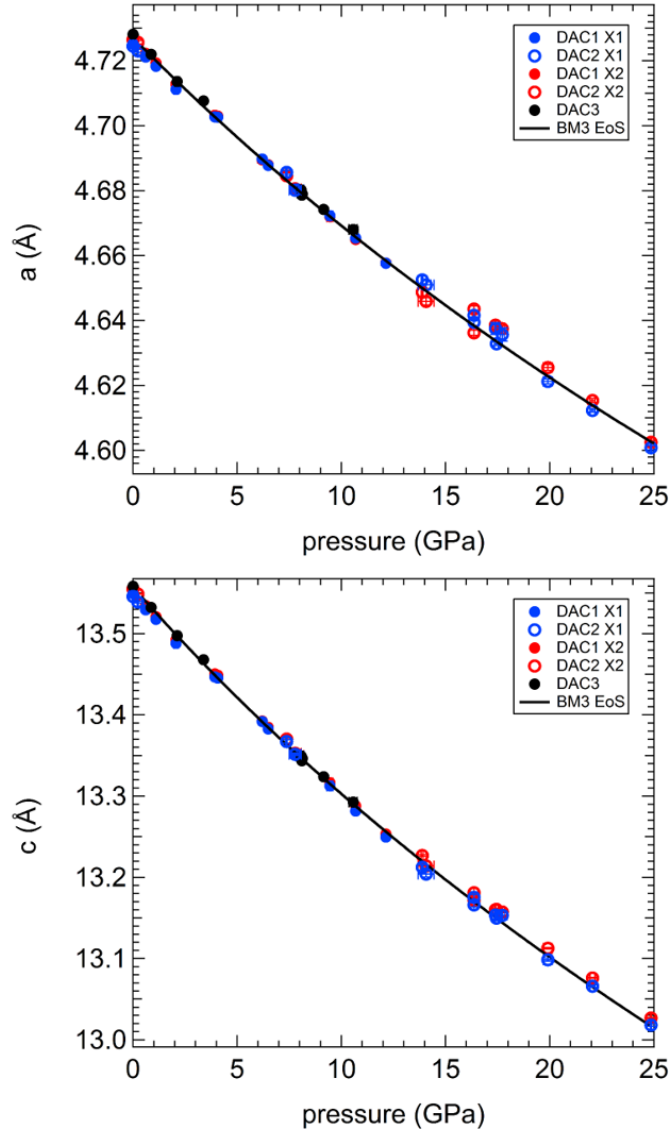
Figure 3-2: *Unit-cell lattice parameters of MgSiO₃ akimotoite from the three DAC experiments as a function of pressure as calculated from the ruby fluorescence: a-axis (top) and c-axis (bottom). The solid lines represent the linear BM3 EoS fits using the parameters reported in Table 3-2. The uncertainties are smaller than the symbol size.*

Table 3-1: *Unit-cell parameters of crystals X1 and X2 measured in the two DAC experiments up to 24.9(1) GPa and of the akimotoite crystal loaded in DAC3. The pressure was calculated using the ruby fluorescence lines following Dewaele et al. (2004).*

	X1			X2		
P_{ruby} (GPa)	a (Å)	c (Å)	V (Å^3)	a (Å)	c (Å)	V (Å^3)
DAC1						
0.001(1)	4.7253(5)	13.5493(12)	262.00(5)	4.7258(5)	13.5528(4)	262.12(5)
0.60(5)	4.7212(3)	13.5295(6)	261.16(3)	4.7223(4)	13.5345(3)	261.38(3)
1.10(1)	4.7183(1)	13.5177(4)	260.62(2)	4.7194(4)	13.5209(4)	260.80(4)
2.07(11)	4.7112(2)	13.4881(5)	259.28(2)	4.7129(6)	13.4927(5)	259.54(7)
3.93(1)	4.7027(4)	13.4467(9)	257.54(4)	4.7032(3)	13.4505(3)	257.67(3)
4.07(1)	4.7026(4)	13.4453(9)	257.50(4)	4.7030(3)	13.4489(2)	257.61(3)
6.20(6)	4.6898(4)	13.3919(9)	255.08(4)	4.6895(9)	13.3925(9)	255.06(10)
6.48(6)	4.6878(3)	13.3828(8)	254.69(3)	4.6880(4)	13.3847(5)	254.75(4)
7.88(3)	4.6806(2)	13.3509(4)	253.30(2)	4.6801(4)	13.3524(5)	253.27(4)
8.00(20)	4.6803(2)	13.3496(5)	253.25(2)	4.6799(4)	13.3502(5)	253.22(5)
9.45(14)	4.6723(4)	13.3126(9)	251.68(4)	4.6720(3)	13.3166(4)	251.73(3)
10.68(3)	4.6654(4)	13.2817(8)	250.36(4)	4.6650(5)	13.2880(6)	250.43(5)
12.14(6)	4.6577(5)	13.2495(11)	248.92(5)	4.6577(6)	13.2534(10)	249.00(7)
DAC2						
0.001(1)	4.7245(7)	13.5460(16)	261.85(7)	4.7265(4)	13.5550(3)	262.24(4)
0.23(3)	4.7230(5)	13.5389(11)	261.55(5)	4.7257(5)	13.5490(5)	262.04(6)
7.37(3)	4.6856(6)	13.3672(20)	254.16(6)	4.6846(9)	13.3702(9)	254.11(10)
13.88(5)	4.6525(12)	13.2125(33)	247.68(12)	4.6487(14)	13.2270(13)	247.55(15)
14.07(38)	4.6510(14)	13.2042(37)	247.36(14)	4.6459(12)	13.2140(10)	247.01(13)
16.37(1)	4.6395(10)	13.1661(27)	245.43(9)	4.6363(9)	13.1718(8)	245.19(9)
16.37(1)	4.6416(12)	13.1756(33)	245.83(12)	4.6436(9)	13.1811(12)	246.14(10)
17.40(2)	4.6375(18)	13.1537(48)	244.99(17)	4.6386(7)	13.1602(9)	245.22(8)
17.72(10)	4.6357(20)	13.1532(55)	244.79(20)	4.6375(9)	13.1575(10)	245.06(9)
17.44(9)	4.6328(6)	13.1498(16)	244.42(6)	4.6376(11)	13.1606(13)	245.12(12)
19.91(21)	4.6212(7)	13.0986(20)	242.25(7)	4.6255(9)	13.1126(10)	242.97(10)
22.05(12)	4.6123(5)	13.0661(14)	240.72(5)	4.6154(6)	13.0762(7)	241.23(6)
24.86(3)	4.6008(6)	13.0180(17)	238.64(6)	4.6025(5)	13.0268(6)	238.98(6)
7.79(28)	4.6802(6)	13.3516(16)	253.27(6)	4.6806(8)	13.3527(9)	253.34(9)
DAC3						
0.001(1)	4.7282(1)	13.5585(1)	262.50(2)			
0.87(3)	4.7219(3)	13.5322(2)	261.30(4)			
2.12(11)	4.7136(3)	13.4977(2)	259.72(3)			
3.39(3)	4.7077(1)	13.4681(1)	258.49(1)			
8.07(11)	4.6802(2)	13.3494(2)	253.23(3)			
8.13(1)	4.6790(4)	13.3464(4)	253.05(4)			
9.15(1)	4.6743(4)	13.3239(3)	252.11(5)			
8.10(20)	4.6786(8)	13.3437(6)	252.95(8)			
10.57(20)	4.6680(8)	13.2928(6)	250.85(9)			
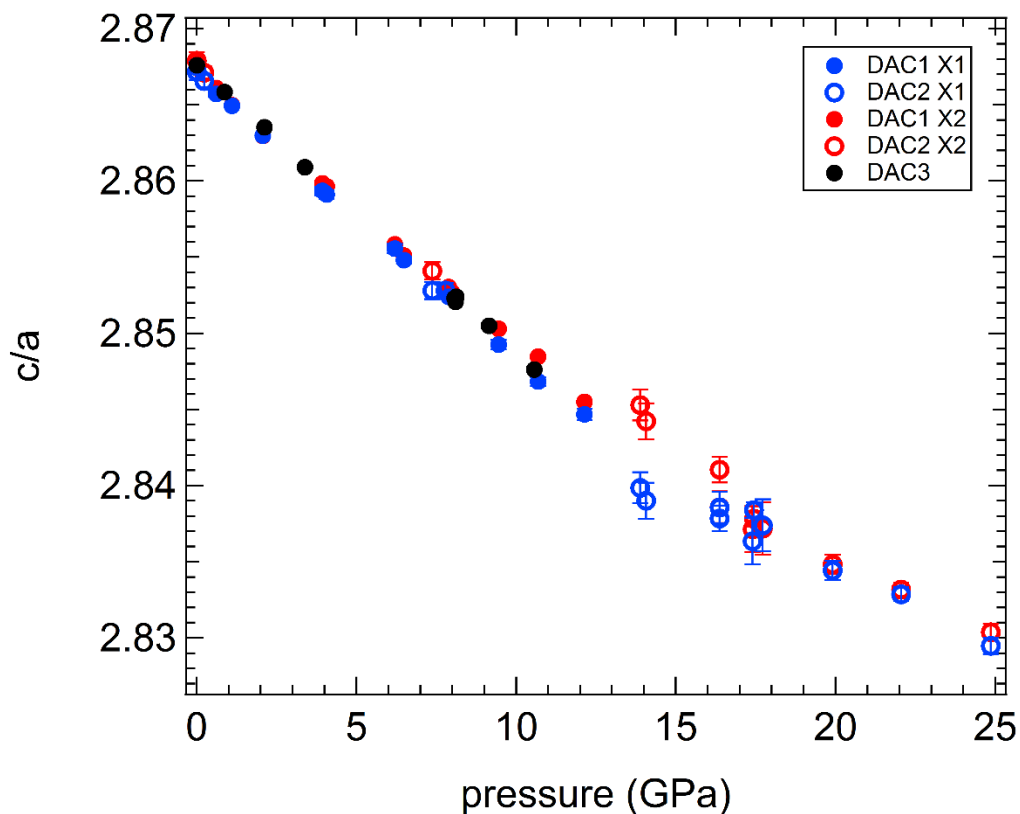
Figure 3-3: *c/a ratio of akimotoite for all three DAC experiments as a function of pressure. The data scatter between 14 and 17 GPa for DAC2 (X1 and X2) is likely explained by the onset of non-hydrostatic stresses. These were released by heating the cell up to 200 °C for 30 min.*

The unit-cell volumes (Table 3-1) obtained for $MgSiO_3$ akimotoite during the three different DAC runs were plotted against the pressure calculated from the ruby fluorescence lines using the pressure calibration reported by Dewaele et al. (2004) (Figure 3-4). The volumes measured for crystal X2 in DAC2 are larger than the volumes of crystal X1. The reflections of X2 were also broader than those of X1 even after heating the DAC2. Therefore, the X2 unit-cell parameters were excluded for the EoS fitting.
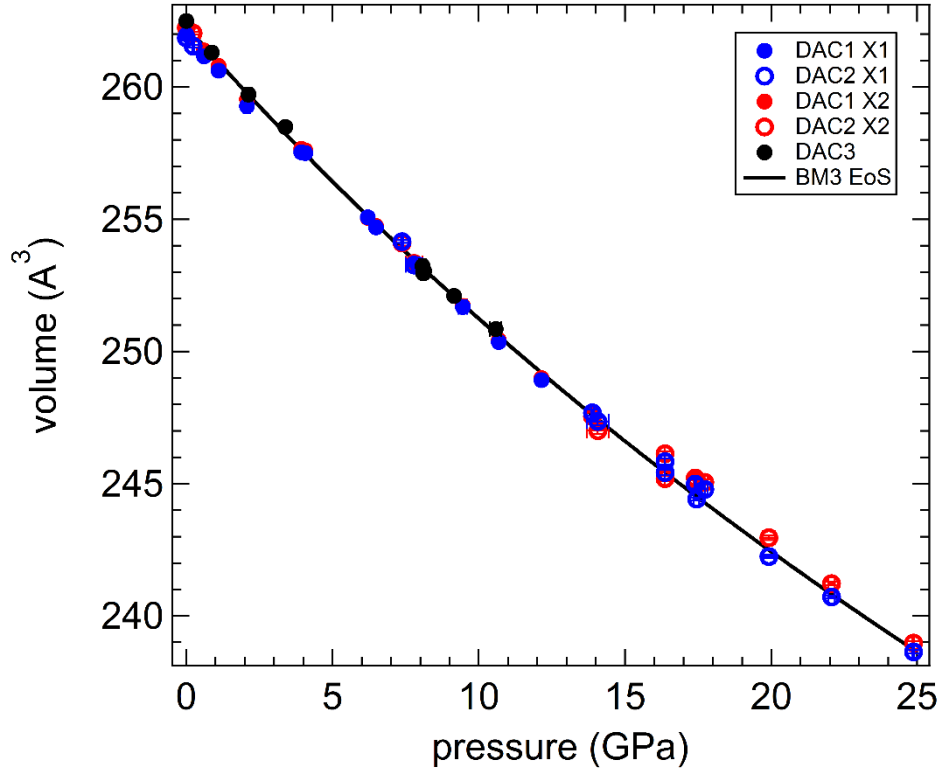
Figure 3-4: *Unit-cell volumes of MgSiO₃ akimotoite measured in all three DAC runs versus the pressure determined using the ruby fluorescence calibration by Dewaele et al. (2004). The volumes are in good agreement for DAC1 and DAC3, however, for DAC2, broadening of the reflections of X2 caused a deviation to larger volumes (open red symbols). The solid black curve represents the BM3 EoS fitted using the parameters reported in Table 3-2. The uncertainties are smaller than the symbol size.*

3.2.1 Bulk compressibility of MgSiO₃ akimotoite

In order to choose the truncation of the BM EoS to use (see section 2.7.4), the F_E-f_E plot was calculated for all three data sets of DAC1, 2 and 3 individually combined in Figure 3-5. The data points can be fitted with a straight line, $F_E = 209(1) + 367(76) f_E$, which suggests that a 3rd oder BM EoS (BM3 EoS) need to be used. In these plots, the intersect with the F_E-axis represents the isothermal bulk modulus, whereas from the slope a $K' = 5.1$ can be calculated (see section 2.7.4). A BM3 EoS has been, therefore, used to fit the P-V data resulting in the following parameters: V_0 = 262.26(3) A^3, K_0 = 209(2) GPa and K' =4.8(2) (Table 3-2) in excellent agreement with the results of the F_E-f_E plot. The resulting BM3 fitted to the P-V data set is shown in Figure 3-4.
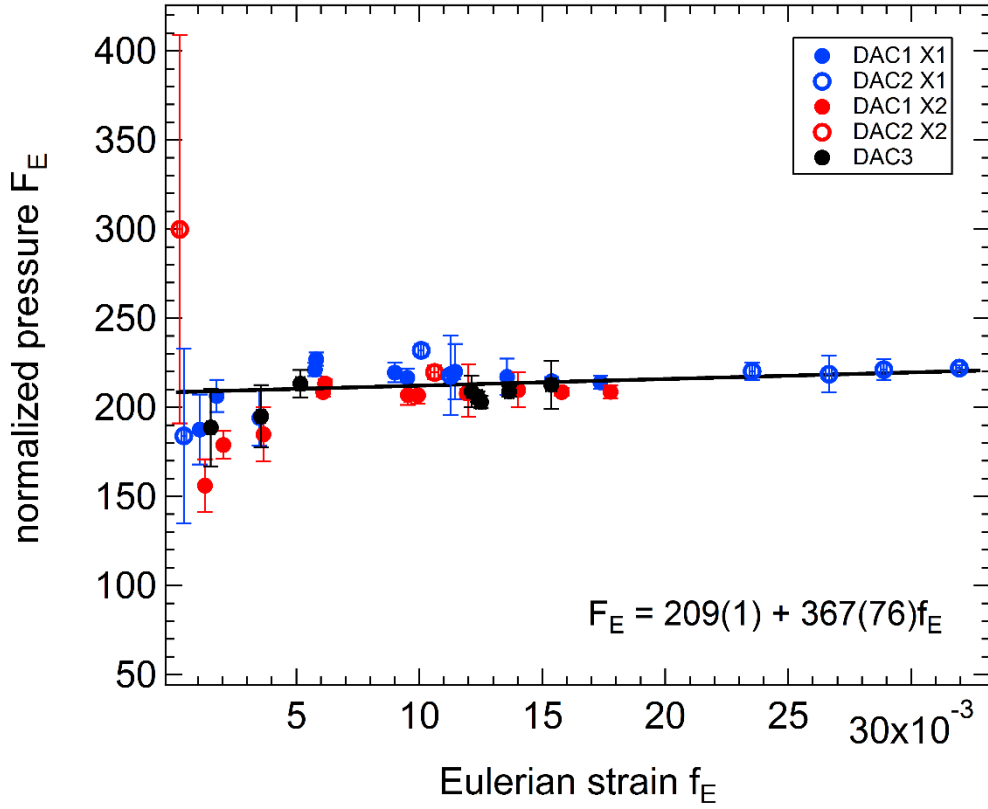
Figure 3-5: *Normalized pressure (F_E) plotted against the Eulerian strain (f_E) for MgSiO₃ akimotoite. The data can be fitted with a straight line intersecting the y-axis at F_E=209(1).*

Table 3-2: *Resulting BM3 EoS parameters for bulk and axial compressibility of akimotoite.*

V_0 (Å³)	262.26(3)
K_0 (GPa)	209(2)
K'	4.8(2)
a_0 (Å)	4.7271(2)
M_0 (GPa)	724(5)
M'	18(1)
c_0 (Å)	13.5576(4)
M_0 (GPa)	461(2)
M'	14(1)

3.2.2 Axial compressibility of MgSiO₃ akimotoite

The unit-cell lattice parameters normalized using the room pressure values a/a_0 and c/c_0 are shown in Figure 3-6. MgSiO₃ akimotoite is clearly more compressible along the c-axis making the compression mechanism with increasing pressure very anisotropic. The normalized pressure also was calculated for the a- and c-axes and plotted versus the Eulerian strain (Figure 3-7 and 3-8). Both F_E-f_E plots could be fitted with a straight line implying the use of a BM3 EoS following the same scheme as for the bulk compressibility. The intersects with the F_E-axes represent the linear moduli, M_a and M_c, respectively, whereas from the slopes a $M' = 22$ for the a-axis and a $M' = 16$ for the c-axis can be calculated (see section 2.7.4). All EoS fitting parameters can be found in Table 3-2. The fitted BM3 EoS describing the compressibility of the a- and c-axes are shown in Figures 3-2 and 3-6. As expected the resulting axial moduli for the a lattice parameter ($M_0 = 724(5)$ GPa) is 1.5 times larger than the axial modulus of the c lattice parameter ($M_0 = 461(2)$ GPa) (Table 3-2) confirming the large anisotropy of the axial compressibility.
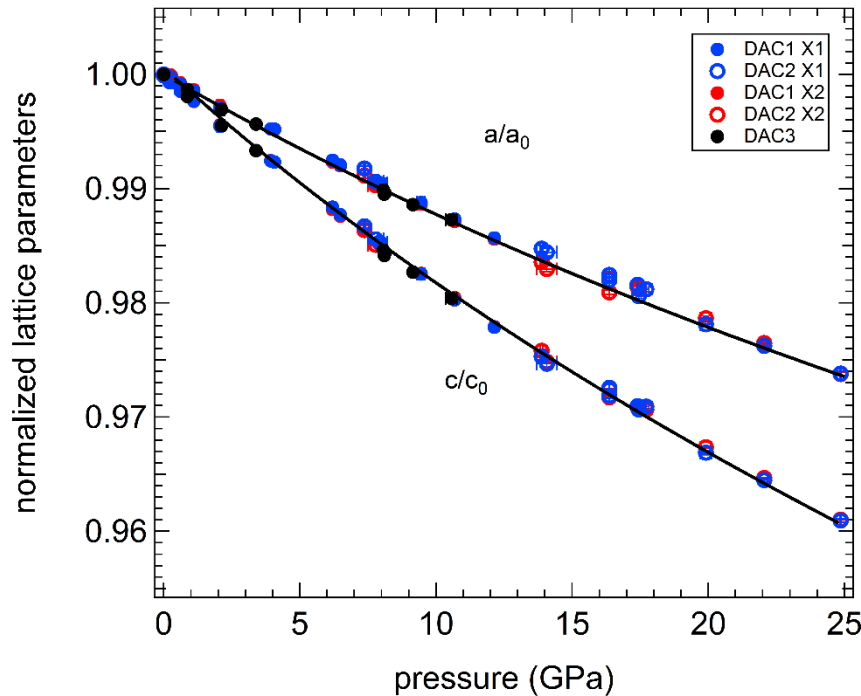
Figure 3-6: *Normalized unit-cell lattice parameters a/a_0 and c/c_0 as a function of pressure. The c-axis is more compressible than the a-axis. The solid lines are BM3 EoS fits using the parameters reported in Table 3-2. The uncertainties are smaller than the symbol size.*
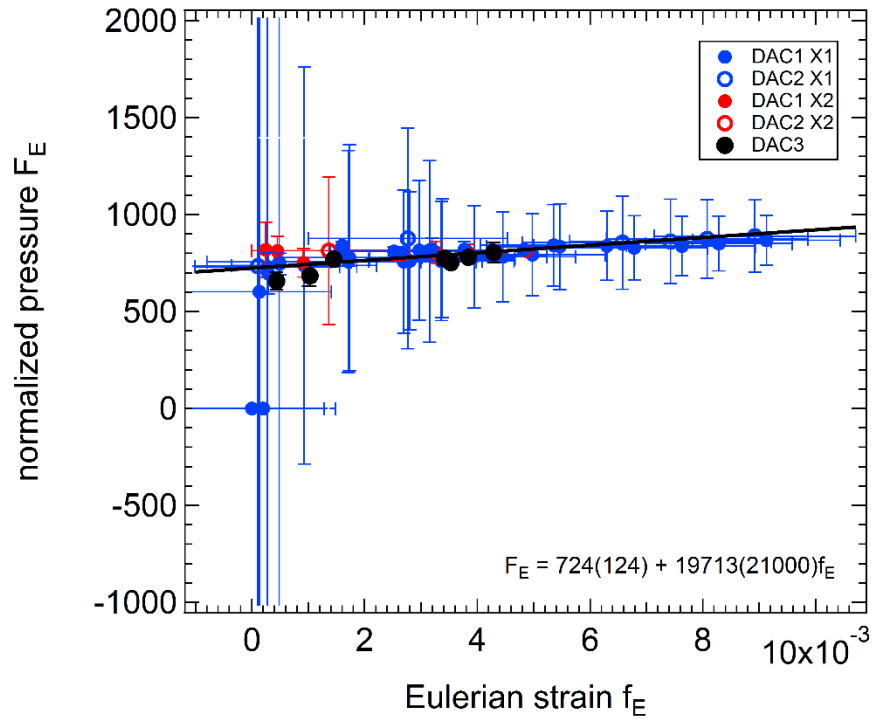
Figure 3-7: *Normalized pressure (F_E) plotted against the Eulerian strain (f_E) for the a-axis. The data can be fitted with a straight line intersecting the y-axis at F_E=724(124).*
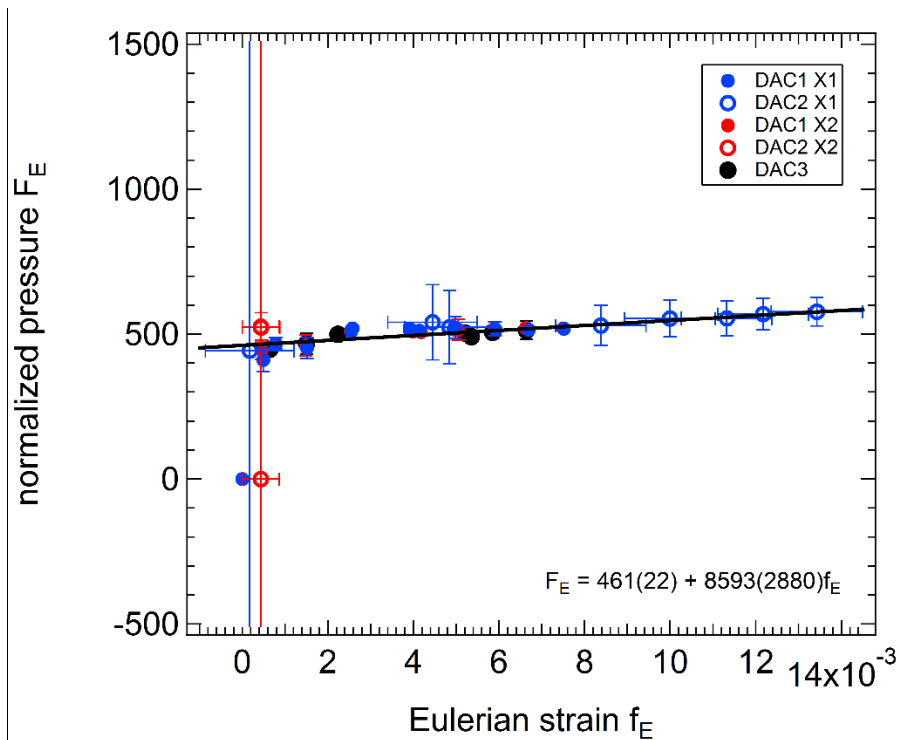
Figure 3-8: *Normalized pressure (F_E) plotted against the Eulerian strain (f_E) for the c-axis. The data can be fitted with a weighted line intersecting the y-axis at F_E=461(22).*

3.2.3 Compressibility of MgSiO₃ akimotoite in comparison with literature data

The bulk compressibility of $MgSiO_3$ akimotoite can be compared to compressibility studies reported in the literature. So far, the compressibility of $MgSiO_3$ akimotoite has been studied only for polycrystalline samples. One study investigated the compressibility of $MgSiO_3$ akimotoite using a DAC (Reynard et al. 1996) with H_2O as pressure transmitting medium up to 28 GPa. Two other studies were performed in the large-volume press up to 16 and 25 GPa, respectively (Wang et al. 2004, Zhou et al. 2014). The volumes obtained in the mentioned studies were normalized with respect to their measured room pressure values and compared to the data obtained in the present study on single-crystals of $MgSiO_3$ akimotoite (black circles) (Figure 3-9). The black line corresponds to the BM3 EoS parameters reported in Table 3-2. The normalized volumes from Wang et al. (2004) and Zhou et al. (2014) appear slightly more compressible than the data presented in this study, whereas the volumes reported by Reynard et al. (1996) are clearly much stiffer.

The *P-V* data reported by Reynard et al. (1996), Wang et al. (2004) and Zhou et al. (2014) were refitted using the EoSfitGUI software (Angel et al. 2014) in order to minimize difference created by different fitting procedures. The refitted parameters are reported in Table 3-3. The K_T and *K'* values obtained after refitting the data set of Zhou et al. (2014) are similar to those reported in the original paper, although with a larger V_0 (Table 3-3). Due to a lack in resolution, the *P-V* data by Wang et al. (2004) were refitted with a 2nd-oder Birch-Murnagham (BM2) EoS with *K'* fixed to 4. The resulting K_T are much larger than reported in their study which report a very large *K´*, note however that Wang et al. (2004) fixed the K_T to the value recalculated from that reported by Weidner and Ito (1985) as $K_{S0} = 212$ GPa and refined only V_0 and *K´*. Also Reynard et al. (1996) have fixed the K_T to the value of 212 GPa, without, however, transforming it from adiabatic to isothermal. In addition, they obtained considerably different *K'*s depending on which pressure scale they used. The ruby pressure scale gives a *K'* of 7.5(10) and the EoS of ice VII pressure scale (Hemley et al. 1987) yields a *K'* of 5.6(10). By fitting the data of Reynard et al. (1996) according to the ice VII pressure scale with a BM2 we obtain a much larger K_T as expected from the much stiffer volumes reported in the mentioned study. It is likely that non-hydrostatic stresses were developed inside the DAC experiment of Reynard et al. (1996) due to the use of H_2O as pressure transmitting medium which transforms to ice VII above 2.5 GPa and therefore may produce non-hydrostatic conditions above such pressure (Angel et al. 2005).
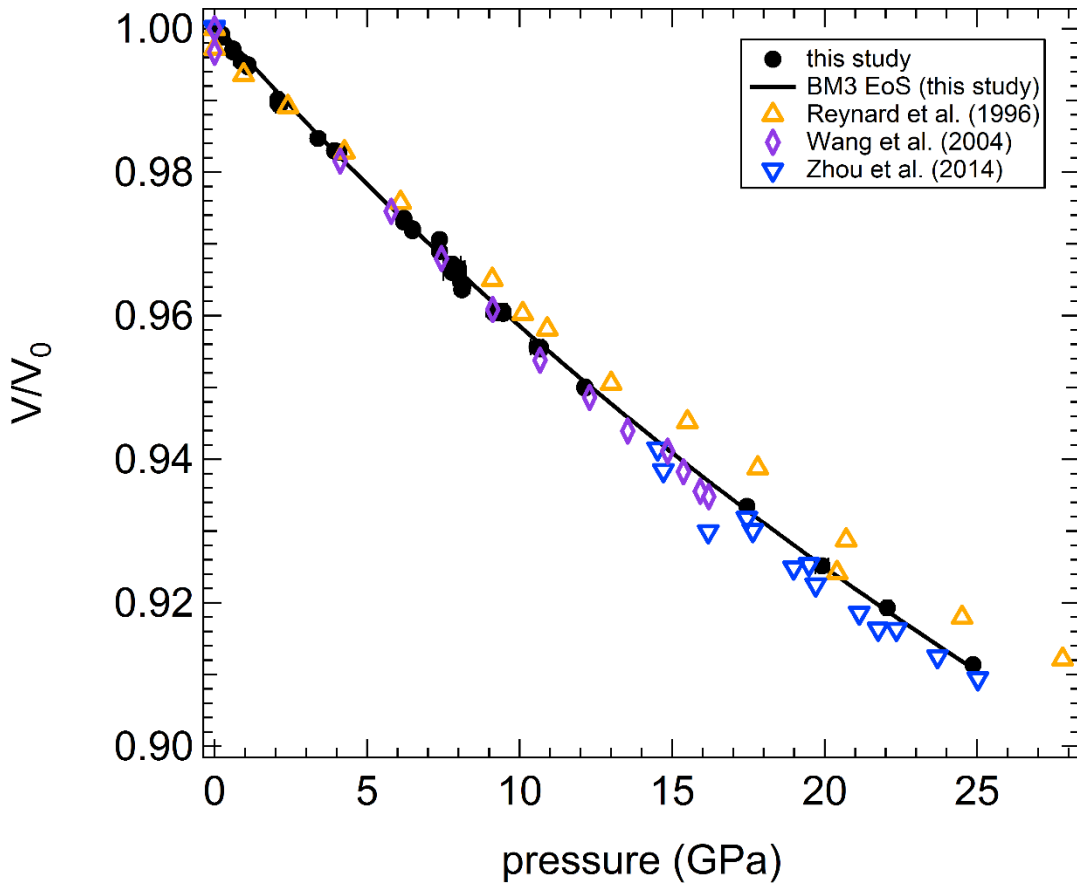
Figure 3-9: *Variation with pressure of the **n**ormalized volumes of MgSiO₃ akimotoite from this study (black circles) in comparison to literature data versus pressure. The solid black line is the BM3 EoS fitted with the parameters reported in Table 3-2. The normalized volumes from Wang et al. (2004) (purple diamonds) and Zhou et al. (2014) (blue triangles) are in agreement with this study, especially at pressures below 15 GPa. The study by Reynard et al. (1996) (orange triangles) strongly deviates to larger volumes which may be explained by non-hydrostatic conditions in their DAC experiment.*

Table 3-3: Comparison of bulk moduli from this study to experimental data from the literature. The refit parameters were obtained by re-fitting the P-V data present in the literature with the EoSFit program.

	V_0 (Å^3)	K_{T0} (GPa)	K_{S0} (GPa)	K'	V_0 (Å^3) (refit)	K_{T0} (GPa) (refit)	K' (refit)
this study	262.26(3)	209(2)	211[a]	4.8(2)			
Weidner and Ito (1985)	263.56		212	-			
Reynard et al. (1996)	262.17(49)	212[b]		5.6(10) or 7.5(10)	262.08(24)	227(7)	4
Wang et al. (2004)	263.9(2)	210[b]		5.6(8)	263.59(3)	229(7)	4
Zhou et al. (2014)	262.53(5)		219.4(7)	4.62(3)	263.36(7)	219(3)	4.6(3)

[a] value recalculated using $K_{S0} = K_{T0} * (1 + \alpha\gamma T)$ *with* $\alpha = 2.44x10^{-5}$ *1/K (Ashida et al. 1988),* $\gamma = 1.18$ *(Stixrude and Lithgow-Bertelloni 2005), T = 298 K*

[b] Reynard et al. (1996) and Wang et al. (2004) fixed the value of K_{T0} after Weidner and Ito (1985)

3.3 Elasticity of MgSiO₃ akimotoite at high pressure

3.3.1 Wave velocities of MgSiO₃ akimotoite

Brillouin spectroscopy measurements were collected at eleven pressure points for DAC1 and DAC2 up to a maximum pressure of 24.9(1) GPa using the Brillouin setup described in section 2.7.5. An example of dispersion curves of v_P, v_{S1} and v_{S2} collected for crystal X1 at the maximum pressure reached in this study is given in Figure 3-10. For the last two pressure points, an overlapping of the diamond v_S (red circles in Figure 3-10) with the akimotoite v_P occurred for different orientation directions; however, the number of observable, i.e. wave velocities, was still sufficient to constrain all elastic stiffness coefficients using the Christoffel equation as described in section 2.7.5.
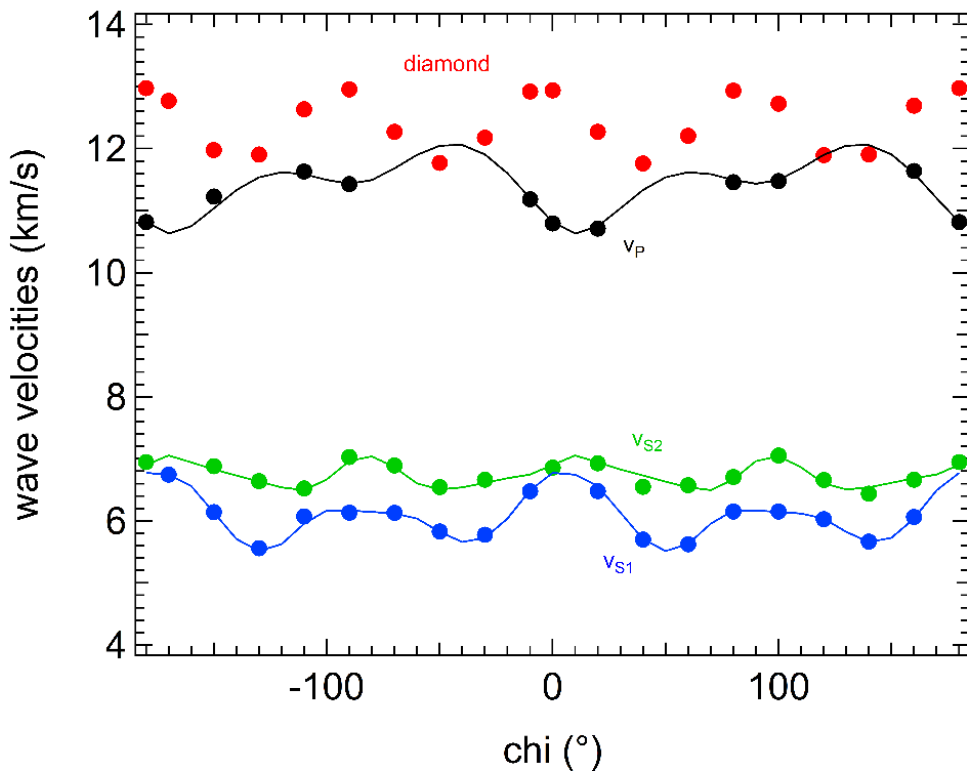
Figure 3-10: *Dispersion curves of v_P (black), v_{S1} (blue) and v_{S2} (green) of crystal X1 at 24.9(1) GPa. With increasing pressure, some of the v_P signals of the sample were masked by the v_S signals of the diamond (red) reducing the amount of signals to be fitted with the Christoffel equation.*

The resulting c_{ij} coefficients obtained at each pressure point are reported in Table 3-4. The uncertainties of the fitted c_{ij}'s (Table 3-4) are below 1 - 2.5 % for c_{11}, c_{33}, c_{44}, c_{12}, c_{13} and around 1-2 GPa for the smallest c_{ij}'s, c_{14} and c_{25}, that range between values of -39 to 23 GPa. Most of the coefficients increase monotonously with increasing density (Figure 3-11), except for c_{14} and c_{25} which decrease with pressure. The c_{ij}'s at ambient pressure are in good agreement with the c_{ij}'s determined by Weidner and Ito (1985) (orange triangles in Figure 3-11) who have investigated a single-crystal of MgSiO$_3$ akimotoite at 16 different orientations. The c_{14} reported in this study is negative likely due to a different setting for the transformation from the trigonal to the orthogonal coordinates. The large differences between all stiffness coefficients (Figure 3-11) is stressing the fact that akimotoite is a highly anisotropic mineral.
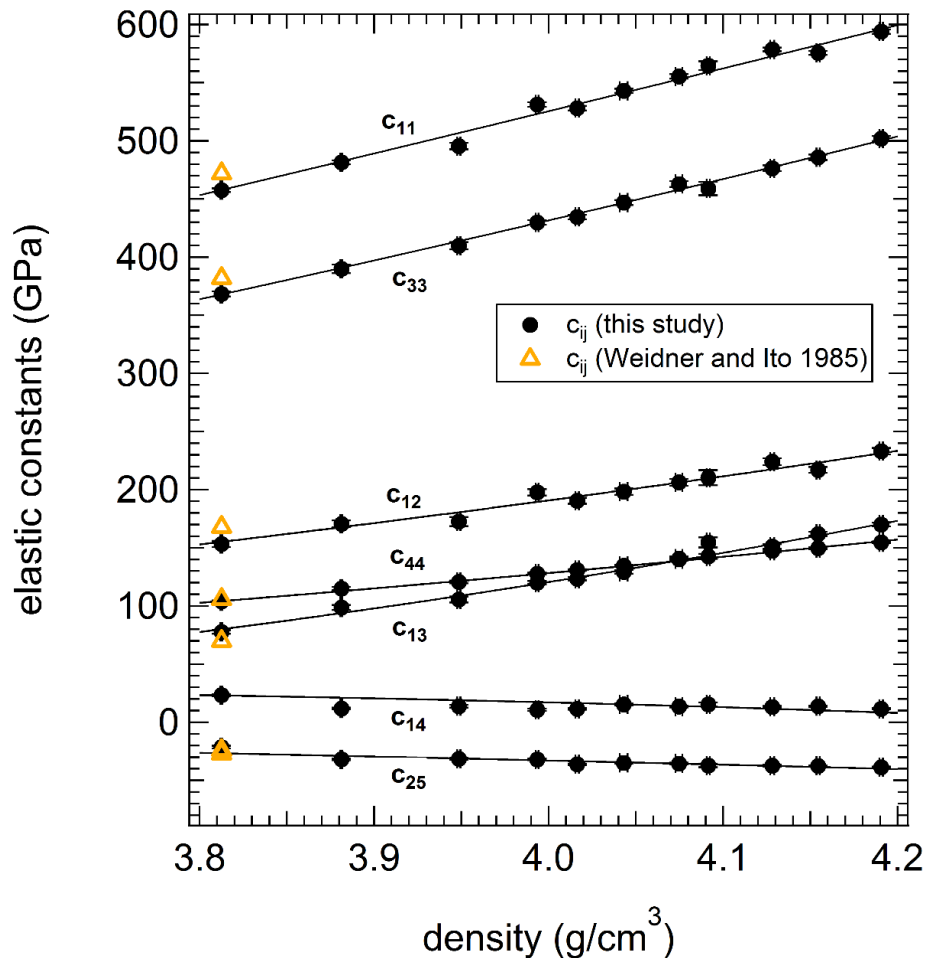
Figure 3-11: *Variation with pressure of the stiffness coefficients cij of akimotoite. The large anisotropy of MgSiO₃ akimotoite can be seen in the large difference between all stiffness coefficients. The black solid lines represent BM3 EoS fits through the stiffness coefficients. The uncertainties are smaller than the symbol size.*

Table 3-4: *Single-crystal stiffness coefficients c_{ij}'s, absolute pressure (P_{abs}), pressure calculated using the ruby calibration reported by Dewaele et al. (2004) and density measured by single-crystal X-ray diffraction. The RVH average bulk (isothermal K_T and adiabatic K_S) and shear moduli are reported, as well as the aggregate velocities v_P and v_S. K_T was calculated using the relation: $\boldsymbol{K_{S0} = K_{T0} * (1 + \alpha\gamma T)}$ with $\alpha = 2.44x10^{-5}$ 1/K (Ashida et al. 1988), $\gamma = 1.18$ (Stixrude and Lithgow-Bertelloni 2005) and T = 298 K.*

P_{abs}	P_{ruby}	density	c_{11}	c_{33}	c_{44}	c_{12}	c_{13}	c_{14}	c_{25}	K_T	K_S	G	v_P	v_S
(GPa)	(GPa)	(g/cm³)	(GPa)	(GPa)	(GPa)	(GPa)	(GPa)	(GPa)	(GPa)	(GPa)	(GPa)	(GPa)	(km/s)	(km/s)
0.00	0.001(1)	3.8125(5)	458(2)	368(2)	104(1)	153(3)	78(2)	23(1)	-21(2)	206(1)	208(1)	130(1)	10.01(2)	5.85(2)
3.87	3.93(1)	3.8813(5)	482(2)	390(4)	115(1)	171(3)	99(2)	12(1)	-32(1)	227(1)	229(1)	137(1)	10.27(2)	5.93(2)
7.88	7.79(3)	3.9486(9)	496(3)	410(3)	121(1)	173(4)	105(2)	14(1)	-31(1)	236(2)	238(2)	143(1)	10.39(2)	6.01(2)
10.68	10.68(3)	3.9934(8)	531(2)	430(2)	128(1)	198(3)	120(1)	11(1)	-32(1)	258(1)	260(1)	149(1)	10.69(1)	6.11(1)
12.15	12.14(6)	4.0163(11)	528(2)	434(2)	131(1)	190(3)	124(1)	12(1)	-36(1)	258(1)	260(1)	150(1)	10.68(1)	6.12(1)
13.90	14.07(38)	4.0430(22)	543(2)	447(2)	135(1)	198(3)	129(2)	15(1)	-35(1)	267(1)	269(1)	154(1)	10.81(1)	6.17(1)
16.03	16.37(1)	4.0748(20)	555(2)	463(2)	140(1)	206(3)	141(2)	14(1)	-36(1)	278(1)	281(1)	158(1)	10.95(2)	6.22(1)
17.17	17.44(10)	4.0915(10)	565(4)	459(6)	143(2)	210(6)	155(4)	15(2)	-37(2)	287(3)	289(3)	158(1)	11.03(4)	6.22(3)
19.72	19.91(21)	4.1282(12)	579(2)	476(3)	147(1)	224(3)	151(2)	13(1)	-37(1)	293(1)	296(1)	163(1)	11.11(2)	6.28(1)
21.60	22.05(12)	4.1545(9)	576(2)	486(2)	150(1)	217(3)	162(2)	14(1)	-38(1)	297(1)	300(1)	164(1)	11.14(1)	6.28(1)
24.23	24.86(3)	4.1906(10)	594(2)	502(2)	155(1)	233(3)	170(2)	11(1)	-39(1)	310(1)	313(1)	167(1)	11.28(1)	6.32(1)

Note $c_{66} = 0.5\ (c_{11} - c_{12})$

The Reuss and Voigt bounds of the bulk and shear moduli were calculated using the c_{ij}'s and the s_{ij}'s obtained inverting the elastic tensor (see Section 2.7.3) and are shown in Figure 3-12 as a function of density. As proposed by Watt et al. (1976), the arithmetic average has been used to calculate the Reuss-Voigt-Hill average which represents the aggregate bulk and shear moduli of a composite material. The resulting Reuss-Voigt-Hill average bulk and shear moduli obtained from the Brillouin spectroscopy measurements are shown in Figure 3-12 (black symbols). The adiabatic bulk modulus of 208(1) GPa obtained from Brillouin spectroscopy is slightly smaller than the recalculated adiabatic bulk modulus obtained from EoSfit of 211(2) GPa.
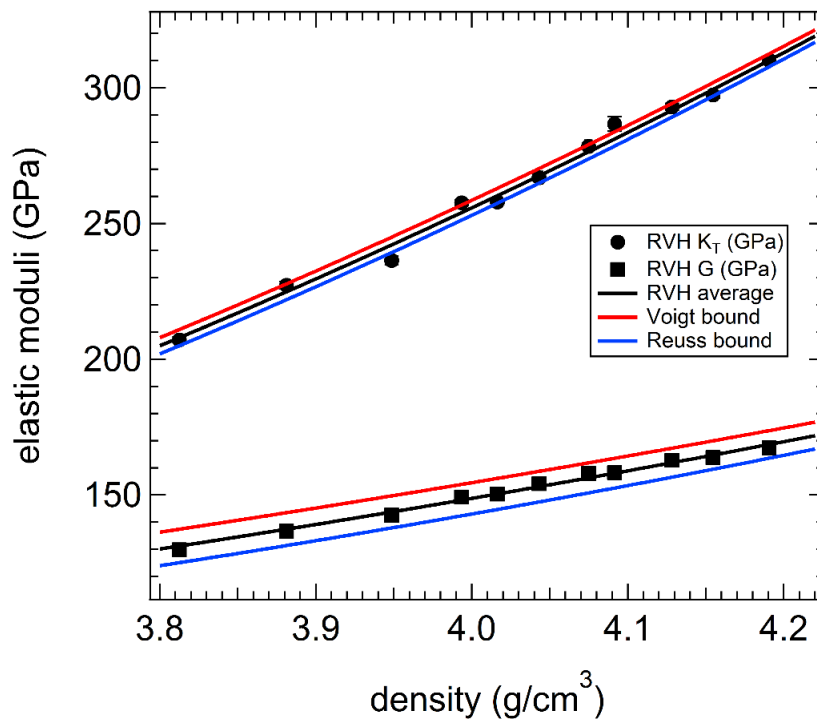
Figure 3-12: *Elastic moduli K_T and G versus density. The black circles are the RVH average isothermal bulk and shear moduli determined experimentally. The solid lines represent BM3 EoS fits through the RVH average (black), the upper Voigt bound (red) and the lower Reuss bound (blue). The uncertainties are smaller than the symbol size.*

The aggregate compressional and shear wave velocities, were calculated following equations (17) and (18), respectively, by using the elastic moduli determined with the Reuss-Voigt-Hill average and density measured using single-crystal X-ray diffraction on the same crystals (Figures 3-13 and 3-14). The difference between the Reuss and Voigt bounds for both the longitudinal and shear wave velocities are ~0.3 km/s and decrease slightly with increasing pressure indicating a decrease in anisotropy (Figures 3-13 and 3-14).
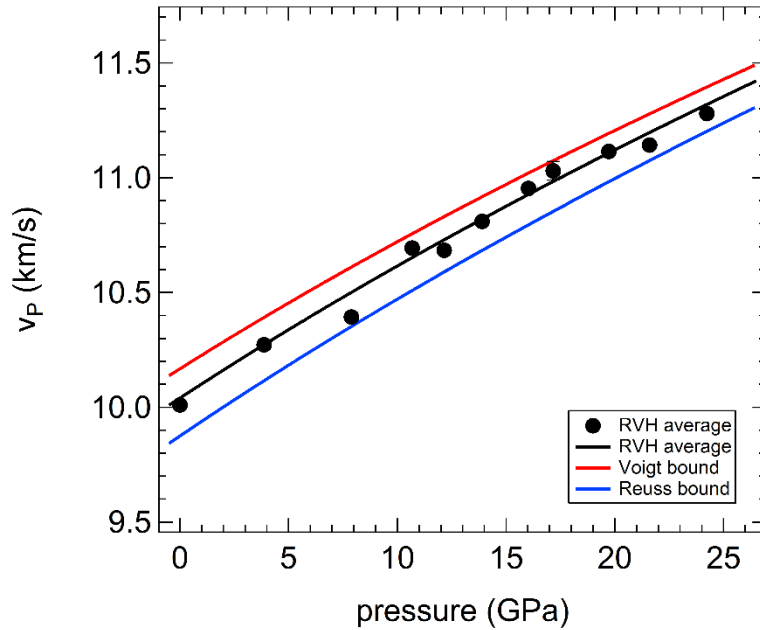
Figure 3-13: *Pressure dependence of the longitudinal aggregate velocities* v_P. *The Voigt (red) and Reuss (blue) bounds were plotted to show the range of possible longitudinal wave velocities through MgSiO₃ akimotoite. The black circles represent the experimentally determined aggregate* v_P *calculated from the RVH-average versus the absolute pressure and the black line correspond to a BM3 EoS fit through this data set. The uncertainties are smaller than the symbol size.*
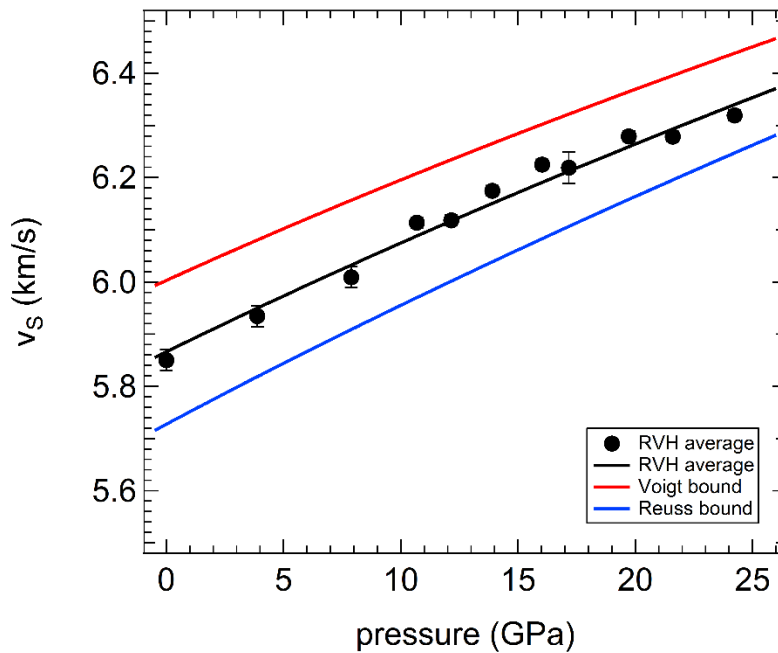
Figure 3-14: *Pressure dependence of the shear aggregate velocities* v_S. *The Voigt (red) and Reuss (blue) bounds were plotted to show the range of possible shear wave velocities through MgSiO₃ akimotoite. The black circles represent the experimentally determined aggregate* v_S *calculated from the RVH-average versus the absolute pressure and the black line correspond to a BM3 EoS fit through this data set.*

A comparison between the absolute pressures calculated using equation (28) and the pressures determined by the ruby fluorescence shift using the calibration reported by Dewaele et al. (2004) is plotted in Figure 3-15. Both pressures are in agreement within 2.5 % uncertainty (black solid lines) of the ruby pressure scale up to 25 GPa. The ruby pressure may deviate from the absolute pressure due to non-hydrostatic stresses. Note that the absolute pressure appears smaller than that measured with ruby when the broadening of the reflections during single-crystal X-ray diffraction were observed due to stresses in the DAC (e.g. between 13-17 GPa and > 22 GPa).
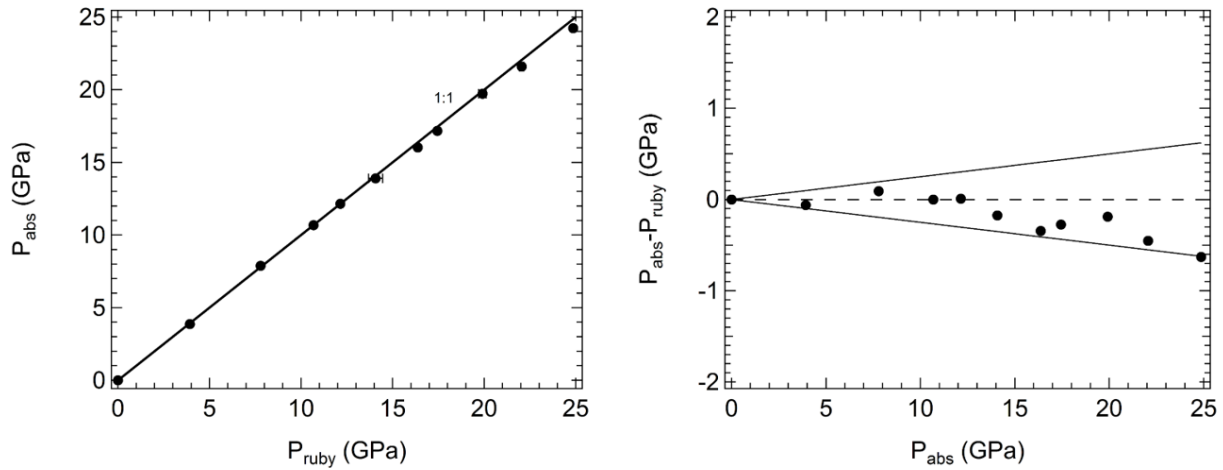
Figure 3-15: *Comparison of the absolute pressure calculated using the bulk modulus K_T, K' and the density determined during the Brillouin experiment with the ruby pressure calculated using the ruby fluorescence pressure calibration reported by Dewaele et al. (2004). The black lines in the plot on the right side represent the uncertainty (2.5 %) of the ruby pressure scale.*

3.3.2 Elastic compliances and axial compressibility

Knowledge of the full elastic tensor and of the elastic compliance tensor (as described in section 2.7.3, Table 3-5) allows the calculation of the axial compressibility β according to the following equations:

$$\beta_1 = s_{11} + s_{12} + s_{13} \qquad \qquad \text{(eq. 45)}$$

$$\beta_3 = s_{31} + s_{32} + s_{33} \qquad \qquad \text{(eq. 46)}$$

where β_1 and β_3 are the axial compressibility for the *a*- and *c*-axis, respectively

The linear compressibility can also be obtained by X-ray diffraction as shown in Chapter 3.2 by fitting the *a*- and *c* lattice parameters with a BM3 EoS. In this case, the linear compressibility β can be calculated from the linear moduLiat each pressure point according to the equations:

$$\beta = \frac{1}{M} \qquad \text{(eq. 47)}$$

The compressibility for both the *a*- and *c*-axes determined independently from the full elastic tensor (black) and X-ray diffraction (red) are plotted in Figure 3-16. The data calculated from the two different methods are in excellent agreement with one another for the stiffer *a*-axis, however for the *c*-axis the X-ray data suggest a slightly more compressible behavior than the Brillouin data.

Table 3-5: *Compliance coefficients for akimotoite obtained by inverting the stiffness matrix as described in section 2.7.3.*

P_{abs} (GPa)	s_{11} (GPa^{-1})	s_{12} (GPa^{-1})	s_{13} (GPa^{-1})	s_{31} (GPa^{-1})	s_{32} (GPa^{-1})	s_{33} (GPa^{-1})
0.00	0.00262	-0.00089	-0.00036	-0.00036	-0.00036	0.00287
3.87	0.00255	-0.00089	-0.00042	-0.00042	-0.00042	0.00278
7.88	0.00246	-0.00083	-0.00042	-0.00042	-0.00042	0.00266
10.68	0.00234	-0.00083	-0.00042	-0.00042	-0.00042	0.00256
12.15	0.00236	-0.00081	-0.00044	-0.00044	-0.00044	0.00255
13.90	0.00230	-0.00080	-0.00043	-0.00043	-0.00043	0.00249
16.03	0.00226	-0.00078	-0.00045	-0.00045	-0.00045	0.00243
17.17	0.00225	-0.00076	-0.00050	-0.00050	-0.00050	0.00252
19.72	0.00221	-0.00079	-0.00045	-0.00045	-0.00045	0.00238
21.60	0.00221	-0.00075	-0.00049	-0.00049	-0.00049	0.00238
24.23	0.00217	-0.00077	-0.00048	-0.00048	-0.00048	0.00231
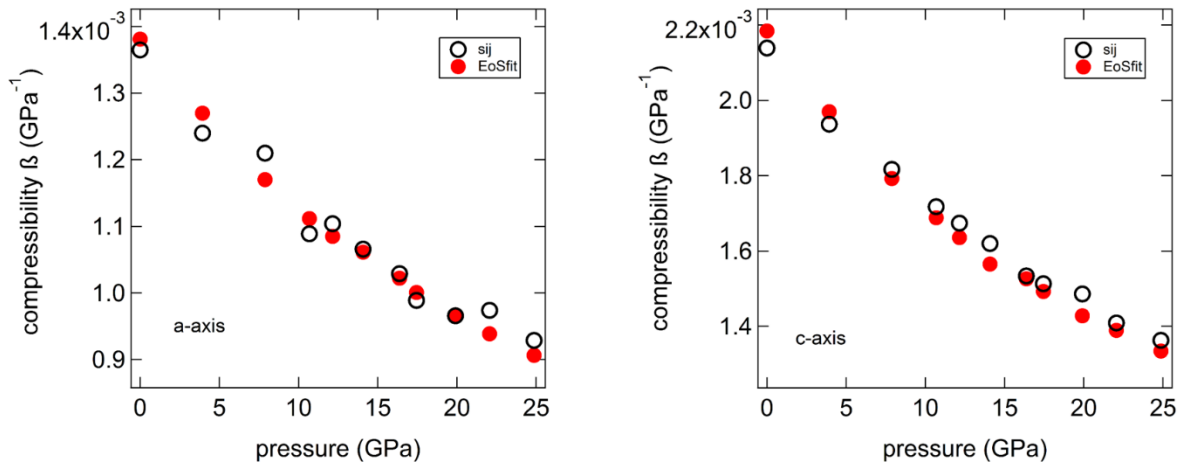
Figure 3-16: Calculated compressibility of the a-axis (left) and of the c-axis(right) up to pressures of the transition zone using the full elastic tensor determined by Brillouin spectroscopy (black) and the BM3 EoS fit of the unit-cell axes of akimotoite (red). The resulting compressibilities obtained with the two independent methods are in good agreement.

3.3.3 Comparison of the wave velocities of MgSiO₃ akimotoite with literature

The longitudinal and shear wave velocities of $MgSiO_3$ akimotoite at room temperature can be compared to four studies published in the literature. The first study by Weidner and Ito (1985) has been performed at room pressure and temperature on a single-crystal of $MgSiO_3$ akimotoite using Brillouin spectroscopy. Their resulting wave velocities (orange triangles in Figure 3-17 and 3-18), v_P and v_S are slightly faster than the RVH average velocities determined in this study, however, lie well between the Reuss and Voigt bounds. Another experimental study investigating the elastic properties of polycrystalline $MgSiO_3$ akimotoite using ultrasonic interferometry (Zhou et al. 2014) obtained longitudinal and shear wave velocities that are faster (green circles in Figures 3-17 and 3-18) than those reported in this study, in particular the v_P even exceed the Voigt bound determined in this study. A possible explanation for this discrepancy may be that the sample of Zhou et al. (2014) have partially transformed to $MgSiO_3$ bridgmanite during the heating cycles performed in the ultrasonic measurements. The presence of a minor phase is not easily recognized by means of energy-dispersive X-ray diffraction and a small amount of bridgmanite would be sufficient to increase the wave velocities as well as changing their pressure dependence. Da Silva et al. (1999) conducted a computational study on $MgSiO_3$ akimotoite using

the ab initio pseudo-potential method obtaining longitudinal and shear wave velocities (purple lines in Figures 3-17 and 3-18) which lie very close to the Voigt bound. Their pressure dependence is not as steep as that shown in the present study, moreover, the room pressure bulk and shear moduli reported by Da Silva et al. (1999) are much larger ($K_0 = 222$ GPa and $G_0 = 144$ GPa) likely due to the fact that the study has been performed at 0 K. A very recent study (Hao et al. 2019) (pink lines in Figures 3-17 and 3-18) used density functional theory to compute the elastic parameters of akimotoite up to 30 GPa and 2000 K and reported a $K_{T0} = 202$ GPa and $G_0 = 126$ GPa at 298 K. The v_P and v_S reported by Hao et al. (2019) are slower than those experimentally determined in this study.
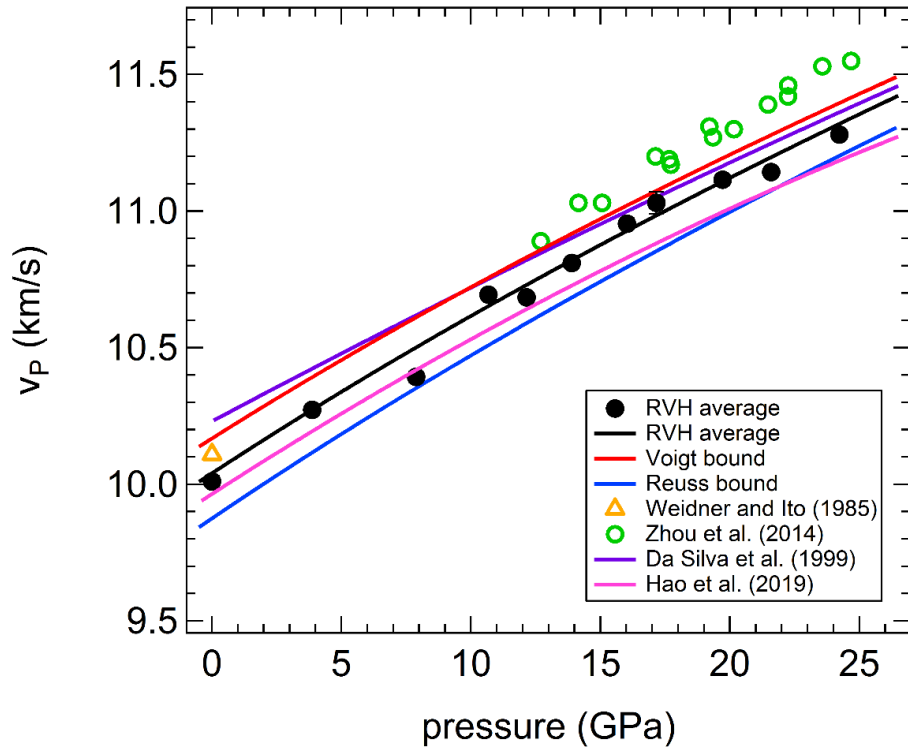
Figure 3-17: *Comparison of the longitudinal aggregate wave velocities of MgSiO₃ akimotoite obtained in this study with those experimentally determined using Brillouin spectroscopy by Weidner and Ito (1985), an ultrasonic study by Zhou et al. (2014) and with those obtained in two computational studies (Da Silva et al. 1999 and Hao et al. 2019). The uncertainties are smaller than the symbol size.*
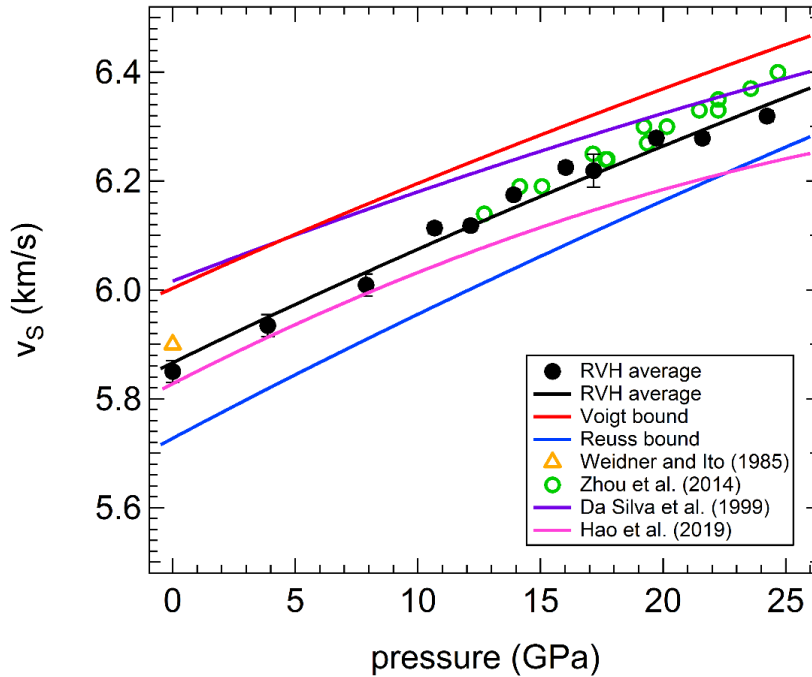
Figure 3-18: *Comparison of the shear aggregate wave velocities of MgSiO₃ akimotoite obtained in this study with those experimentally determined using Brillouin spectroscopy by Weidner and Ito (1985), an ultrasonic study by Zhou et al. (2014) and with those obtained in two computational studies (Da Silva et al. 1999 and Hao et al. 2019).*

3.4 Anisotropic behavior of MgSiO₃ akimotoite at transition zone pressures

The velocity distributions for akimotoite at room pressure and at 24.9(1) GPa are shown in Figures 3-19 and 3-20. In all lower hemispheres shown in Figures 3-19 and 3-20, the crystallographic *a*-axis points towards east (90°) and the *c*-axis points towards the reader. The fastest velocities are marked with black squares and the slowest velocities with white circles, respectively. The fastest velocities in the hemispheres do not travel along crystallographic axes as also reported by the molecular dynamics study of Zhang et al. (2005) and by the ab-initio study of Da Silva et al. (1999) whereas among the slowest velocities, only v_{S2} travels along the crystallographic *c*-axis. With increasing pressure, the difference between the maximum and minimum velocities decrease gradually, however, the distribution of the anisotropies remains the same (Figures 3-19 and 3-20). In comparison to the velocity distribution determined in this study, the ones obtained using the elastic coefficients by Weidner and Ito (1985) are rotated clockwise by 30° (Figure 3-19, right). This rotation was found to be caused by a negative c_{14} coefficient, whereas the c_{14} in this study is positive. Unfortunately, Weidner and Ito (1985) do not report

which setting they have used for the transformation from the trigonal to an orthogonal system to describe the acoustic wave velocities directions. It is very likely that they have chosen the crystallographic *a*-axis to be along the orthogonal X-axis, contrary to this study which has *a** along X (see section 2.7.5). The different notation would account for the 30° rotation, leaving the velocity distributions unchanged and, as expected given the similarity of the c_{ij}, practically identical to those calculated in this study (Figure 3-19). Zhang et al. (2005) reported the velocity propagation directions at 25 GPa and 1300 K but opposite to this study, they have reported the velocity propagation direction in the X-Y and Y-Z azimuthal planes. The velocity propagation in the X-Y plane is comparable to those from this study (Figure 3-20). Judging from the shape of v_P, they likely chose the X-Z plane rather than the Y-Z plane as labelled in their figure. If this is true, also these velocity distributions of the X-Z plane are comparable to those obtained from Brillouin spectroscopy at 25 GPa. Also the shear wave splitting pattern of Zhang et al. (2005) follows that of this study (Figure 3-20 upper right) if the X-Z planes is assumed indicating that no shear wave splitting occurs along the c-axis and the maximum shear wave splitting is randomly distributed. No rotation was observed relative to Zhang et al. (2005) indicating that the same reference system has been used.

The v_P anisotropy as well as the S-wave polarization anisotropy, Av_P and Av_{SP}, calculated using eq. 29 and 30, respectively, are plotted against pressure in Figure 3-21. Av_{SP} is roughly 1.5 times larger than Av_P, moreover both anisotropies smoothly decrease with increasing pressure from 32 to 26 % and from 19 to 13 %, respectively, making akimotoite the most anisotropic mineral in the transition zone. The Av_P and Av_{SP} anisotropies at room pressure calculated from the elastic tensor by Weidner and Ito (1985) are slightly larger (21 and 35 %) than the anisotropies determined in this study (19 and 32 %). The computational study by Zhang et al. (2005) report a Av_{SP} ~2 % larger at room pressure (blue lines in Figure 3-21) but with a more pronounced decrease with pressure, whereas Av_P is 3 % smaller, decreases with pressure, but above 15 GPa starts to increase again. Da Silva et al. (1999) report smaller Av_P and Av_{SP} by ~3 and 5%, respectively, however their data present a very similar behavior with pressure as that reported in this study. The best agreement between a computational study and the experimentally determined anisotropies from this study is given by the values reported by Hao et al. (2019) (pink in Figure 3-21). Both Av_P and Av_{SP} of Hao et al. (2019) are less than 1.5 % different from those obtained in this study and have a very similar trend as a function of pressure.
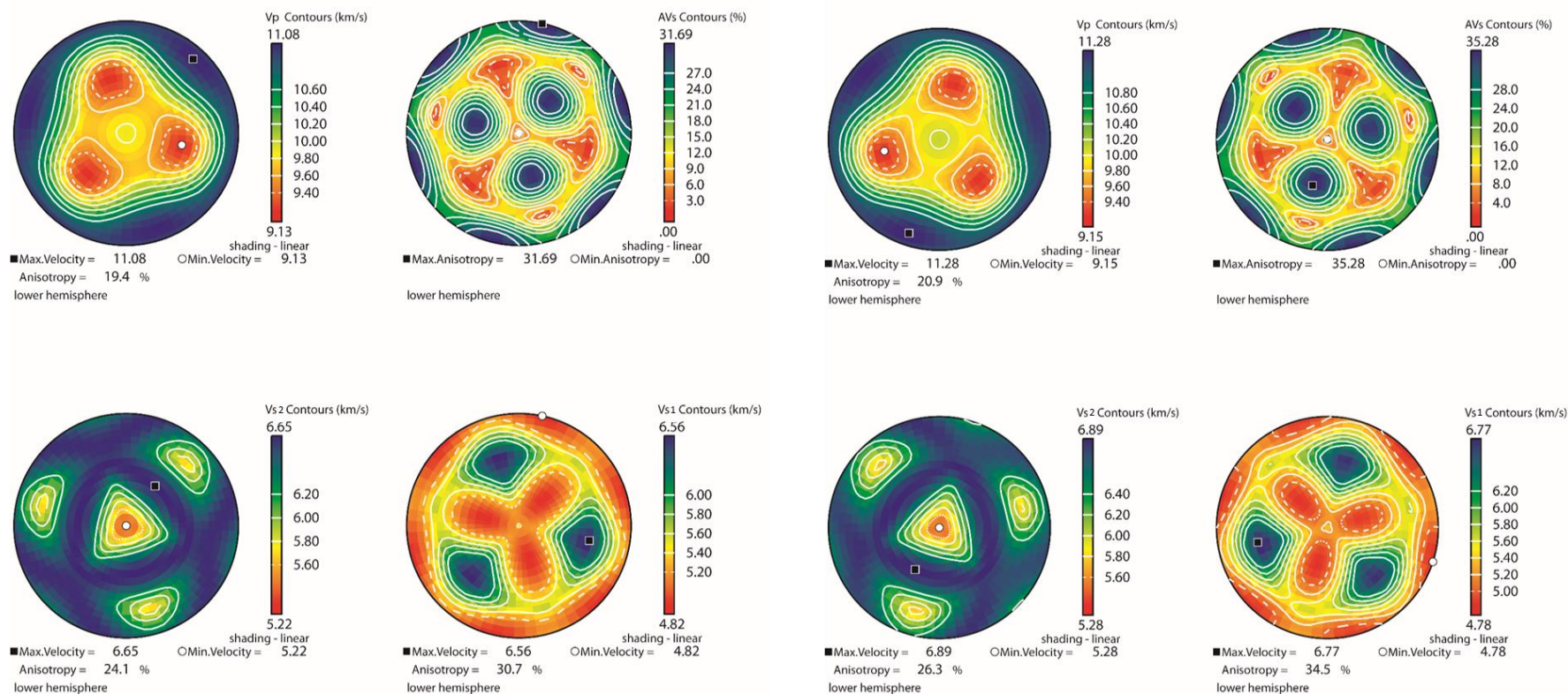
Figure 3-19: *Velocity distributions of MgSiO₃ akimotoite at room pressure obtained using the program Anis2k written by Mainprice (1990) using the elastic coefficients determined in this study (left) and Weidner and Ito (1985) (right) and represented in the lower hemisphere. v_P anisotropies (upper left), v_{S1} and v_{S2} anisotropies (lower left and right, respectively), S-wave polarization anisotropy Av_{SP} (upper right). Blue and red colors correspond to the fastest and slowest wave velocities, respectively. The distribution of propagation directions of the P- and S-wave velocities between this study and Weidner and Ito (1985), appears identical except for a rotation of 30°.*

98
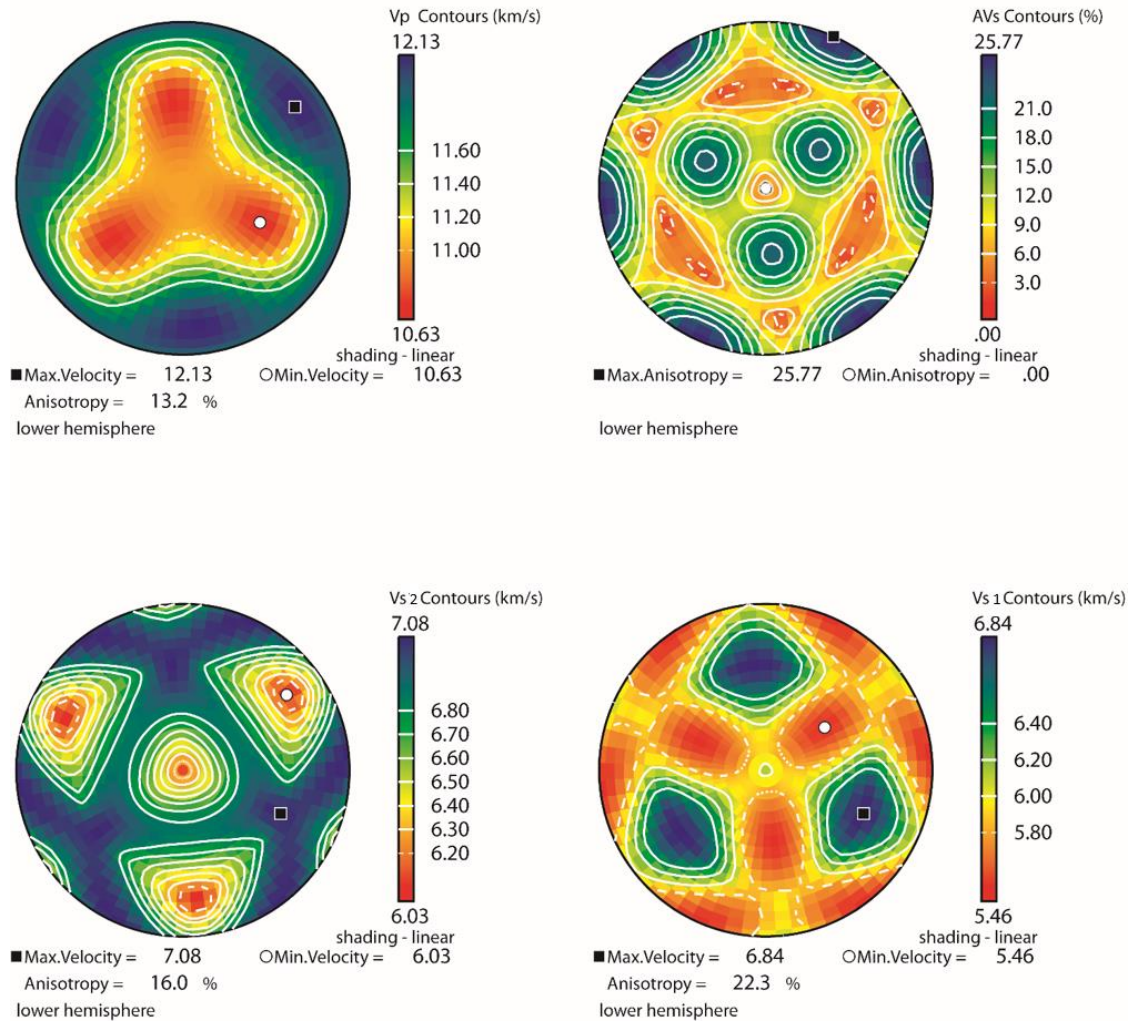
Figure 3-20: *Velocity distributions of MgSiO₃ akimotoite at 25 GPa obtained using the program Anis2k written by Mainprice (1990) for the elastic coefficients determined in this study and represented in the lower hemishere. v_P anisotropies (upper left), v_{S1} and v_{S2} anisotropies (lower left and right, respectively), S-wave polarization anisotropy Av_{SP} (upper right). Blue and red colors correspond to the fastest and slowest wave velocities, respectively. With increasing pressure, the P- and S- wave anisotropies decrease, however, the overall velocity distribution remains the same.*

To interpret the anisotropies observed by seismological studies, it is important to also consider the evolution of the anisotropies at high temperature. Zhang et al. (2005) found that with temperatures up to 1500 K, the Av_P and Av_{SP} will increase by ~3% and ~6%, respectively, making the anisotropies similar to the ones at ambient conditions. They modelled the anisotropic features of an assemblage consisting of 58% ringwoodite, 35% akimotoite and 7% Ca-perovskite and found that it resembled the anisotropic features found in akimotoite.
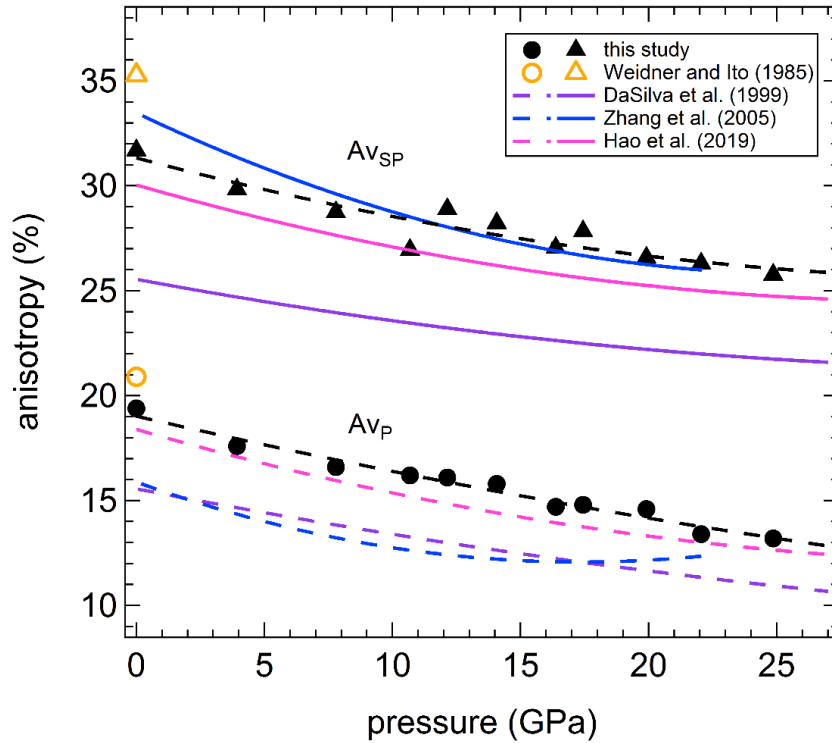
Figure 3-21: *P-wave anisotropy (Av_P) and S-wave polarization anisotropy (Av_{SP}) of $MgSiO_3$ akimotoite with increasing pressure. The uncertainties are smaller than the symbol size. For comparison, the anisotropies calculated using the elastic tensor at room pressure by Weidner and Ito (1985) and three computational studies (Da Silva et al. 1999; Zhang et al. 2005 and Hao et al. 2019) also are reported.*

The preferred alignment (CPO) of akimotoite crystals at high pressure and temperature have been investigated experimentally by Shiraishi et al. (2008). At temperatures of 1573 K, the *c*-axis aligns parallel to the compression direction, whereas at 1273 K the *c*-axis was found to align parallel to the shear direction and therefore perpendicular to the compression direction. This indicates that in a polycrystalline akimotoite sample the P-, S_1- and S_2- wave propagation is very slow parallel to the compression direction at temperatures of 1573 K or slow parallel to the shear direction at 1273 K since along the *c*-axis, all the velocities are slow compared to other directions. This also implies a reduction in Av_P and Av_{SP} in a polycrystalline aggregate as already described by Shiraishi et al. (2008) compared to the anisotropies in a single-crystal of akimotoite. The Tonga subduction zone has two distinct slab segments, the northern and southern part, where P-waves propagate slower in slab normal direction or slower in slab sinking direction, respectively (Shiraishi et al. 2008). Relating this to the CPO found experimentally in akimotoite, the difference in seismic anisotropy was interpreted to be caused by a difference in temperature

with the northern segment being colder (~1273 K) and the southern segment to be hotter (~1573 K) (Shiraishi et al. 2008). The observation of seismic anisotropy in the Tonga slab at transition zone pressures was attributed exclusively to the presence of akimotoite since the other two transition zone minerals ringwoodite and majorite are almost isotropic (Shiraishi et al. 2008).

3.5 High-pressure structural evolution of MgSiO₃ akimotoite

Structural refinements were performed on intensity data collected at four pressure points. Bond distances and volumes of the MgO_6 and SiO_6 octahedra are reported Table 3-6. The MgO_6 and SiO_6 octahedral volumes decrease smoothly with increasing pressure with MgO_6 being more compressible than SiO_6 ($K_0 = 157(10)$ GPa and $K_0 = 390(57)$ GPa, respectively, using BM2 EoS) (Figure 3-22) and are in good agreement with those reported by Yamanaka et al. (2005) investigating the structure of MgSiO₃ akimotoite up to 7.8 GPa (open black symbols in Figure 3-22).
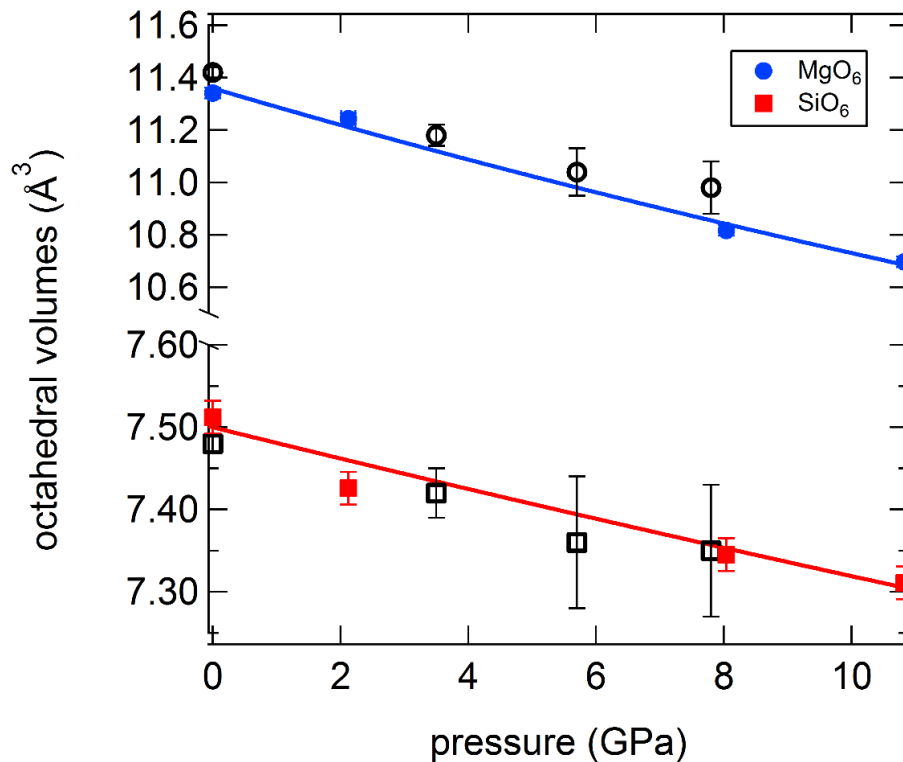
Figure 3-22: *Octahedral volumes of the MgO₆ (blue) and SiO₆ (red) octahedra in the MgSiO₃ akimotoite structure up to 10.8(1) GPa. The solid lines represent BM2 EoS through the data sets. The octahedral volumes are in good agreement with those reported by Yamanaka et al. (2005).*

Table 3-6: *Octahedral volumes and individual Si-O and MgO bond distances obtained from structural refinement measurements on MgSiO₃ akimotoite at four pressure points up to 10.8(1) GPa.*

P_{ruby} (GPa)	V MgO$_6$ (Å^3)	V SiO$_6$ (Å^3)	Mg-O1 (Å)	Mg-O2 (Å)	Si-O1 (Å)	Si-O2 (Å)
0.001(1)	11.34(3)	7.51(2)	1.995(2)	2.173(2)	1.761(2)	1.825(2)
2.12(11)	11.24(3)	7.43(2)	1.986(2)	2.160(2)	1.758(1)	1.820(1)
8.04(1)	10.82(3)	7.35(2)	1.968(2)	2.130(2)	1.747(1)	1.812(2)
10.83(3)	10.70(3)	7.31(2)	1.958(2)	2.122(2)	1.741(2)	1.812(2)

The variation with pressure of the bond distances Mg-O1, Mg-O2, Si-O1 and Si-O2 are shown in Figure 3-23. Linearized second order BM (BM2) equations of state have been used to describe the bond distance behavior with pressure. The Mg-O bonds are more compressible than the Si-O bonds, moreover Mg-O2 compress more rapidly than Mg-O1 having linear moduli of 531(40) GPa and 385(22) GPa, respectively. This can be expected since longer bonds are usually more compressible. In contrast to that, the Si-O1 and Si-O2 bonds are stiffer with linear moduli of 880(90) GPa and 1379(282) GPa, respectively, making the Si-O2 bond the stiffest of all bonds in the akimotoite structure in spite of it being longer than Si-O1. This can be explained by the position of the Si-O1 and Si-O2 bonds in the SiO_6 octahedra. The longer Si-O2 bonds are directly connected to the MgO_6 octahedra not allowing them to vary much whereas the oxygens of the shorter Si-O1 bonds are not bonded to anything pointing towards the void in the akimotoite structure and allowing them to move freely. The data by Yamanaka et al. (2005) support this observation.
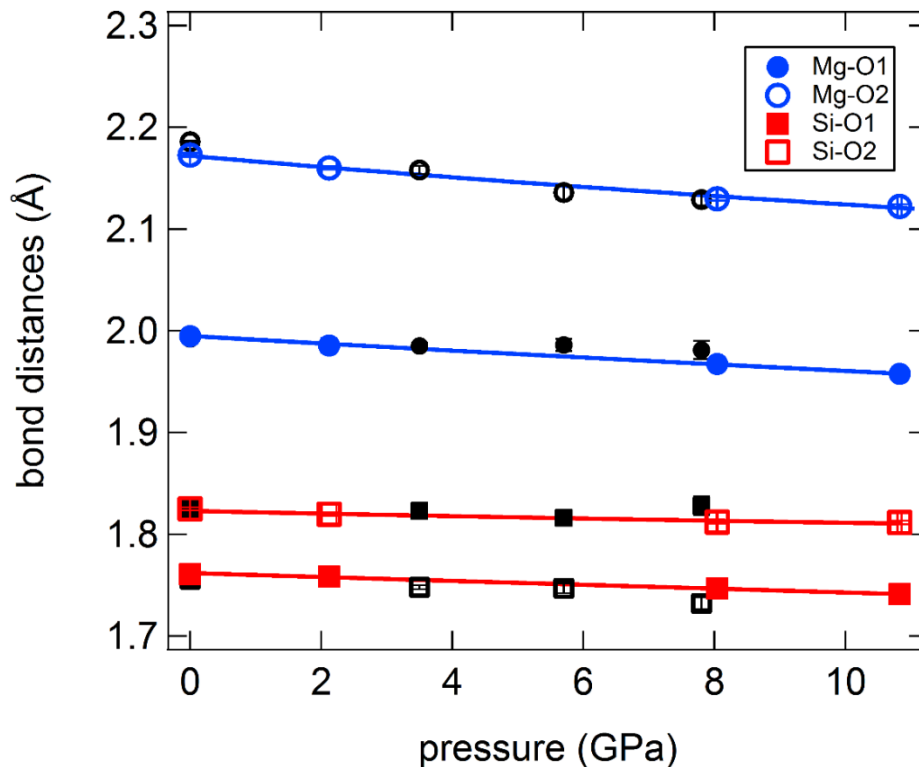
Figure 3-23: Change in bond distances of Mg-O1, Mg-O2, Si-O1 and Si-O2 up to 10.8(1) GPa. The uncertainties are smaller than the symbol size. No change in compression mechanism can be observed up to this maximum pressure reached in this study which is supported by the data measured by Yamanaka et al. (2005) shown with the black symbols. The solid curves represent BM2 EoS fits of the individual bond distances.

The axial compressibility of akimotoite is highly anisotropic as shown in Figure 3-8 indicating that the c-axis is much more compressible than the a-axis. The compression along the c direction can be described by means of the distance between the Mg and Si cations that are located in opposite octahedra in two adjacent layers (Figure 1-5) and are not influenced by the compression along the a-axis. The main compression along the a direction, instead can be described by means of the distance between the oxygens forming the edges of the face-sharing octahedra that are perpendicular to the c-axis. The change in Mg-Si and O-O distance with increasing pressure is shown in Figure 3-24. The compressibility of the two distances has been described using linearized BM2 equations shown as solid curves in Figure 3-24. The Mg-Si distance is more compressible having a linear modulus of 458(56) GPa relative to the O-O distance which has a linear modulus of 859(199) GPa very similar to that of the incompressible Si-O1 bond. It appears therefore that the face-sharing octahedra are primarily responsible for the very stiff a-axis and as a consequence determine the anisotropy of the akimotoite structure.
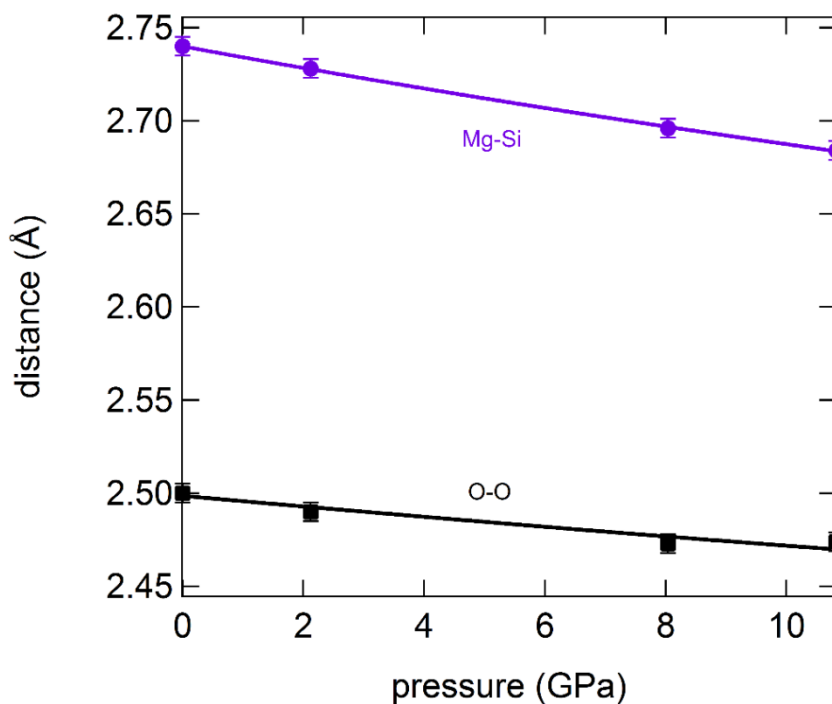
Figure 3-24: Changes with pressure in the distance between two oxygens forming the face-sharing octahedra and the distance between the Mg and Si cations from two adjacent octahedral layers representing the main compressions along the a- and c-axes, respectively. The Mg-Si distance decreases more rapidly with pressure relative to the O-O distance. The solid curves represent BM2 EoS fits through the individual data sets.

4. The effect of Al substitution on the structure and elasticity of akimotoite

4.1 Structural evolution in the MgSiO$_3$ akimotoite-Al$_2$O$_3$ corundum solid solution

In order to understand the effect of Al on the unit-cell parameters and structure of akimotoite, eight single-crystals having different compositions in the MgSiO$_3$ akimotoite-Al$_2$O$_3$ corundum solid solution were investigated (see chapter 2.5.1 for the syntheses details). Unfortunately, it was only possible to synthesize one Al-rich akimotoite single-crystal, whereas corundum crystals with a maximum MgSiO$_3$ content of 25 % could be obtained.

4.1.1 The crystal structures of MgSiO$_3$ akimotoite and Al$_2$O$_3$ corundum

MgSiO$_3$ akimotoite and Al$_2$O$_3$ corundum have very similar structures consisting of octahedral layers. In MgSiO$_3$ akimotoite, Mg and Si occupy alternating layers as described in section 1.3 (Figure 1-5), whereas in corundum, all octahedra are occupied by Al with a consequent increase in symmetry from $R\overline{3}$ of akimotoite to $R\overline{3}c$ (No.167) (Figure 4-1).
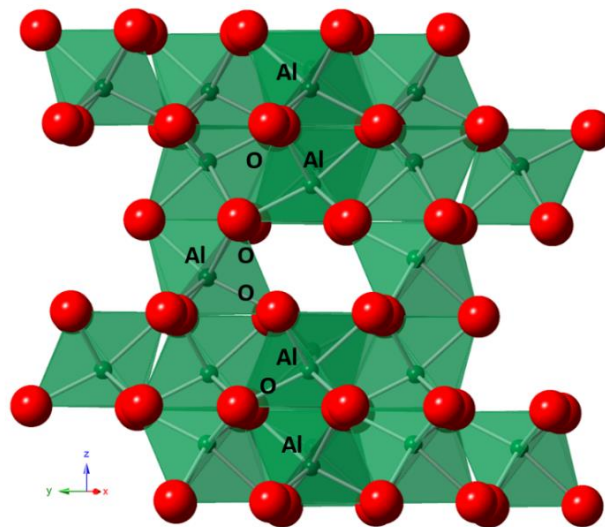
Figure 4-1: *Crystal structure of Al$_2$O$_3$ corundum at ambient conditions. Corundum crystallizes in the $R\overline{3}c$ space group and consists of alternating layers of AlO$_6$ (green) octahedra. The increase in symmetry relative to the akimotoite structure is due to the chemical equivalence of all octahedra.*

So far, no study has investigated whether a complete solid solution between the two end-members is possible neither the mixing behavior of MgSiO$_3$ akimotoite-Al$_2$O$_3$ corundum. Moreover, structure refinements on single-crystal data are only available for the end-members MgSiO$_3$ akimotoite and Al$_2$O$_3$ corundum (Horiuchi et al. (1982) and Finger and Hazen (1978), respectively).

4.1.2 Change in unit-cell parameters in the akimotoite-corundum solid solution

The unit-cell lattice parameters measured for the investigated samples in the akimotoite-corundum solid solution are reported in Table 4-1 and plotted versus the Al content in Figure 4-2. The unit-cell parameters obtained for two polycrystalline samples Ak97.5 and Ak80 using both the Bruker diffractometer (Table 4-1) and energy-dispersive XRD (EDXRD) during the ultrasonic measurements performed at APS (Tale 4-3), as well as the unit-cell parameters of the polycrystalline samples studied by Akaogi et al. (2002) also are plotted in Figures 4-2. The variation of the *a*- and *c*-axes with Al content is strongly not linear; the *a* lattice parameter increases rapidly once the Al$_2$O$_3$ component is incorporated into the akimotoite structure and even more rapidly when MgSiO$_3$ is incorporated into the corundum structure, whereas the *c* lattice parameter has a negative deviation from linearity. As a consequence, the *c/a* ratio for the akimotoite-rich samples decreases rapidly, whereas the corundum-rich samples have very similar values of *c/a* ratios (Figure 4-2). The MgSiO$_3$ akimotoite-Al$_2$O$_3$ corundum solid solution appears, therefore, strongly non-ideal, moreover, the very different behavior of samples close to the two end-members suggests that substitution of Al$_2$O$_3$ into akimotoite gives rise to structural distortion very different from those occurring when MgSiO$_3$ is substituted into corundum, hence, it is very likely that an immiscibility gap is present around the 50:50 compositions. Note, however, that due to the opposite behavior of the *a* and *c* the unit-cell axes, the unit-cell volume variation along the MgSiO$_3$ akimotoite-Al$_2$O$_3$ corundum solid solution appears very close to linear (Figure 4-3). Literature data on volumes measured on polycrystalline Al$_2$O$_3$-bearing akimotoite samples (open circles, Akaogi et al. 2002) and polycrystalline MgSiO$_3$-bearing corundum (open squares, Liu et al. 2016 and personal communication; open diamonds, Irifune et al. 1996) are also reported for comparison. The majority of the data follow the solid line joining the two end-member values obtained in this study, although the MgSiO$_3$-bearing corundum samples present a larger scatter,

likely due to the fact that the X-ray diffraction measurements were performed on samples for which the $MgSiO_3$-rich corundum was either a minor phase or presented very small grain size. Also the unit-cell volumes of the end-member akimotoite (open triangle, Wang et al. 2004) and corundum (open rhomb, Higo et al. 2018) reported in Figure 4.3 show larger values than those obtained from our single-crystal study. Those measurements were performed on polycrystalline samples using energy-dispersive X-ray diffraction with synchrotron radiation.
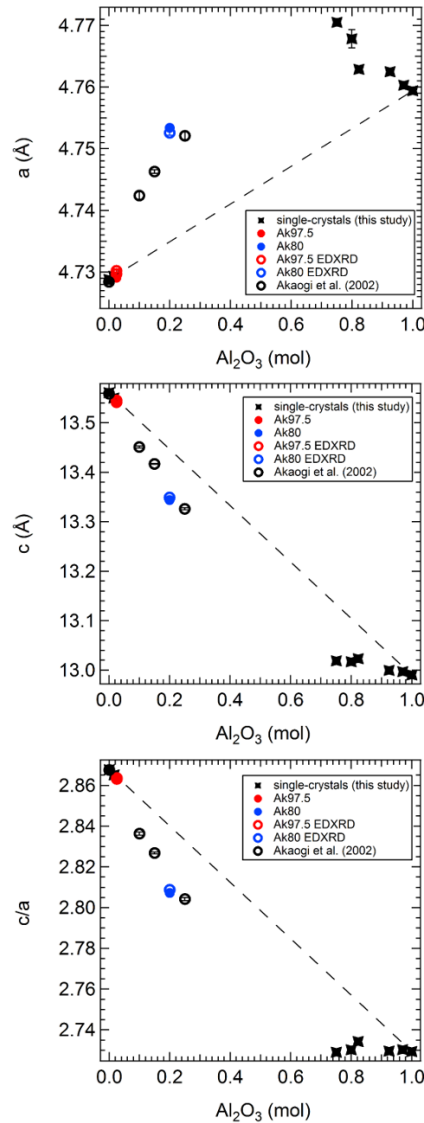
Figure 4-2: *Evolution of the a and c unit-cell lattice parameters and of the resulting c/a ratio in the MgSiO₃ akimotoite - Al₂O₃ corundum solid solution. The black stars represent the single-crystals synthesized in this study. The red and blue circles are the lattice parameters obtained from polycrystalline samples using the Bruker micro-focus diffractometer (solid) and energy-dispersive X-ray diffraction (EDXRD, open)). The open black circles are the lattice parameters of Al-bearing akimotoite from Akaogi et al. (2002). The uncertainties are smaller than the symbol size.*
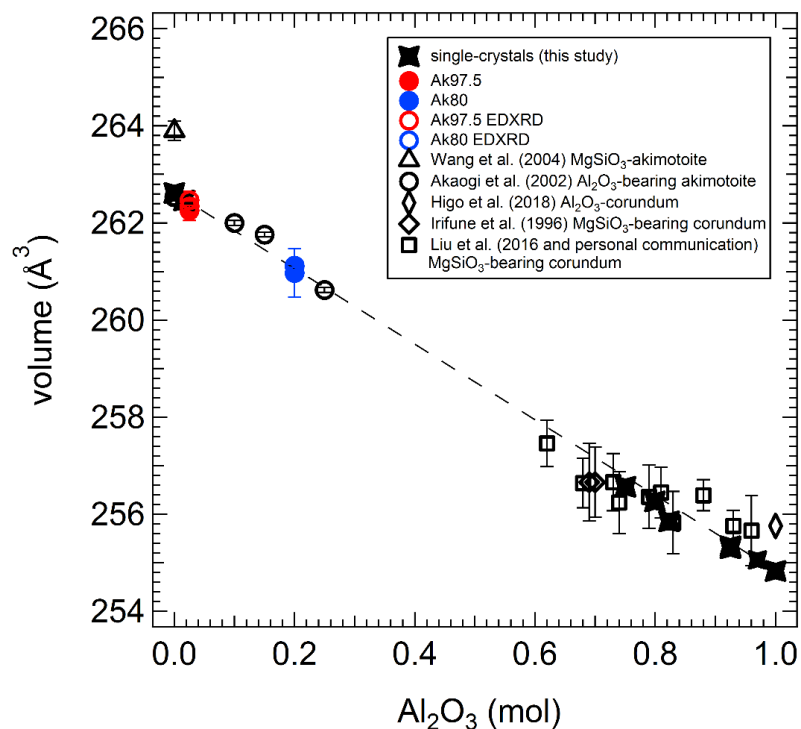
Figure 4-3: *Comparison of the unit-cell volumes of all (Al_2O_3-bearing) akimotoite and ($MgSiO_3$-bearing) corundum data available in literature versus the Al content. The majority of the data follow the line drawn between the $MgSiO_3$ akimotoite and Al_2O_3 corundum end-member.*

It is interesting to notice that the *a*-axis of the Cor81 sample is slightly smaller and the *c*-axis is slightly larger than the trend observed for all other $MgSiO_3$-bearing corundum single-crystals (Figure 4-2). In other words, the *a* and *c* values of this crystal are closer to the ideal mixing trend described by the line between the end-members. A careful analysis by means of a single-crystal X-ray diffraction measurement on the Huber diffractometer revealed that the 0 0 3 reflection which is extinct in space group $R\bar{3}c$ was actually present suggesting an incipient ordering of Mg and Si into the corundum structure. No other reflections consistent with space group $R\bar{3}c$ were strong enough to be detected, however this is not surprising since they are very weak even in the akimotoite end-member. For all other $MgSiO_3$-rich corundum single-crystals the 0 0 3 reflection was not present. The Cor81 sample was synthetized at relatively low temperature (1673 K) (Table 2-1) while all other $MgSiO_3$-bearing corundum single-crystals were synthesized at much higher temperatures (more than 1873 K) (Table 2-1). The low temperature may have enhanced some ordering of Mg and Si which was maintained during quenching. This suggest that ordering decreases, even if only minimally, the non-ideality of the akimotoite-corundum solid solution.

Table 4-1: *Unit-cell parameters determined on eight single-crystals and two polycrystalline samples in this study.*

experiment		Al_2O_3 (mol)	a (Å)	c (Å)	V (Å^3)
S6925	Ak100	0.000	4.7288(1)	13.5609(4)	262.62(1)
S7179	Ak99	0.008	4.7293(1)	13.5502(1)	262.47(1)
I796	Cor75	0.751	4.7703(3)	13.0189(4)	256.56(3)
I789	Cor80	0.800	4.7678(1)	13.0172(2)	256.27(2)
S7237a	Cor81	0.814	4.7600(2)	130113(5)	255.29(2)
S7156a	Cor92	0.924	4.7625(2)	12.9996(4)	255.34(3)
S7156b	Cor97	0.974	4.7603(15)	12.9969(30)	255.06(6)
S7203	Cor100	1.000	4.7594(6)	12.9903(8)	254.83(7)
S6741	Ak97.5	0.025	4.7291(1)	13.5404(4)	262.26(1)
I444	Ak80	0.203	4.7534(1)	13.3440(6)	261.11(1)

4.1.3 Structural evolution in the akimotoite-corundum solid solution

Structural refinements on eight single-crystals in the solid solution between $MgSiO_3$ akimotoite and Al_2O_3 corundum were performed in order to understand the non-linearity observed in the unit-cell lattice parameters and to elucidate the structural mixing behavior. The resulting octahedral bond distances and volumes are reported in Table 4-2 (the atomic coordinates and displacement parameters are reported in Table A-2 in the appendix). Figure 4-4 shows the change in octahedral volume with incorporating Al into the MgO_6 (orange) and SiO_6 (blue) octahedra and incorporation of Mg and Si into the AlO_6 (green) octahedra. Substitution of Al into the akimotoite structure mainly affects the MgO_6 site given that the ionic radii (i.r.) of Al and Mg are 0.535 Å and 0.72 Å, respectively (Shannon et al. 1976). As expected the MgO_6 octahedral volumes decrease due to the substitution of Al. This is also represented by the decrease in both the Mg-O1 and Mg-O2 bonds (Figure 4-5). Unexpectedly, a small decrease in octahedral volume of the Si site is also visible, in spite of Al being larger than Si (i.r. Si = 0.40 Å; Shannon et al. 1976).
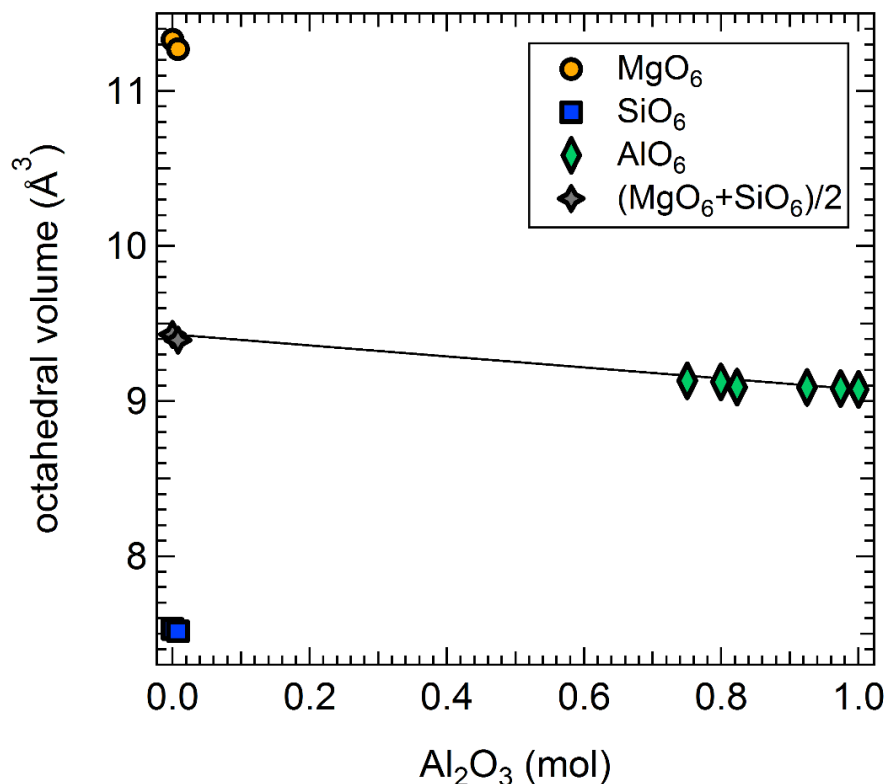
Figure 4-4: *Octahedral volumes of MgO₆ (orange), SiO₆ (blue) and AlO₆ (green). For comparison with the corundum structure, the average octahedral volume between the MgO₆ and SiO₆ have been calculated (grey). The straight line represents the join between the two end-members. The uncertainties are smaller than the symbol size.*

The decrease in octahedral volume for the Si site is mainly due to the decrease of the shortest bond in the akimotoite structure, namely the Si-O1 bond distance (Figure 4-5) while the slightly longer Si-O2 bonds remain the same. Note that the Si-O1 bond in akimotoite is more compressible than the Si-O2 bond, due to the connection of the longer Si-O2 bonds to the MgO₆ octahedra not allowing them to vary much as the shorter Si-O1 bonds that are not bonded to another octahedron and point towards the void in the akimotoite structure as described in Chapter 3.5. Substitution of Mg and Si into the corundum structure gives rise to a slight increase of the AlO₆ octahedral volume (Figure 4-4). Ordering of Mg and Si in alternating octahedra may locally occur, however, only for single-crystal Cor81 it has been detected as described in the previous section. When considering the average bond distances and volumes of the two octahedra of akimotoite (grey stars in Figures 4-4 and 4-5) the MgSiO₃-bearing corundum samples appear to follow an ideal behavior, only Ak99 and Cor81, which have complete or partial ordering of Mg and Si, respectively, appear to slightly deviate from the linear trend.

experiment	Mg-O1 (Å)	Mg-O2 (Å)	average bond length (Å)	octahedral volume (Å³)	OAV	QEP	Si-O1 (Å)	Si-O2 (Å)	average bond length (Å)	octahedral volume (Å³)	OAV	QEP
Ak100	1.9912(5)	2.1753(7)	2.0833	11.3311	0.0442	1.0442	1.7624(5)	1.8262(5)	1.7943	7.5312	0.0178	1.0154
Ak99	1.9867(7)	2.1717(8)	2.0792	11.2706	0.0445	1.0438	1.7603(6)	1.8257(6)	1.7931	7.5168	0.0182	1.0153
	Al-O1 (Å)	Al-O2 (Å)										
Cor75	1.9777(7)	1.8576(4)	1.9176	9.1327	0.0313	1.0206						
Cor80	1.9766(8)	1.8571(5)	1.9168	9.1247	0.0312	1.0203						
Cor81	1.9734(7)	1.8551(5)	1.9143	9.0914	0.0309	1.0201						
Cor92	1.9731(7)	1.8556(5)	1.9143	9.0886	0.0307	1.0202						
Cor97	1.9729(7)	1.8545(6)	1.9137	9.0817	0.0309	1.0203						
Cor100	1.9713(7)	1.8557(10)	1.9135	9.0765	0.0302	1.0203						
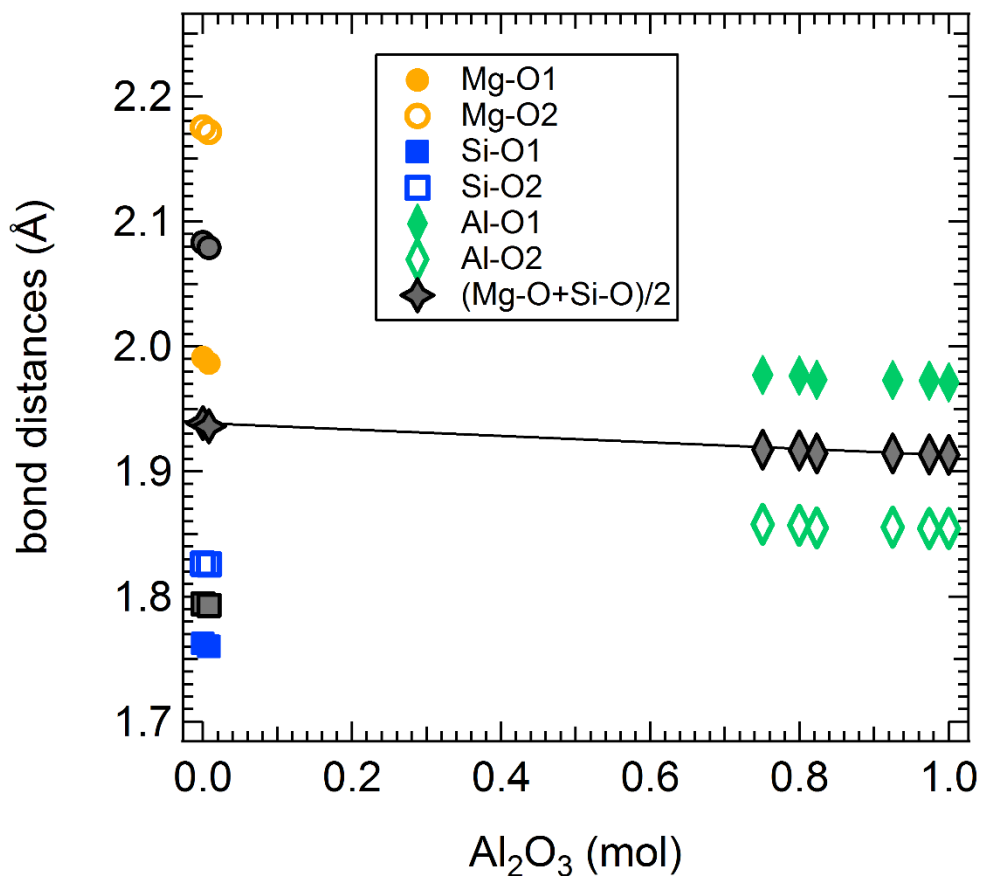
Figure 4-5: *Evolution of the individual bond distances in the MgO_6 (orange), SiO_6 (blue) and AlO_6 (green) octahedra. For comparison, the average of all bond distances (grey stars for akimotoite and grey diamonds for corundum) have been calculated. The straight line represents the join between the two end-members. The uncertainties are smaller than the symbol size.*

Both the MgO_6 and SiO_6 octahedra get more distorted with incorporating Al into the structure as can be seen in the octahedral angle variance (OAV) that increase for both octahedra (Figure 4-6). Note that the distortion of the MgO_6 octahedron is already quite large. The AlO_6 octahedra of the corundum structure have a distortion which is in between the MgO_6 and the SiO_6 octahedra, such distortion (OAV) increases slightly with increasing Mg and Si content.

The distance between octahedral layers is described by the distance between the Mg^{2+} and Si^{4+} cations in the akimotoite structure or between alternating Al^{3+} cations in the corundum structure (Figure 4-7). This distance decreases with increasing Al content, likely due to a decrease in repulsions among the cations in adjacent layers, so that the cations residing at the Mg site is moving toward the center of the octahedron with increasing Al substitutions. This variation is,

however, not linear and is more pronounced close to the akimotoite end-member, suggesting that the substitution of even a small amount of Al^{3+} has a major effect on the akimotoite structure (Figure 4-7). The distance between the two Al^{3+} cations increases with the substitution of Mg and Si into the corundum structure but the change is not as rapid as on the akimotoite side. The change in distance between the cations of two adjacent octahedra does not follow a linear trend (indicated by the black line connecting the two end-members) but clearly has a negative trend. Since this distance is mainly along the *c*-axis, it is very likely that the cations displacement in the octahedral site is responsible for the negative deviation from linearity of the *c*-axis, as well as for the different trends that this axis shows at the two ends of the akimotoite-corundum solid solution (Figure 4-2).
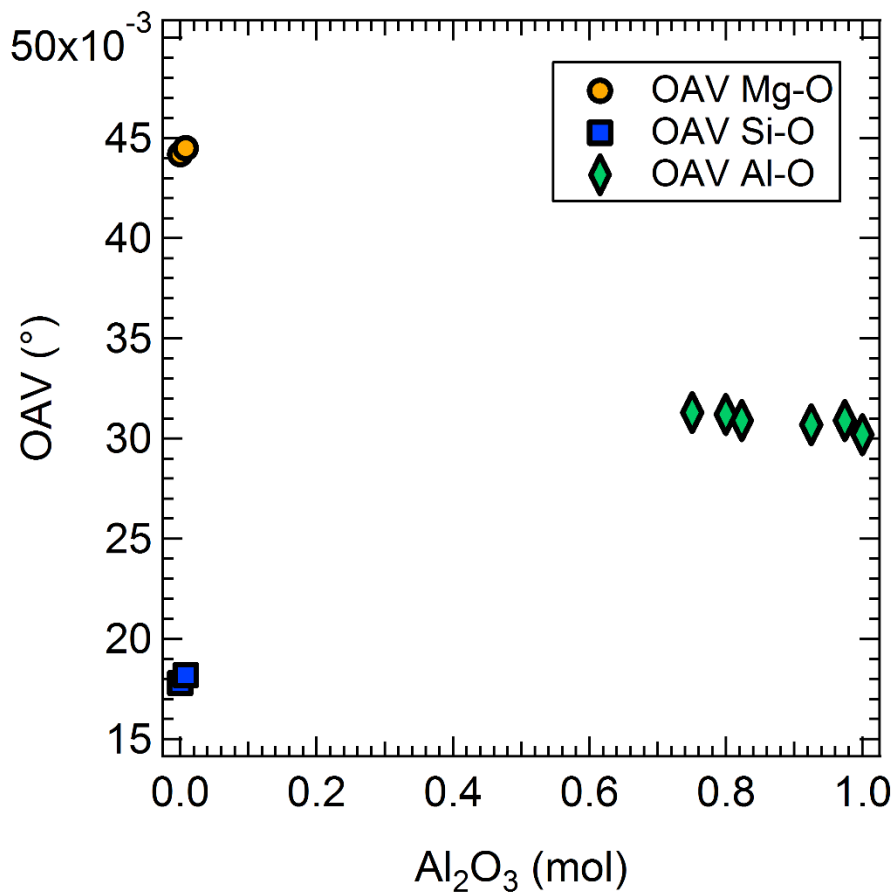
Figure 4-6: *Change in the octahedral angle variance (OAV) in the akimotoite-corundum solid solution. The MgO$_6$, SiO$_6$ and AlO$_6$ octahedra get more distorted when Al or Mg and Si are substituted into the end-member structures. The uncertainties are smaller than the symbol size.*
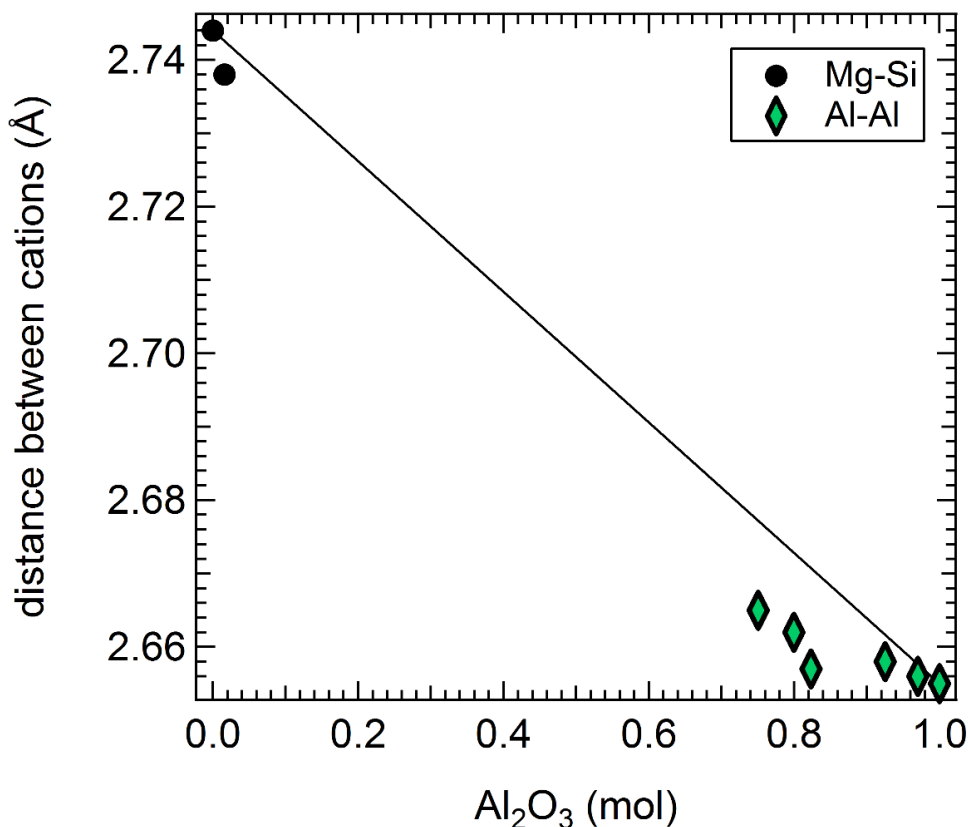
Figure 4-7: *Variation with Al₂O₃ content of the distance between the cations in two adjacent octahedral layers, namely Mg^{2+} and Si^{4+} in the akimotoite structure (black circles) or Al^{3+} and Al^{3+} in the corundum structure (green diamonds). Even the incorporation of a small amount of Al into the akimotoite structure majorly decreases the distance of the two cations. The shift in the cation position mainly takes place in the MgO_6 octahedra. On the other hand, the substitution of Mg and Si into the corundum structure gives rise to an increase of the distance between the cations. The uncertainties are smaller than the symbol size.*

The oxygen distance along the edges of face-sharing MgO_6 and SiO_6 octahedra for akimotoite and AlO_6 octahedra for corundum, which lie almost parallel to the *a*-axis increases rapidly at the corundum-rich side (Figure 4-8) which can therefore explain the positive trend observed in the *a* unit-cell lattice parameter as described in Figure 4-2. It is expected that the oxygens distance in Al-rich akimotoite increases as well since a rapid increase on the akimotoite side also was observed for the *a* unit-cell parameter (Figure 4-2), however, a single-crystal of akimotoite with a larger Al content is needed to confirm this hypothesis.
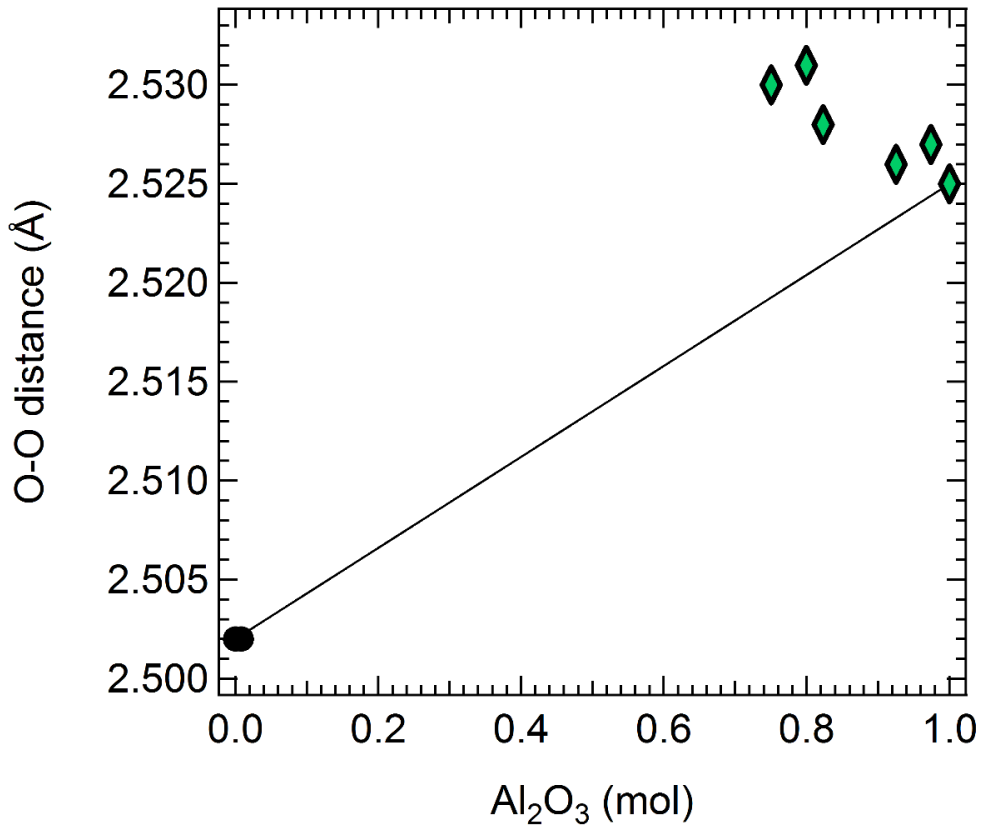
Figure 4-8: *Variation with Al$_2$O$_3$ content of the distance between oxygens along the edges of face-sharing octahedra. A rapid increase can be observed on the corundum-rich side which can explain the positive trend of the a-axis described in Figure 4-2. The uncertainties are smaller than the symbol size.*

4.2 The influence of Al on the wave velocities of akimotoite at transition zone pressures

4.2.1 Wave velocities of Al-bearing akimotoite

Three ultrasonic experiments were conducted at APS on Al-bearing samples: T2083 and T2269 for Ak97.5 and T2270 for Ak80. X-ray diffraction, ultrasonic measurements and X-ray radiography for sample length determination were performed up to 24 GPa and 1100 K as described in detail in section 2.8. The resulting unit-cell parameters of the akimotoite samples as well as of the MgO and Au pressure markers are reported in Table 4-3, whereas the sample lengths and acoustic wave velocities are shown in Table 4-4.

The pressures calculated from the EoS of Au (Tsuchiya 2003) and MgO (Dewaele et al. 2000) differ of up to 3 GPa, especially at high pressures (Table 4-3). This may be due to non-hydrostatic stresses which may develop during compression and would affect the soft MgO and Au pressure markers differently. However, since at every pressure and temperature point both compressional and shear wave velocities as well as density of the akimotoite samples are collected, absolute pressure can be calculated as described in section 2.8.7. A comparison between the absolute pressure and the pressure values obtained from the pressure markers is given in section 4.2.2.

Experiments T2083 and T2270 could be recovered after the ultrasonic experiments and showed no change in composition or texture with respect to the starting assemblage implying that no phase transformation happened during high pressure and temperature (Figure 4-9). This observation is in agreement with the fact that the energy-dispersive diffraction patterns present the same features at all pressure and temperature points collected during the experiments. Experiment T2269 containing Ak97.5 could not be recovered after the ultrasonic experiment because during the last heating cycle akimotoite transformed into majoritic garnet identified using X-ray diffraction. After decompression, the octahedron was too brittle, probably due to the transformation and fell apart.
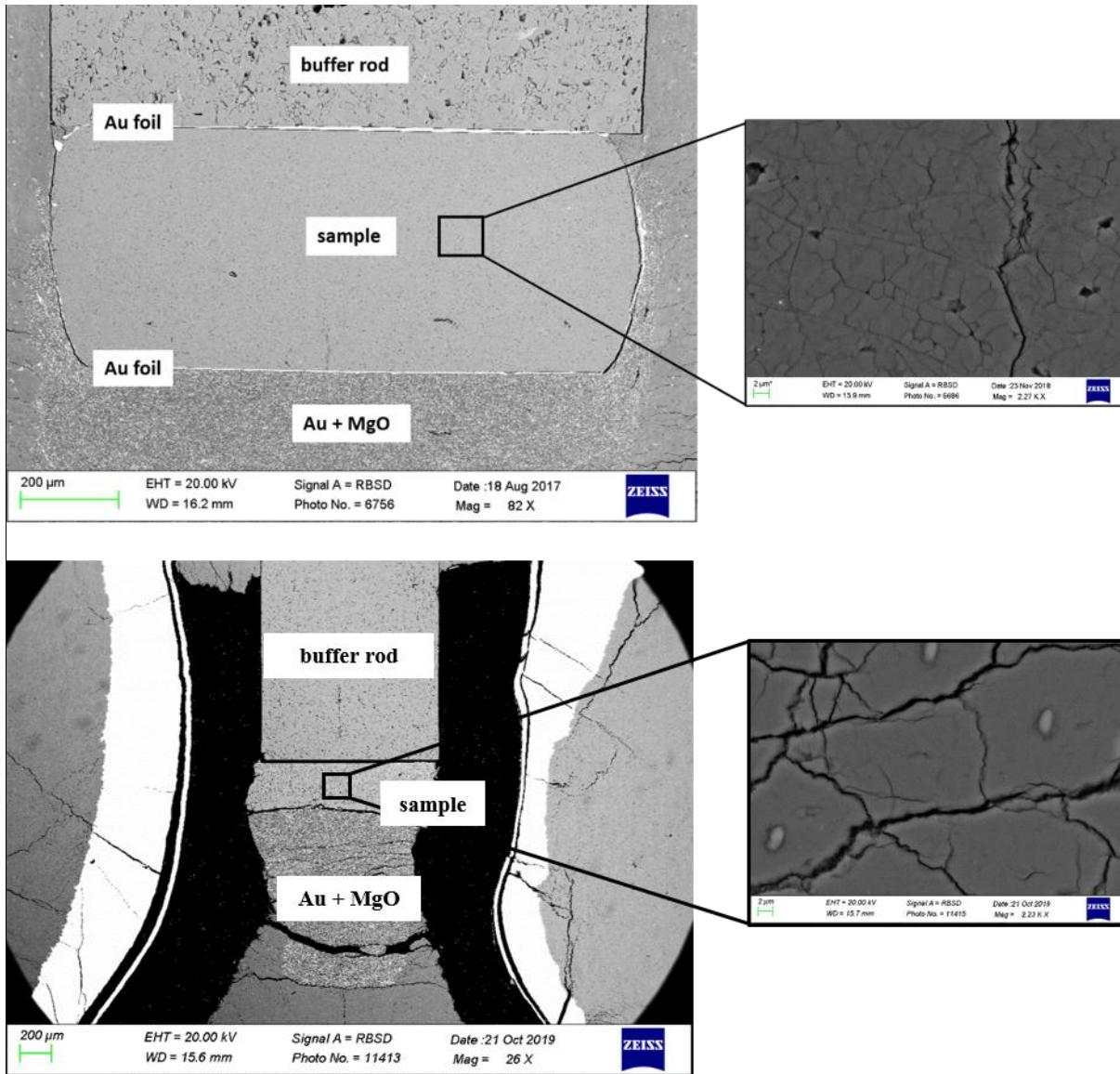
Figure 4-9: *Recovered experiments T2083 (top, containing Ak97.5) and T2270 (bottom, containing Ak80) after the synchrotron experiments. No change in grain size or composition was observed. T2270 was heavily cracked during the very fast decompression, having large cracks in both sample and assembly. EMP analyses after the experiment led to damage to the sample indicated by the bright spots.*

Table 4-3: *Unit-cell lattice parameters of Au and MgO pressure markers, calculated pressures from the equation of states for Au (Tsuchiya 2003) and for MgO (Dewaele et al. 2000) and the unit-cell lattice parameters for Ak97.5 (T2083 and T2269) and Ak80 (T2270) akimotoite samples obtained from energy-dispersive X-ray diffraction.*

a_{Au} (Å)	a_{MgO} (Å)	Au P (GPa)	MgO P (GPa)	temperature (K)	a_{aki} (Å)	c_{aki} (Å)	V_{aki} (Å³)
						Ak97.5	
T2083							
4.0783(2)	4.2112(1)	0.0001	0.0001	300	4.7302(3)	13.545(2)	262.47(2)
4.0635(5)	4.1956(2)	1.88	1.83	300	4.7008(6)	13.427(2)	256.95(4)
4.0278(8)	4.1645(4)	6.95	5.75	300	4.6724(3)	13.309(2)	251.62(3)
4.0001(4)	4.1359(3)	11.53	9.70	300	4.6528(4)	13.235(2)	248.13(3)
3.9913(3)	4.1253(2)	13.10	11.24	300	4.6451(5)	13.211(2)	246.86(4)
3.9801(3)	4.1133(2)	15.18	13.06	300	4.6350(3)	13.158(2)	244.81(2)
3.9682(4)	4.1006(2)	17.52	15.05	300	4.6232(5)	13.119(2)	242.84(3)
3.9638(5)	4.0946(2)	18.41	16.01	300	4.6166(5)	13.097(1)	241.74(3)
3.951(3)	4.0815(2)	21.11	18.20	300	4.6029(5)	13.058(2)	239.59(3)
3.9434(3)	4.0733(2)	22.79	19.58	300	4.5938(6)	13.043(2)	238.37(3)
3.9725(3)	4.0981(2)	20.13	18.24	800	4.6251(5)	13.129(2)	243.22(3)
3.9678(3)	4.0947(2)	19.66	17.59	600	4.6220(5)	13.125(2)	242.83(3)
3.9625(2)	4.0894(2)	18.68	16.86	300	4.6182(5)	13.110(2)	242.15(3)
3.9541(3)	4.081(2)	20.45	18.26	300	4.6093(5)	13.082(2)	240.70(3)
3.9631(3)	4.0861(2)	22.00	20.20	800	4.6146(5)	13.096(2)	241.51(3)
3.9590(3)	4.0830(2)	21.46	19.51	600	4.6129(6)	13.086(2)	241.14(3)
3.9541(3)	4.0783(2)	20.45	18.72	300	4.6082(5)	13.085(2)	240.64(4)
3.9479(3)	4.0707(2)	21.79	20.03	300	4.5988(6)	13.067(2)	239.33(3)
3.9721(3)	4.0925(2)	22.31	21.02	1100	4.6314(6)	13.144(2)	244.16(3)
3.9658(2)	4.0863(1)	22.50	21.10	950	4.6244(6)	13.128(2)	243.14(3)
3.9658(2)	4.0864(2)	21.45	20.15	800	4.6245(6)	13.133(2)	243.23(3)
3.9633(2)	4.0840(2)	20.57	19.35	600	4.6253(6)	13.120(2)	243.08(3)
3.9579(2)	4.0800(2)	19.64	18.43	300	4.6199(6)	13.114(2)	242.40(3)

Table 4-3 continued.

a_{Au} (Å)	a_{MgO} (Å)	Au P (GPa)	MgO P (GPa)	temperature (K)	a_{aki} (Å)	c_{aki} (Å)	V_{aki} (Å^3)
T2269							
4.0799(3)	4.2121(2)	0.00	0.00	300	4.7297(3)	13.542(1)	262.34(2)
4.0100(5)	4.1456(2)	10.10	8.44	300	4.6681(8)	13.254(2)	250.13(6)
4.0457(3)	4.1746(2)	6.73	6.17	600	4.6972(9)	13.392(3)	255.90(7)
4.0348(3)	4.1664(2)	6.12	5.62	300	4.6824(7)	13.355(3)	253.58(6)
3.9671(3)	4.1001(1)	18.06	15.27	300	4.6287(13)	13.120(3)	243.43(6)
3.9928(4)	4.1172(2)	15.22	14.19	600	4.6431(18)	13.165(5)	245.79(8)
3.9806(3)	4.1097(1)	15.39	13.75	300	4.6402(22)	13.163(6)	245.45(10)
3.9444(2)	4.0718(1)	22.92	19.99	300	4.5996(9)	13.068(3)	239.44(6)
3.9697(2)	4.0922(1)	20.99	19.34	800	4.6238(12)	13.110(4)	242.73(6)
3.9650(2)	4.0882(1)	20.54	18.79	600	4.6204(9)	13.097(3)	242.14(6)
3.9582(2)	4.0835(1)	19.90	17.99	300	4.6159(12)	13.087(3)	241.48(7)
3.9502(2)	4.0751(1)	21.63	19.42	300	4.6067(11)	13.088(3)	240.53(6)
3.9656(2)	4.0867(1)	21.81	20.24	800	4.6231(11)	13.096(5)	242.40(7)
3.9614(2)	4.0828(1)	21.28	19.69	600	4.6194(8)	13.101(3)	242.12(5)
3.9549(2)	4.0784(2)	20.61	18.85	300	4.6128(10)	13.105(3)	241.48(5)
						Ak80	
T2270							
4.0775(2)	4.2173(1)	0.00	0.00	300	4.7526(4)	13.349(2)	261.12(3)
4.0080(2)	4.1369(3)	10.03	10.42	300	4.6771(5)	13.128(2)	248.70(3)
4.0305(2)	4.1585(3)	6.41	7.37	300	4.6972(5)	13.199(2)	252.21(3)
4.0049(2)	4.1327(3)	10.56	11.03	300	4.6766(5)	13.111(2)	248.33(3)
3.9922(2)	4.1198(2)	12.79	12.97	300	4.6690(5)	13.079(2)	246.91(3)
3.9809(2)	4.1078(2)	14.88	14.84	300	4.6541(6)	13.041(2)	244.62(3)
3.9730(2)	4.0986(3)	16.40	16.32	300	4.6514(5)	13.015(2)	243.85(3)
3.9603(2)	4.0865(2)	18.98	18.33	300	4.6311(7)	12.977(3)	241.02(4)
3.9485(2)	4.0727(3)	21.49	20.71	300	4.6146(7)	12.931(3)	238.48(4)
3.9366(1)	4.0574(2)	24.16	23.46	300	4.6119(8)	12.872(4)	237.10(5)

The variation of P- and S- wave velocities of Ak97.5 (red) and Ak80 (blue) at room temperature up to pressures of the transition zone are shown in Figures 4-10. Note that two independent synchrotron experiments for the composition Ak97.5 are plotted. Both data sets are in excellent agreement confirming the reproducibility of the measurements. The wave velocities of the $MgSiO_3$ end-member determined by Brillouin spectroscopy (Chapter 3.3) and ultrasonic interferometry (Zhou et al. 2014) as well as the wave velocities of majoritic garnet (Pamato et al. 2016) are reported in Figure 4-10 for comparison. Wave velocities of akimotoite and Al-bearing akimotoite are faster than those of majoritic garnet (Pamato et al. 2016), although it appears that both v_P and v_S become slower with increasing Al content relative to the akimotoite end-member. This is surprising since the wave velocities of Al_2O_3-corundum (Higo et al. 2006, 2018) are faster than those of akimotoite (Figure 4-10). This is the first time that a so strong non-ideal behavior is observed since usually the wave velocities of mixed compositions lie between those of the two end-members even when they do not follow a linear behavior.

High-temperature high-pressure data have been collected for the Ak97.5 compositions up to 1100 K following the T-P path shown in Figure 2-23 (Chapter 2). The ultrasonic and energy-dispersive XRD measurements were conducted during cooling down which allowed stress to be released inside the assembly. The stress release resulted in pressure drops during most of the heating cycles (Table 4-3 and Figure 2-23). Due to fluctuating thermocouple readings when heating up the assembly during run T2270 (Ak80) it was not possible to measure the wave velocities at high-temperature for this sample. High-temperature compressional and shear wave velocities for Ak97.5 are plotted in Figure 4-11 together with the room temperature data.
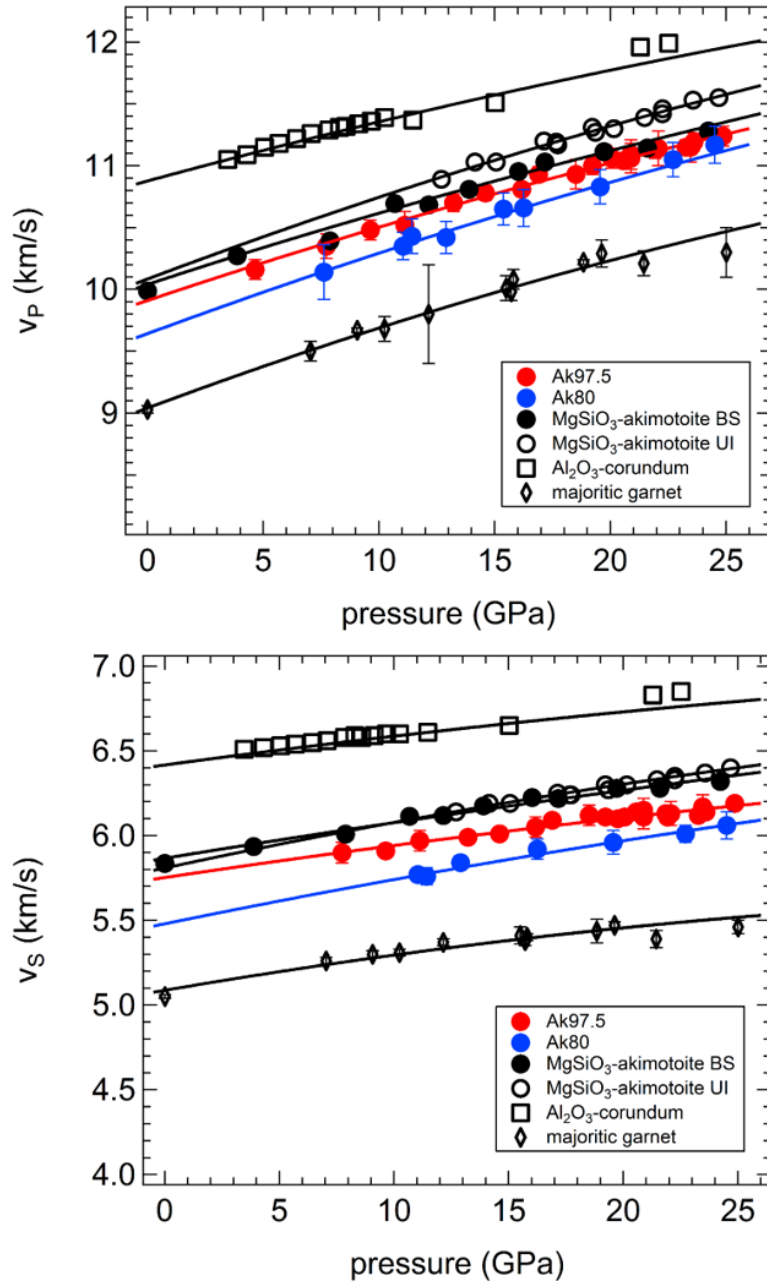
Figure 4-10: *Compressional (top) and shear (bottom) wave velocities of Ak97.5 (red) and Ak80 (blue) up to pressures of the transition zone. Wave velocities decrease with increasing Al content relative to the wave velocities of the $MgSiO_3$ akimotoite end-member obtained using Brillouin spectroscopy (solid black circles, this study) and ultrasonic interferometry (open black circles, Zhou et al. 2014). Note that the wave velocities of Al-bearing akimotoite do not fall in between the $MgSiO_3$ akimotoite and Al_2O_3 corundum end-members (squares, Higo et al. 2006, 2018), however, are still faster than the wave velocities of majoritic garnet (diamonds, Pamato et al. 2016). The solid curves represent Debye-Mie-Grüneisen EoS fits through the individual data sets.*

Table 4-4: Compressional and shear wave velocities of two Al-bearing akimotoite samples Ak97.5 (runs T2083 and T2269) and Ak80 (run T2270) calculated from the two-way travel times and sample lengths reported at pressure and temperature during the ultrasonic measurements. The density has been simultaneously measured using energy-dispersive X-ray diffraction.

absolute P (GPa)	temperature (K)	density (g/cm^3)	travel time (x10^{-9}s)		sample length (x10^{-6} m)	v_p (km/s)	v_s (km/s)
			Ak97.5				
T2083			P-wave	S-wave			
0.0001	300	3.8128			504.31		
4.65	300	3.8947	98.20		499.02	10.16(8)	
9.63	300	3.9772	94.40	167.40	494.79	10.48(8)	5.91(3)
13.22	300	4.0332	92.00	164.47	492.39	10.70(7)	5.99(3)
14.60	300	4.0539	91.20	163.73	491.71	10.78(6)	6.01(3)
16.90	300	4.0878	89.80	161.20	490.98	10.93(6)	6.09(3)
19.22	300	4.1210	88.30	159.00	485.83	11.00(7)	6.11(4)
20.56	300	4.1398	88.00	158.20	485.83	11.04(6)	6.14(3)
23.27	300	4.1769	87.00	158.53	484.88	11.15(6)	6.12(3)
24.86	300	4.1982	86.40	156.87	485.72	11.24(8)	6.19(3)
20.98	800	4.1145	89.45	163.70	487.74	10.91(6)	5.96(4)
20.48	600	4.1212	88.80	160.20	485.64	10.94(6)	6.06(3)
20.06	300	4.1328	88.30	159.80	488.51	11.06(8)	6.11(3)
21.85	300	4.1576	87.40	158.85	486.95	11.14(7)	6.13(3)
23.05	800	4.1436	87.80	160.00	481.39	10.97(6)	6.02(4)
22.54	600	4.1500	87.53	159.53	483.09	11.04(7)	6.06(4)
21.93	300	4.1587	87.50	159.37	486.74	11.13(7)	6.11(3)
23.60	300	4.1814	86.60	157.87	484.42	11.19(7)	6.14(3)
21.40	1100	4.0987	89.00	163.00	481.29	10.82(6)	5.91(3)
21.84	950	4.1160	88.60	162.33	481.67	10.87(6)	5.93(3)
20.97	800	4.1144	88.40	161.53	482.57	10.92(7)	5.97(6)
20.18	600	4.1169	88.00	160.40	483.72	10.99(6)	6.03(4)
19.76	300	4.1286	87.40	159.15	485.40	11.11(6)	6.10(3)

Table 4-4 continued.

absolute P (GPa)	temperature (K)	density (g/cm^3)	travel time (x10^{-9}s)		sample length (x10^{-6} m)	v_p (km/s)	v_s (km/s)
			Ak97.5				
T2269			P-wave	S-wave			
0.0001	300	3.8146			511.37		
11.12	300	4.0008	75.00	132.20	394.34	10.52(11)	
6.87	600	3.9108	76.75	135.02	392.40	10.23(10)	5.97(6)
7.73	300	3.9464	75.68	132.71	391.70	10.35(11)	5.81(6)
18.51	300	4.1110	69.81	124.64	381.37	10.93(12)	5.90(6)
17.05	600	4.0716	70.24	126.72	376.53	10.72(11)	6.12(6)
16.17	300	4.0772	69.71	124.32	376.25	10.80(12)	5.94(6)
23.46	300	4.1795	66.88	120.96	372.91	11.15(12)	6.05(6)
21.57	800	4.1228	67.50	123.20	367.90	10.90(14)	6.17(7)
21.31	600	4.1329	67.63	122.28	370.30	10.95(12)	5.97(6)
20.88	300	4.1442	67.20	120.80	371.65	11.06(12)	6.06(7)
22.07	300	4.1606	67.28	122.24	374.59	11.14(14)	6.15(7)
21.96	800	4.1284	66.72	121.20	363.14	10.89(12)	6.13(7)
21.34	600	4.1333	67.09	121.76	367.63	10.96(15)	5.99(7)
20.88	300	4.1443	66.24	120.24	367.44	11.09(12)	6.04(7)
			Ak80				
0.0001	300	3.8397			513.73		
11.04	300	4.0315	70.19	125.92	363.12	10.35(11)	5.77(4)
7.62	300	3.9754	69.36		351.55	10.14(22)	
11.42	300	4.0375	67.04	121.50	349.77	10.43(14)	5.76(5)
12.90	300	4.0607	67.31	120.16	350.66	10.42(13)	5.84(4)
15.38	300	4.0987	63.20		336.42	10.65(13)	
16.25	300	4.1117	60.80	109.42	323.96	10.66(15)	5.92(6)
19.56	300	4.1599	59.52	108.16	322.18	10.83(14)	5.96(7)
22.71	300	4.2042	57.65	106.00	318.62	11.05(14)	6.01(5)
24.51	300	4.2287	55.84	102.88	311.86	11.17(15)	6.06(8)
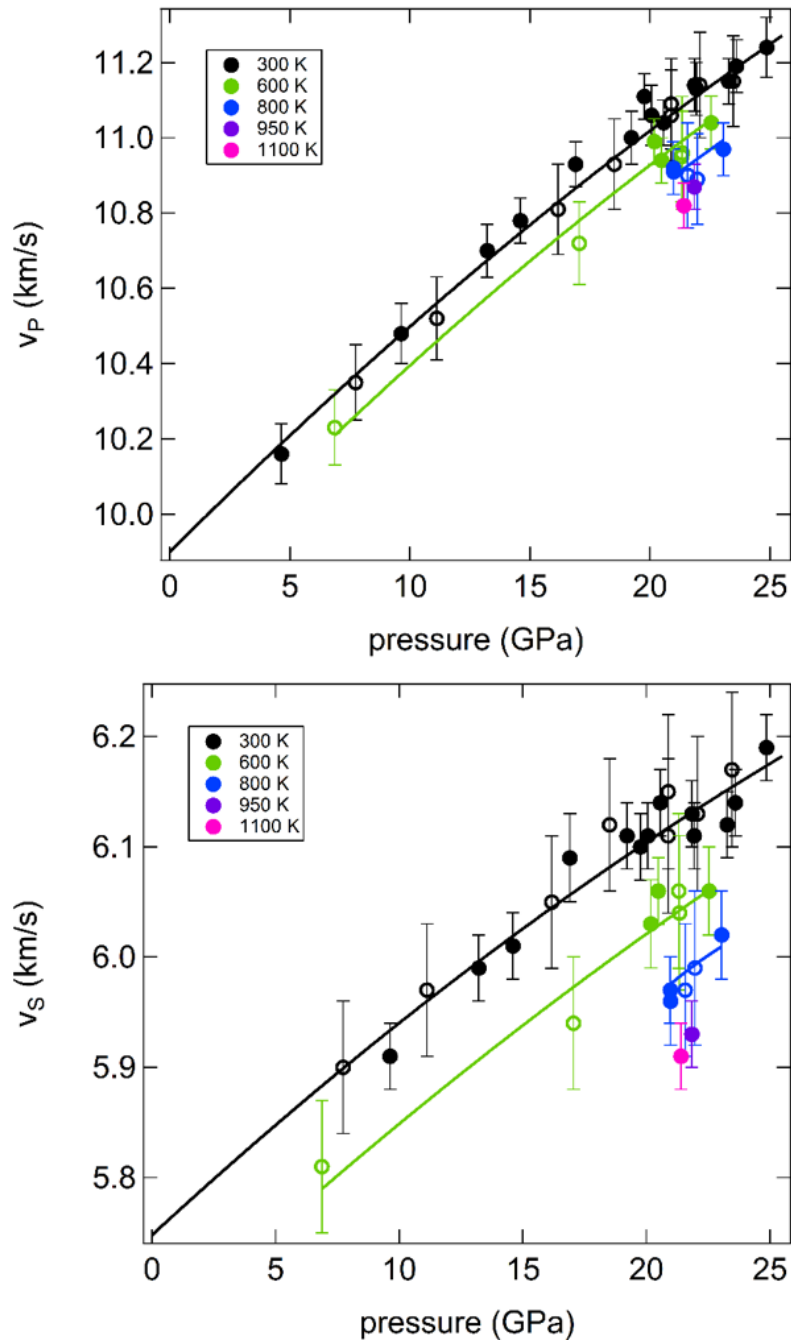
Figure 4-11: *High-temperature compressional (top) and shear (bottom) wave velocities of Ak97.5 up to 1100 K. The wave velocities of two independent experiments (T2083, solid symbols and T2269, open symbols) have been performed with samples having the same composition. The solid curves represent Debye-Mie-Grüneisen EoS fits through the data sets.*

124

In order to obtain the elastic properties of Al-bearing akimotoite at high pressure and high temperature, first the room temperature data were fitted with the third order finite strain procedure described in detail in Chapter 2.8.7. This formalism also was used for the Ak80 data for which no high-temperature experiment was possible. The elastic parameters obtained are listed in Table 4-5. The room- and high-temperature ultrasonic data of Ak97.5 were then fitted using a Debye-Mie-Grüneisen equation of state following the formalism reported in Stixrude and Lithgow-Bertelloni (2005) and described in chapter 2.8.8. Note that in this case an isothermal bulk modulus is used in the fitting procedure First V_0, K_{T0}, K', G_0 and G' were fitted by minimizing the difference between experimental and calculated values. The values obtained for K_{S0}, K', G_0 and G' are in good agreement with those obtained using the formulism derived from the 3rd order EoS reported in Davies and Dziewonski (1975) for Ak97.5 once the transformation from K_{S0} to K_{T0} is taken into account (see Table 4-5). Then, also the high-temperature parameters γ, q and η_S were fitted together with all other parameters (Table 4-5). The high-temperature parameters γ, q and η_S were determined to be within the uncertainties of the values reported by Stixrude and Lithgow-Bertelloni (2005). The resulting fits for both samples Ak97.5 and Ak80 at room temperature are shown in Figure 4-10 and the high temperature fitting of the Ak97.5 sample is shown in Figure 4-11.

The wave velocities reported by Zhou et al. (2014) and by Higo et al. (2018) have been re-fitted using the same thermodynamically consistent Debye-Mie-Grüneisen formalism (Stixrude and Lithgow-Bertelloni 2005) in order to compare the resulting elastic parameters since Zhou et al. (2014) and Higo et al. (2018) have used linear relations to fit their data. For the high-temperature parameters γ, q and η_S, the values reported for akimotoite and corundum in Stixrude and Lithgow-Bertelloni (2005) have been used. The adiabatic bulk modulus K_{T0} of akimotoite has a lower value (213(1) GPa) than that reported by Zhou et al. (2014) (K_{S0} = 219.4(7) GPa), and a higher K' (5.1(1) relative to 4.62(3)). Moreover, the adiabatic bulk modulus now lies closer to the one determined using Brillouin spectroscopy in this study (K_{S0} = 208(1) GPa, chapter 3.2) and in the study of Weidner and Ito (1985) (212 GPa). The shear modulus G and its pressure derivative G' are very similar to the values reported previously (new fitting: 130(1) GPa and 1.9(1), Zhou et al. (2014): 132.1(7) and 1.63(4)). For the corundum end-member, the Debye-Mie-Grüneisen fit was performed using also room temperature data reported by Higo et al. (2006). All parameters are very comparable to the values reported by Higo et al. (2018) as can be seen in Table 4-5.

The resulting elastic parameters show that akimotoite is more compressible with increasing Al content (Table 4-5). This is also shown by the normalized volumes of the individual akimotoite samples Ak97.5, Ak80 and the volumes obtained for the akimotoite end-member (Chapter 3.1) plotted against absolute pressure (Figure 4-12).
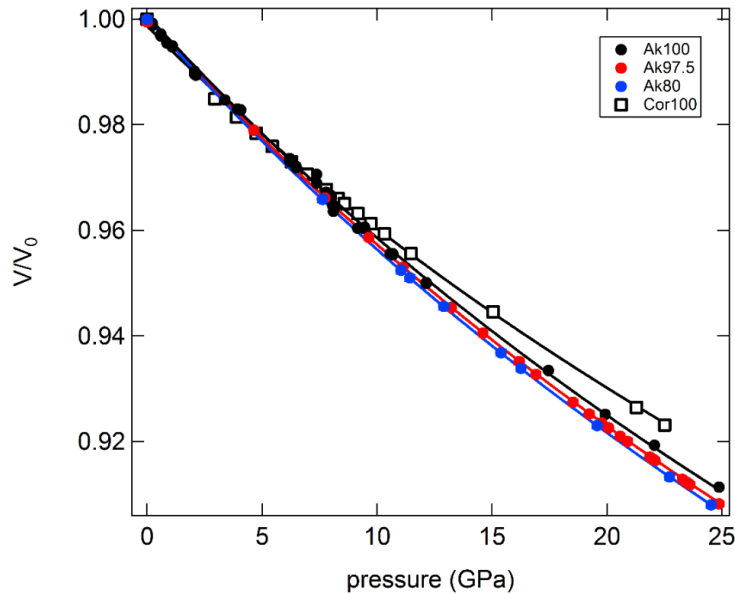
Figure 4-12: Variation with pressure of the volumes of Ak100, Ak97.5 and Ak80 and Cor100 (Higo et al. 2006, 2018) normalized with respect to their room pressure values. The compressibility increases with increasing Al content. Opposite to that Cor100 is stiffer than Ak100. The solid lines represent BM3 EoS fits using the bulk moduli and their first pressure derivative reported in Table 3-2 and Table 4-5. The uncertainties are smaller than the symbol size.

The compressibility of the normalized unit-cell parameters *a* and *c* is shown in Figure 4-13. The *a*-axis is more compressible with increasing Al content, however, the *c*-axis becomes less compressible. Linearized BM3 EoS have been used to fit the *P* - unit-cell axes data and the resulting parameters are reported in Table 4-6. This indicates that the incorporation of Al into the akimotoite structure decreases the anisotropy of the axial compression. The variation of the *c/a* ratio (Figure 4-14) reflects the decrease in anisotropy, in fact for Ak80 this decreases only slightly with pressure given the similar values of M_0 of the two unit-cell axes (Table 4-6). For Ak97.5 the variation of the *c/a* ratio is similar to that of the end-member at low pressure, whereas at pressure larger than 17 GPa it remains almost constant due to the larger M_0' of the *c*-axis with respect to that of the *a*-axis.

Table 4-5: *EoS parameters of Ak97.5 and Ak80 obtained using the third-order finite strain equation derived from Davies and Dziewonski (1975) and the Mie-Grüneisen EoS after Stixrude and Lithgow-Bertelloni (2005). The EoS parameters of $MgSiO_3$ akimotoite (Stixrude and Lithgow-Bertelloni 2005; Zhou et al. 2014), Al_2O_3 corundum (Higo et al. 2018) and majoritic garnet (Pamato et al. 2016) are reported.*

	V_0 (cm³/mol)	K_0 (GPa)	K_0'	G_0 (GPa)	G'	γ_0	η_{s0}	q	θ_{Debye} (K)
Ak97.5		204(1)	4.9(1)	126(1)	1.6(1)				
	26.34	204(1)	4.8(1)	126(1)	1.6(1)	1.2	2.8	1.7	919
Ak80		198(1)	5.2(1)	116(1)	1.8(1)				
	26.21	197(1)	5.2(1)	115(1)	1.8(1)				
MgSiO₃-aki (Stixrude and Lithgow-Bertelloni 2005)	26.35	211(4)	4.5(5)	132(8)	1.6(5)	1.18(13)	2.7(10)	1.3(10)	850(100)
MgSiO₃-aki (Zhou et al. 2014)	26.35	219.4(7)	4.62(3)	132.1(7)	1.63(4)				
MgSiO₃-aki (new fitting)	26.28	213	5.1	130	1.9	1	2.5	1.3	943
Al₂O₃-cor (Higo et al. 2018)	25.58[a]	251.2(18)	4.21(10)	164.1(7)	1.59(3)	1.32(4)[a]	2.8(2)[a]	1.3(2)[a]	933(3)[a]
Al₂O₃-cor (new fitting)	25.57	255(1)	3.9(1)	167(1)	1.4(1)	1.15	2.48	1.41	1033
Py76Mj24 (Pamato et al. 2016)	11.34	167(2)	4.7(2)	91.8(7)	1.4(1)	1[b]	1.3	1.4[b]	791

[a]values taken from Stixrude and Lithgow-Bertelloni (2005)

[b]values taken from Xu et al. (2008)
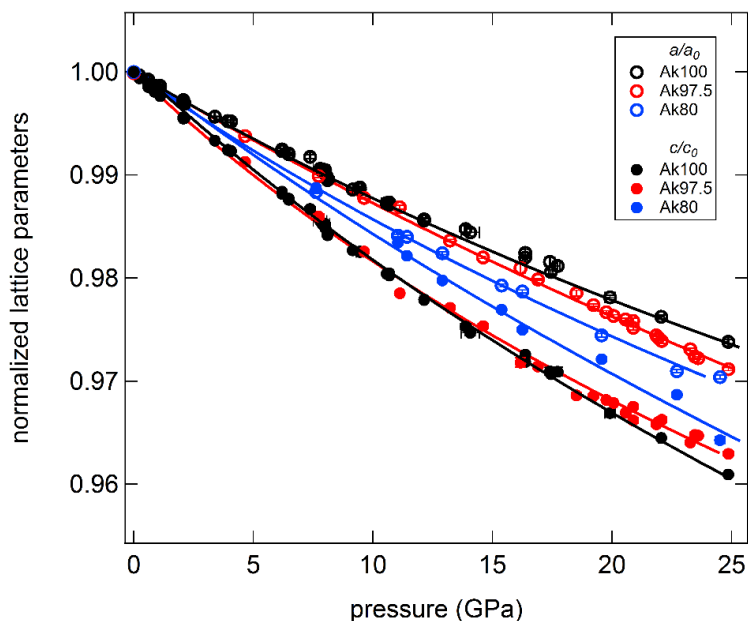
Figure 4-13: *Variation with pressure of the unit-cell lattice parameters normalized with respect to their room pressure values for Ak97.5 (red), Ak80 (blue) and the $MgSiO_3$ end-member as determined in Chapter 3 (black). With increasing Al content, the axial anisotropy decreases. The solid lines represent BM3 EoS fits through the individual data sets. The uncertainties are smaller than the symbol size.*
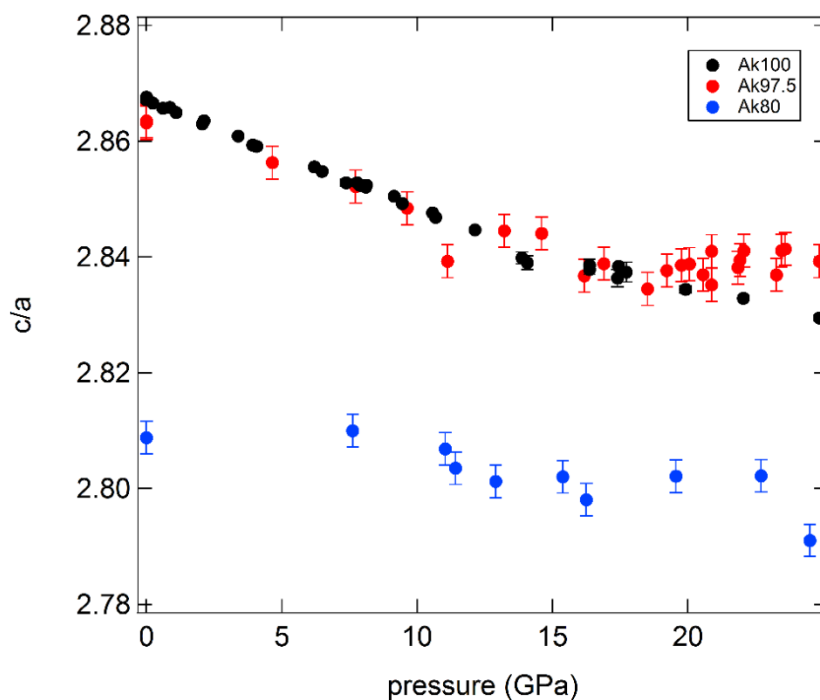
Figure 4-14: *Variation with pressure of the c/a ratio for Ak97.5 (red), Ak80 (blue) and the $MgSiO_3$ end-member (Ak100) as determined in Chapter 3 (black). The c/a ratio of Ak80 is much smaller compared to Ak100 and Ak97.5.*

Table 4-6: Resulting BM3 EoS fitting parameters for the axial compressibility of Ak97.5 and Ak80.

	Ak97.5	Ak80
a_0 (Å)	4.7298(4)	4.752(1)
M_0 (GPa)	758(12)	610(27)
M'	9(1)	18(3)
c_0 (Å)	13.544(4)	13.352(7)
M_0 (GPa)	451(21)	593(45)
M'	19(3)	8(4)

4.2.2 Absolute pressure determination

The simultaneous determination of the wave velocities of akimotoite and its density at pressure and temperature allows the calculation of the absolute pressure reached during the large volume press experiments without having to rely on secondary pressure markers such as MgO and Au. The absolute pressures were calculated for both the Ak97.5 and Ak80 synchrotron experiments using the formulism described in chapter 2.8.7 and are reported in Table 4-4. The difference between the absolute pressure values and the Au pressure values is plotted in Figure 4-15. The Au pressure calculated for experiment T2083 deviates from the absolute pressure by up to 2.5 GPa possibly due to non-deviatoric stresses affecting the soft pressure markers. During experiment T2269 (Ak97.5) and T2270 (Ak80), stresses have been released by heating up to 600 K multiple times during compression. In both experiments, the difference between Au and absolute pressure values are slightly smaller than for T2083 (Figure 4-15). The use of a hard pellet of MgO+Au as pressure marker probably hinders the accommodation of stresses during compression creating large deviation from the elastic behavior of these very soft materials.
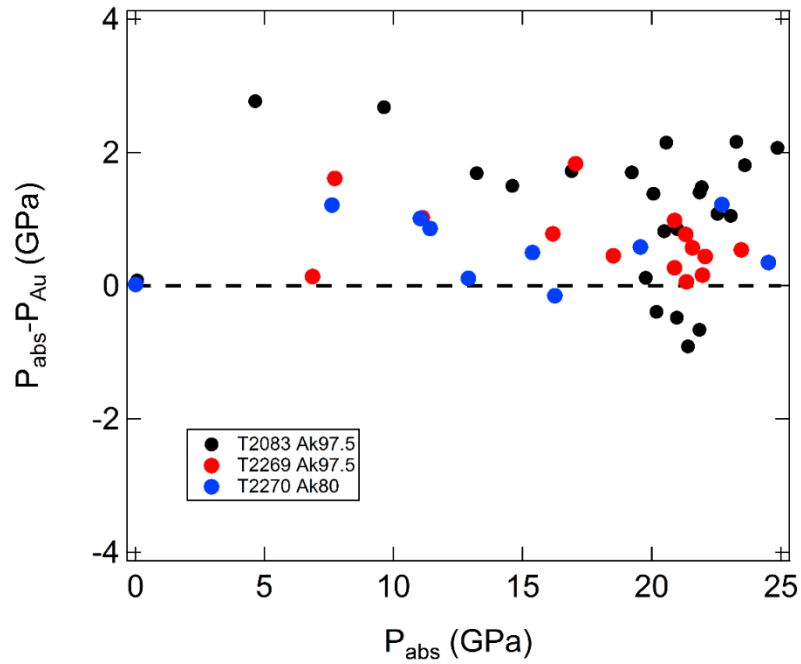
Figure 4-15: *Comparison between the absolute pressure values and those obtained from the pressure standard Au. The Au pressure scale is up to 2.5 GPa lower than the absolute pressure. The larger deviations are observed for experiment T2083. During experiment T2269 and T2270, the stresses have been released by heating up to 600 K during compression.*

5. The effect of Fe and Al substitution on the elasticity of akimotoite

5.1 Unit-cell parameters of Fe- and Al-bearing akimotoite

In order to understand the effect of Fe and Al on the unit-cell parameters of akimotoite, X-ray diffraction data from several studies on Al- and/or Fe-bearing akimotoite found in meteorites (Miyajima et al. 2007, Ferroir et al. 2008, Bindi et al. 2017, Tschauner et al. 2018) and one experimental study on Fe-bearing akimotoite (Ito and Yamada 1982) were compiled and compared to the unit-cell parameters of Fe- and Al-bearing akimotoite (Fe10 and Fe10Al10) investigated in this study (Table 2-1). The unit-cell parameters a and c, as well as the corresponding volumes are shown in Figure 5-1 and 5-2, respectively.

In Fe-bearing akimotoite, the main substitution mechanism is substitution of Fe^{2+} into the Mg site. The variation of the a- and c-axes with increasing $FeSiO_3$ component appears to be linear, (Figures 5-1, 5-2) The Fe10 sample which was synthesized for this study (Table 2-1) appears to have slightly larger a, c and V values (Figures 5-1 and 5-2) than the trend described by the natural samples and those synthetized by Ito and Yamada (1982) for which only unit-cell volumes were reported in the original paper. Note that the synthesis of sample Fe10 was performed at a temperature of 1123 K, much lower than the synthesis temperatures ranging between 1273 and 1673 K used in the study of Ito and Yamada (1982) or the temperatures recorded in shocked meteorite veins (e.g. Sharp et al. 1997). Lower temperatures can increase the disorder inside the akimotoite structure due to slow kinetics during the synthesis run.

In Fe,Al-bearing akimotoite a coupled substitution is expected, i.e. Fe is therefore assumed to be ferric in order to balance the Al content. Fe- and Al-bearing akimotoite found in meteorites (Ferroir et al. 2008) have unit-cell parameters volumes close to the trend described by the Fe-rich akimotoite (Figure 5-2). The unit-cell parameters for the Fe,Al-bearing akimotoite investigated by Miyajima et al. (2007), however, deviate significantly from the trend found for $FeSiO_3$-bearing akimotoites and those of Ferroir et al. (2008) with the a-axis being much smaller than expected, whereas the c-axis and V are larger than the trend.
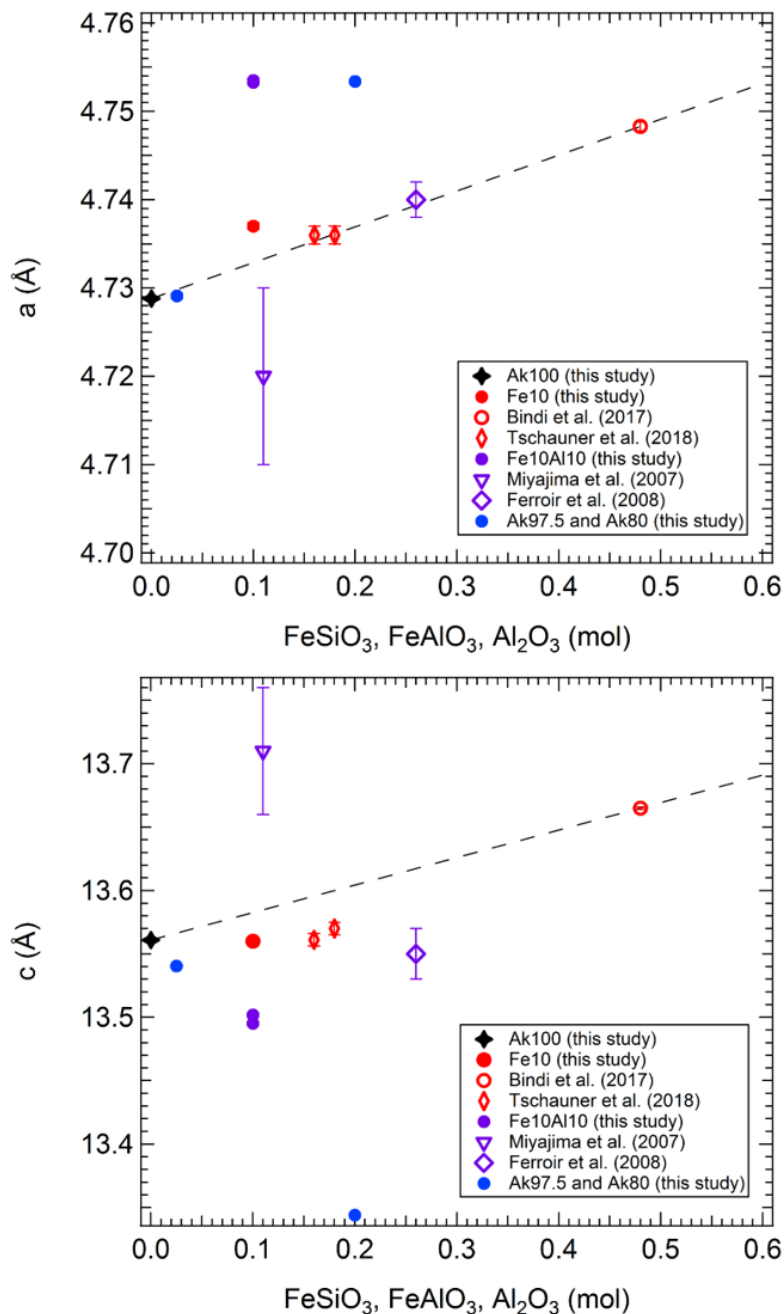
Figure 5-1: *Influence of FeSiO₃ and FeAlO₃ substitutions on the unit-cell parameters a and c of akimotoite. All Fe-bearing (red) and Fe- and Al-bearing akimotoite (purple) unit-cell parameters obtained from XRD measurements on natural akimotoite found in meteorites are compared to samples Fe10 and Fe10Al10 investigated in this study. The unit-cell parameters of Ak100 (Chapter 3) and Ak97.5 and Ak80 (Chapter 4) also are plotted for comparison. The dashed line serves as guide to the eye assuming a linear trend between Ak100 and Mg-rich hemleyite (Bindi et al. 2017).*
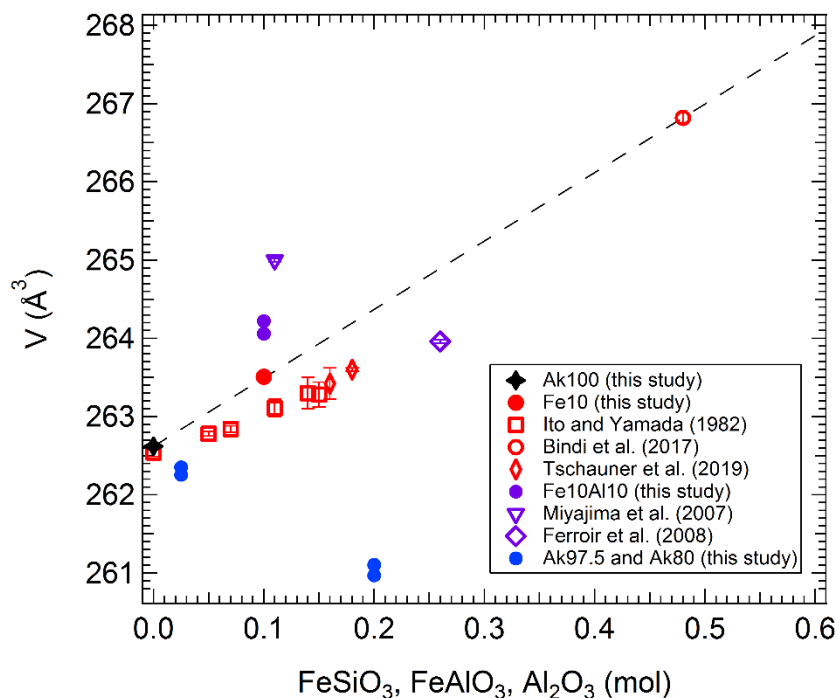
Figure 5-2: *Influence of FeSiO₃ and FeAlO₃ substitutions on the unit-cell volume of akimotoite. The Fe-bearing akimotoite (red) consist of natural and synthetic samples whereas the Fe- and Al-bearing akimotoites (purple) are natural akimotoite found in meteorites. Samples Fe10 and Fe10Al10 investigated in this study, as well as Ak100 (Chapter 3) and Ak97.5 and Ak80 (Chapter 4) are plotted with filled symbols. The dashed line serves as guide to the eye assuming a linear trend between Ak100 and Mg-rich hemleyite (Bindi et al. 2017).*

Sample Fe10Al10 investigated in this study, instead, shows the opposite behavior with the *a*-axis being larger and the *c*-axis being smaller (Figure 5-2) then the trend defined by the Fe-bearing akimotoites. In particular, the *c*-axis appears to follow the trend defined by the Al-bearing akimotoites (described in Chapter 4.1), whereas the *a*-axis is as large as that of sample Ak80. As a results the unit-cell volume of sample Fe10Al10 is larger than the Fe10 sample, in spite of the substitution of smaller cations. This may be due to some order/disorder effect, for example Fe^{3+} could substitute not only Mg, but also Si in the akimotoite structure, however, single-crystal structural data are required for testing such hypothesis.

5.2 The influence of Fe substitution on the wave velocities of akimotoite

One ultrasonic experiment (T2082) was performed on a Fe-bearing akimotoite sample (Fe10). Ultrasonic measurements, X-ray diffraction and X-ray radiography for sample length determination were conducted up to 26.4 GPa and 1100 K as described in detail in section 2.8. Also for this experiment, MgO and Au were used as secondary pressure markers. Their unit-cell lattice parameters and calculated pressures using the EoS reported by Tsuchiya (2003) and Dewaele et al. (2000) are reported in Table 5-1. As for the experiments in Chapter 4.2, the MgO and Au pressures differed by up to 4 GPa possibly due to a different stress distribution on the pressure markers. The absolute pressure could be calculated from the wave velocities and density of akimotoite and is reported in Table 5-2 as well as the travel times, sample lengths and compressional and shear wave velocities of Fe-bearing akimotoite.

After the synchrotron experiment, the assembly T2082 was recovered, cut from top to bottom and polished to perform X-ray diffraction and SEM analyses (Figure 5-3). Electron backscattering imaging showed that brighter secondary phases formed along the grain boundaries of the akimotoite crystals. These additional phases were not present at the beginning of the experiments and due to their very small concentration could not be detected neither in situ by means of the EDXRD nor using the Bruker micro-focus diffractometer on the recovered synchrotron sample. However, the Mössbauer spectrum of the same recovered sample could be fitted with three distinct doublets (Figure 5-4). The dark green doublet is making up 67(1) % of the total Fe and can be clearly attributed to the Fe^{2+} substituted into the MgO_6 site in akimotoite having an isomer shift (IS) of 1.039(2) and a quadrupole splitting (QS) of 1.740(4). This is comparable to the IS and QS obtained for akimotoite (McCammon et al. personal communication).

Table 5-1: Unit-cell lattice parameter of Au and MgO pressure markers, calculated pressures according to Tsuchiya (2003) and Dewaele et al. (2000), respectively and unit-cell lattice parameters of Fe10 at different pressures and temperatures.

a_{Au} (Å)	a_{MgO} (Å)	Au P (GPa)	MgO P (GPa)	temperature (K)	a_{aki} (Å)	c_{aki} (Å)	V_{aki} (Å³)
T2082							
4.0786(3)	4.2113(1)	0.0001	0.00	300	4.7370(4)	13.560(2)	263.51(3)
4.0513(5)	4.1943(2)	3.54	2.00	300	4.7037(5)	13.453(2)	257.78(3)
4.0333(5)	4.1768(3)	6.15	4.17	300	4.6901(6)	13.367(2)	254.65(4)
4.0180(5)	4.1603(3)	8.56	6.32	300	4.6769(5)	13.317(2)	252.26(3)
4.0063(6)	4.1451(4)	10.51	8.40	300	4.6668(5)	13.269(2)	250.27(4)
3.9907(4)	4.1290(2)	13.26	10.71	300	4.6539(7)	13.216(3)	247.90(4)
3.9802(3)	4.1183(2)	15.22	12.31	300	4.6459(7)	13.171(3)	246.20(4)
3.9665(3)	4.1023(2)	17.91	14.79	300	4.6293(7)	13.132(2)	243.72(4)
3.9590(3)	4.0947(3)	19.47	16.01	300	4.6247(6)	13.122(2)	243.06(3)
3.9543(4)	4.0891(2)	20.47	16.93	300	4.6090(7)	13.102(3)	241.03(4)
3.9451(4)	4.0776(2)	22.48	18.86	300	4.5979(7)	13.074(3)	239.37(4)
3.9346(4)	4.0664(2)	24.87	20.80	300	4.5888(8)	13.043(3)	237.86(5)
3.9644(3)	4.0906(2)	21.80	19.47	800	4.6116(9)	13.129(1)	241.80(5)
3.9606(3)	4.0867(2)	21.19	18.91	600	4.6094(7)	13.114(3)	241.30(4)
3.9546(2)	4.0810(2)	20.40	18.28	300	4.6056(7)	13.106(3)	240.76(4)
3.9485(2)	4.0752(2)	21.73	19.27	300	4.5986(7)	13.090(3)	239.73(4)
3.9585(2)	4.0827(1)	23.00	20.78	800	4.6075(7)	13.099(3)	240.83(4)
3.9542(3)	4.0792(2)	22.53	20.17	600	4.6092(8)	13.081(3)	240.68(4)
3.9487(3)	4.0746(2)	21.68	19.37	300	4.5963(8)	13.099(3)	239.65(5)
3.9363(3)	4.0626(2)	24.48	21.48	300	4.5921(7)	13.049(3)	238.31(4)
3.9500(3)	4.0734(2)	24.80	22.37	800	4.6040(7)	13.063(3)	239.79(4)
3.9462(3)	4.0704(2)	24.26	21.68	600	4.5940(8)	13.084(3)	239.14(5)
3.9450(3)	4.0680(2)	22.50	20.52	300	4.5929(7)	13.075(3)	238.87(4)
3.9707(3)	4.0920(1)	22.64	21.12	1100	4.6396(7)	13.135(2)	244.87(5)
3.9690(3)	4.0891(1)	21.92	20.65	950	4.6374(7)	13.132(2)	244.58(4)
3.9662(2)	4.0863(1)	21.43	20.18	800	4.6298(6)	13.135(2)	243.83(4)
3.9617(2)	4.0825(1)	20.96	19.61	600	4.6280(7)	13.121(3)	243.38(4)
3.9568(2)	4.0778(2)	19.93	18.82	300	4.6247(6)	13.113(2)	242.89(4)
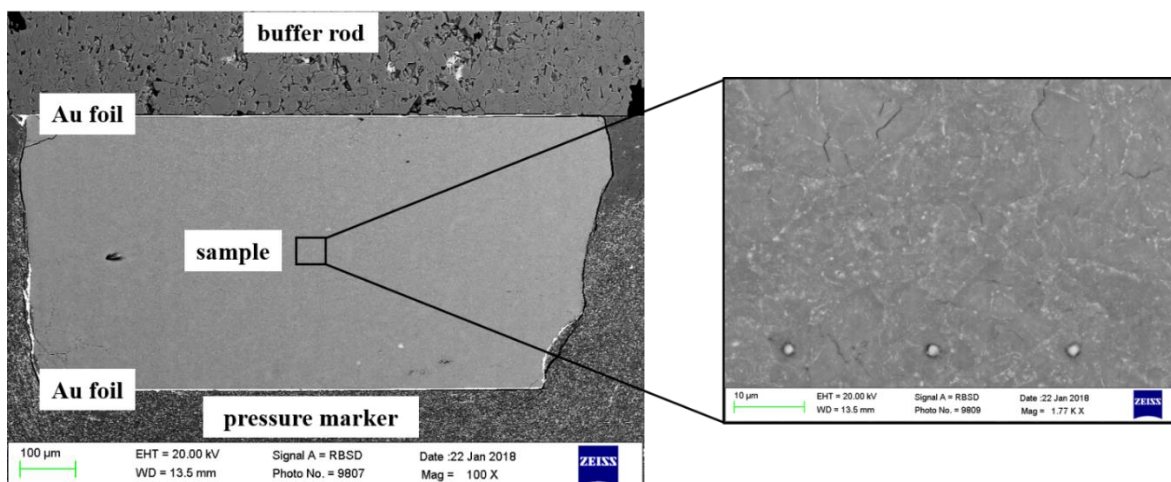
Figure 5-3: *Electron backscattering image of the multi-anvil assembly after the high pressure and temperature ultrasonic experiment. Zooming inside the sample reveals that secondary phases were formed possibly during the high temperature cycle that was performed at 1100 K. The three white spots in the zoomed-in image represent sample damage from the electron beam during EMP analyses.*
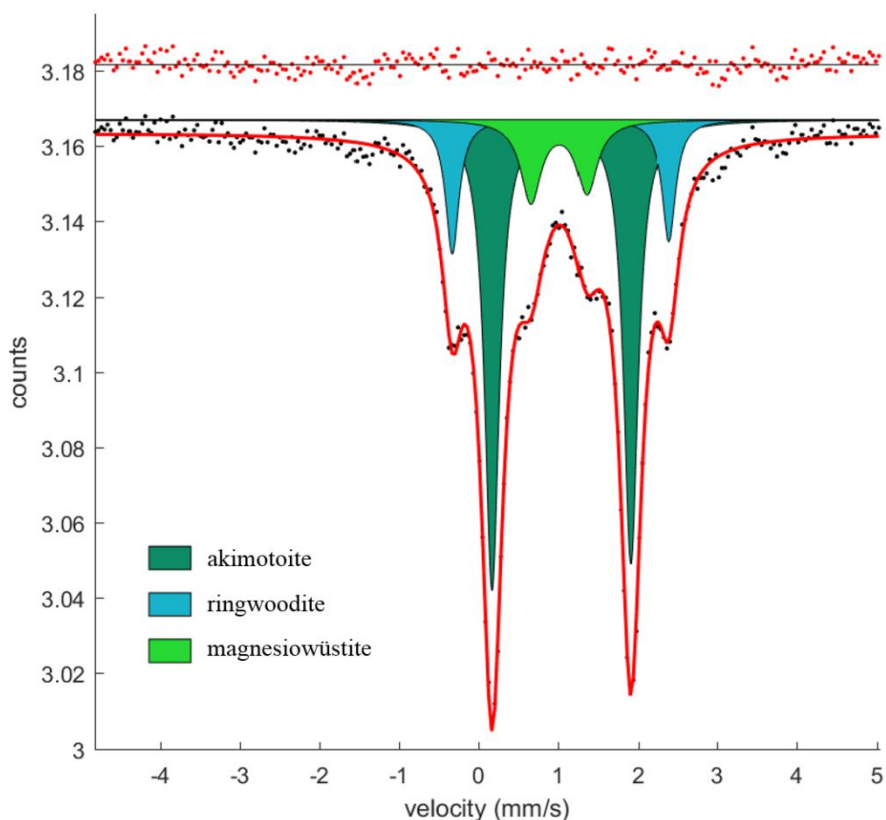
Figure 5-4: *Mössbauer spectrum of the Fe-bearing akimotoite sample after the synchrotron experiment. The dark green doublet (68(1) %) is attributed to Fe^{2+} at the octahedral site of akimotoite, the blue doublet most likely represents Fe^{2+} at the octahedral site of ringwoodite and the bright green doublet has characteristic IS and QS for Fe^{2+} in magnesiowüstite.*

The blue doublet with a IS 1.027(7) of and a QS of 2.72(2) represents most likely the Fe^{2+} in the octahedral site of ringwoodite (Lyubutin et al. 2013) and correspond to 17(1) % of the total Fe. The light green doublet has IS and QS values of 1.01(1) and 0.70(3), representative of Fe^{2+} at the octahedral site of magnesiowüstite (e.g. McCammon et al. 2004, Otsuka et al. 2010) and corresponds to 16(1) % of the total Fe in the sample. The phase diagram of Fe-bearing akimotoite (Figure 1-7) confirms that the possible additional phases are ringwoodite and magnesiowüstite although at higher pressures relative to the conditions applied during the synchrotron experiment or for a higher $FeSiO_3$ content. This implies that the single-phase stability field of Fe-bearing akimotoite is even smaller than assumed by Ito and Yamada (1982) who reported that at a temperature of 1373 K, akimotoite containing 10 mol.% FeO is stable at least up to ~24-25 GPa. The composition of akimotoite recovered after the synchrotron experiment and determined from the Mössbauer spectrum is $Mg_{0.93}Fe_{0.07}SiO_3$ i.e. it contains 0.03 atoms per formula unit less than the starting composition of $Mg_{0.9}Fe_{0.1}SiO_3$. This change in composition results in a negligible change of the unit-cell lattice parameters explaining why it was not possible to identify the transformation using EDXRD.

The compressional and shear wave velocities of Fe-bearing akimotoite (Fe10) at room temperature are shown in Figure 5-5 in comparison to the wave velocities of the akimotoite end-member determined using Brillouin spectroscopy (Chapter 3) and ultrasonic interferometry (Zhou et al. 2014) as well as of the Al-bearing akimotoites (Chapter 4.2). Fe-bearing akimotoite has slower compressional and shear wave velocities relative to the $MgSiO_3$ end-member and comparable to the velocities of Ak80. As for the Al-bearing akimotoite samples, the room temperature data were fitted using the third-order finite strain equations derived from the expression of Davies and Dziewonski (1975) as described in chapter 2.8.7. The resulting adiabatic bulk and shear moduli and their first pressure derivatives are K_{S0} = 197(1) GPa, K' = 5.2(1), G = 121(1) GPa and G' = 1.5(1).

High-temperature data have been obtained during three heating cycles up to 800 K and one final heating cycle up to 1100 K (Figure 5-6). Shear wave velocities from the last heating cycle up to 1100 K may show some evidence for a change in the phase assemblage in from of a velocity increase by ~ 0.1 km/s at 600 and 800 K relative to the shear wave velocities collected during previous heating cycles at those temperatures. The secondary phases observed in the recovered

sample were therefore formed very likely only during the fourth heating cycle that was performed up to 1100 K at 22.6 GPa. Interestingly, no significant velocity difference was observed for the compressional wave velocities during the last heating cycle (Figure 5-6). All data, except for those collected during the last heating cycle were fitted using the Debye-Mie-Grüneisen equation of state after Stixrude and Lithgow-Bertelloni (2005) reported in chapter 2.8.8. As initial values for the bulk and shear moduli and their first pressure derivatives, the EoS parameters obtained by fitting the room temperature data were used. First, V_0, K_T, K', G and G' were let free to vary, then all elastic parameters were refined simultaneously to minimize the discrepancy between the experimental and calculated wave velocities. The resulting elastic parameters obtained are V_0 = 26.44 cm^3/mol, K_{T0} = 197(1) GPa, K' = 5.3(1), G = 123(1) GPa, G' = 1.4(1), γ = 1.19, q = 2.4 and η_S = 2.9.
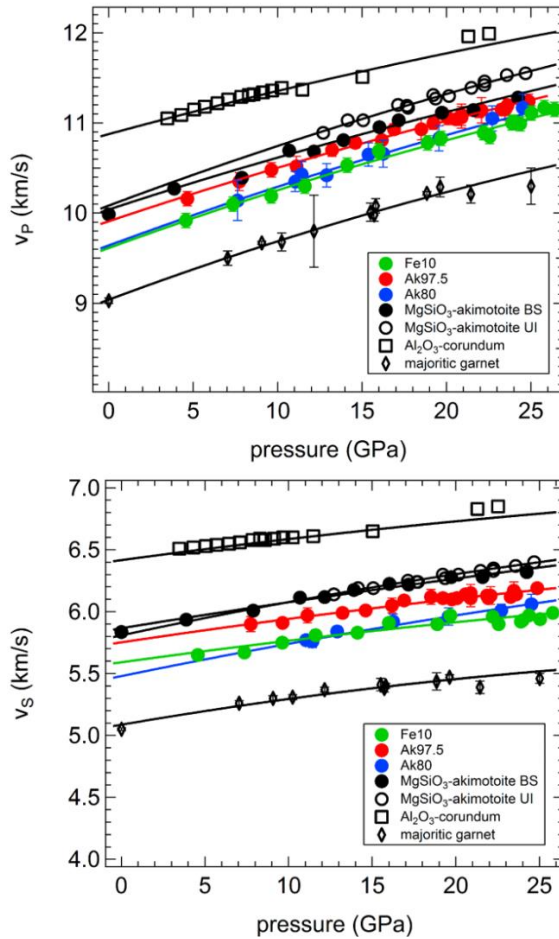
Figure 5-5: *Compressional (top) and shear (bottom) wave velocities of Fe-bearing akimotoite (Fe10, green) in comparison to the MgSiO₃ akimotoite end-member (black circles), Ak97.5 and Ak80 (red and blue, respectively). The wave velocities of Fe10 are slower with respect to the end-member and comparable to Ak80, however, with Ak80 having a different slope.*

Table 5-2: Compressional (v_P) and shear wave velocities (v_S) calculated from the travel time and sample length at different pressures and temperatures, as well as the density for the Fe10 akimotoite samples.

absolute P (GPa)	temperature (K)	density (g/cm³)	travel time (x10⁻⁹s)		sample length (x10⁻⁶ m)	v_p (km/s)	v_s (km/s)
T2082			P-wave	S-wave			
0.0001	300	3.9155(4)			511.40		
4.57	300	4.0025(5)	100.60	176.80	499.20	9.92(8)	5.65(4)
7.35	300	4.0517(6)	98.40	175.20	496.80	10.10(8)	5.67(4)
9.62	300	4.0900(5)	96.80	171.60	493.20	10.19(8)	5.75(4)
11.61	300	4.1226(6)	95.53	169.40	492.00	10.30(8)	5.81(4)
14.11	300	4.1620(7)	93.00	168.00	489.60	10.53(8)	5.83(4)
15.99	300	4.1908(7)	91.40	165.20	488.40	10.69(8)	5.91(4)
18.88	300	4.2335(7)	90.60	165.47	488.40	10.78(8)	5.90(4)
19.67	300	4.2449(6)	90.40	164.00	489.60	10.83(8)	5.97(4)
22.20	300	4.2807(7)	89.67	163.80	488.40	10.89(8)	5.96(4)
24.36	300	4.3104(7)	88.20	162.40	484.80	10.99(8)	5.97(4)
26.40	300	4.3377(8)	87.40	162.30	487.20	11.15(8)	6.00(4)
23.17	800	4.2669(9)	91.20	167.87	487.20	10.68(8)	5.80(4)
22.95	600	4.2758(7)	90.20	165.93	486.00	10.78(8)	5.86(4)
22.55	300	4.2855(7)	89.60	164.80	486.00	10.85(8)	5.90(4)
23.88	300	4.3038(7)	89.00	165.40	489.60	11.00(8)	5.92(4)
24.40	800	4.2842(7)	90.20	166.60	486.00	10.78(8)	5.83(4)
23.74	600	4.2869(7)	89.50	165.60	486.00	10.86(8)	5.87(4)
23.98	300	4.3052(8)	88.90	165.20	489.60	11.01(8)	5.93(4)
25.79	300	4.3295(7)	88.50	165.20	494.40	11.17(8)	5.99(4)
25.74	800	4.3028(7)	89.27	165.93	484.80	10.86(8)	5.84(4)
25.74	600	4.3144(8)	88.80	166.50	489.60	11.03(8)	5.88(4)
25.03	300	4.3194(8)	88.60	165.60	492.00	11.11(8)	5.94(4)
21.12	1100	4.2134(8)	92.80	168.93	487.20	10.50(8)	5.77(4)
20.72	950	4.2185(7)	91.33	166.53	481.20	10.54(8)	5.78(4)
20.88	800	4.2315(7)	92.07	166.33	489.60	10.64(8)	5.89(4)
20.48	600	4.2393(7)	91.30	164.53	490.80	10.75(8)	5.97(4)
19.87	300	4.2479(7)	90.33	164.00	489.60	10.84(8)	5.97(4)
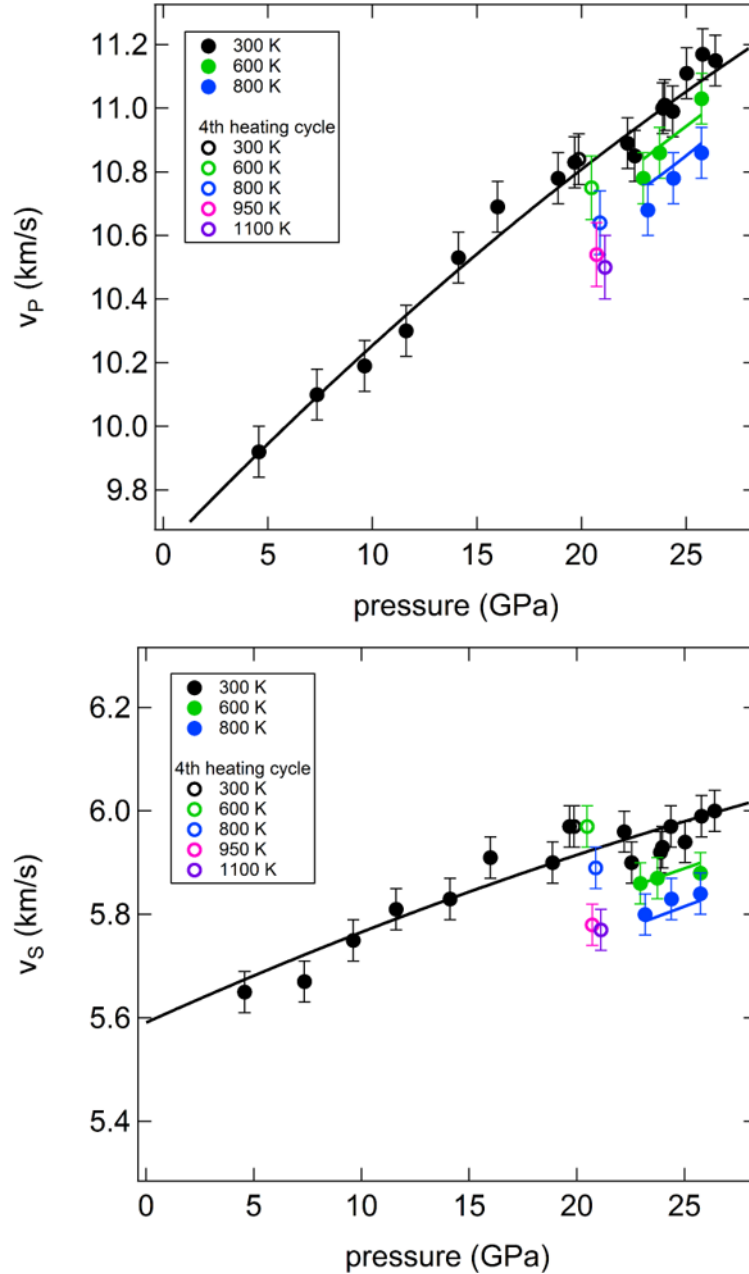
Figure 5-6: *Compressional (top) and shear (bottom) wave velocities of Fe-bearing akimotoite (Fe10) up to a temperature of 800 K. Four heating cycles were performed during the synchrotron experiment T2082. The shear wave velocities obtained during the 4th heating cycle appear faster relative to the velocities of the previous three heating cycles likely due to partial transformation of the sample.*

5.3 The influence of Fe and Al substitution on the wave velocities of akimotoite

Two synchrotron experiments T2267 and T2452 were conducted for samples containing 10 mol.% FeO and 10 mol.% Al_2O_3 (Fe10Al10) (Table 2-1). Ultrasonic measurements, X-ray diffraction and X-ray radiography were performed up to a maximum pressure of 23 GPa for T2267 and T2452. Au and MgO were used as pressure markers (Tsuchiya 2003, Dewaele et al. 2000). The unit-cell parameters of Au and MgO, their corresponding calculated pressure and the unit-cell parameters of Fe10Al10 akimotoite are reported in Table 5-3. The travel times, sample lengths as well as the compressional and shear wave velocities obtained are reported in Table 5-4. Both experiments could be recovered after the synchrotron experiment and investigated using XRD, SEM and EMP. No change in composition or texture could be observed (Figure 5-7).

The compressional and shear wave velocities at room temperature are shown in Figure 5-8. The wave velocities of Fe10Al10 are much slower than those of the $MgSiO_3$ end-member and even slower than any of the Fe- or Al-bearing akimotoite samples studied in the previous sections. Both v_P and v_S are similar to the wave velocities of majoritic garnet. Fitting of the room temperature data using the third-order finite strain equations derived from Davies and Dziewonski (1975) resulted in the following elastic parameters: $K_{S0} = 171(1)$ GPa, $K' = 5.4(1)$, $G = 103(1)$ GPa and $G' = 1.5(1)$.

High-temperature data were only obtained for run T2267, at 5.7 and 19 GPa and 573 K (Figure 5-9). For the fitting procedure following the Debye-Mie-Grüneisen equation of state after Stixrude and Lithgow-Bertelloni (2005) the elastic parameters obtained at room temperature were used as initial values and refined again first. Then the high-temperature parameters reported in Stixrude and Lithgow-Bertelloni (2005) for Fe-bearing akimotoite were initially used and q was fixed to 1.0. The fitting resulted in the following elastic parameters: $V_0 = 26.52$ cm^3/mol, $K_{T0} = 174(1)$ GPa, $K' = 5.0(1)$, $G = 102(1)$ GPa, $G' = 1.5(1)$, $\gamma = 1.1$ and $\eta_S = 3.8$. The fitting of the room temperature data is plotted in Figures 5-8 and 5-9.
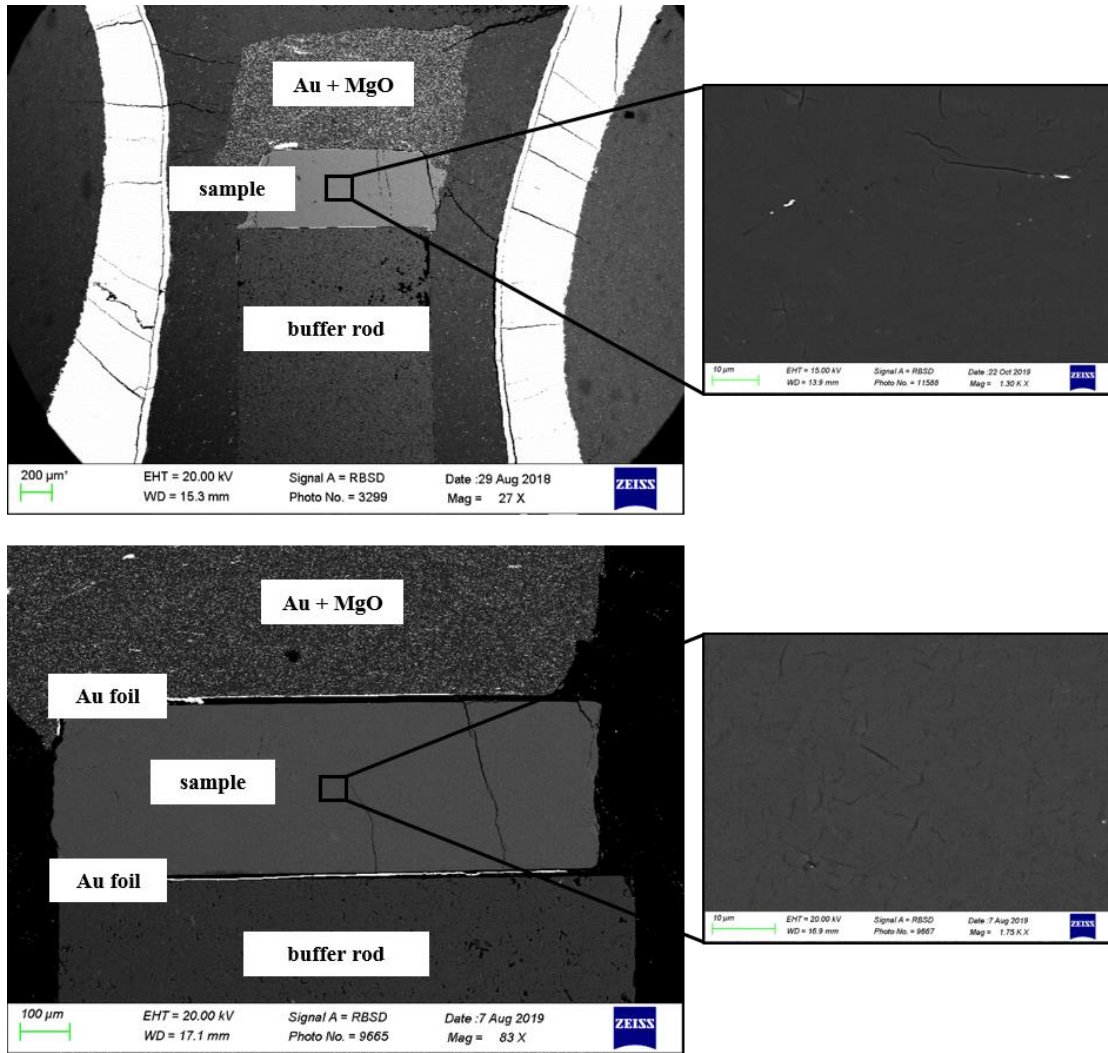
Figure 5-7: *Recovered experiments T2267 (top) and T2452 (bottom) for sample Fe10Al10. The samples appear very homogeneous and no change in texture or composition was observed after the high pressure synchrotron experiments.*

Table 5-3: *Unit-cell lattice parameters of the pressure marker Au and MgO, calculated pressures following Tsuchiya (2003) and Dewaele et al. (2000), respectively, and unit-cell lattice parameters of the Fe10Al10 akimotoite samples from two experimental runs T2267 and T2452.*

a_{Au} (Å)	a_{MgO} (Å)	Au P (GPa)	MgO P (GPa)	temperature (K)	a_{aki} (Å)	c_{aki} (Å)	V_{aki} (Å^3)
			T2267				
4.0788(2)	4.2103(1)	0.00	0.00	300	4.7535(3)	13.502(1)	264.22(2)
4.0199(3)	4.1626(3)	8.28	5.89	300	4.6879(4)	13.260(2)	252.37(3)
4.0585(3)	4.1971(2)	4.30	2.75	573	4.7183(5)	13.383(2)	258.03(4)
4.0465(3)	4.1874(2)	4.24	2.72	300	4.7103(4)	13.335(2)	256.22(3)
3.9986(2)	4.1353(2)	11.88	9.66	300	4.6699(5)	13.192(2)	249.14(3)
3.9821(3)	4.1192(2)	14.89	12.02	300	4.6509(5)	13.124(2)	245.85(3)
3.9715(3)	4.1061(2)	16.96	14.04	300	4.6404(4)	13.078(2)	243.88(3)
3.9604(3)	4.0942(2)	19.21	15.93	300	4.6332(4)	13.061(2)	242.80(3)
3.9480(3)	4.0795(2)	21.88	18.37	300	4.6122(5)	13.025(2)	239.95(3)
3.9679(3)	4.0950(2)	19.55	17.24	573	4.6353(5)	13.069(2)	243.18(3)
3.9618(2)	4.0906(2)	18.93	16.52	300	4.6319(4)	13.064(2)	242.73(3)
3.9495(2)	4.0788(2)	23.40	19.92	300	4.6153(5)	13.026(2)	240.30(3)
3.9394(3)	4.0672(2)	25.64	21.92	300	4.6043(6)	12.998(2)	238.63(4)
			T2452				
4.0786(3)	4.2136(2)	0.00	0.00	300	4.7533(2)	13.495(1)	264.06(2)
4.0170(3)	4.1456(3)	10.69	10.10	300	4.7036(6)	13.269(2)	254.23(4)
4.0022(3)	4.1286(3)	13.15	12.55	300	4.6871(5)	13.206(2)	251.26(4)
3.9919(4)	4.1165(4)	14.96	14.36	300	4.6709(6)	13.165(2)	248.75(4)
3.9755(4)	4.0944(3)	18.02	17.85	300	4.6505(6)	13.094(2)	245.24(4)
3.9570(6)	4.0757(4)	21.75	20.99	300	4.6251(6)	13.038(2)	241.54(4)
3.9376(6)	4.0532(5)	26.01	25.00	300	4.6055(7)	12.985(3)	238.52(4)
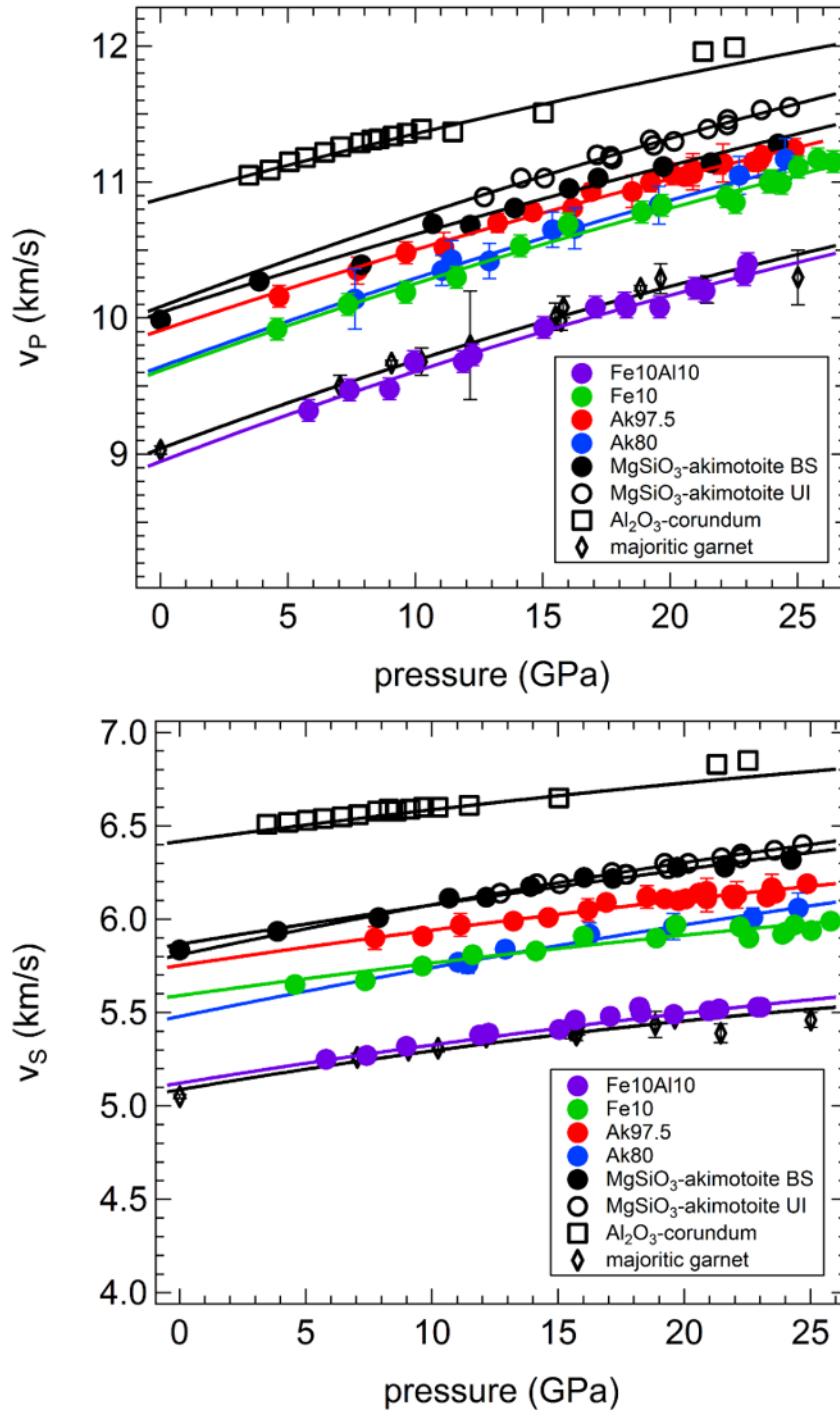
Figure 5-8: *Compressional and shear wave velocities of Fe- and Al-bearing akimotoite (Fe10Al10, purple) in comparison to the wave velocities of the end-member akimotoite (black circles), Al-bearing akimotoite (red, Ak97.5 and blue, Ak80) and Fe-bearing akimotoite (Fe10, green). Both v_P and v_S of Fe10Al10 are very similar to the wave velocities of majoritic garnet (Pamato et al. 2016).*

Table 5-4: *P- and S-wave travel times, sample lengths and resulting compressional and shear wave velocities of Fe10Al10 obtained during two synchrotron experiments (T2267 and T2452) as well as the corresponding densities.*

absolute P (GPa)	temperature (K)	density (g/cm³)	travel time (x10⁻⁹s)		sample length (x10⁻⁶ m)	v_p (km/s)	v_s (km/s)
			P-wave	S-wave			
T2267							
0.0001	300	3.9004(3)			540.78		
8.98	300	4.0835(5)	110.24	196.21	522.41	9.48(8)	5.32(4)
5.65	573	3.9940(5)	113.60	205.44	523.58	9.22(8)	5.10(4)
5.80	300	4.0221(5)	112.16	199.25	522.65	9.32(8)	5.25(4)
11.88	300	4.1364(5)	107.52	193.44	520.29	9.68(8)	5.38(4)
15.04	300	4.1917(5)	104.48	191.57	518.59	9.93(8)	5.41(4)
17.06	300	4.2256(5)	102.88	189.28	518.40	10.08(8)	5.48(4)
18.21	300	4.2444(5)	102.24	186.88	516.62	10.11(8)	5.53(4)
21.37	300	4.2949(5)	100.64	186.03	513.46	10.20(8)	5.52(4)
19.02	573	4.2378(5)	103.04	191.52	514.13	9.98(8)	5.37(4)
18.28	300	4.2456(5)	101.92	186.67	513.51	10.08(8)	5.50(4)
20.97	300	4.2886(6)	100.48	186.35	513.27	10.22(8)	5.51(4)
22.90	300	4.3186(7)	99.36	185.33	512.72	10.32(8)	5.53(4)
T2452							
0.0001	300	3.9027(3)			365.50		
7.41	300	4.0537(6)	70.72	127.20	334.89	9.47(8)	5.27(4)
9.95	300	4.1015(6)	66.56		322.29	9.68(8)	
12.24	300	4.1429(6)	64.00	115.65	311.49	9.73(8)	5.39(4)
15.67	300	4.2023(6)		113.34	309.69		5.46(4)
19.58	300	4.2666(6)	61.28	112.45	308.79	10.08(8)	5.49(4)
23.03	300	4.3206(7)	58.88	110.77	306.09	10.40(8)	5.53(4)
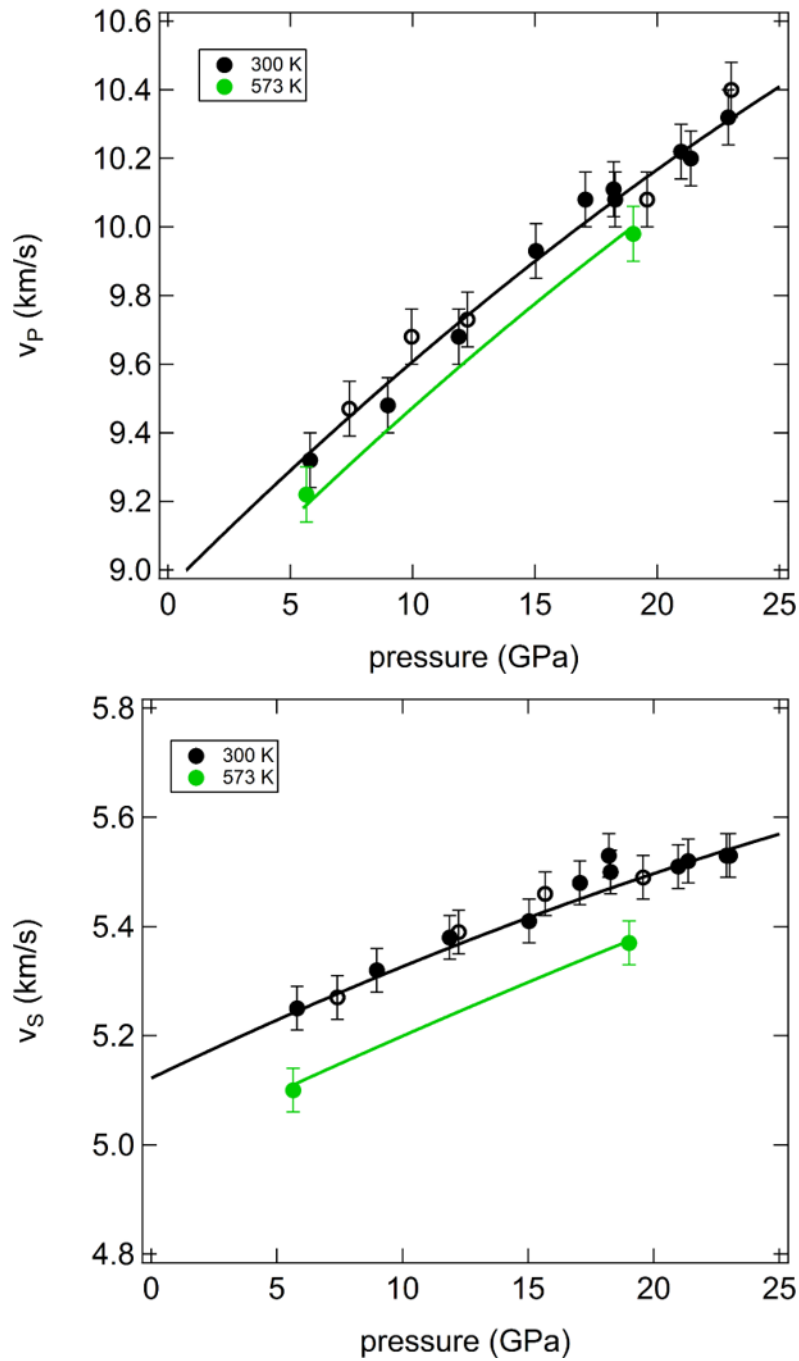
Figure 5-9: *Compressional and shear wave velocities of Fe10Al10 from two independent synchrotron experiments (solid: T2267, open: T2452) at room temperature and 573 K. Only two points at 573 K could be measured during experiment T2267 (green solid circles).*

5.4 The influence of Fe and Al on the axial and bulk compressibility of akimotoite

The normalized unit-cell parameters *a* and *c* for Fe10 and Fe10Al10 are plotted in Figure 5-10 as well as those of the akimotoite end-member. Linear BM3 EoS were used to describe the axial compressibility of Fe10 and Fe10Al10 and the resulting elastic parameters are reported in Table 5-5. The compressibility of the *a*-axis is majorly influenced by the substitution of Fe and Al and although the room pressure linear incompressibility are similar (the Fe10Al10 is slightly more compressible than the Fe10) the very low *M′* implies that both samples are more and more compressible with increasing pressure than the akimotoite end-member. Also the compressibility of the *c*-axis is very similar between the two samples and larger than for Ak100, however both Fe10 and Fe10Al10 have a large first pressure derivative and therefore their c-axes become stiffer with pressure. The anisotropy of compression is smaller than that of the end-member, however the structural reason for this decrease in anisotropy is likely different than that responsible for the anisotropic axial behavior of the Al-bearing akimotoites, since in the latter samples the a-axis become more compressible and the c-axis much stiffer with respect to the end-member. Structural analyses, however, are needed to characterize such behavior. The resulting *c/a* ratio of Fe10 (Figure 5-11) is comparable to the end-member at pressures below ~17 GPa but flattens out above ~17 GPa, likely due to the stiffening of the *c*-axis, whereas for the Fe10Al10 sample the variation with pressure of the c/a ratio is less pronounce, likely due to the smaller anisotropy of the axial compressibility of this sample.
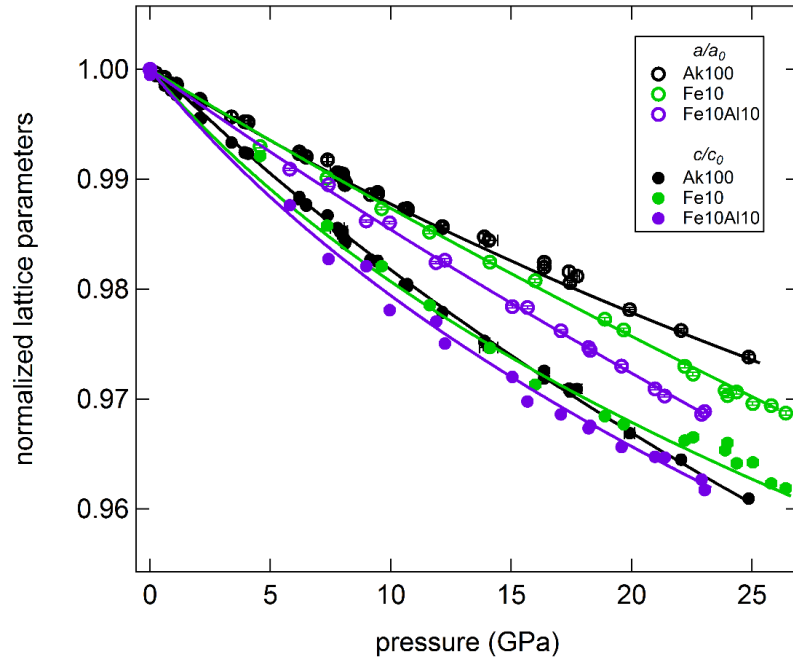
Figure 5-10: *Unit-cell a and c parameters of Fe10, Fe10Al10 and the MgSiO₃ end-member (Chapter 3) normalized with respect to their room pressure values. The solid lines represent the BM3 EoS fits through the individual data sets.*
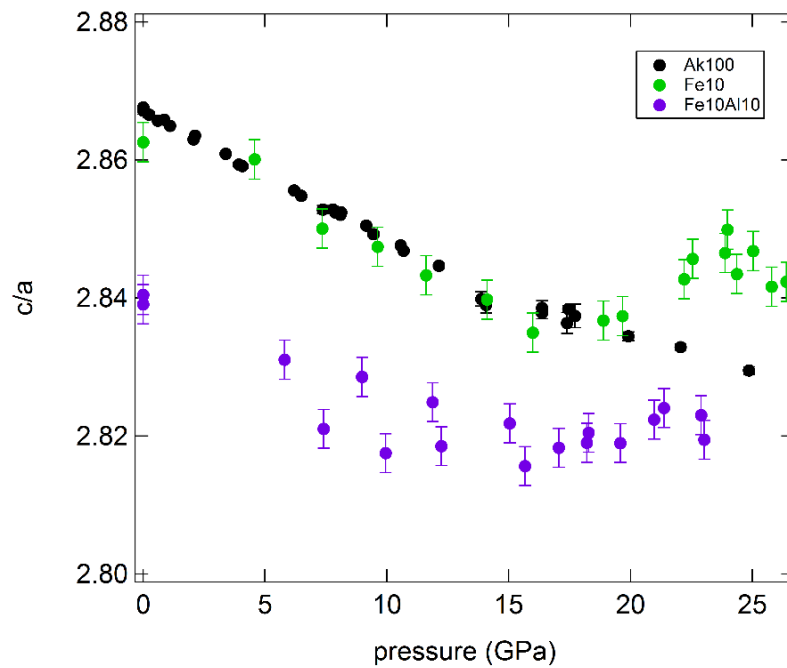
Figure 5-11: *c/a ratio of Fe10, Fe10Al10 and the MgSiO₃ end-member (Chapter 3). The c/a ratio of Fe10 and Fe10Al10 flatten out at high pressures likely because of the decrease in the anisotropy of the axial compressibility observed for both compositions.*

148

Table 5-5: *Linear BM3 EoS parameters for axial compressibility of Fe10 and Fe10Al10.*

	Fe10	Fe10Al10
a_0 (Å)	4.736(1)	4.7533(6)
M_0 (GPa)	756(30)	643(15)
M'	6(2)	8(2)
c_0 (Å)	13.57(1)	13.499(4)
M_0 (GPa)	391(50)	366(23)
M'	28(7)	27(5)

The major change in the compressibility of the *a*-axis of Fe10 and Fe10Al10 compared to that of the end-member leads to a pronounced change in bulk compressibility where Fe10Al10 is much more compressible than Fe10 or $MgSiO_3$ akimotoite (Figure 5-12) also indicated by the lower bulk moduli obtained from the wave velocities in Chapters 5.1 and 5.2. One difference is that the Fe in Fe10 was exclusively ferrous whereas in Fe10Al10 the majority of Fe was found to be ferric (Table 2-1). This can have a major influence on the substitution mechanism as already seen for the coupled substitution of Al for Mg and Si (Chapter 4.2). For Fe10, most likely all Fe^{2+} enters the Mg site whereas for Fe10Al10 a coupled substitution Fe^{3+} + Al replacing Mg + Si need to be considered. It is therefore possible that some of the Fe^{3+} enters the Si site increasing significantly the octahedral compressibility. Structural refinements on Fe- and Al-bearing akimotoite single-crystals are necessary to identify the cause of this change in compressibility.
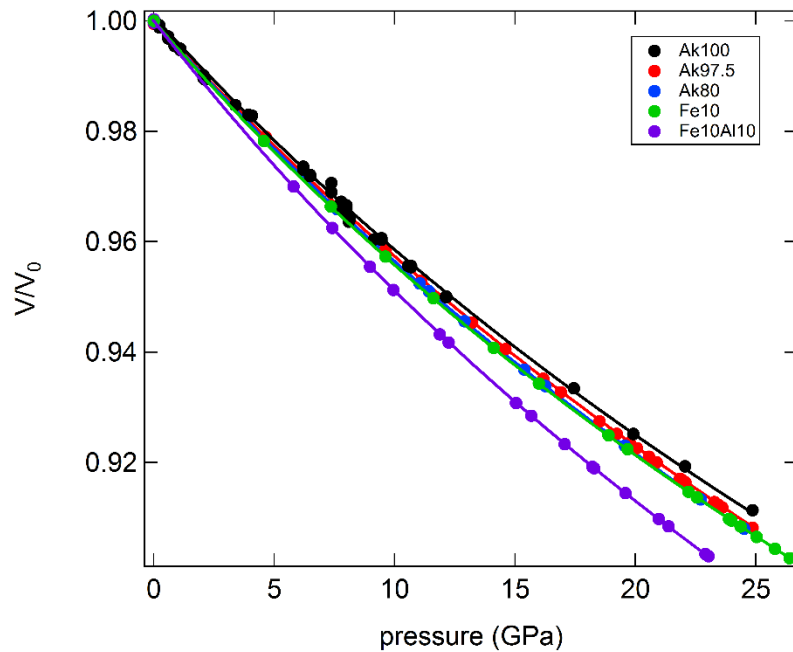
Figure 5-12: *Variation with absolute pressure of the unit-cell volumes of Fe10 and Fe10Al10 normalized with respect to their room pressure volumes. Fe10 and especially Fe10Al10 are more compressible than the akimotoite end-member. The solid lines represent BM3 EoS fits. The uncertainties are smaller than the symbol size.*

5.5 Absolute pressure determination

Absolute pressure of T2082 (Fe10), T2267 and T2452 (Fe10Al10) has been calculated and compared to the pressures obtained from the secondary pressure marker Au following the equations of state from Tsuchiya (2003) (Tables 5-1 and 5-3, Figure 5-13). The difference between absolute pressure and the pressure determined from the unit-cell parameter of Au is plotted versus absolute pressure in Figure 5-13. As for the Al-bearing akimotoite experiments, the absolute pressures are up to 2.5 GPa different from those calculated using the pressure marker for T2082 and T2267. The Au pressure in run T2452 instead is much larger ~ 2-3 GPa relative to the absolute pressure. These results suggest that using a secondary pressure marker in multi-anvil experiments may lead to large errors in the pressure determination.
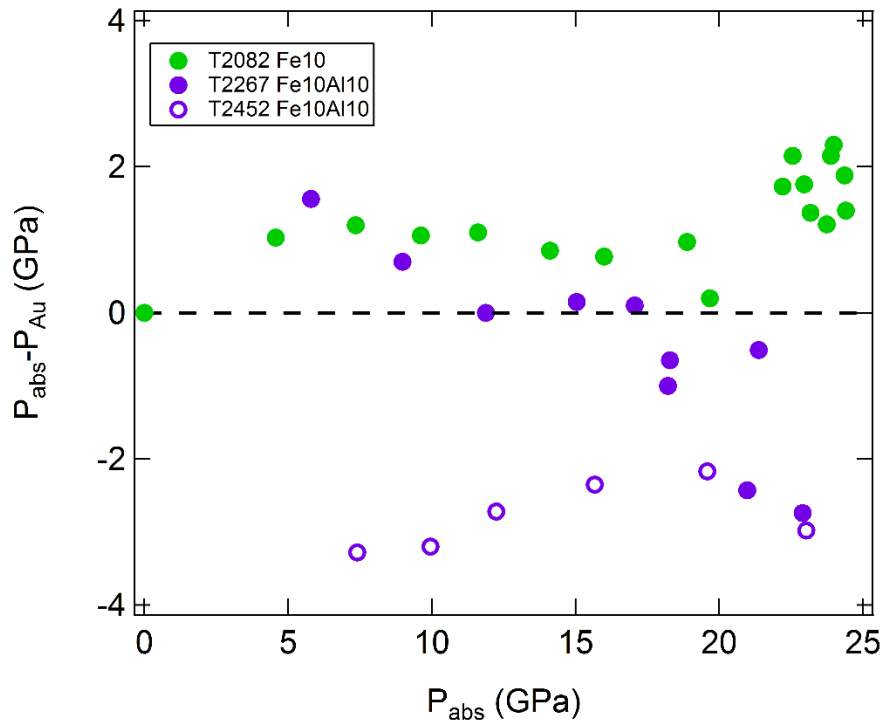
Figure 5-13: *Discrepancy between absolute pressure and the pressure in experiments T2082 (Fe10), T2267 and T2452 (Fe10Al10) obtained from the pressure marker Au using the EoS reported in Tsuchiya (2003). The discrepancy between absolute and Au pressure possibly arise due to deviatoric stresses on the relatively soft Au pressure marker.*

6. Velocity model for a harzburgite lithology at basal transition zone conditions

The principal objective of this thesis is to examine whether akimotoite can play a role in explaining the relatively high seismic velocities determined by seismic reference models (e.g. PREM and Ak135, see Chapter 1) for the base of the transition zone. Previous studies have shown that v_P and v_S estimated for typical mantle peridotite compositions are slower than seismic reference models between approximately 550 and 660 km depth (Irifune et al. 2008, Pamato 2014, Pamato et al. 2016). The only mineral phase that could potentially raise velocities at these depths is akimotoite as shown by Zhou et al. (2014) for the akimotoite end-member. Akimotoite has a limited stability field in fertile peridotite compositions but has been synthesized from harzburgitic compositions at depths of the lower transition zone. In this section, previous experimental studies on the stability field of akimotoite are first examined and a thermodynamic model is used to determine the proportion of akimotoite that forms from a harzburgitic composition at basal transition zone conditions. These phase relations are then used to estimate densities and seismic wave velocities for a harzburgite composition at the same conditions, which are then compared with seismic reference models and similar estimates made for basaltic (MORB) and fertile peridotite compositions. The consequences for the formation of mantle discontinuities are also examined.

6.1 Elastic parameters of akimotoite end-member compositions $MgSiO_3$, Al_2O_3 and $FeSiO_3$

In order to determine the properties of akimotoite within realistic mantle compositions a model is required that can describe these properties over the required compositional range. Experiments where akimotoite has been synthesised within mantle bulk compositions show that it contains relatively minor (<1 wt.%) concentrations of Cr, Ti, Na and Ca, which cannot significantly influence the elastic properties. Describing akimototite properties in the system $MgSiO_3$-Al_2O_3-$FeSiO_3$ should, therefore, be sufficient whereby the concentrations of Al_2O_3 and FeO in mantle akimotoite are unlikely to be greater than 10 wt.%. The bulk elastic properties of a mineral in a solid solution Ψ_{SS} can be described by a linear summation of individual elastic properties of the corresponding end-members assuming an ideal solid solution following

$$\Psi_{SS} = \frac{1}{\sum_{i=1}^{n} \frac{1}{m_i V_i} \sum_{i=1}^{n} \frac{m_i V_i}{\Psi_i}}$$

(eq. 48)

where Ψ_i are the elastic properties of component i, m_i and V_i are the mole and volume fraction of component i, respectively, and n is the amount of end-members in the solid solution (Chantel 2012). The assumption of such an ideal solid solution is problematic, however, as shown in the case of Al-bearing akimotoite since the wave velocities of Ak97.5 ($Mg_{0.977(11)}Al_{0.043(12)}Si_{0.980(8)}O_3$) and Ak80 ($Mg_{0.820(7)}Al_{0.405(7)}Si_{0.775(11)}O_3$) were clearly shown to not lie between those of the $MgSiO_3$ akimotoite and Al_2O_3 corundum end-members (Chapter 4.2) as had been previously assumed (Stixrude and Lithgow-Bertelloni 2005). Investigations of the unit-cell parameters and structural properties in the akimotoite-corundum solid solution (Chapter 4.1) confirmed that this solid solution is non-ideal and that very likely no complete mixing between the two end-members can occur. Therefore, the elastic properties of a fictive Al_2O_3 akimotoite end-member were derived from the experimental data that extend to an Al_2O_3 content of only 20 mol.%, but which more than covers the range expected in the mantle. The end-member properties were refined from these data using the thermo-elastic self-consistent model of Stixrude and Lithgow-Bertelloni (2005) in conjunction with the previously determined properties for the $MgSiO_3$ end-member and using equation (48) to determine the solid solution properties. For the substitution of Fe^{2+} replacing Mg in the akimotoite structure, the elastic properties of a fictive $FeSiO_3$ akimotoite end-member were also refined using the same model described in Chapter 2.8.8 and again assuming ideal behavior in the $MgSiO_3$-$FeSiO_3$ solid solution modeled using equation (48).

Firstly, the elastic properties of the $MgSiO_3$ akimotoite end-member were determined by fitting the compressional and shear wave velocities obtained from Brillouin spectroscopy (Chapter 3.3). Then, the elastic properties of the fictive Al_2O_3 akimotoite end-member were refined by fitting the two Al-bearing akimotoite data sets Ak97.5 and Ak80 (Chapter 4.2) at room temperature simultaneously and fixing those of the $MgSiO_3$ end-member. The high temperature elastic parameters proposed by Xu et al. (2008) for the Al_2O_3 end-member were found to be consistent with the high temperature data of Ak97.5. All eight parameters V_0, K_{T0}, K'_0, G_0, G'_0, γ_0, q_0 and η_{S0} for both $MgSiO_3$ and Al_2O_3 end-members are reported in Table 6-1. The wave velocities obtained for $MgSiO_3$ akimotoite, Ak97.5 and Ak80 calculated using the elastic parameters

refined for both end-members are shown in Figure 6-1 combined with the compressional and shear wave velocities obtained from Brillouin spectroscopy for Ak100 and ultrasonic interferometry for Ak97.5 and Ak80. The calculated compressional wave velocities are in excellent agreement with the measured velocities for all investigated compositions. The modelled shear wave velocities for Ak100 and Ak80 are as well in good agreement, however, are slightly faster than those measured for Ak97.5, which slightly exceed the uncertainties in a few instances. Nonetheless, the Al_2O_3 properties are derived from 2 independent data sets, which indicates that the linear behavior implied by equation (48) is sufficient for describing the variation in the elastic properties over this range of Al_2O_3 content.

The elastic properties of the $FeSiO_3$ akimotoite end-member were determined similarly by fixing the elastic properties of the end-member $MgSiO_3$ akimotoite and refining the eight parameters to the data set Fe10 (Chapter 5.2), by first refining the room temperature data set followed by the high temperature wave velocities. The resulting properties are reported in Table 6-1. The comparison between the calculated and measured wave velocities is shown in Figure 6-2 which are in excellent agreement.
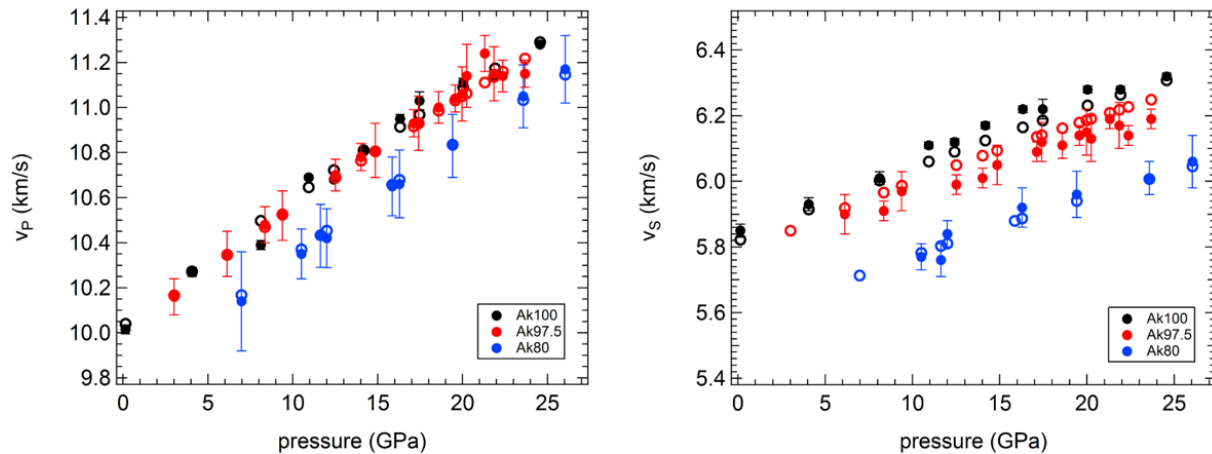
Figure 6-1: *Calculated (open symbols) and measured (solid symbols) compressional (left) and shear (right) wave velocities of Ak100, Ak97.5 and Ak80. The calculated and measured velocities are in excellent agreement, only the calculated shear wave velocities were determined to be slightly faster than the measured ones.*

Table 6-1: *Thermodynamic parameters for mineral end-members employed in the calculation of phase relations and seismic wave velocities. Akimotoite terms were refined in this study while the equation of state terms for garnet are taken from Pamato et al. (2016). Data for Ca-perovskite were fitted using the recent experimental results from Gréaux et al. (2019) and Thomson et al. (2019) and were used to update the velocities calculated for peridotite and MORB compositions. Values in bold are from Xu et al. (2008) and were found to be consistent with the experimental data for akimotoite obtained in this study and the experimental data of Pamato et al. (2016).*

	F_0 (kJ/mol)	V_0 (cm^3/mol)	K_0 (GPa)	K_0'	G_0 (GPa)	G'	γ_0	q	η_{s0}	θ_0 (K)
Akimotoite										
$MgSiO_3$	-1414	26.35	210	4.3	129	1.7	**1.19**	**2.4**	**2.8**	**928**
Al_2O_3	-1586	25.58	180	6.5	90	1.2	**1.32**	**1.3**	**2.8**	**933**
$FeSiO_3$		27.15	220	6.0	80	0.6	**1.19**	**2.4**	**3.2**	**856**
Garnet										
$Mg_3Al_2Si_3O_{12}$	**-5940**	**113.08**	171	4.2	**94**	**1.4**	**1.01**	1.4	1.2	804
$Mg_4Si_4O_{12}$	**-5686**	113.97	160	5.6	86	**1.4**	**0.98**	1.5	1.4	779
$Fe_3Al_2Si_3O_{12}$		**115.43**	175	3.7	**96**	1.1	**1.06**	1.4	**2.1**	**741**
$Ca_3Al_2Si_3O_{12}$		**125.12**	**167**	3.9	109	1.2	1.05	1.9	2.4	823
Ringwoodite										
Mg_2SiO_4		**39.49**	**185**	**4.2**	123	**1.4**	**1.11**	**2.4**	**2.3**	**891**
Fe_2SiO_4		**41.86**	**213**	**4.2**	92	**1.4**	**1.26**	**2.4**	**1.8**	**652**
Ca-Perovskite										
$Ca_4Si_4O_{12}$		10.98	229	4.5	131	1.46	1.6	2	2.3	800
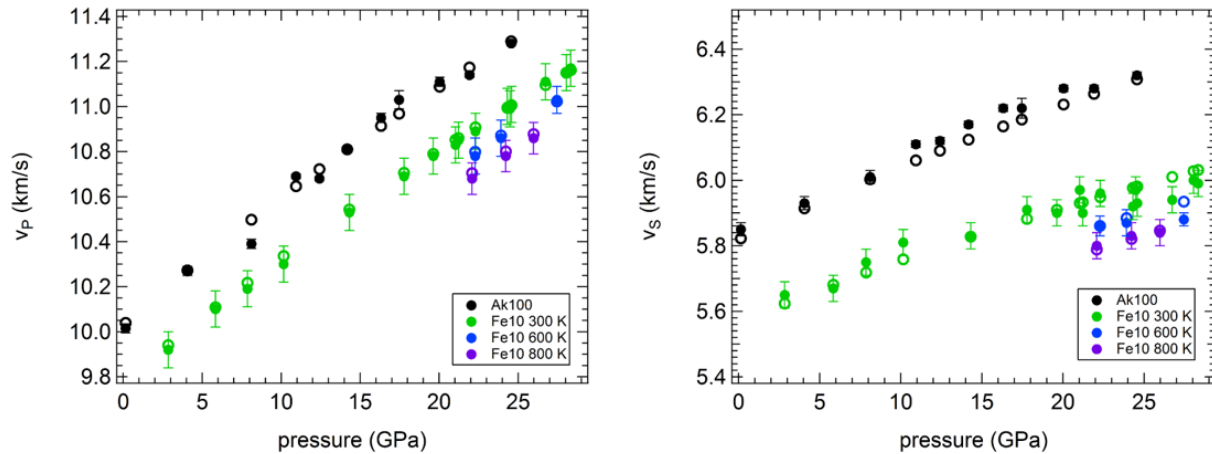
Figure 6-2: *Calculated (open symbols) and measured (solid symbols) compressional (left) and shear (right) wave velocities of Ak100 and Fe10 at 300 K, 600 K and 800 K. The calculated and measured velocities are in excellent agreement.*

6.2 Phase relations in akimotoite

The stability field of $MgSiO_3$ akimotoite can be seen to be bounded by majorite garnet at lower pressure and high temperature and bridgmanite at higher pressure as summarized in Figure 6-3. The conditions of the triple junction between these three phases varies between studies but is generally reported in the range between 20 to 23 GPa, with most studies proposing a temperature of approximately 2100 K (Ishii et al. 2011, Hirose et al. 2001, Yu et al. 2011, Hernández et al. 2015). The experimental study of Ishii et al. (2011) fits broadly in the midrange of these estimates and is also consistent with the phase relations of Kubo and Akaogi (2000) in the $MgSiO_3$-Al_2O_3 system. Furthermore, the pressure determinations by Ishii et al. (2011) are consistent with the recent in situ study of Ishii et al. (2018), where measures were taken to ensure accurate pressure determinations and complete agreement between bridgmanite formation and the depth of the 660 km discontinuity was found.
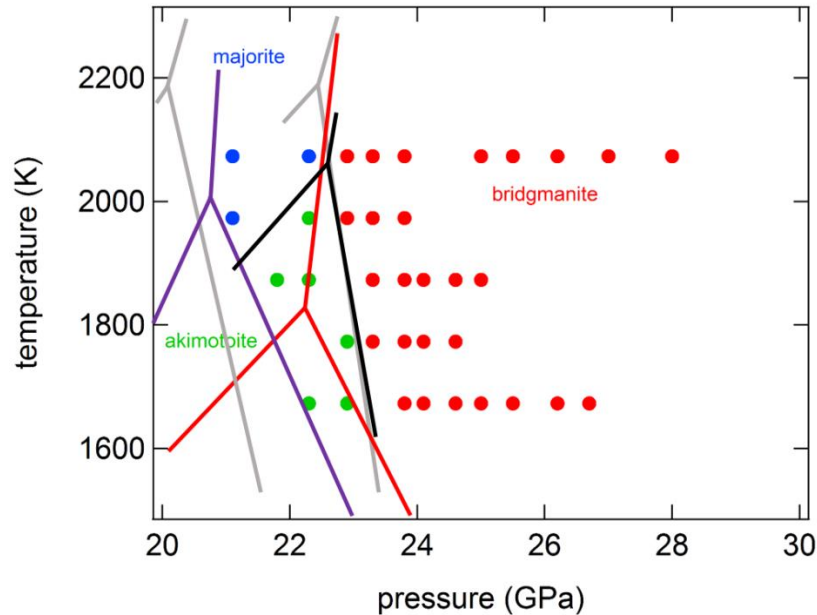
Figure 6-3: *Triple point phase relations of majorite, akimotoite and bridgmanite in the MgSiO₃*
system. Experimental data points are from Ishii et al. (2011) with the phase boundaries shown as
black lines. Grey phase boundaries are from in situ experiments of Hirose et al. (2001) using
either the Au equation of state of Anderson et al. (1989) (lower pressure) or Jamieson et al.
(1982) (higher pressure). Phase boundaries of Yu et al. (2011) and Hernández et al. (2015)
determined using first principles calculations are shown as red and purple curves, respectively.

Mantle adiabatic temperatures, which are in the region of 1900 K at the base of the transition
zone (Katsura et al. 2010), pass through the akimotoite stability field. In Al-bearing systems,
however, the field of majoritic garnet expands. In fertile peridotite bulk compositions, which
contain approximately 5 wt.% Al_2O_3 (Table 1-1), experiments indicate that only a very minor
akimotoite stability field occurs at the lower range of plausible adiabatic temperatures (e.g.
Hirose 2002). For more refractory mantle bulk compositions, however, such as harzburgite with
generally < 1 wt. % Al_2O_3 (Table 1-1), a significant akimotoite stability field has been reported in
experimental studies, although there is some disagreement on the exact pressure conditions of
this field, which will vary with the bulk composition but also strongly with temperature (Ishii et
al. 2011, 2019 and Hirose 2002). The experiments of Irifune and Ringwood (1987) and Zhang et
al. (2013) performed using a harzburgitic composition at temperatures between 1573 and 1773 K
indicate an akimotoite field between approximately 22 and 23 GPa where it comprises up to
10 vol.% of the assemblage. More recent experiments on the same composition by Ishii et al.
(2019) at 1873K, i.e. closer to adiabatic temperatures, indicate an akimotoite field between 19

and 21 GPa, which comprises up to 15 vol. % of the assemblage. In this case the stability field is lower than those proposed by studies in the $MgSiO_3$ system which, as shown later, cannot be due to other elements expanding the akimotoite stability field. In fact, the stability and proportion of akimotoite in Al-bearing systems will be determined essentially by the partitioning of Al between akimotoite and coexisting garnet (Irifune and Ringwood 1987, Akaogi et al. 2002).

6.2.1 Partitioning of Al between coexisting phases

As shown in Figure 6-4, existing experiments performed using complex bulk compositions such as peridotite and harzburgite provide very poor constraints on the Al contents of coexisting garnet and akimotoite and there appears to be very little consistency within or between the different studies (Irifune and Ringwood 1987, Ishii et al. 2011, 2019, Hirose 2002, Zhang et al. 2013). This is likely caused by sluggish kinetics of equilibration between the phases and also because the Al contents are strongly pressure and temperature dependent for which there are significant uncertainties at these conditions.
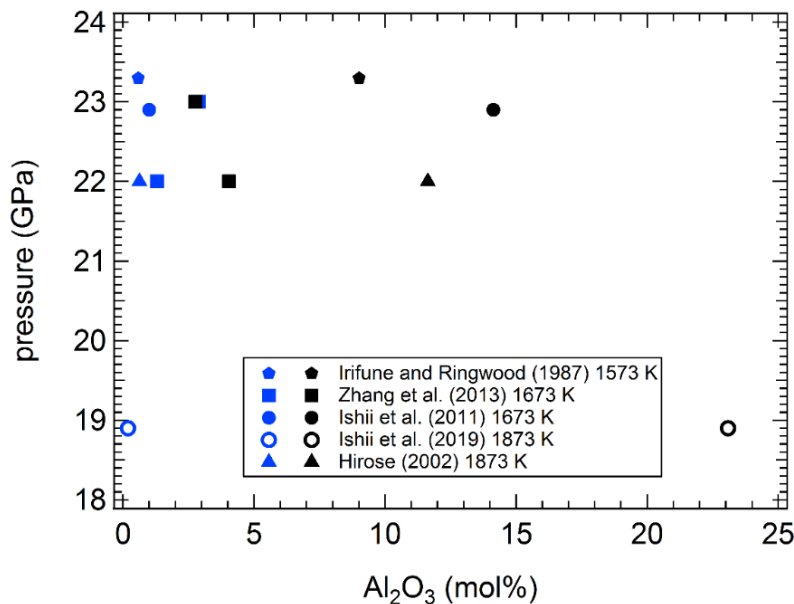
Figure 6-4: Coexisting akimotoite (blue) and majoritic garnet (black) compositions from experiments performed on peridotite and harzburgite compositions at temperatures between 1573 and 1873 K. The Al contents of coexisting garnet and akimotoite have very little consistency within or between the different studies (Irifune and Ringwood 1987; Zhang et al. 2013; Ishii et al. 2011, 2019; Hirose 2002).

A much clearer idea of akimotoite stability can be obtained from the phase equilibria experiments performed by Kubo and Akaogi (2000) in the $MgSiO_3$-Al_2O_3 system at 1873 K, which is close to adiabatic temperatures at depths of the lower transition zone. These experiments employed glassy starting compositions which crystallized to particular assemblages at different pressures. In Figure 6-5 these results are plotted with symbols that indicate the crystallized phases from each composition analyzed using X-ray diffraction. Grain sizes likely remained small in these experiments, which reduced diffusion distances and likely helped to promote the attainment of equilibrium. The extent of the akimotoite field in addition to the composition of coexisting garnet is relatively well constrained by these experiments. These phase relations will not change significantly through the addition of Fe or Ca to the system, because neither element partitions strongly into akimotoite (e.g. Hirose 2002, Ishii et al. 2011, Zhang et al. 2013), and therefore the results also provide good constraints on the stability of akimotoite even in more complex systems. Akaogi et al. (2002) fitted a thermodynamic model to these data but attempts to reproduce this model failed likely due to errors in the description.
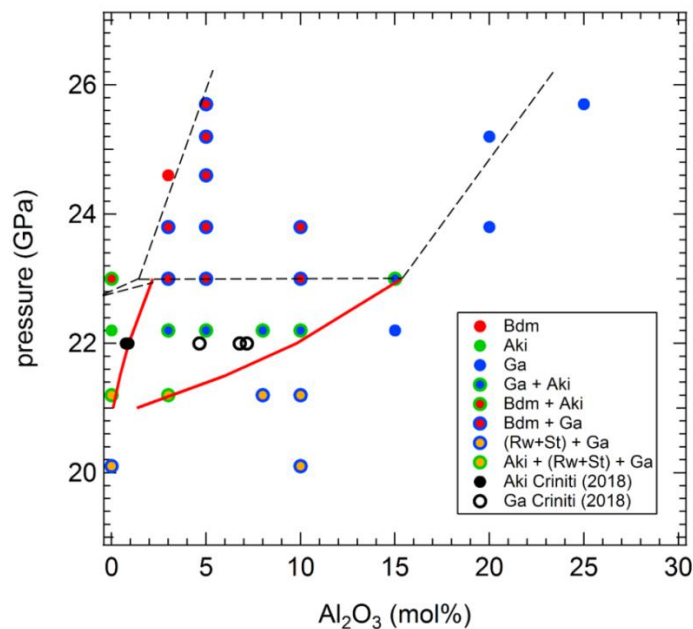
Figure 6-5: *Phase relations in the $MgSiO_3$-Al_2O_3 system determined by Kubo and Akaogi (2000) at 1873 K are shown by the symbols that indicate the bulk Al compositions from which the different phase assemblages crystallized. Black circles indicate actual measured compositions of akimotoite (solid) and garnet (open) found to coexist in experiments performed on $Mg_{0.9}Fe_{0.1}Al_{0.05}Si_{0.95}O_3$ + 1 wt.% H_2O and ($Mg_{0.95}Fe_{0.05}Al_{0.025}Si_{0.975}O_3$ + 1 wt.% H_2O bulk compositions (Criniti 2018). The red curves indicate the results of a thermodynamic model describing the Al_2O_3 contents of coexisting akimotoite and garnet.*

Instead a new model was obtained from these phase relations, and those reported by Ishii et al. (2011) for the MgSiO$_3$ end-member, using the thermodynamic formalism of Stixrude and Lithgow-Bertelloni (2011) and employing the equation of state data for MgSiO$_3$ and Al$_2$O$_3$ akimotoite determined in this study as described in Chapter 6.1. This model in the MgSiO$_3$-Al$_2$O$_3$ system provides the basis for determining the stability and proportion of akimotoite in a harzburgitic composition.

To describe MgSiO$_3$-Al$_2$O$_3$ mixing between the two coexisting solid solutions, the equilibria

$$\text{Mg}_4\text{Si}_4\text{O}_{12}\ (\text{garnet}) = 4\text{MgSiO}_3\ (\text{akimotoite}) \qquad \text{(eq. 49)}$$

and

$$\text{Mg}_3\text{Al}_2\text{Si}_3\text{O}_{12}\ (\text{garnet}) = 3\text{MgSiO}_3\ (\text{akimotoite}) + \text{Al}_2\text{O}_3\ (\text{akimotoite}) \qquad \text{(eq. 50)}$$
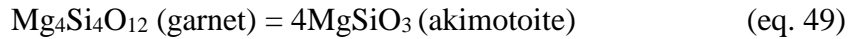
are employed for which two conditions of equilibrium can be defined:

$$\Delta G^{\circ}_{[49]} = -RT ln \frac{\left[a^{Ak}_{MgSiO_3}\right]^4}{\left[a^{Gt}_{Mg_4Si_4O_{12}}\right]} \qquad \text{(eq. 51)}$$

and

$$\Delta G^{\circ}_{[50]} = -RT ln \frac{\left[a^{Ak}_{MgSiO_3}\right]^3 \left[a^{Ak}_{Al_2O_3}\right]}{\left[a^{Gt}_{Mg_3Al_2Si_3O_{12}}\right]} \qquad \text{(eq. 52)}$$

$\Delta G^{\circ}_{[49]}$ and $\Delta G^{\circ}_{[50]}$ describe the standard state Gibbs free energy change for equilibrium (49) and (50), respectively, at the pressure and temperature of interest. $a^{Ak}_{MgSiO_3}$ is the activity of the MgSiO$_3$ component in akimotoite, $a^{Ak}_{Al_2O_3}$ is the activity of the Al$_2$O$_3$ component in akimotoite, $a^{Gt}_{Mg_4Si_4O_{12}}$ is the activity of the majorite component in garnet and $a^{Gt}_{Mg_3Al_2Si_3O_{12}}$ is the activity of the pyrope component in garnet. In agreement with Akaogi et al. (2002), ideal mixing is assumed for both solid solutions. For the garnet solid solution, locally ordered replacement of AlAl by

MgSi is assumed to occur on the octahedral site, which means, for example, that $a^{Gt}_{Mg_4Si_4O_{12}}$ is equal to the mole fraction of $Mg_4Si_4O_{12}$ in the solid solution. For akimotoite, the locally ordered replacement of $MgSiO_3$ by Al_2O_3 is assumed which means that $a^{Ak}_{MgSiO_3}$ equates to the mole fraction of $MgSiO_3$ in the solid solution. Values of $\Delta G°$ of akimotoite and majorite garnet end-members at the pressure (P) and temperature (T) of interest were determined using the equations of Stixrude and Lithgow-Bertelloni (2005, 2011) who use a Mie-Grüneisen type equation of state as described in Appendix A2.

All parameters used are reported in Table 6-1. For akimotoite, the equation of state terms used were those refined in this study (see section 6.1). For garnet, the equation of state data of Pamato et al. (2016) were used but values of F_0 were assumed from Xu et al. (2008). In order to match the pressure of equilibrium (49) determined by Ishii et al. (2011) the value of F_0 initially proposed by Xu et al. (2008) for $MgSiO_3$ akimotoite was decreased by 4 kJ/mol. F_0 for Al_2O_3 akimotoite was also lowered by 4 kJ/mol in order to match the Al content of garnet for the highest pressure occurrence of akimotoite in the results of Kubo and Akaogi (2000). The phase diagram shown in Figure 6-5 (red lines) was then calculated by simultaneously solving equations (51) and (52) to determine the Al contents of the coexisting akimotoite and garnet phases. The calculation reproduces the phase relations of Kubo and Akaogi (2000) very well, particularly given that only two parameters have been adjusted and the remaining terms are provided by equation of state data derived completely independently (Table 6-1). For comparison coexisting compositions obtained by Criniti (2018) from a hydrated composition designed to grow large crystals of akimotoite are also shown (Figure 6-5). Although these data are not in perfect agreement at the pressure estimated for these quenched experiments of 22 GPa, the agreement with the thermodynamic model becomes better once a pressure uncertainty of at least 0.5 GPa is taken into consideration. As can be seen from the thermodynamic model, phase equilibria experiments are only effective at determining the phase relations if the pressures can be determined very accurately. The coexisting Al concentrations also are strongly dependent on temperature which further raises challenges for the experimental determination of these phase relations.

The stability of akimotoite in more complex systems can also be understood from this phase diagram. A fertile peridotite composition contains approximately 5 mol.% Al_2O_3 but because

ringwoodite takes little Al_2O_3, the phase relations of the remaining phases akimotoite and garnet are equivalent to crossing the two phase region in Figure 6-5 at a composition of approximately 11 mol.% Al_2O_3. At this composition the akimotoite field occurs only over a small pressure interval of approximately 0.8 GPa and the proportion of akimotoite formed would be at most one fifth of that of garnet. For a harzburgite composition containing < 1 mol.% Al_2O_3, once ringwoodite is removed the remaining system contains approximately 3 mol.% Al_2O_3 which implies a stability field for akimotoite that extends over approximately 2 GPa and a proportion that dominates that of garnet over most of this pressure interval.

6.2.2 Partitioning of Fe between coexisting phases

To make a more accurate assessment of the proportion and composition of akimotoite in a harzburgite composition, information on the interphase partitioning of Fe and Mg is required. The Fe-Mg exchange coefficient $K_{D\,Fe-Mg}^{Ak-Rw}$ between akimotoite and ringwoodite for example is defined as

$$K_{D\,Fe-Mg}^{Ak-Rw} = \frac{X_{Fe}^{Ak} X_{Mg}^{Rw}}{X_{Fe}^{Rw} X_{Mg}^{Ak}}$$

(eq. 53)

where X_{Fe}^{Ak} is the mole fraction of iron (for this model assumed to be all Fe^{2+}) in akimotoite i.e. the molar ratio of $Fe^{2+}/(Fe^{2+}+Mg)$ and X_{Fe}^{Rw} describes the mole fraction of Fe in ringwoodite, accordingly. X_{Mg}^{Ak} is the mole fraction of Mg in akimotoite (i.e. $Mg/(Fe^{2+}+Mg)$) and X_{Mg}^{Rw} is the mole fraction of Mg in ringwoodite. Figure 6-6 shows values for the Fe-Mg K_D between garnet and ringwoodite and akimotoite and ringwoodite determined from previous experimental studies (Irifune and Ringwood 1987; Hirose 2002; Ishii et al. 2011; Zhang et al. 2013). Although in many of these experiments the Al concentration between phases likely did not reach equilibrium Fe-Mg exchange should be much faster. Fe-Mg K_D values of approximately 0.8 for exchange between garnet and ringwoodite are assumed and in very good agreement with other studies (e.g. Frost 2003). The Fe-Mg K_D between akimotoite and ringwoodite appears to be temperature dependent and reaches a value of approximately 0.3 at temperatures of 1873 K.
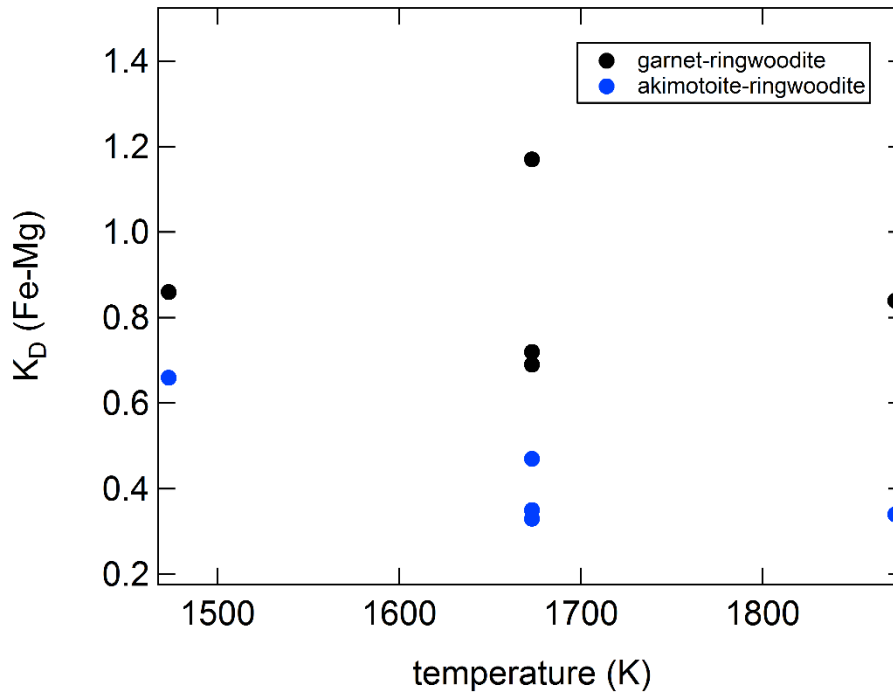
Figure 6-6: *The Fe-Mg exchange coefficient K_D determined for garnet-ringwoodite and akimotoite-ringwoodite from the experiments of Irifune and Ringwood (1987), Hirose (2002), Ishii et al. (2011) and Zhang et al. (2013).*

6.2.3 The composition of akimotoite in a harzburgitic composition

Following the results of previous experiments (e.g. Zhang et al. 2013, Ishii et al. 2019) harzburgite comprises three phases at lower transition zone conditions, ringwoodite, garnet and akimotoite. Using the harzburgitic composition given in Table 1-1, the compositions and proportions of the three phases can be determined at a given pressure using a mass balance calculation. For this calculation it is assumed that all Cr and Ca are incorporated in garnet, which is in agreement with experimental studies (e.g. Hirose 2002, Ishii et al. 2011, Zhang et al. 2013). The Al contents of akimotoite and garnet are then determined from the thermodynamic model shown in Figure 6-5 while the Fe contents of the phases are constrained from the Fe-Mg K_D values determined in the previous section. The resulting phase proportions are shown in Figure 6-7 calculated at conditions of a typical mantle adiabat (Katsura et al. 2010). At 23 GPa, corresponding to 648 km depth, akimotoite can incorporates a maximum amount of 3 mol.% FeO and 2 mol.% Al_2O_3 which is within the range of akimotoite compositions reported for harzburgitic assemblages (Hirose 2002, Zhang et al. 2013, Ishii et al. 2019).

164
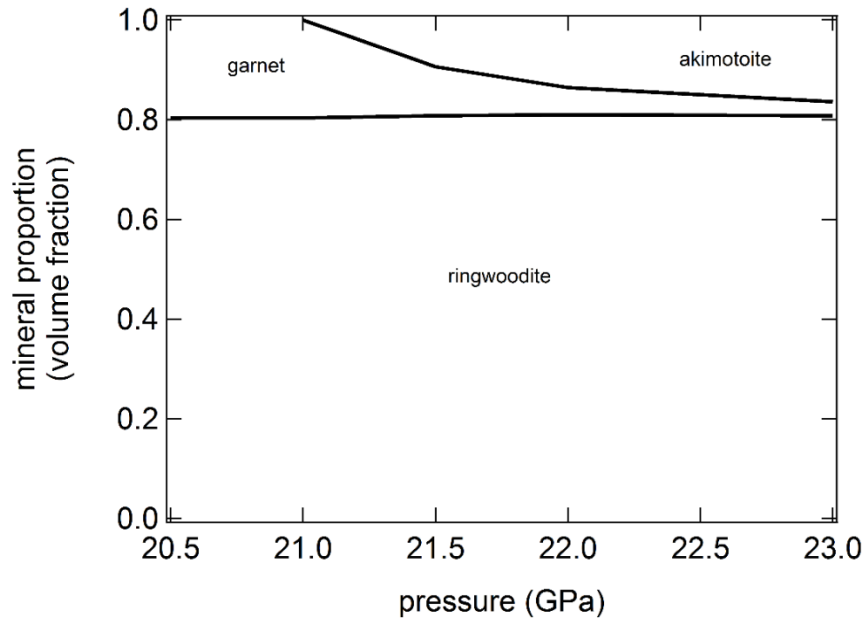
Figure 6-7: *The phase relations for a harzburgite composition along a mantle adiabat (Katsura et al. 2010) determined using mass balance and the constraints provided by the thermodynamic model in Figure 6-5 and the Fe-Mg K_D relations in Figure 6-6.*

6.3 Velocity and density models for a harzburgitic lithology at basal transition zone pressures

The proportions determined in the previous section and the mineral compositions are then used with the elastic properties reported in Table 6-1 to determine v_P and v_S for a harzburgitic composition between 20.5 GPa and 23 GPa, equivalent to depths between 586 and 648 km, along a mantle adiabat (Katsura et al. 2010) (Figure 6-8). The results indicate that below 21 GPa, before the onset of akimotoite formation (Figure 6-7), the calculated wave velocities are slightly below those of PREM, as shown already by Pamato et al. (2016). As the proportion of akimotoite in harzburgite increases, however, starting from 21 GPa, the compressional and shear wave velocities increase quite sharply up to 22 GPa, where the majority of garnet has been replaced by akimotoite (Figures 6-7 and 6-8). At this pressure, corresponding to 624 km depth, the calculated wave velocities intersect the PREM model for v_P and PREM and AK135 for v_S. The calculated velocities then remain in very good agreement with those of the seismic reference models up to 23 GPa corresponding to 648 km depth. The bulk density of the harzburgite lies between the AK135 and PREM reference models close to the bulk density of peridotite for the whole pressure range calculated (Figure 6-8).

165
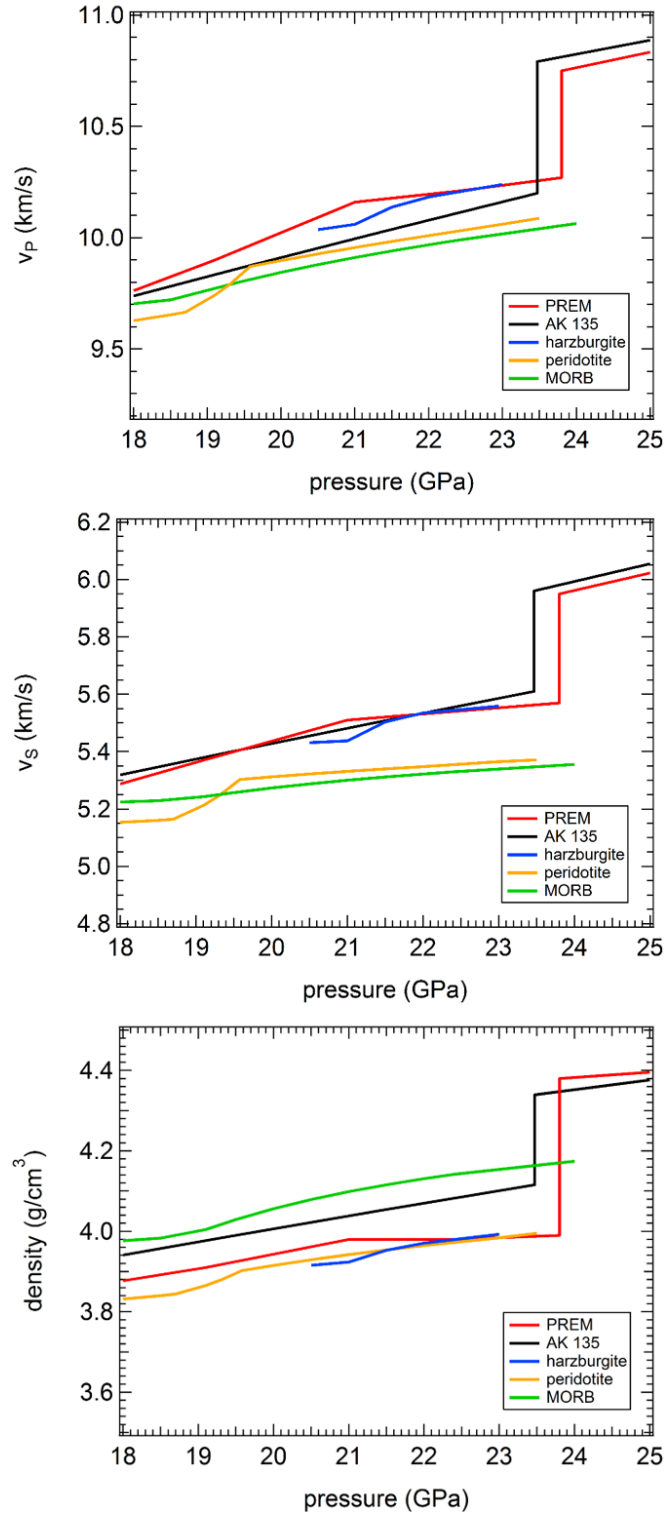
Figure 6-8: *Determinations of v_P, v_S and density for harzburgite, peridotite and MORB compositions along a mantle adiabat at lower transition zone conditions. The seismic 1D reference models PREM (Dziewonski and Anderson 1981) and AK135 (Kennet et al. 1995) are shown for comparison.*

The calculations for the harzburgitic lithology can then be compared with those determined for fertile peridotite and MORB by Pamato et al. (2016). These previous velocity and density calculations have been updated, however, with a new determination of the elastic properties for $CaSiO_3$ perovskite using the recent experimental results of Gréaux et al. (2019) and Thomson et al. (2019), with fitting parameters given in Table 6-1. The exsolution of $CaSiO_3$ perovskite was suggested in the past to lead to increased wave velocities (Siogeikin and Bass 2002, Irifune et al. 2008) and it has even been proposed that the exsolution of $CaSiO_3$ perovskite from majoritic garnet in peridotite and MORB lithologies could lead to a sufficiently sharp jump in velocity to cause a seismic discontinuity (Saikia et al. 2007). Using the updated elastic properties in the calculation, however, results in a decrease in v_P and v_S for peridotite and MORB compared with previous estimates and the change in gradient resulting from $CaSiO_3$ peroskite formation is hardly perseptable. The discrepancy between the seismic reference models and the mineralogical calculations as described by Pamato et al. (2016), therefore, further increases.

The mineral models shown in Figure 6-8 indicate that the formation of Fe- and Al bearing akimotoite in a harzburgitic lithology results in an increase in the bulk compressional and shear wave velocities to levels that match those of the seismic reference models PREM and AK135 at the base of the transition zone. In particular, as a result of the formation of akimotoite, v_S determined for the harzburgite composition matches both reference models almost perfectly over this pressure range. Any other plausible mantle composition results in lower velocities at these conditions and any significant mixing of peridotite and MORB material would also result in velocities being lower than the reference models. The presence of a harzburgite layer on top of the 660 km discontinuity is indeed plausible, at least on a regional scale, as seismic tomography shows that subducted lithospheric mantle stagnates around this depth, likely due to the bouyany experienced by cold material on nearing the lower mantle (Fukao et al. 2001, 2009, Fukao and Obayashi 2013). The tomography model of Fukao and Obayashi (2013), for example, shows regions of fast seismic velocities on top of the 660 km discontinuity most likely due to subduction of the western pacific plate beneath Eastern Asia and from the subduction of the Nazca Plate beneath South America. The fast anomaly results from subduction beneath Japan, for example, appears to extend at depths between 550-620 km for at least 2000 km westward beneath Korea and Northern China. The disappearance of this anomaly further to the west most likely results from it descending into the lower mantle, rather than reaching thermal equilibrium, which

should take much longer (Fukao and Obayashi 2013). Such regions must raise globally averaged seismic wave velocities due mainly to the thermal anaomaly but also due to the presence of depleted mantle portions of the subducted lithosphere. However, although their lateral extent is hard to judge, they likely make up much less than 10 % of the volume of the mantle at the base of the transition zone and to a certain extent their influence on global velocities should be counter balanced by hot anomalies that bring global velocity estimates down (Fukao and Obayashi 2013). Therefore, if there is a prevalence of harzburgitic material in the average mantle at this depth interval it likely reflects either a process that concentrates harzburgitic material globally at this depth or implies that the average mantle is more harzburgite rich than previously considered. The first possibility was considered in numerical thermo-chemical mantle convection simulations of Nakagawa et al. (2012) who examined how MORB and mantle residues with varying levels of melt depletion may separate in a convecting mantle due to density contrasts. The model indicates that subducted MORB and its residue end up comprising most of the mantle as a result of homogenisation processes being very slow (Stracke et al. 2012). The model of Nakagawa et al. (2012) shows signifciant concentrations of subducted MORB in the lower mantle, which leaves the remaining mantle on average more depleted. This would provide a good explanation for the existence of more harzburgitic material in the upper mantle and transition zone. In detail, however, the model shows no particular preferential enrichment of very depleted material above the 660 km discontinuity. This may actually be due to the presence of akimotoite in such harzburgite material. Akimotoite undergoes the phase transformation to bridgmanite, and becomes denser in the ambient mantle at lower pressures compared to more garnet-rich fertile mantle and is, therefore, more likely to concentrate beneath the 660 km discontinuity than above it (Irifune and Ringwood 1987). In fact, some seismic observations even find evidence for a possible enrichment of harzburgite material below the 660 km discontinuity in some regions, for the same reason (Maguire et al. 2017). On the other hand, geochemical studies have argued that strongly depleted mantle could make up more of the source of both ocean island basalts and MORB than previously considered (Stracke et al. 2012, 2019). The results reported in Figure 6-8 certainly support this view that the upper mantle and transition zone may contain more melt depleted material than previously considered due to the generally denser basaltic component of subducting lithosphere being preferentially partitioned into the lower mantle.

The transformation interval of garnet to akimotoite in the harzburgite lithology was calculated to be between 21 GPa (600 km depth) and 22 GPa (624 km depth) along a typical mantle adiabat (Katsura et al. 2010). This corresponds to a transition depth range of only ~ 24 km, which is comparable to the ~ 20 km transition interval of the wadsleyite-ringwoodite transformation at 520 km depth (e.g. Frost 2003). Due to its sharpness and impedance contrast, the 520 km discontinuity appears to be almost globally detectable (e.g. Shearer 1990). The impedance contrasts $\Delta(v_P\rho)$ and $\Delta(v_S\rho)$ for the wadsleyite-ringwoodite transformation determined from the peridotite model in Figure 6-8 are 3.9 % and 4.4 %, respectively, with velocity and density contrasts of Δv_P = 2.2 %, Δv_S = 2.7 % and $\Delta\rho$ = 1.6 %. If it can be demonstrated that the impedance contrasts are similar for the garnet-akimotoite transformation, then this would imply that the transition should be similarly visible. The compressional and shear wave velocity contrasts for the garnet-akimotoite transition in the harzbugitic composition are calculated to be Δv_P = 1.2 %, Δv_S = 1.8 % and $\Delta\rho$ = 1.2 %. The resulting impedance contrasts $\Delta(v_P\rho)$ = 2.4 % and $\Delta(v_S\rho)$ = 3.0 % are approximatly 30 % smaller but may still be sufficient to produce a seismic discontinuity under certain conditions. Indeed, multiple discontinuities around 660 km depth have been observed in several studies (e.g. Niu and Kawakatsu 1996, Simmons and Gurrola 2000, Castillo et al. 2001, Ai et al. 2003). Simmons and Gurrola (2000) and Castillo et al. (2001) have observed a seismic discontinuity, for example, between 610 and 640 km, which can be attributed to the depth of the garnet-akimotoite transition determined in this study. The discontinuity was observed regionally below subduction zone settings (e.g. Simmons and Gurrola 2000, Castillo et al. 2001, Ai et al. 2003), which would be consistent with a stronger garnet-akimotoite transition in colder mantle due to the expansion of the akimotoite field to higher Al_2O_3 concentrations at the expense of garnet (Akaogi et al. 2002). The transformation from garnet shown in Figure 6-7 would go to completion at lower temperatures and would do so over a narrower depth interval. If the ambient transition zone and upper mantle contain more harzburgite than previously considered, then the fact that the discontinuity would become stronger at lower temperatures may explain why it is not observed globally like the wadsleyite-ringwoodite transition.

7. Conclusions

This thesis focused on investigating the elasticity of MgSiO$_3$ akimotoite, its structural behaviour at high pressure as well as the influence of Fe and Al substitution on the elasticity and structure of akimotoite. The following conclusions can be drawn:

1) For the first time, the equation of state of the MgSiO$_3$ akimotoite end-member has been determined on a single-crystal of akimotoite up to pressures compatible with the base of the transition zone, i.e. to the pressure of akimotoite stability. Both bulk and axial compressibility have been investigated and compared to literature data which exists only on polycrystalline akimotoite samples. The results were refined to give an isothermal bulk modulus, K_T, of 209(2) GPa and $K' = 4.8$ (2) in good agreement with previous room pressure Brillouin measurements (Weidner and Ito 1985) but inconsistent with several compression studies on polycrystalline samples.

2) The full elastic tensor of MgSiO$_3$ akimotoite has been experimentally determined using a combination of Brillouin spectroscopy and single-crystal X-ray diffraction as a function of density in a diamond anvil cell up to 25 GPa. Compressional and shear wave velocities were compared to literature data and were found to be slower than wave velocities determined using ultrasonic interferometry in the multianvil press, particularly in v_P. Additionally, knowledge of all elastic coefficients allows the investigation of the anisotropic behavior of akimotoite up to pressures of its stability field. Pressure decreased the anisotropy only slightly and this is off set by the effects of temperature once the results of ab initio simulations are considered (Zhang et al. 2005). MgSiO$_3$ akimotoite remains the most elastically anisotropic mineral in the transition zone and its presence provides one of the only explanations for seismic anisotropy observations made, for example, on the Tonga slab at the base of the transition zone (Shiraishi et al. 2008).

3) The structural evolution of MgSiO$_3$ akimotoite has been investigated up to 10.8 GPa by collecting full-intensity data at high pressures under quasi-hydrostatic conditions in a diamond anvil cell. No phase transition was observed up to the highest pressure investigated in this study. Essential information about the compression mechanisms were obtained

allowing the anisotropic axial compressibility of akimotoite to be understood in terms of octahedral compression. The oxygens lying along the a-axis form the edges of faces shared between octahedra, and as such have a very small degree of freedom giving rise to a stiff direction, whereas perpendicular to these faces, i.e. along the c-axis, the compression of the octahedra is much easier.

4) Structure refinements on eight single-crystals along the $MgSiO_3$ akimotoite – Al_2O_3 corundum solid solution have been performed in order to understand the influence of Al_2O_3 on the akimotoite structure and $MgSiO_3$ on the corundum structure, respectively. Changes in unit-cell lattice parameters and octahedral bond lengths imply that the accommodation mechanisms of Al_2O_3 substitution in $MgSiO_3$ akimotoite and of $MgSiO_3$ substitution in corundum are fundamentally different.

5) The influence of Al on the elastic properties of akimotoite was investigated up to the pressure and temperature stability conditions of akimotoite using ultrasonic interferometry and in situ energy-dispersive X-ray diffraction. It was found that the incorporation of Al substitution results in a decrease in wave velocities relative to the $MgSiO_3$ end-member. Note that wave velocities of corundum, which is often assumed to be the Al_2O_3 end-member of akimotoite due to the similar structure, are faster than those of akimotoite. This is the first time, to my knowledge, that the elastic properties of samples with mixed compositions do not lie between the two end-members of a proposed solid solution. The axial compressibility of the a- and c-axes also becomes less anisotropic with increasing Al content.

6) The influence of Fe on the elasticity of akimotoite was investigated up to transition zone pressures and 800 K using ultrasonic interferometry and in situ energy-dispersive X-ray diffraction. The substitution of Fe^{2+} on to the Mg site was found to decrease the wave velocities relative to the $MgSiO_3$ end-member. The incorporation of Fe into the structure also majorly influences the compression mechanism of the a-axis, making it more compressible, whereas the c-axis seems to be mostly unaffected.

7) Incorporation of both Fe^{3+} and Al into the akimotoite structure follows a coupled substitution and results in a strong decrease in compressional and shear wave velocities up to transition zone pressures investigated using ultrasonic interferometry and in situ energy-dispersive X-ray diffraction. Fe and Al combined seem to have an even larger effect on the compressibility of the a-axis, whereas the c-axis behaves similarly to the end-member akimotoite. There is most likely a

disordered distribution of Fe^{3+} and Al between the Mg and Si sites, where Fe^{3+} substitution occurs also onto the Si site, which would explain the major changes in compressibility. Structure refinements Fe^{3+}- and Al-bearing akimotoite single-crystals are needed to fully understand the influence of this coupled substitution on the akimotoite structure.

8) The experimental data obtained in this study were used to derive the elastic properties of fictive Al_2O_3 and $FeSiO_3$ akimotoite end-members. The high-temperature parameters obtained in this fitting procedure are in good agreement with values reported in literature. The incorporation of Al into coexisting garnet and akimotoite was calculated from a thermodynamic model derived using the results of previous phase equilibria experiments and the $MgSiO_3$ and Al_2O_3 akimotoite end-member equations of state data determined in this study. The results of this calculation reproduce some phase equilibria studies from the literature but are in poor agreement with experiments performed on harzburgitic bulk compositions, likely due to experimental difficulties in the attainment of equilibrium. Furthermore, the distribution of Fe between coexisting akimotoite and ringwoodite and garnet and ringwoodite was determined from previous studies. Using the constraints provided by these data and the thermodynamic model in a mass balance calculation, the mineral proportions of coexisting akimotoite, garnet and ringwoodite were calculated for a harzburgitic lithology along an adiabat at basal transition zone conditions. A thermo-elastic self-consistent model was then used to calculate v_P, v_S and density for this harzburgite assemblage between 21 and 23 GPa. The results were found to be in near perfect agreement with the predictions of global 1 dimensional seismic reference models at the same conditions. The wave velocities of fertile peridotite and MORB compositions, updated using recent data on $CaSiO_3$ perovskite, on the other hand were determined to be significantly slower than the reference models. These findings strongly support the existence of melt-depleted harzburgitic material at the base of the transition zone. This material is unlikely to be only present due to stagnation of recently subducted lithosphere and is more likely to reflect a greater abundance of harzburgitic material in the upper mantle and transition zone as a whole. This conclusion is in agreement with some geochemical (Stracke et al. 2019) and geodynamic studies (Nakagawa et al. 2012).

9) The garnet-akimotoite transformation was found to occur between 21 and 22 GPa corresponding to a depth range of only 24 km which is comparable to the depth interval of the

wadsleyite-ringwoodite transition at 520 km depth. The determined impedance contrasts of the garnet-akimotoite transformation are approximately 30 % weaker than the wadsleyite-ringwoodite transformation implying that this transition may be seismically visible. Indeed, several seismic observations have indicated the existence of multiple discontinuities around the 660 km-discontinuity in subduction zone settings of which the shallower discontinuity between 610 and 640 km depth can be attributed to the garnet-akimotoite transformation. The visibility of this discontinuity in subduction zone settings is consistent with an expansion in the akimotoite stability field, relative to that of garnet, at lower temperatures.

References

Agee C.B. (1998) Phase transformations and seismic structure in the upper mantle and transition zone. In: Hemley R.J. (ed) Ultrahigh-Pressure Mineralogy. Mineralogical Society of America Reviews in Mineralogy 37, pp. 165-203.

Ai, Y., Zheng, T., Xu, W., Yumei, H. and Dong, D. (2003) A complex 660 km discontinuity beneath northeast China. Earth and Planetary Science Letters, 212, 63-71.

Anderson, D.L. and Bass, J.D. (1986) Transition region of the Earth's upper mantle. Nature 320, 321-328.

Anderson, O.L., Isaak, D.G. and Yamamoto, S. (1989) Anharmonicity and the equation of state for gold. Journal of Applied Physics, 65, 1534.

Angel, R.J. (2000) Reviews in Mineralogy and Geochemistry, Vol. 41, High-Temperature and High-Pressure Crystal Chemistry. Mineralogical Society of America, Washington, DC, Ch. 2: Equations of State, pp. 35-59.

Angel, R.J. (2003) Automated profile analysis for single-crystal diffraction data. Journal of Applied Crystallography, 36, 295-300.

Angel, R.J. (2004) Absorption corrections for diamond-anvil pressure cells implemented in the software package Absorb6.0. Journal of Applied Crystallography, 37, 486-492.

Angel, R.J., Zhao, J. and Bujak, M. (2005) Hydrostatic limits of pressure-transmitting media by single-crystal diffraction (abs). 2005 Salt Lake City Annual Meeting, Paper No. 155-7.

Angel, R.J., Jackson, J.M., Reichmann, H.J. and Speziale, S. (2009) Elasticity measurements on minerals: a review. European Journal of Mineralogy, 21, 525-550.

Angel, R.J. and Finger, L.W. (2011) SINGLE: a program to control single-crystal diffractometers. Journal of Applied Crystallography, 44, 247-251.

Angel, R.J., Alvaro, M., and Gonzalez-Platas, J. (2014) EosFit7c and a Fortran module (library) for equation of state calculations. Zeitung für Kristallographie, 229(5), 405-419.

Akaogi, M., Tanaka, A. and Ito, E. (2002) Garnet-ilmenite-perovskite transitions in the system $Mg_4Si_4O_{12}$-$Mg_3Al_2Si_3O_{12}$ at high pressures and high temperatures: phase

equilibria, calorimetry and implications for mantle structure. Physics of the Earth and Planetary Interiors, 132, 303-324.

Armstrong, K. (2018) Redox Evolution of the Early Earth's Mantle. PhD thesis, University of Bayreuth, pp. 187.

Ashida, T., Kume, S., Ito, E. and Navrotsky, A. (1988) $MgSiO_3$ ilmenite: heat capacity, thermal expansivity, and enthalpy of transformation. Physics and Chemistry of Minerals, 16, 239-245.

Ballmer, M.D., Houser, C., Hernlund, J.W., Wentzcovitch, R.M. and Hirose, K. (2017) Persistence of strong silica-enriched domains in the Earth's lower mantle. Nature Geoscience, 10, 236-240.

Bindi, L., Chen, M. and Xie, X. (2017) Discovery of the Fe-analogue of akimotoite in the shocked Suizhou L6 chondrite. Scientific Reports, 7, 42674.

Birch, F. (1947) Finite Elastic Strain of Cubic Crystals. Physical Review, 71, 809.

Bolfan-Casanova, N., Keppler, H. and Rubie, D.C. (2000) Water partitioning between nominally anhydrous minerals in the $MgO-SiO_2-H_2O$ system up to 24 GPa: implications for the distribution of water in the Earth's mantle. Earth and Planetary Science Letters, 182, 209-221.

Bolfan-Casanova, N., Keppler, H. and Rubie, D.C. (2002) Hydroxyl in $MgSiO_3$ akimototie: A polarized and high-pressure IR study. American Mineralogist, 87, 603-608.

Buchen, J. (2018) The Elastic Properties of Wadsleyite and Stishovite at High Pressures-Tracing Deep Earth Material Cycles. PhD thesis, University of Bayreuth, pp. 199.

Cammarano, F., Goes, S., Deuss, A. and Giardini, D. (2005) Is a pyrolitic adiabatic mantle compatible with seismic data? Earth and Planetary Science Letters, 232, 227-243.

Campbell, I.H. and O'Neill, H.StC. (2012) Evidence against a chondritic Earth. Nature, 483, 553-558.

Castillo, J., Mocquet, A. and Saracco, G. (2001) Wavelet transform: a tool for the interpretation of upper mantle converted phases at high frequency. Geophysical Research Letters, 28, 4327-4330.

Chantel, J. (2012) Measurement of elastic properties of silicates at realistic mantle pressures. PhD thesis, University of Bayreuth, pp. 154.

Chantel, J., Manthilake, G.M., Frost, D.J., Beyer, C., Boffa Ballaran, T., Jing, Z. and Wang, Y. (2016) Elastic wave velocities in polycrystalline $Mg_3Al_2Si_3O_{12}$-pyrope garnet to 24 GPa and 1300 K. American Mineralogist, 101, 991-997.

Creagh, D. and Hubbell, J. (1992) International Tables of Crystallography, Vol. C. Kluwer Academic Publishers, Dordrecht, Ch. 4.2.4: X-ray absorption (or attenuation) coefficients, pp. 220-230.

Criniti, G. (2018) Akimotoite in the $MgSiO_3$-Al_2O_3-$FeSiO_3$ system: synthesis and characterization. Research Project Report, University of Bayreuth, pp. 28.

Da Silva, C.R.S., Karki, B.B., Stixrude, L. and Wentzcovitch, R.M. (1999) Ab initio study of the elastic behavior of $MgSiO_3$ ilmenite at high pressure. Geophysical Research Letters, 26, 943-946.

Davies, G.F. and Dziewonski, A.M. (1975) Homogeneity and constitution of the Earth's lower mantle and outer core. Physics of the Earth and Planetary Interiors, 10, 336-343.

De Grave, E., Vandenberghe, R.E. and Dauwe, C. (2005) ILEEMS: Methodology and applications to iron oxides. Hyperfine Interactions, 161, 147-160.

Dewaele, A., Fiquet, G., Andrault, D. and Hausermann, D. (2000) P-V-T equation of state of periclase from synchrotron radiation measurements. Journal of Geophysical Research, 105, 2869-2877.

Dewaele, A., Loubeyre, P. and Mezouar, M. (2004) Equations of state of six metals above 94 GPa. Physical Review B, 70, 094112.

Dyar, M.D., Agresti, D.G., Schaefer, M.W., Grant, C.A. and Sklute, E.C. (2006) Mössbauer spectroscopy of Earth and planetary materials. Annual Review of Earth and Planetary Science, 34, 83-125.

Dziewonski, A.M. and Anderson, D.L. (1981) Preliminary reference Earth model. Physics of the Earth and Planetary Interiors, 25, 297-356.

Farrugia, L.J. (1999) *WinGX* suite for small-molecule single-crystal crystallography. Journal of Applied Crystallography, 32, 837-838.

Ferroir, T., Beck, P., Van de Moortèle, B., Bohn, M., Reynard, B., Simionovici, A., El Goresy, A. and Gillet, P. (2008) Akimotoite in the Tenham meteorite: Crystal chemistry and high-pressure transformation mechanisms. Earth and Planetary Science Letters, 275, 26-31.

Finger, L.W. and Hazen, R.M. (1978) Crystal structure and compression of ruby to 46 kbar. Journal of Applied Physics, 49, 5823-5826.

Frost, D.J. (2003) The structure and sharpness of $(Mg,Fe)_2SiO_4$ phase transformations in the transition zone. Earth and Planetary Science Letters, 216, 313-328.

Frost, D.J. (2008) The upper mantle and transition zone. Elements, 4, 171-176.

Fukao, Y., Widiyantoro, S. and Obayashi, M. (2001) Stagnant slabs in the upper and lower mantle transition region. Reviews of Geophysics, 39(3), 291-323.

Fukao, Y., Obayashi, M., Nakakuki, T. and the Deep Slab Project Group (2009) Stagnant slab: a review. Annual Review of Earth and Planetary Science, 37, 19-46.

Fukao, Y. and Obayashi, M. (2013) Subducted slabs stagnant above, penetrating through, and trapped below the 660 km discontinuity. Journal of Geophysical Research: Solid Earth, 118, 5920-5938.

Gasparik, T. (1990) Phase relations in the transition zone. Journal of Geophysical Research, 95, 15,751-15,769.

Gréaux, S., Irifune, T., Higo, Y., Tange, Y., Arimoto, T., Liu, Z. and Yamada, A. (2019) Sound velocity of $CaSiO_3$ perovskite suggests the presence of basaltic crust in the Earth's lower mantle. Nature, 565, 218-221.

Green, D.H., Hibberson, W.O. and Jaques, A.L. (1979) Petrogenesis of mid-ocean ridge basalts. In: McElhinny, M.W. (ed) The Earth: Its Origin, Structure and Evolution, London: Academic Press, pp. 269-299.

Hao, S., Wang, W., Qian, W. and Wu, Z. (2019) Elasticity of akimotoite under the mantle conditions: Implications for multiple discontinuities and seismic anisotropies at the depth of ~600-750 km in subduction zones. Earth and Planetary Science Letters, 528, 115830.

Hart, S.R. and Zindler, A. (1986) In search of a bulk-earth composition. Chemical Geology, 57, 247-267.

Hemley, R.J., Jephcoat, A.P., Mao, H.K., Zha, C.S., Finger, L.W. and Cox, D.E. (1987) Static compression of H_2O-ice to128 GPa (1.28 Mbar). Nature, 330, 737-740.

Hernández, E.R., Brodholt, J. and Alfè, D. (2015) Structural, vibrational and thermodynamic properties of Mg_2SiO_4 and $MgSiO_3$ minerals from first-principles simulations. Physics of the Earth and Planetary Interiors, 240, 1-24.

Higo, Y., Inoue, T., Li, B., Irifune, T. and Liebermann, R.C. (2006) The effect of iron on the elastic properties of ringwoodite at high pressure. Physics of the Earth and Planetary Interiors, 159, 276-285.

Higo, Y., Irifune, T. and Funakoshi, K. (2018) Simultaneous high-pressure high-temperature elastic velocity measurement system up to 27 GPa and 1873 K using ultrasonic and synchrotron X-ray techniques. Review of Scientific Instruments, 89, 014501.

Hirose, K., Komabayashi, T., Murakami, M. and Funakoshi, K. (2001) In situ measurements of the majorite-akimotoite-perovskite phase transition boundaries in $MgSiO_3$. Geophysical Research Letters, 28, 4351-4354.

Hirose, K. (2002) Phase transitions in pyrolitic mantle around 670-km depth: Implications for upwelling of plumes from the lower mantle. Journal of Geophysical Research, 107 (B4), 2078.

Horiuchi, H., Hirano, M., Ito, E. and Matsui, Y. (1982) $MgSiO_3$ (ilmenite-type): single crystal X-ray diffraction study. American Mineralogist, 67, 788-793.

Irifune, T. and Ringwood, A.E. (1987) Phase transformations in a harzburgite composition to 26 GPa: implications for dynamical behavior of the subducting slab. Earth and Planetary Science Letters, 86, 365-376.

Irifune, T., Koizumi, T. and Ando, J. (1996) An experimental study of the garnet-perovskite transformation in the system $MgSiO_3$-$Mg_3Al_2Si_3O_{12}$. Physics of the Earth and Planetary Interiors, 96, 147-157.

Irifune, T., Higo, Y., Inoue, T., Kono, Y., Ohfuji, H. and Funakoshi, K. (2008) Sound velocities of majorite garnet and the composition of the mantel transition region. Nature, 451, 814-817.

Ishii, T., Kojitani, H. and Akaogi, M. (2011) Post-spinel transitions in pyrolite and Mg_2SiO_4 and akimotoite-perovskite transition in $MgSiO_3$: Precise comparison by high-pressure high-temperature experiments with multi-sample cell technique. Earth and Planetary Science Letters, 309, 185-197.

Ishii, T., Kojitani, H. and Akaogi, M. (2018) Phase relations and mineral chemistry in pyrolitic mantle at 1600-2200 °C under pressures up to the uppermost lower mantle: Phase transitions around the 660-km discontinuity and dynamics of upwelling hot plumes. Physics of the Earth and Planetary Interiors, 274, 127-137.

Ishii, T., Kojitani, H. and Akaogi, M. (2019) Phase relations of harzburgite and MORB up to the uppermost lower mantle conditions: precise comparison with pyrolite by multisample cell high-pressure experiments with implications to dynamics of subducted slabs. Journal of Geophysical Research: Solid Earth, 124, 3491-3507.

Ishii, T., Huang, R., Myhill, R., Fei, H., Koemets, I., Liu, Z., Maeda, F., Yuan, L., Wang, L., Druzhbin, D., Yamamoto, T., Bhat, S., Farla, R., Kawazoe, T., Tsujino, N., Kulik, E., Higo, Y., Tange, Y. and Katsura, T. (2019) Sharp 660-km discontinuity controlled by extremely narrow binary post-spinel transition. Nature Geoscience, 12, 869-872.

Ito, E. and Yamada, H. (1982) High-pressure research in geophysics, D. Reidel, Dordrecht. Stability Relations of Silicate Spinels, Ilmenites, and Perovskites, pp. 405-419.

Jackson, I., Niesler, H. and Weidner, D.J. (1981) Explicit correction of ultrasonically determined elastic wave velocities for transducer-bond phase shifts. Journal of Geophysical Research, 86, 3736-3748.

Jamieson, J.C., Fritz, J.N. and Manghani, M.H. (1982) Pressure measurement at high temperature in x-ray diffraction studies: gold as primary standard, in: High-Pressure Research in Geophysics, S. Akimoto and M.H. Manghani (eds.), CAPJ, Tokyo, pp. 27-48.

Kantor, I., Prakapenka, V., Kantor, A., Dera, P., Kurnosov, A., Sinogeikin, S., Dubrovinskaia, N. and Dubrovinsky, L. (2012) BX90: A new diamond anvil cell design for X-ray diffraction and optical measurements. Review of Scientific Instruments, 83, 125102.

Kato, T. (1986) Stability relation of $(Mg,Fe)SiO_3$ garnets, major constituents in the Earth's interior. Earth and Planetary Science Letters, 77, 399-408.

Katsura, T., Yoneda, A., Yamazaki, D., Yoshino, T. and Ito, E. (2010) Adiabatic temperature profile in the mantle. Physics of the Earth and Planetary Interiors, 183, 212-218.

Kawai, N., Tachimori, M. and Ito, E. (1974) A High Pressure Hexagonal Form of $MgSiO_3$. Proc. Japan Acad, 50, 378-380.

Kennet, B.L.N., Engdahl, E.R. and Buland, R. (1995) Constraints on seismic velocities in the Earth from traveltimes. Geophysical Journal International, 122, 108-124.

King, H.E. and Finger, L.W. (1979) Diffracted Beam Crystal Centering and Its Application to High-Pressure Crystallography. Journal of Applied Crystallography, 12, 374-378.

Kubo, A. and Akaogi, M. (2000) Post-garnet transitions in the system $Mg_4Si_4O_{12}$-$Mg_3Al_2Si_3O_{12}$ up to 28 GPa: phase relations of garnet, ilmenite and perovskite. Physics of the Earth and Planetary Interiors, 121, 85-102.

Kurnosov, A., Kantor, I., Boffa Ballaran, T., Lindhardt, S., Dubrovinsky, L., Kuznetov, A. and Zehnder, B.H. (2008) A novel gas-loading system for mechanically closing of various types of diamond anvil cells. Review of Scientific Intstruments, 79, 045110.

Kurnosov, A., Marquardt, H., Frost, D.J., Boffa Ballaran, T. and Ziberna, L. (2017) Evidence for a Fe^{3+}-rich pyrolitic lower mantle from (Al,Fe)-bearing bridgmanite elasticity data. Nature, 543, 543-546.

Larson, A.C. and Von Dreele, R.B. (2004) General Structure Analysis System (GSAS), Los Alamos National Laboratory Report LAUR 86-748.

Leisure, R.G. (2017) Ultrasonic Spectroscopy. Applications in Condensed Matter Physics and Materials Science. Cambridge University Press, United Kingdom, Ch. 4, Experimental Methods, pp. 94-119.

Liu, L.-G. (1982) Speculations on the composition and origin of the Earth. Geochemical Journal, 16, 287-310.

Liu, Z., Irifune, T., Nishi, M., Tange Y., Arimoto, T. and Shinmei, T. (2016) Phase relations in the system $MgSiO_3$-Al_2O_3 up to 52 GPa and 2000 K. Physics of the Earth and Planetary Interiors, 257, 18-27.

Long, G., Cranshaw, T. and Longworth, G. (1983) The ideal Mössbauer effect absorber thickness. Mössbauer Effect Reference and Data Journal, 6(2), 42-49.

Lyubutin, I.S., Lin, J.-F., Gavriliuk, A.G., Mironovich, A.A, Ivanova, A.G., Roddatis, V.V. and Vasiliev, A.L. (2013) Spin transition of Fe^{2+} in ringwoodite $(Mg,Fe)_2SiO_4$ at high pressures. American Mineralogist, 98, 1803-1810.

Maguire, R., Ritsema, J. and Goes, S. (2017) Signals of 660 km topography and harzburgite enrichment in seismic images of whole-mantle upwellings. Geophysical Research Letters, 44, 3600-3607.

Mainprice, D. (1990) A Fortran program to calculate seismic anisotropy from the lattice preferred orientation of minerals. Computers and Geosciences, 16(3), 385-393.

Mainprice, D. (2015) Seismic anisotropy of the deep Earth from a Mineral and Rock Physics Perspective. In: Treatise on Geophysics, 2nd edition, Vol 2. Schubert, G. (ed). Oxford: Elsevier, pp. 487-538.

McCammon, C.A., Lauterbach, S., Seifert, F., Langehorst, F. and van Aken, P.A. (2004) Iron oxidation state in lower mantle mineral assemblages I. Empirical relations derived from high-pressure experiments. Earth and Planetary Science Letters, 222, 435-449.

Michael, P.J. and Bonatti, E. (1985) Peridotite composition from the North Atlantic: regional and tectonic variations and implications for partial melting. Earth and Planetary Science Letters, 73, 91-104.

Miyajima, N., El Goresy, A., Dupas-Bruzek, C., Seifert, F., Rubie, D.C., Chen, M. and Xie, X. (2007) Ferric iron in Al-bearing akimotoite coexisting with iron-nickel metal in a shock-melt vein in an L-6 chondrite. American Mineralogist, 92, 1545-1549.

Murakami, M., Ohishi, Y., Hirao, N. and Hirose, K. (2012) A perovskitic lower mantle inferred from high-pressure, high-temperature sound velocity data. Nature, 485, 90-94.

Murnaghan, F. (1937) Finite Deformations of an Elastic Solid. American Journal of Mathematics, 59, 235-260.

Nakagawa, T., Tackley, P.J., Deschamps, F. and Connolly, J.A.D. (2012) Radial 1-D seismic strucutres in the deep mantle in mantle convection simulations with self-consistently calculated mineralogy. Geochemistry Geophysics Geosystems, 13, Q11002.

Niesler, H. and Jackson, I. (1989) Pressure derivatives of elastic wave velocities from ultrasonic interferometric measurements on jacketed polycrystals. The Journal of the Acoustical Society of America, 86, 1573.

Niu, F. and Kawakatsu, H. (1996) Complex structure of mantle discontinuities at the tip of the subducting slab beneath northeast China. Journal of Physics of the Earth, 44, 701-711.

Nowacki, A., Kendall, J.-M., Wookey, J. and Pemberton, A. (2015) Mid-mantle anisotropy in subduction zones and deep water transport. Geochemistry Geophysics Geosystems, 16, 764-784.

Nye, J.F. (1985) Physical properties of crystals: their representation by tensors and matrices. Oxford Science Publications, 322 pp.

Ohtani, E., Kagawa, N. and Fujino, K. (1991) Stability of majorite $(Mg,Fe)SiO_3$ at high pressures and 1800 °C. Earth and Planetary Science Letters, 102, 158-166.

O'Neill, H.St.C. and Palme, H. (1998) The Earth's mantle: Composition, Structure, and Evolution. Cambridge University Press. Ch.1: Composition of the Silicate Earth: Implications for Accretion and Core Formation, pp. 3-126.

Otsuka, K., McCammon C.A. and Karato, S. (2010) Tetrahedral occupancy of ferric iron in $(Mg,Fe)O$: Implications for point defects in the Earth's lower mantle. Physics of the Earth and Planetary Interior, 180, 179-188.

Pamato, M. (2014) Single-crystal elasticity of Al-rich phases in the Earth's transition zone and lower mantle. PhD thesis, University of Bayreuth, pp. 194.

Pamato, M.G., Kurnosov, A., Boffa Ballaran, T., Frost, D.J., Ziberna, L., Giannini, M., Speziale, S., Tkachev, S.N., Zhuralev, K.K. and Prakapenka, V.B. (2016) Single crystal elasticity of majoritic garnets: Stagnant slabs and thermal anomalies at the base of the transition zone. Earth and Planetary Science Letters, 451, 114-124.

Poirier, J.-P. (2000) Introduction to the Physics of the Earth's Interior. Second Edition, Cambridge University Press, Cambridge, 312 pp.

Prescher, C., McCammon, C. and Dubrovinsky, L. (2012) MossA: a proram for analyzing energy-domain Mössbauer spectra from conventional and synchrotron sources. Journal of Applied Crystallography, 45, 329-331.

Putnis, A. (1992) Introduction to Mineral Sciences. Cambridge University Press, Cambridge, 457 pp.

Ralph, R.L. and Finger, L.W. (1982) A Computer Program for Refinement of Crystal Orientation Matrix and Lattice Constants from Diffractometer Data with Lattice Symmetry Constraints. Journal of Applied Crystallography, 15, 537-539.

Reynard, B., Fiquet, G., Itié, J.-P. and Rubie, D.C. (1996) High-pressure X-ray diffraction study and equation of state of $MgSiO_3$ ilmenite. American Mineralogist, 81, 45-50.

Ringwood, A.E. (1962) A model for the upper mantle. Journal of Geophysical Research, 67, 857-867.

Ringwood, A.E. and Irifune, T. (1988) Nature of the 650-km seismic discontinuity: implications for mantle dynamics and differentiation. Nature, 331, 131-136.

Ringwood, A.E. (1994) Role of the transition zone and 660 km discontinuity in mantle dynamics. Physics of the Earth and Planetary Interiors, 86, 5-24.

Robinson, K., Gibbs, G.V. and Ribbe, P.H. (1971) Quadratic elongation: a quantitative measure of distortion in coordination polyhedra. Science, 172, 567-570.

Saikia, A., Frost, D.J., Rubie, D.C. (2008) Splitting of the 520-Kilometer Seismic Discontinuity and Chemical Heterogeneity in the Mantle. Science, 319, 1515-1518.

Sawamoto, H. (1987) High-Pressure Research in Mineral Physics, American Geophysical Union, Washington, D.C., Phase Diagram of $MgSiO_3$ at Pressures up to 24 GPa and Temperatures up to 2200 °C: Phase Stability and Properties of Tetragonal Garnet., pp. 209-219.

Shannon, R.D. (1976) Revised effective ionic radii and systematic studies of interatomic distances in halides and chalcogenides. Acta Crystallographica, A32, 751-767.

Shatskiy, A., Fukui, H., Matsuzaki, T., Shinoda, K., Yoneda, A., Yamazaki, D., Ito, E. and Katsura, T. (2007) Growth of large (1 mm) $MgSiO_3$ perovskite single-crystals: A thermal gradient method at ultrahigh pressure. American Mineralogist, 92, 1744-1749.

Sharp, T.G., Lingemann, C.M., Dupas, C. and Stöffler, D. (1997) Natural occurrence of $MgSiO_3$-ilmenite and evidence for $MgSiO_3$-perovskite in a shocked L chondrite. Science, 277, 352-355.

Shearer P.M. (2000) Upper mantle seismic discontinuities. In: Karato, S.-I., Forte, A.M., Liebermann, R.C., Masters, G., Stixrude, L. (eds) Earth's Deep Interior: Mineral Physics and Tomography From the Atomic to the Global Scale. Geophysical Monograph, 117, pp. 115-131.

Sheldrick, G. (2008) A short history of SHELX. Acta Crystallographica, A64, 112-122.

Shiraishi, R., Ohtani, E., Kanagawa, K., Shimojuku, A. and Zhao, D. (2008) Crystallographic preferred orientation of akimotoite and seismic anisotropy of Tonga slab. Nature, 455, 657-660.

Simmons, N.A. and Gurrola, H. (2000) Multiple seismic discontinuities near the base of the transition zone in the Earth's mantle. Nature, 405, 559-562.

Sinogeikin, S.V. and Bass, J.D. (2000) Single-crystal elasticity of pyrope and MgO to 20 GPa by Brillouin scattering in the diamond cell. Physics of the Earth and Planetary Interiors, 120, 43-62.

Stachel, T., Brey, G.P. and Harris, J.W. (2005) Elements, March 2005, v.1. Inclusions in Sublithospheric Diamonds: Glimpses of Deep Earth, pp. 73-78.

Stixrude, L. and Lithgow-Bertelloni, C. (2005) Thermodynamics of mantle minerals - I. Physical properties. Geophysical Journal International, 162, 610-632.

Stixrude, L. and Lithgow-Bertelloni, C. (2011) Thermodynamics of mantle minerals - II. Phase equilibria. Geophysical Journal International, 184, 1180-1213.

Stracke, A. (2012) Earth's heterogeneous mantle: A product of convection-driven interaction between crust and mantle. Chemical Geology, 330-331, 274-299.

Stracke, A., Genske, F., Berndt, J. and Koornneef, J.M. (2019) Ubiquitous ultra-depleted domains in Earth's mantle. Nature Geoscience, 12, 851-855.

Sun, S.-S. (1982) Chemical composition and origin of the earth's primitive mantle. Geochimica and Cosmochimica Acta, 46, 179-192.

Thomson, A.R., Kohn, S.C., Bulanova, G.P., Smith, C.B., Araujo, D., EIMF and Walter, M.J. (2014) Origin of sub-lithospheric diamonds from the Juina-5 kimberlite (Brazil): costraints from carbon isotopes and inclusion compositions. Contributions to Mineralogy and Petrology, 168, 1081.

Thomson, A.R., Crichton, W.A., Brodholt, J.P., Wood, I.G., Siersch, N.C., Muir, J.M.R., Dobson, D.P. and Hunt, S.A. (2019) Seismic velocities of $CaSiO_3$ perovskite can explain LLSVPs in Earth's lower mantle. Nature, 643-647.

Toby, B.H. (2001) EXPGUI, a graphical user interface for GSAS. Journal of Applied Crystallography, 34, 210-213.

Tomioka, N. and Fujino, K. (1997) Natural $(Mg,Fe)SiO_3$-Ilmenite and –Perovskite in the Tenham Meteorite. Science, 277, 1084-1086.

Trots, D.M., Kurnosov, A., Vasylechko, L., Berkowski, M., Boffa Ballaran, T. and Frost, D.J. (2011) Elasticity and equation of state of $Li_2B_4O_7$. Physics and Chemistry of Minerals, 38, 561-567.

Tschauner, O., Ma, C., Prescher, C. and Prakapenka, V.B. (2018) Structure analysis and conditions of formation of akimotoite in the Tenham chondrite. Meteoritics and Planetary Science, 53, 62-74.

Tsuchiya, T. (2003) First-principles prediction of the *P-V-T* equation of state of gold and the 660-km discontinuity in Earth's mantle. Journal of Geophysical Research, 108, B10, 2462.

Vacher, P., Mocquet, A. and Sotin, C. (1998) Computation of seismic profiles from mineral physics: the importance of the non-olivine components for explaining the 660 km depth discontinuity. Physics of the Earth and Planetary Interiors, 106, 275-298.

Van der Hilst, R., Engdahl, R., Spakman, W. and Nolet, G. (1991) Tomographic imaging of subducted lithosphere below northwest Pacific island arcs. Nature, 353, 37-43.

Voigt, W. (1928) Lehrbuch der Kristallphysik (mit Ausschluß der Kristalloptik), Teubner, Stuttgart.

Wang, Y., Uchida, T., Zhang, J., Rivers, M.L. and Sutton, S.R. (2004) Thermal equation of state of akimotoite $MgSiO_3$ and effects of the akimotoite-garnet transformation on seismic structure near the 660 km discontinuity. Physics of the Earth and Planetary Interiors, 143-144, 57-80.

Watt, J.P., Davies, G.F. and O'Connell, R.J. (1976) The elastic properties of composite materials. Review of Geophysics, 14, 541-563.

Weidner, D.J. and Ito, E. (1985) Elasticity of $MgSiO_3$ in the ilmenite phase. Physics of the Earth and Planetary Interiors, 40, 65-70.

Weidner, D.J. and Wang, Y. (2000) Earth's Deep Interior: Mineral Physics and Tomography From the Atomic to the Global Scale. Geophysical Union. Phase Transformations: Implications for Mantle Structure, pp. 215-235.

Whitfield, C.H., Brody, E.M. and Bassett, W.A. (1976) Elastic moduli of NaCl by Brillouin scattering at high pressure in a diamond anvil cell. Review of Scientific Instruments, 47, 942.

Wookey, J. Kendall, J.M. and Barruol, G. (2002) Mid-mantle deformation inferred from seismic anisotropy. Nature, 415, 777-780.

Xu, W., Lithgow-Bertelloni, C., Stixrude, L. and Ritsema, J. (2008) The effect of bulk composition and temperature on mantle seismic structure. Earth and Planetary Science Letters, 275, 70-79.

Yamanaka, T., Komatsu, Y., Sugahara, M. and Nagai, T. (2005) Structure change of $MgSiO_3$, $MgGeO_3$, and $MgTiO_3$ ilmenites under compression. American Mineralogist, 90, 1301-1307.

Yu, Y.G., Wentzcovitch, R.M., Vinograd, V.L. and Angel, R.J. (2011) Thermodynamic properties of $MgSiO_3$ majorite and phase transitions near 660 km depth in $MgSiO_3$ and Mg_2SiO_4: A first principle study. Journal of Geophysical Research, 116, B02208.

Zhang, Y., Zhao, D. and Matsui, M. (2005) Anisotropy of akimotoite: A molecular dynamics study. Physics of the Earth and Planetary Interiors, 151, 309-319.

Zhang, Y., Wang, Y., Wu, Y., Bina, C.R., Jin, Z. and Dong, S. (2013) Phase transitions of harzburgite and buckled slab under eastern China. Geochemistry Geophysics Geosystems, 14, 1182-1199.

Zhou, C., Gréaux, S., Nishiyama, N., Irifune, T. and Higo, Y. (2014) Sound velocities measurement on $MgSiO_3$ akimotoite at high pressures and high temperatures with simultaneous in situ X-ray diffraction and ultrasonic study. Physics of the Earth and Planetary Interiors, 228, 97-105.

Appendix

A1: Atomic coordinates and displacement parameters

Table A-1: *Atom coordinates, equivalent isotropic and anisotropic displacement parameters obtained for MgSiO₃ akimotoite in DAC3.*

	x	y	z	U_{11}	U_{22}	U_{33}	U_{23}	U_{13}	U_{12}	U_{iso}
0.0001(1) GPa										
Mg	0.0000	0.0000	0.3599(1)	0.0040(6)	0.0040(6)	0.0044(7)	0.0000	0.0000	0.0020(3)	0.0042(4)
Si	0.0000	0.0000	0.1578(1)	0.0023(5)	0.0023(5)	0.0023(5)	0.0000	0.0000	0.0011(2)	0.0023(4)
O	0.3222(4)	0.0372(4)	0.2402(1)	0.0038(5)						
2.1(1) GPa										
Mg	0.0000	0.0000	0.3598(1)	0.0048(4)	0.0048(4)	0.0051(5)	0.0000	0.0000	0.0024(2)	0.0049(3)
Si	0.0000	0.0000	0.1577(1)	0.0028(4)	0.0028(4)	0.0045(4)	0.0000	0.0000	0.0014(2)	0.0034(3)
O	0.3215(3)	0.0363(4)	0.2403(1)	0.0044(4)						
8.04(1) GPa										
Mg	0.0000	0.0000	0.3593(1)	0.0033(5)	0.0033(5)	0.0047(6)	0.0000	0.0000	0.0016(3)	0.0037(4)
Si	0.0000	0.0000	0.1573(1)	0.0020(4)	0.0020(4)	0.0033(4)	0.0000	0.0000	0.0010(2)	0.0025(3)
O	0.3214(4)	0.0357(4)	0.2409(1)	0.0034(4)						
10.83(3) GPa										
Mg	0.0000	0.0000	0.3592(1)	0.0054(5)	0.0054(5)	0.0055(6)	0.0000	0.0000	0.0027(3)	0.0054(4)
Si	0.0000	0.0000	0.1573(1)	0.0039(5)	0.0039(5)	0.0039(5)	0.0000	0.0000	0.0019(2)	0.0039(4)
O	0.3221(5)	0.0353(5)	0.2411(1)	0.0051(4)						

Table A-2: *Atom coordinates, equivalent isotropic and anisotropic displacement parameters obtained for single-crystals in the MgSiO₃ akimotoite-Al₂O₃ corundum solid solution.*

	x	y	z	U_{11}	U_{22}	U_{33}	U_{23}	U_{13}	U_{12}	U_{iso}
Ak100										
Mg	0.0000	0.0000	0.3601(1)	0.0062(2)	0.0062(2)	0.0062(2)	0.0000	0.0000	0.0031(1)	0.0062(1)
Si	0.0000	0.0000	0.1578(1)	0.0044(1)	0.0044(1)	0.0050(2)	0.0000	0.0000	0.0022(1)	0.0046(1)
O	0.3221(1)	0.0365(1)	0.2402(1)	0.0046(2)	0.0057(2)	0.0057(2)	0.0008(1)	0.0002(1)	0.0024(2)	0.0054(1)
Ak99										
Mg	0.0000	0.0000	0.3601(1)	0.0040(2)	0.0040(2)	0.0043(2)	0.0000	0.0000	0.0020(1)	0.0041(1)
Al	0.0000	0.0000	0.3601(1)	0.0040(2)	0.0040(2)	0.0043(2)	0.0000	0.0000	0.0020(1)	0.0041(1)
Si	0.0000	0.0000	0.1577(1)	0.0025(1)	0.0025(1)	0.0035(2)	0.0000	0.0000	0.0013(1)	0.0029(1)
O	0.3222(2)	0.0362(2)	0.2403(1)	0.0029(2)	0.0042(2)	0.0041(3)	0.0007(2)	-0.0001(2)	0.0017(2)	0.0038(1)
Cor75										
Al	0.0000	0.0000	0.3524(1)	0.0052(2)	0.0052(2)	0.0073(3)	0.0000	0.0000	0.0026(1)	0.0059(2)
Mg	0.0000	0.0000	0.3524(1)	0.0052(2)	0.0052(2)	0.0073(3)	0.0000	0.0000	0.0026(1)	0.0059(2)
Si	0.0000	0.0000	0.3524(1)	0.0052(2)	0.0052(2)	0.0073(3)	0.0000	0.0000	0.0026(1)	0.0059(2)
O	-0.3062(2)	0.0000	0.2500	0.0089(3)	0.0094(4)	0.0084(4)	-0.0011(2)	-0.0005(1)	0.0047(2)	0.0088(2)
Cor80										
Al	0.0000	0.0000	0.3522(1)	0.0054(3)	0.0054(3)	0.0067(3)	0.0000	0.0000	0.0027(1)	0.0058(2)
Mg	0.0000	0.0000	0.3522(1)	0.0054(3)	0.0054(3)	0.0067(3)	0.0000	0.0000	0.0027(1)	0.0058(2)
Si	0.0000	0.0000	0.3522(1)	0.0054(3)	0.0054(3)	0.0067(3)	0.0000	0.0000	0.0027(1)	0.0058(2)
O	-0.3065(2)	0.0000	0.2500	0.0084(3)	0.0087(4)	0.0077(4)	-0.0010(3)	-0.0005(1)	0.0044(2)	0.0082(3)

	x	y	z	U_{11}	U_{22}	U_{33}	U_{23}	U_{13}	U_{12}	U_{iso}
Cor81										
Al	0.0000	0.0000	0.3521(1)	0.0056(3)	0.0056(3)	0.0067(3)	0.0000	0.0000	0.0028(1)	0.0060(2)
Mg	0.0000	0.0000	0.3521(1)	0.0056(3)	0.0056(3)	0.0067(3)	0.0000	0.0000	0.0028(1)	0.0060(2)
Si	0.0000	0.0000	0.3521(1)	0.0056(3)	0.0056(3)	0.0067(3)	0.0000	0.0000	0.0028(1)	0.0060(2)
O	-0.3066(2)	0.0000	0.2500	0.0080(3)	0.0083(4)	0.0077(4)	-0.0008(2)	-0.0004(1)	0.0042(2)	0.0080(2)
Cor92										
Al	0.0000	0.0000	0.3522(1)	0.0049(3)	0.0049(3)	0.0053(3)	0.0000	0.0000	0.0024(1)	0.0050(2)
Mg	0.0000	0.0000	0.3522(1)	0.0049(3)	0.0049(3)	0.0053(3)	0.0000	0.0000	0.0024(1)	0.0050(2)
Si	0.0000	0.0000	0.3522(1)	0.0049(3)	0.0049(3)	0.0053(3)	0.0000	0.0000	0.0024(1)	0.0050(2)
O	-0.3063(2)	0.0000	0.2500	0.0063(3)	0.0061(4)	0.0061(4)	0.0003(3)	0.0002(1)	0.0031(2)	0.0062(3)
Cor97										
Al	0.0000	0.0000	0.3522(1)	0.0049(2)	0.0049(2)	0.0044(3)	0.0000	0.0000	0.0025(1)	0.0047(2)
Mg	0.0000	0.0000	0.3522(1)	0.0049(2)	0.0049(2)	0.0044(3)	0.0000	0.0000	0.0025(1)	0.0047(2)
Si	0.0000	0.0000	0.3522(1)	0.0049(2)	0.0049(2)	0.0044(3)	0.0000	0.0000	0.0025(1)	0.0047(2)
O	-0.3065(2)	0.0000	0.2500	0.0055(3)	0.0056(3)	0.0050(3)	0.0007(2)	0.0003(1)	0.0028(2)	0.0054(2)
Cor100										
Al	0.0000	0.0000	0.3522(1)	0.0044(2)	0.0044(2)	0.0053(3)	0.0000	0.0000	0.0022(1)	0.0047(2)
O	0.3063(2)	0.0000	0.2500	0.0047(3)	0.0049(4)	0.0060(4)	0.0009(2)	0.0005(1)	0.0024(2)	0.0052(2)

A2: Thermodynamic calculations

The thermo-elastic self-consistent model by Stixrude and Lithgow-Bertelloni (2005) is used to determine the elastic properties of akimotoite at high pressure and temperature. The Helmholtz free energy $F(V,T)$ is described by

$$F(V,T) = F_0 + F_C(V,T_0) + [F_{TH}(V,T) - F_{TH}(V,T_0)] \qquad \text{(eq. A1)}$$

which is divided into three terms: F_0 is the reference term, $F_C(V,T_0)$ describes a cold compression at room temperature and ΔF_{TH} is the thermal contribution. V is the molar volume, T is the temperature and 0 indicates values at room pressure and temperature. $F_C(V,T_0)$ is calculated using the BM EoS according to:

$$F_C(V,T_0) = 9K_0V_0(f^2/2 + a_1 f^3/3) \qquad \text{(eq. A2)}$$

with

$$f = \frac{1}{2}\left[\left(\frac{V_0}{V}\right)^{2/3} - 1\right] = -\varepsilon \qquad \text{(eq. A3)}$$

and

$$a_1 = \frac{3}{2}(K_0' - 4) \qquad \text{(eq. A4)}$$

where K_0 and K_0' are the isothermal bulk modulus and its pressure derivative.

The Helmholtz free energy thermal contribution $F_{TH}(V,T_0)$ of the solid end-members is determined by the formula

$$F_{TH}(V,T_0) = 9nRT \left(\frac{T}{\theta}\right)^3 \int_0^t ln(1 - e^{-t})t'dt \qquad \text{(eq. A5)}$$

where n is the number of atoms in the akimotoite unit cell, R is the gas constant, $t = \frac{\theta}{T}$ and the Debye temperature θ is calculated according to:

$$\theta = \theta_0 exp\left[\frac{\gamma_0 - \gamma}{q_0}\right] \qquad \text{(eq. A6)}$$

with the Grüneisen parameter γ defined as:

$$\gamma = \gamma_0 \left(\frac{V}{V_0}\right)^{q_0} \tag{eq. A7}$$

where q_0 is a constant.

The Gibbs free energy is calculated from the Helmholtz free energy $F(V,T)$ at the volume V of interest according to:

$$G_{(P,T)} = F_{(V,T)} + PV \tag{eq. A8}$$

where the pressure P is described by two separate terms

$$P = P_{BM} + P_{TH} \tag{eq. A9}$$

with

$$P_{BM} = 3K_0 f (2f + 1)^{5/2} (1 - fa) \tag{eq. A10}$$

and

$$P_{TH} = \frac{\gamma}{V} \left[E_{TH(V,T)} - E_{TH(V,T_0)}\right] \tag{eq. A11}$$

$E_{TH(V,T)}$ is calculated using:

$$E_{TH(V,T)} = 9nRT \left(\frac{T}{\theta}\right)^3 \int_0^t \frac{t^3}{(e^t - 1)} dt \tag{eq. A12}$$

Acknowledgements

(Eidesstattliche) Versicherungen und Erklärungen

(§ 9 Satz 2 Nr. 3 PromO BayNAT)

Hiermit versichere ich eidesstattlich, dass ich die Arbeit selbstständig verfasst und keine anderen als die von mir angegebenen Quellen und Hilfsmittel benutzt habe (vgl. Art. 64 Abs. 1 Satz 6 BayHSchG).

(§ 9 Satz 2 Nr. 3 PromO BayNAT)

Hiermit erkläre ich, dass ich die Dissertation nicht bereits zur Erlangung eines akademischen Grades eingereicht habe und dass ich nicht bereits diese oder eine gleichartige Doktorprüfung endgültig nicht bestanden habe.

(§ 9 Satz 2 Nr. 4 PromO BayNAT)

Hiermit erkläre ich, dass ich Hilfe von gewerblichen Promotionsberatern bzw. -vermittlern oder ähnlichen Dienstleistern weder bisher in Anspruch genommen habe noch künftig in Anspruch nehmen werde.

(§ 9 Satz 2 Nr. 7 PromO BayNAT)

Hiermit erkläre ich mein Einverständnis, dass die elektronische Fassung meiner Dissertation unter Wahrung meiner Urheberrechte und des Datenschutzes einer gesonderten Überprüfung unterzogen werden kann.

(§ 9 Satz 2 Nr. 8 PromO BayNAT)

Hiermit erkläre ich mein Einverständnis, dass bei Verdacht wissenschaftlichen Fehlverhaltens Ermittlungen durch universitätsinterne Organe der wissenschaftlichen Selbstkontrolle stattfinden können.

……………………………………………………………………………………….

Ort, Datum, Unterschrift